Journal of
Mechanics of
Materials and Structures

See inside back cover or http://www.jomms.org for submission guidelines.

RELIABILITY OF FIRST-ORDER SHEAR DEFORMATION MODELS FOR SANDWICH BEAMS

LORENZO BARDELLA

We are interested in sandwich beams whose skin may be *thick* (as defined by H. G. Allen) and whose core stiffness along the sandwich longitudinal axis may be large enough to influence the deflection (that is, we also account for nonantiplane sandwiches), whereas the core is such that it is allowed to disregard its deformability along its height (the direction of the applied load). For such sandwiches we are particularly interested in investigating the reliability of simple models, such as the first-order shear deformation models, for accurate computation of the deflection in the linear elastic range. We therefore compare different theories on the basis of finite element simulations and focus on the case of a propped cantilever beam supporting a uniform load. In fact, this boundary value problem leads to slightly different conclusions than those previously drawn based on statically determinate cases, such as in three-point bending. The analysis suggests that known models may be largely inaccurate in predicting sandwich behaviour under bending and shear, depending on a peculiarity of the actual sandwich kinematics indirectly describing the interaction between skins and core, in turn due both to material and geometrical properties and to boundary conditions.

1. Introduction

We focus on the reliability of simple models for the accurate computation of the *macroscopic* deflection of sandwich beams, subjected to bending and shear, in the linear elastic range. We use the term macroscopic, as in [Mai et al. 2007], to indicate that part of the deformation that in a homogeneous beam would be described by the Timoshenko theory; this means that we neglect the deformation due to local stress concentrations, which may be extremely important, under certain boundary conditions, in sandwiches having extremely soft cores along the thickness direction [Frostig et al. 1992]. In particular, in the analytical models presented, we will always consider cores able to keep skin distance constant during deformation, besides, of course, being able to transmit shear stresses between the skins. Finite element simulations will show that this is true for quite a large ratio between the elastic moduli of skins and core, provided that the boundary conditions are properly modelled. We will also consider sandwiches whose core stiffness along the longitudinal axis may be relevant, as this may happen in some important applications [Bunn and Mottram 1993; Bardella and Genna 2001]; in other words, the sandwiches here analysed are not necessarily *antiplane*, a term introduced by Allen [1969] to mean a sandwich whose core has negligible normal stress along the longitudinal axis, so that the shear stresses may be taken as uniform.
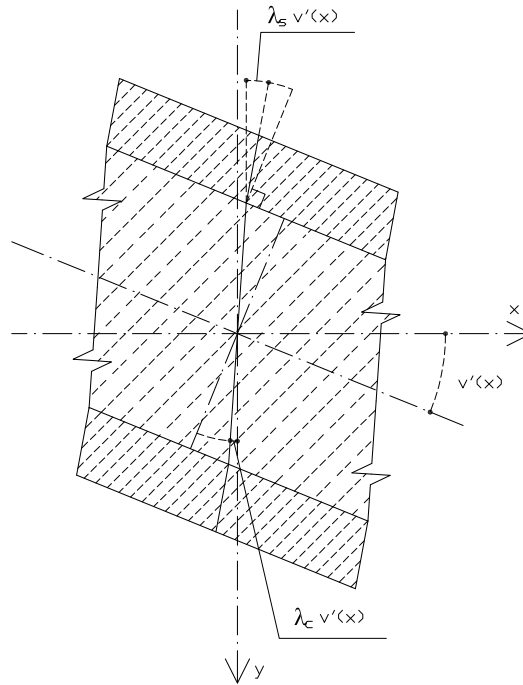
Figure 1. Parameters used for modelling the kinematics of a sandwich beam having identical skins.

We restrict our attention to sandwiches whose skins have identical geometrical and mechanical properties.[1] Also, the load is symmetric with respect to the width of the beam, so that there is no torsion.

It is well known that the relatively high shear compliance of sandwich beams makes an important contribution to their macroscopic deflection [Allen 1969]. Unfortunately, because of the complex kinematics involved, the analytical computation of such a deflection is quite a difficult task, even in the linear elastic range. The relevant kinematics can be approximately represented as in Figure 1. It consists of a piecewise linear warping described by three unknown functions v, λ_c, and λ_s, such that $v(x)$ is the deflection of the sandwich longitudinal axis x and, denoting with $'$ a derivative with respect to x, $\lambda_c(x)v'(x)$ and $\lambda_s(x)v'(x)$ are the total cross section rotations of the core and of the skins, respectively. This description has been used in [Bardella and Genna 2000] as an extension of the kinematics adopted by Allen [1969] (who assumed $\lambda_s = 1$), in order to also account for the effect of not-so-thin skins. Yu [1959] and Krajcinovic [1971] also used the same piecewise linear kinematics for the flexural problem,[2] but they described it in terms of different sets of independent functions of x. Krajcinovic choice allows one to uncouple the Euler–Lagrange equations obtained by minimising the total potential energy (TPE) functional, but the further differentiation required to obtain such a simplification makes things harder concerning the specification of the boundary conditions.

---

[1]The extension of the methods described to the case of unequal skins is conceptually simple, albeit analytically entangled.

[2]The kinematics employed in [Krajcinovic 1971] also account for the core compressibility along y and for the bulging; however, these modes of deformation turn out to be related to the axial problem (for which the beam remains straight), uncoupled to the bending problem.

A considerable amount of literature exists on laminate beam models based on kinematics richer than the linear along y involved in the Timoshenko beam model, where transverse normal lines remain straight during deformation, but inclined with respect to the longitudinal axis depending on the amount of shear; this simple model for laminate beams is referred to as first-order shear deformation (FOSD) theory (see, for example, the review of Ghugal and Shimpi [2001]). The zigzag kinematics described in Figure 1 is the base for the so-called discrete-layer theories, often more accurate, but computationally more difficult to deal with than the equivalent single-layer theories; the latter define the displacement field along the longitudinal axis x as a C^∞ continuous polynomial function of y. Examples of single-layer theories are the third-order model of Silverman [1980], which applies to thick-skinned and nonantiplane sandwiches as those here concerned, or the second and third-order shear deformation theories of Khdeir and Reddy [1997], applied to cross-ply laminated beams. More insight on the distinctions among different approaches for the analysis of laminate structures, albeit for plates, can be found in [Yu et al. 2008] and references therein.

Here, in order to test, discuss, and get insight on the reliability of FOSD models (the simplest among the equivalent single-layer models), we compare their predictions with those of models based on the piecewise linear kinematics of Figure 1 and the results of finite element simulations.

In particular, we focus on a propped cantilever sandwich beam supporting a uniform transversal load. This example is of particular interest since, contrary to some statically determinate structures (such as the three-point bending [Bardella and Genna 2000], the four-point bending, and the simply-supported beam subjected to uniform load [Minelli 2007]), its deflection is inaccurately represented by all of the following models:

(i) The model ensuing from the analytical procedure put forward by Bardella and Genna [2000] in order to minimise the TPE, written in terms of the zigzag kinematics of Figure 1, based on the assumption that λ_c and λ_s are constant (that is, independent upon x).

(ii) The model for thick skins and nonantiplane core deriving from Allen's superposition theory [Allen 1969] (still one of the most quoted models for sandwiches).

(iii) The FOSD theory in which the shearing rigidity [Timoshenko and Gere 1990] is evaluated on the basis of the Jourawsky approach [1856] and an energy principle, as accomplished by Bardella and Genna [2000; 2001] (see also [Bert 1973]).

Instead, the finite element solution of the propped cantilever sandwich beam is pretty well represented by the TPE approach in which the variation of λ_c and λ_s along x is accounted for, and this can be recognised by resorting to the Ritz method.

This notwithstanding, the third method listed above, which can be reasonably assumed to be the best possible FOSD model, may be extremely useful in the design because of its simplicity and accuracy (as already been shown for a few cases in [Bardella and Genna 2001; Minelli 2007]; see also [Gordaninejad and Bert 1989]). On the basis of our analysis, we then put forward that this method can be successfully employed when the structure is such that λ_c and λ_s are approximately independent on x, so that, in our opinion, one of the main goals becomes reaching a deep insight on this topic.

Outline of the paper. The paper is organised as follows. In Section 2 we provide and discuss the formulae relevant for the examples concerned in the paper, and also summarise the theory related to the methods

(i) and (iii) listed above, originally developed in [Bardella and Genna 2000]. In particular, Section 2.1 deals with the approach based on the TPE, in Section 2.2 we give the relevant results related to Allen's superposition method, and Section 2.3 summarises the FODT exploiting Jourawsky's approximate theory of shear and, for the sake of completeness, also considers other possible FOSD methods, including the "thin skin" approximation [Allen 1969]. In Section 3 we compare the results obtained from the application of the above theoretical models with those of finite element simulations. We close, in Section 4, with a discussion and some remarks.

2. The linear elastic deflection of a sandwich beam

We consider a sandwich beam of total length l and width b, consisting of three homogeneous layers. The sandwich has skins with identical thickness, t, and identical mechanical properties, whose relevant Young and shear moduli are denoted by E_s and G_s, respectively. The thickness of the core is indicated with the symbol c, so that the distance between the centres of the two skins is $d = c + t$. The relevant Young and shear moduli of the core are E_c and G_c. Let us recall that, with reference to the terminology used in [Allen 1969], we are interested in a sandwich with thick skins and a nonantiplane core.

2.1. *The total potential energy approach.* The TPE minimum principle requires the choice of an admissible displacement field over the sandwich. This approach leads rapidly to quite involved computations. In [Allen 1969] it is used only in conjunction with the Ritz method, to obtain approximate solutions for sandwiches with antiplane core and skins whose shear deformability turns out to be negligible. As said, we refer our calculations to the kinematics sketched in Figure 1, from which it is straightforward to compute the longitudinal strain ε_x and the engineering shear strain γ_{xy}, then the relevant normal and shear stresses,[3] and write the TPE functional Ψ for a sandwich beam subjected to a transversal (meaning acting along y) force P and a transversal distributed load $q(x)$ as

$$\Psi(v, \lambda_c, \lambda_s) = \frac{G_c bc}{2} \int_0^l \left[(1 - \lambda_c) v' \right]^2 dx + \frac{E_c bc^3}{24} \int_0^l \left[\left(\lambda_c v' \right)' \right]^2 dx + G_s bt \int_0^l \left[(1 - \lambda_s) v' \right]^2 dx$$

$$+ \frac{E_s bt^3}{12} \int_0^l \left[\left(\lambda_s v' \right)' \right]^2 dx + \frac{E_s bt}{4} \int_0^l \left\{ \left[(c\lambda_c + t\lambda_s) v' \right]' \right\}^2 dx - P\delta - \int_0^l q(x) v(x) \, dx, \quad (1)$$

in which δ is the displacement of the point where P is applied.[4] The actual solution of the problem corresponds to

$$\min_{(v, \lambda_c, \lambda_s) \in \mathcal{H}} \Psi(v, \lambda_c, \lambda_s),$$

---

[3]The computed normal and shear stresses are respectively $\sigma_x^{(i)} = E_i \varepsilon_x^{(i)}$ and $\tau_{xy}^{(i)} = G_i \gamma_{xy}^{(i)}$, with $i = s$ in the skins and $i = c$ in the core. For isotropic materials the *correct* constitutive law would be $\sigma_x^{(i)} = [E_i / (1 - \nu_i^2)] \varepsilon_x^{(i)}$, where ν_i is the Poisson ratio, which links the longitudinal strain with the longitudinal stress for the beam plane stress state characterised by the further kinematic constraint of imposing a vanishing direct strain component along y. Anyway, since the use of that relation would make the beam too stiff, we replace it with the Young modulus E_i, as usual in the engineering calculations for homogeneous beams. This is actually based on the hypothesis of taking a zero direct stress component along y, so $\sigma_y = 0$; such a stress assumption is incompatible with the kinematic approach which the TPE principle is based on, but, as is well known, works for homogeneous beams. The removal of this assumption is a key point in the higher-order theory proposed by Frostig et al. [1992], in which the sandwich core is treated as a plane stress continuum.

[4]If the sandwich were subjected also to axial loading (by, for instance, a distributed load $r(x)$), Ψ would also be dependent on the centre displacement component along x, u_c (see [Krajcinovic 1971] about how to account also for the bulging deformation

where $\mathcal{H}$ is the set enclosing all the compatible fields. Usually the only requirement on λ_c and λ_s is that they be suitably smooth, whereas v must always satisfy some essential boundary conditions, because in any constrained section x_0 at least one of the values $v(x_0)$ and $v'(x_0)$ is preassigned. A case in which one also has to impose essential boundary conditions on λ_c and λ_s is that of a simply-supported beam end with no warping allowed, for which $\lambda_c(x_0) = \lambda_s(x_0)$ (or even $\lambda_c(x_0) = \lambda_s(x_0) = 1$); however, this case, which has been shown to lead to an unfavourable sandwich behaviour [Krajcinovic 1971], will not be considered here.

Within this approach, the bending moment $M(x)$ and the shear force $V(x)$ are given by

$$M = \tfrac{1}{6} E_s bt^3 (\lambda_s v')' + \tfrac{1}{2} E_s btd \big[(c\lambda_c + t\lambda_s)v' \big]' + \tfrac{1}{12} E_c bc^3 (\lambda_c v')', \tag{2}$$

and

$$V = [G_c bc(1 - \lambda_c) + 2G_s bt(1 - \lambda_s)]v'. \tag{3}$$

The TPE approach proposed by Allen [1969] is characterised by neglecting the shear compliance of the skins, $G_s \to \infty$. In this case, it is immediately recognisable from the functional (1) that the minimum of $\Psi(v, \lambda_c, \lambda_s)$ is attained when $\lambda_s = 1$ and $\lambda_c \in [-t/c, 1]$, the limits of this range corresponding to both $G_c \to 0$ and $E_c \to 0$ or $G_c \to \infty$, respectively. The fact that λ_c can be either positive or negative implies that this modelling allows the core to be subjected to normal stresses, σ_x, whose moment resultant M_c has opposite sign with respect to the moment M applied to the whole cross section, even though, under this circumstance, M_c is usually far smaller than M. This behaviour, here and henceforth called "normal stress inversion", will be appreciated in discussing the finite element simulation described in Section 3.2.

Moreover, let us note that even though the same elastic moduli are chosen for skins and core, the resulting model remains richer than that described by the Timoshenko theory for homogeneous beams since in this case, as well as in general, $\lambda_c \neq \lambda_s$, and the warping still occurs. On the other hand, by taking the limit $t \to 0$, the model approximates that of Timoshenko in which the shearing rigidity, equal to $G_c bc$, is, as is well known, overestimated.

Only by imposing $\lambda_c(x) = \lambda_s(x)$ it is possible to single out from (2) the *effective* bending stiffness

$$D = E_s \left(\frac{bt^3}{6} + \frac{btd^2}{2} \right) + E_c \frac{bc^3}{12}. \tag{4}$$

Although $\lambda_c(x) = \lambda_s(x)$ seems to be a crude approximation, for it means neglecting the warping, (4) is a completely standard and widely accepted result for a thick skinned and nonantiplane sandwich (see, for example, [Allen 1969; Zenkert 1997], and the methods of Sections 2.2 and 2.3). Hence, in the TPE approach the *hidden* bending stiffness should be lower than D.

Setting to zero the first variation of (1) provides a nonlinear differential system of three Euler–Lagrange equations in the three unknown functions $v(x)$, $\lambda_c(x)$, and $\lambda_s(x)$, and the natural boundary conditions. Solving the Euler–Lagrange equations is complicated, so we skip it, whereas it is of some interest to

---

mode), as

$$\Psi(v, \lambda_c, \lambda_s, u_c) = \tfrac{1}{2} G_c bc \int_0^l (1 - \lambda_c)^2 (v')^2 dx + \tfrac{1}{24} E_c bc^3 \int_0^l (\lambda_c' v' + \lambda_c v'')^2 dx$$
$$+ G_s bt \int_0^l (1 - \lambda_s)^2 (v')^2 dx + \tfrac{1}{4} E_s bt \int_0^l \big[(c\lambda_c' + t\lambda_s')v' + (c\lambda_c + t\lambda_s)v'' + u_c' \big]^2 dx$$
$$+ E_c bc \int_0^l (u_c')^2 dx + \tfrac{1}{12} E_s bt^3 \int_0^l (\lambda_s' v' + \lambda_s v'')^2 dx - P\delta - \int_0^l q(x)v(x)dx - \int_0^l r(x)u_c(x)dx.$$

consider the natural boundary conditions related to λ_c and λ_s. In fact, in the case of a simply-supported, free to warp, and moment-free beam end (for example, in $x = x_0$), a plausible set of conditions satisfying the natural boundary conditions reads

$$v''(x = x_0) = 0, \qquad \lambda_c'(x = x_0) = 0, \qquad \lambda_s'(x = x_0) = 0. \tag{5}$$

In particular, in the three-point bending, such conditions hold both in $x = 0$ and $x = l$.

The λ-constrained method. As proposed in [Bardella and Genna 2000], the TPE can be simplified if λ_c and λ_s are assumed to be constant (that is, independent upon x). This is a compatible restriction and, also, it is at least consistent with the natural boundary conditions (5) for the case of a simply-supported beam section. This approximation, whose reliability will be discussed later on, allows the derivation of analytical solutions. The TPE functional (1) becomes

$$\Psi_C(v, \lambda_c, \lambda_s) = \frac{G_c bc}{2}(1 - \lambda_c)^2 \int_0^l (v')^2 dx + \frac{E_c bc^3}{24}\lambda_c^2 \int_0^l (v'')^2 dx + G_s bt(1 - \lambda_s)^2 \int_0^l (v')^2 dx$$
$$+ \frac{E_s bt}{4}(c\lambda_c + t\lambda_s)^2 \int_0^l (v'')^2 dx + \frac{E_s bt^3}{12}\lambda_s^2 \int_0^l (v'')^2 dx - \int_0^l q(x)v(x)\,dx - P\delta.$$

By imposing the stationarity of Ψ_C with respect to the kinematic parameters, v, λ_c, and λ_s, one obtains

 (i) an ordinary fourth-order differential equation governing the deformed shape $v(x)$,

 (ii) the natural boundary conditions on $v(x)$, and

(iii) two optimum integral equations furnishing the values of both λ_c and λ_s, in terms of $v(x)$, as

$$\lambda_c = \frac{12G_c \int_0^l (v')^2 dx - 6E_s t^2 \lambda_s \int_0^l (v'')^2 dx}{12G_c \int_0^l (v')^2 dx + (6E_s tc + E_c c^2) \int_0^l (v'')^2 dx}, \qquad \lambda_s = \frac{12G_s \int_0^l (v')^2 dx - 3E_s tc\lambda_c \int_0^l (v'')^2 dx}{12G_s \int_0^l (v')^2 dx + 4E_s t^2 \int_0^l (v'')^2 dx}. \tag{6}$$

Here and henceforth we will refer to this strategy for modelling the sandwich deflection as the "λ-constrained method based on the TPE". In the following, for the simple structures of interest here, we will provide analytical solutions for $v(x)$, to be coupled with (6) and given in terms of the parameter

$$\alpha = \sqrt{\frac{12G_c c(1 - \lambda_c)^2 + 24G_s t(1 - \lambda_s)^2}{2E_s t[t^2\lambda_s^2 + 3(c\lambda_c + t\lambda_s)^2] + E_c c^3\lambda_c^2}}, \tag{7}$$

conveniently defined in integrating the Euler–Lagrange equation governing $v(x)$. From the complexity of these solutions, it is evident that this method becomes much too cumbersome for more complicated structures.

Now we try to estimate the *effective* bending stiffness within this method. The assumed independence of λ_c and λ_s on x allows one to define an average curvature

$$\overline{\chi} = \frac{\lambda_c c + \lambda_s t}{d}v'',$$

so that (2) can be rewritten as

$$M = \left(D + \frac{btc}{12}(\lambda_s - \lambda_c)\frac{2E_s t^2 - E_c c^2}{\lambda_c c + \lambda_s t}\right)\overline{\chi}. \tag{8}$$

In regular sandwiches the skins are stiffer than the core, so that $\lambda_s > \lambda_c$ and the sign of the term added to D in the above relation coincides with the sign of

$$\frac{2E_s t^2 - E_c c^2}{\lambda_c c + \lambda_s t}.$$

This is difficult to foresee, although it easily turns out to be negative if the skins are very thin or the core is almost as stiff as the skins.

Three-point bending. In this case $\delta = v(x = l/2)$ is the maximum deflection, $v(x = 0) = v(x = l) = 0$, and $q(x) = 0$. The integration of the Euler–Lagrange equation for v furnishes

$$v(x) = \begin{cases} \dfrac{P\left[\alpha x - \operatorname{sech}(\alpha l/2)\sinh(\alpha x)\right]}{\alpha^3\left[E_s bt^3\lambda_s^2/3 + E_s bt(c\lambda_c + t\lambda_s)^2 + E_c bc^3\lambda_c^2/6\right]}, & x \in [0, l/2], \\ v(l - x), & x \in [l/2, l]. \end{cases} \tag{9}$$

The system constituted by (6)–(7) and (9) can be solved numerically using as initial guesses for α, λ_c, and λ_s the solutions furnished by the Ritz method, by, for instance, approximating $v(x)$ with $\hat{v}(x) = \hat{\delta}\sin(x\pi/l)$. The results of Bardella and Genna [2000; 2001] on three-point bending show a satisfactory accuracy for this method. This therefore gives ground to the hypothesis, also corroborated by the observation (5) about the natural boundary conditions, that in this case λ_c and λ_s are almost constant.

Propped cantilever beam supporting a uniform load p. This case is characterised by $q(x) = p$, $P = 0$, $v(x = 0) = 0$, $v'(x = 0) = 0$, and $v(x = l) = 0$. The integration of the Euler–Lagrange equation for $v(x)$, to be coupled with (6)–(7), reads

$$v(x) = \frac{pl^2}{\alpha^2\left[E_s bt^3\lambda_s^2/3 + E_s bt(c\lambda_c + t\lambda_s)^2 + E_c bc^3\lambda_c^2/6\right]}\left\{ 2\frac{\operatorname{sech}(\alpha l)}{\alpha^2 l^2}[\cosh(\alpha x) - 1] - \left(\frac{x}{l}\right)^2 \right.$$
$$\left. + \frac{2[\operatorname{sech}(\alpha l) - 1] + \alpha^2 l^2}{\alpha^2 l^2[\alpha l - \tanh(\alpha l)]}\left[\tanh(\alpha l)[\cosh(\alpha x) - 1] + \alpha x - \sinh(\alpha x)\right] \right\}. \tag{10}$$

When discussing the results for this case, we will also consider the reaction force R within the support, whose estimate is obtained by evaluating (3) at $x = l$.

The Ritz method. The Ritz method allows the direct, albeit approximated, minimisation of the functional (1), without any constraint on the functions λ_c and λ_s. By exploiting this method, Minelli [2007] has verified that assuming the independence of λ_c and λ_s on x seems to be numerically appropriate for some simply-supported beams subjected to symmetric loading (including three and four-point bending).

Propped cantilever beam subjected to a uniform load. In this paper, we show that the "λ-constrained method based on the TPE" is quite inaccurate for this case, where we can obtain accurate results only by applying the Ritz method to the TPE, by choosing a discretisation dependent on 15 weights, to be determined by setting to zero the first variation of the TPE functional, (1). In particular, λ_s and λ_c are free from essential boundary conditions and have been approximated by means of a third-order polynomial (4 weights) and a seventh-order polynomial (8 weights), respectively, whereas the approximate deflection

$\hat{v}(x)$ has been chosen to depend on 3 weights ($w_1 \equiv \hat{v}(l/2)$, w_2, and w_3) in such a way that the natural boundary condition imposing zero overall moment at the support is a priori fulfilled[5], as

$$\hat{v}(x) = 4w_1\left[3\left(\frac{x}{l}\right)^2 - 5\left(\frac{x}{l}\right)^3 + 2\left(\frac{x}{l}\right)^4\right] + w_2\left[-\frac{5}{8}\left(\frac{x}{l}\right)^2 + \frac{19}{8}\left(\frac{x}{l}\right)^3 - \frac{11}{4}\left(\frac{x}{l}\right)^4 + \left(\frac{x}{l}\right)^5\right]$$
$$+ w_3\left[-\frac{27}{16}\left(\frac{x}{l}\right)^2 + \frac{93}{16}\left(\frac{x}{l}\right)^3 - \frac{41}{8}\left(\frac{x}{l}\right)^4 + \left(\frac{x}{l}\right)^6\right]. \quad (11)$$

2.2. *The Allen superposition method.* We give the formulae for the Allen superposition method [Allen 1969], applied to the cases we are concerned with here. The method was formulated for antiplane sandwiches and then extended to the nonantiplane case by adopting the further approximation that the displacement field along the sandwich core be linear.

Three-point bending. The maximum deflection [Allen 1969] is given by

$$\delta = \frac{Pl^3}{48D} + \frac{Pl}{4\hat{G}\hat{A}}\left(1 - \frac{E_s bt^3}{6D}\right)^2\left(1 - \frac{2}{\alpha_A l}\tanh\frac{\alpha_A l}{2}\right),$$

in which D is the bending stiffness as given by (4),

$$\hat{A} = \frac{bd^2}{c}, \quad \hat{G} = \frac{G_c}{1 + \dfrac{c^2}{6nt(t+c)}}, \quad n = \frac{E_s}{E_c}, \quad \alpha_A = \sqrt{\frac{6\hat{G}\hat{A}}{E_s bt^3\left(1 - \dfrac{1}{1+3(d/t)^2}\right)}}.$$

Note that for the antiplane case $\hat{G} = G_c$.

Propped cantilever beam supporting a uniform load. For this case we have derived the relevant results as follows. Allen's method gives the deflection as the superposition of two transversal displacements as $v(x) = v_1(x) + v_2(x)$, where, for the case concerned here,

$$v_1(x) = -\frac{6}{E_s bt(t^2+3d^2)}\left[\frac{C_1}{\alpha_A^3}\sinh(\alpha_A x) + \frac{C_2}{\alpha_A^3}\cosh(\alpha_A x) + \frac{p}{6}\left(lx^3 - \frac{x^4}{4}\right) - R\frac{x^3}{6}\right] + C_4\frac{x^2}{2} + C_5 x + C_6,$$

$$v_2(x) = \frac{6}{\alpha_A^2 E_s bt^3}\left[\frac{C_1}{\alpha_A}\sinh(\alpha_A x) + \frac{C_2}{\alpha_A}\cosh(\alpha_A x) + \frac{p}{2}(2lx - x^2) - Rx\right] + C_3,$$

in which R is the reaction force within the support (at $x = l$) that, together with the six integration constants C_i ($i = 1, \ldots, 6$) must be obtained by imposing seven independent boundary conditions. In Allen's method some boundary conditions are arbitrary. Based on the finite element model employed in order to test the various theories presented, we have chosen the boundary conditions

$$v_1(x = 0) = 0, \qquad v_1'(x = 0) = 0, \qquad v_1(x = l) = 0,$$
$$v_2(x = 0) = 0, \qquad v_2'(x = 0) = 0, \qquad v_2(x = l) = 0,$$
$$\left(1 + \frac{3d^2}{t^2}\right)v_1''(x = l) + v_2''(x = l) = 0,$$

---

[5]The λ-constrained method is useful also because it could be exploited to obtain good shape functions, such as (10) for the propped cantilever beam. However, finding the optimum discretisation for the functions involved in the TPE is beyond the scope of this paper.

the last one imposing that the overall moment must vanish at $x = l$. In solving this system a limit of this model immediately emerges: the estimate of the reaction R turns out to be equal to the classical value of the homogeneous Bernoulli beam theory, $R = 3pl/8$, independently upon the sandwich geometry and material constants. We obtain for the midspan displacement

$$v\left(\frac{l}{2}\right) = \frac{pl^4}{32 E_s bt\,(t^2 + 3d^2)}\left\{1 + \frac{18}{(\alpha_A l)^2}\left(\frac{d}{t}\right)^2\left[6 - \left(1 + \frac{10}{\alpha_A l}\sinh\frac{\alpha_A l}{2}\right)\operatorname{sech}^2\frac{\alpha_A l}{4}\right]\right\},$$

where, by the way, we would find it artificial to single out a "pure bending term" involving the bending stiffness D given by (4).

2.3. *First-order shear deformation models.*

Beside their analytical complication, both the Allen and the total potential energy methods have other drawbacks, most notably that of failing to yield accurate (or, even, *correct*) results for special cases, such as that of thin skins, or that of a homogeneous beam. For this reason FOSD models are developed in order to try and obtain the simplest possible models able to predict the sandwich deflection. Within this framework, the deflection of a sandwich beam is computed, under general loading and constraint conditions, by exploiting the well known formulae for the homogeneous Timoshenko beam. Each different FOSD model is characterised by a different choice of the shearing rigidity S [Timoshenko and Gere 1990], whereas there seems to be complete agreement among researchers about the use of the bending stiffness D provided by (4).

For statically determinate beams, the maximum deflection reads

$$\delta = \frac{Ql^3}{\omega_1 D} + \frac{Ql}{\omega_2 S},$$

where l is the beam length, Q is a proper combination of the transversal loads applied to the beam (Q is the magnitude of their resultant if they are all equally oriented), and ω_1 and ω_2 are numerical constants which depend on both loading and constraint conditions.[6]

Instead, in the case of a propped cantilever beam supporting a uniform transversal load p, the formulae for the midspan displacement and the reaction force within the support, respectively, read

$$v\left(\frac{l}{2}\right) = \frac{pl^4}{24D + 8l^2 S}\left(\frac{21}{16} + \frac{l^2 S}{24D} + \frac{3D}{l^2 S}\right), \qquad R = \frac{12D + 3l^2 S}{24D + 8l^2 S}\,pl.$$

In general, a complicated problem arises from the need to evaluate the sandwich shearing rigidity S.[7] In fact, as already pointed out, the presence of a relatively soft core and of thick skins makes the kinematics of a sandwich beam much different from that of a standard homogeneous beam. Hence, one of the limits of this approach is that it cannot predict local stress concentrations, that, in sandwich beams in which the

---

[6]For instance, for a simply-supported beam subjected to four-point bending,

$$\omega_1 = \frac{32}{\left(1 - l_p/l\right)\left[1 - \frac{1}{3}\left(1 - l_p/l\right)^2\right]}, \qquad \omega_2 = \frac{4}{1 - l_p/l}, \tag{12}$$

where l_p is the distance between the two symmetrically applied concentrated loads, each of magnitude $P/2$, and $Q = P$. Of course the particular case of three-point bending is obtained by setting $l_p = 0$ in (12), so that $\omega_1 = 48$ and $\omega_2 = 4$.

[7]Even for homogeneous beams there is a body of literature, starting with Timoshenko [1921], about how to evaluate the shearing rigidity; see [Renton 1991; Hutchinson 2001] and references therein.

stiffness of the core is much lower than that of the skins, are amplified due to the inapplicability of Saint-Venant's principle. For instance, this approach neither can account for the stiffening due to overhangs (which is instead qualitatively describable with Allen's superposition theory [Allen 1969]), nor has any chance to capture the "normal stress inversion" in the core (as defined in Section 2.1).

A FOSD model based on an energy principle and Jourawsky's theory. Bardella and Genna [2000] have put forward a FOSD model based on the classical approximate shear force treatment by Jourawsky [1856] and on an energy principle by which it is possible to obtain the estimate S_E of the shearing rigidity S by equating the external and internal works of deformation,

$$\frac{V^2}{2S_E} = \frac{1}{2} \int_{A_c} \frac{\tau_c^2}{G_c} dA + \frac{1}{2} \int_{A_s} \frac{\tau_s^2}{G_s} dA, \tag{13}$$

where V is the shear force applied to the sandwich cross section, τ_c and τ_s are the total shear stresses in the core and skins, respectively, and A_c and A_s are the surfaces occupied by the core and the skins (of areas cb and $2tb$, respectively).

By initially assuming that plane sandwich sections remain plane during the deformation, one can develop the classical beam analysis for shear stresses to evaluate them over the sandwich cross section [Jourawsky 1856]. This allows the shear stresses to be estimated by some averages of them.[8] By considering the shear stress components along the shear force direction y and its normal z, Jourawsky's theory estimates $\overline{\tau}_{xz} = 0$ everywhere, whereas

$$\overline{\tau}_{xy}^{(s)} = \frac{V E_s}{2D}(td + c^2/4 - y^2),$$

$$\overline{\tau}_{xy}^{(c)} = \frac{V}{2D}[E_s td + E_c(c^2/4 - y^2)],$$

so that we take $\tau_s \approx \overline{\tau}_{xy}^{(s)}$ and $\tau_c \approx \overline{\tau}_{xy}^{(c)}$ in (13) and, after some lengthy algebra, we can approximate S_E with the following shear rigidity S_J, that can be written by singling out the form factor of a rectangular homogeneous beam as

$$S_J = \frac{5}{6} \left(\frac{1}{bcG_c(1+\alpha_c)} + \frac{4}{2btG_s(1+\alpha_s)} \right)^{-1}, \tag{14}$$

in which the interaction coefficients α_s and α_c, whose values provide a measure of the deviation from the Reuss bound of the shear stiffness, turn out to be, with $n = E_s/E_c$,

$$\alpha_c = \frac{\dfrac{c^3t}{3n} + c^2t^2\left(1 + \dfrac{7}{3n}\right) + 2ct^3\left(7 + \dfrac{4}{3n}\right) + 35t^4 + \dfrac{32t^5}{c} + \dfrac{32t^6}{3c^2}}{\dfrac{c^4}{6n^2} + \dfrac{5c^2td}{3n} + 5t^2d^2}, \tag{15}$$

---

[8]Accounting for the *exact* linear elastic solution for the shear stresses (for example, provided in [Pagano 1970]) would lead to a much too cumbersome algebraic problem.

$$\alpha_s = \frac{\dfrac{c^6}{n^2 t^4} + \dfrac{12c^5}{nt^3} + \dfrac{12c^4}{t^2}\left(3 + \dfrac{2}{n}\right) + \dfrac{16c^3}{t}\left(9 + \dfrac{1}{n}\right) + 230c^2 + 167ct + 48t^2}{10c^2 + 25ct + 16t^2}. \tag{16}$$

The formulae (14)–(16) particularise nicely to the case of homogeneous beams, obtainable in various ways (for example, $t \to 0$, or $c \to 0$, or $n \to 1$ and $G_c/G_s \to 1$). This result turns out to be an explicit particularisation of the procedure proposed by Bert [1973] for the simplified treatment of the shear deformation in beams with heterogeneous cross section.

We finally note that the shearing rigidity (14)–(16) evaluated by the Jourawsky theory is related to a cubic displacement field that can be somehow richer than the piecewise linear warping the TPE approach is based on (see Figure 1). Therefore, contrary to what was pointed out about the bending stiffness (see Section 2.2), the shearing rigidity hidden behind the TPE minimisation can be higher than (14)–(16). Therefore, between these two methods, we find it difficult to a priori establish which is the most accurate.

The FOSD model based on thin skins and antiplane core. For the sake of completeness, in the discussion we will also consider a simpler model, in which the shearing rigidity is estimated under the assumptions of thin skins and antiplane core [Allen 1969], $S_{TA} = G_c bd$.

Discussion of other FOSD models. In order to avoid the lengthy computation required to obtain (14)–(16), which can be seen to be equivalent to the computation of the so-called form factor, some authors, for some other heterogeneous beams [Mai et al. 2007], prefer a less accurate estimate of the shearing rigidity. This is obtained by scaling the Voigt bound of the shear stiffness by the shear coefficient, defined as the ratio between the maximum shear strain and the shear strain average over the section, still evaluated through Jourawsky's theory [Timoshenko and Gere 1990]. This procedure may lead to highly inaccurate estimates of S (and in fact this is what happens in our benchmark) if the shear moduli of skins and core are very different from each other. In fact, under this circumstance, the Voigt bound is much too large. For this reason, we do not report the expression for the estimate of S related to this scheme, that could instead be appropriate for composite beams whose homogeneous parts all have their centre lying on the neutral axis.

Instead, we found out that multiplying the Reuss bound of the shear stiffness by the ratio between the maximum shear stress and its average turns into a better estimate of S, that reads

$$S_R = \frac{G_c}{1 + 2G_c/G_s} \frac{b^2(c + 2t)^2}{2D}\left(E_s t d + E_c \frac{c^2}{4}\right).$$

Even though the use of S_R will be shown provide better results than those obtainable by employing S_J for the particular example of Section 3.2, in general, S_R is expected to be a worse estimate than S_J, and this is evident from the inadequate particularisation of S_R to the homogeneous case.

3. Comparison with finite element simulations

In order to verify the accuracy of the methods reported in Section 2, we have run some finite element simulations by means of the code ABAQUS [2006], on an arbitrary geometry of sandwich beam for several values of the ratios $n = E_s/E_c$ and t/c.

The mesh (recognisable in the deformed shape of Figure 2, related to a propped cantilever beam supporting a uniform load) consists of eight-noded plane stress continuum elements with reduced integration. The accuracy of the results has been checked by properly refining the mesh. How concentrated loads and constraints are modelled is extremely important when n becomes large, because of the lack of Saint-Venant's principle for these beams. Depending on the way concentrated loads are actually applied, there may be, for instance, the need to account for the core deformation along y [Frostig et al. 1992]. Since we are here interested in the *macroscopic* beam deflection (that neglecting the effects of the load diffusion, as explained in Section 1), in our analyses, concentrated external loads are modelled by applying four equal concentrated forces in the following four points of the section concerned: the top point of the upper skin ($y = -c/2 - t$), both the upper and the lower interface points between skin and core ($y = \pm c/2$), and the bottom of the lower skin ($y = c/2 + t$). Any support is modelled by constraining the displacement along y of all the nodes of the section concerned. Analogously, the encastré condition is enforced by pinning all the section nodes; the deflection is taken as the displacement of the section centre ($y = 0$).
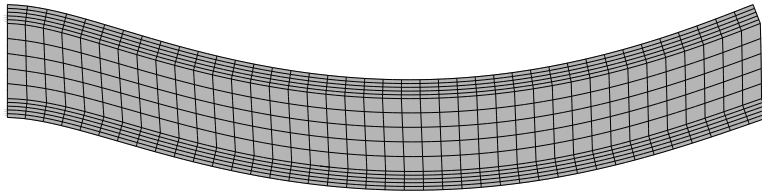

Figure 2. Finite element simulation of the deflection of a propped cantilever beam supporting a uniform load, deformed shape. The relevant geometrical and material parameters are $l = 200\,\text{mm}$, $t = 5\,\text{mm}$, $c = 20\,\text{mm}$, $E_s = 16000\,\text{MPa}$, $G_s = 6154\,\text{MPa}$, $E_c = 100\,\text{MPa}$, and $G_c = 50\,\text{MPa}$.

3.1. ***Three-point bending and other statically determinate cases.*** The results found in [Bardella and Genna 2000; 2001] are shown in Figure 3 for four relevant approaches among those considered in the previous section. The results are given in terms of the percentage error on the midspan deflection, computed using the finite element solution as a reference solution, and plotted against the ratio t/c for four different values of n. In the nonantiplane cases the relevant shear modulus of each layer is obtained by dividing the Young modulus by 2.6, whereas the antiplane case is approximated by $n = 1600000$, $G_s = E_s/2.6$, and $G_c = E_s/6.4$.

It is apparent that the Jourawsky-based FOSD method of page 1196 is the only one exhibiting acceptable accuracy over the whole range of variable considered; also, beside the inaccurate thin skin approximation, it is the only one whose equations particularise without relevant problems to both $t/c \to 0$ and $n \to \infty$.

Beside the fact that the complicated λ-constrained method of minimizing the TPE functional becomes too stiff when the skins are very thin,[9] it is not as accurate as expected. Since Minelli [2007] has verified,

---

[9]This does not hold if the core is antiplane, the case in which the TPE approach becomes difficult to deal with from the numerical viewpoint if $t/c \ll 1$.
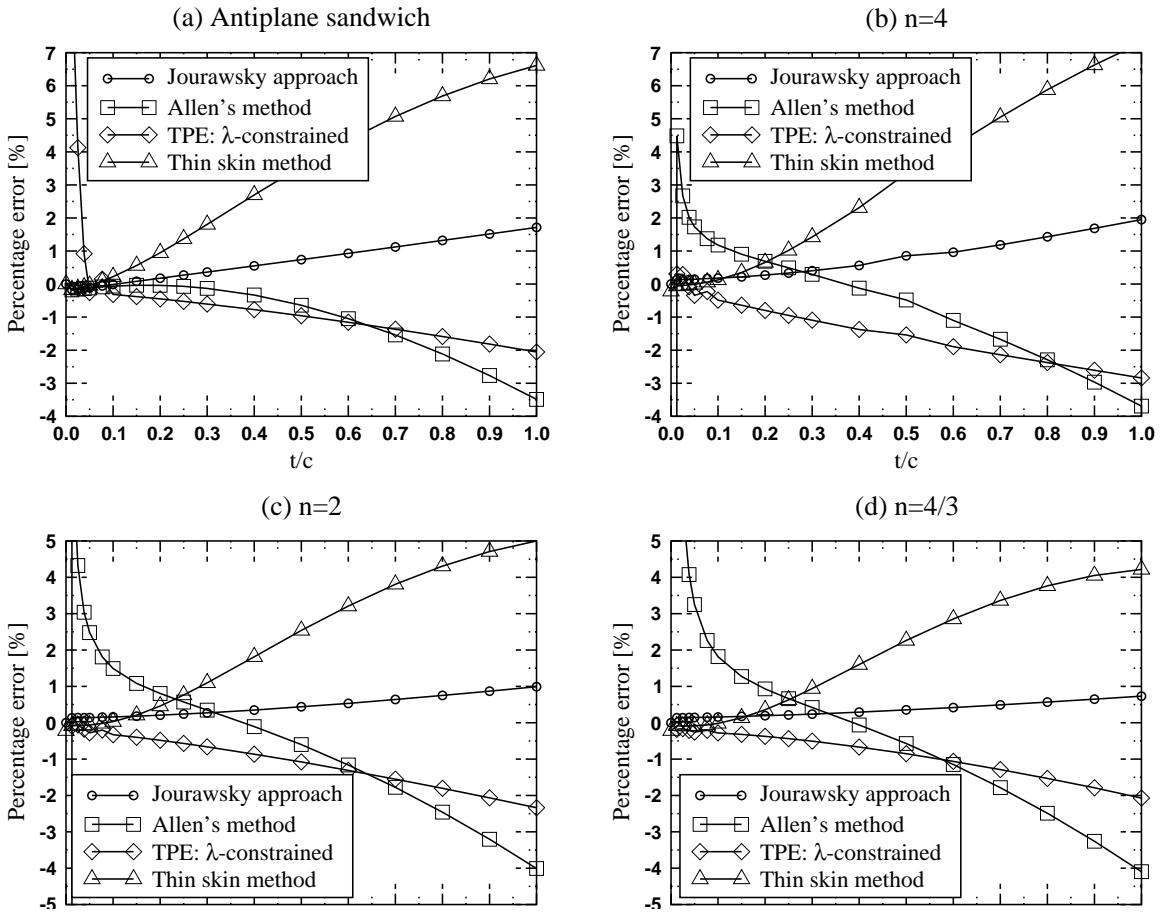
Figure 3. Comparison among different methods for evaluating the maximum deflection of a three-point bending sandwich beam with respect to finite element results, for the antiplane sandwich (upper left) and for $n = 4$, $n = 2$, and $n = \frac{4}{3}$.

by exploiting the Ritz method, that assuming λ_c and λ_s constant is numerically quite appropriate for three-point bending, we argue that the reason for the not-so-good accuracy lies in the inconsistency between the use of a trilinear kinematic model and the strain field ensuing from the shear stress distribution. Hence, the source of error is mostly due to the TPE approach itself, not to the approximated way the minimum is attained with the λ-constrained scheme.

In [Bardella and Genna 2000; 2001] similar results are given for a even larger range of t/c, in particular $t/c \in (0, 3]$. Also, for such unrealistic geometries, the FOSD method based on Jourawsky's theory turns out to be the most accurate, overall.

Similar conclusions as those above have been drawn by Minelli [2007] for other cases, such as those of simply-supported beams subjected to uniform load and four-point bending.

Gordaninejad and Bert [1989], based on [Bert 1973], developed and implemented into finite elements a FOSD model also suitable for sandwiches of unequal skins and layers with bimodular materials, whose

particularisation to the case of a symmetric cross section turns out to be coincident with the Jourawsky-based FOSD method of page 1196. For three different types of cross section, Gordananinejad and Bert successfully tested the method for the cases of cantilever and simply-supported beams subjected to uniform loads, even though they just compared the results with the classical ones, consisting of a FOSD theory in which the shearing rigidity is given by the Voigt upper bound of the shear stiffness.

3.2. *Propped cantilever beam supporting a uniform load.* We consider a sandwich beam characterised by the following relevant geometrical and material parameters: $l = 200$ mm, $t = 5$ mm, $c = 20$ mm, $E_s = 16000$ MPa, $G_s = E_s/2.6$, $E_c = 100$ MPa, and $G_c = E_c/2$. Many other combinations of parameters have been tested without finding any other relevant results beside those emerging from the quite realistic situation underlined by the given data. The finite element deformed shape is given in Figure 2, where, by the way, one can observe the trilinear warping at the simply-supported right end ($x = l$). Moreover, we note that in this case the effect of the core deformation along its thickness is negligible, even though $n = 160$; of course, this is also due to the way in which the constraints have been modelled.

For the models considered, Table 1 reports the percentage errors computed with respect to the finite element solution, referring to the midspan displacement $v(l/2)$, the reaction force R at the right end support ($x = l$), and the moment within the encastré ($x = 0$), computed as $M_0 = pl^2/2 - Rl$. Moreover, we consider the following global percentage errors on the discrepancy between the finite element and theoretical deformed shapes,

$$\mathcal{E}_1 = \frac{\sum_{i=1}^{N} |v_i^{(FE)} - v_i^{(TH)}|}{\sum_{i=1}^{N} |v_i^{(FE)}|} \times 100, \qquad \mathcal{E}_2 = \frac{\sum_{i=1}^{N} (v_i^{(FE)} - v_i^{(TH)})^2}{\sum_{i=1}^{N} (v_i^{(FE)})^2} \times 100, \qquad (17)$$

where $v_i^{(FE)}$ is the displacement evaluated by means of the finite element simulation in the i node on the beam longitudinal axis x, $v_i^{(TH)}$ is the corresponding displacement predicted by the theory considered, and N is the number of nodes lying on x in the mesh employed ($N = 41$, in the case concerned here).

The sole method providing results accurate enough is the direct Ritz method, with the discretisation described in Section 2.1, whose weights for the deflection (11) turn out to be $w_1 \approx 2.9585(p/b)$ mm^3/N,

Percentage errors	Error on $v(l/2)$	Error on R	Error on M_0	$\mathcal{E}_1$, $(17)_1$	$\mathcal{E}_2$, $(17)_1$
TPE: Ritz (15 weights)	−3.23	−1.21	6.72	3.62	0.137
TPE: Ritz (λ_s constant)	−3.35	4.39	−24.4	3.73	0.142
TPE: λ-constrained	−6.40	7.16	−39.9	7.46	0.518
Scaled Reuss bound	12.4	3.84	−21.4	18.6	3.58
Jourawsky approach	21.6	4.50	−25.1	28.5	7.64
Allen's method	26.9	−11.5	64.2	38.6	17.1
Thin skin method	51.2	6.28	−35.0	60.0	33.0

Table 1. Percentage errors, with respect to the results of a finite element simulation, of various models in predicting the midspan deflection $v(l/2)$, the support reaction force R, the encastré moment M_0, and the global deformed shape of a propped cantilever beam subjected to a uniform load. Geometric and material parameters: $l = 200$ mm, $t = 5$ mm, $c = 20$ mm, $E_s = 16000$ MPa, $G_s = 6154$ MPa, $E_c = 100$ MPa, and $G_c = 50$ MPa.
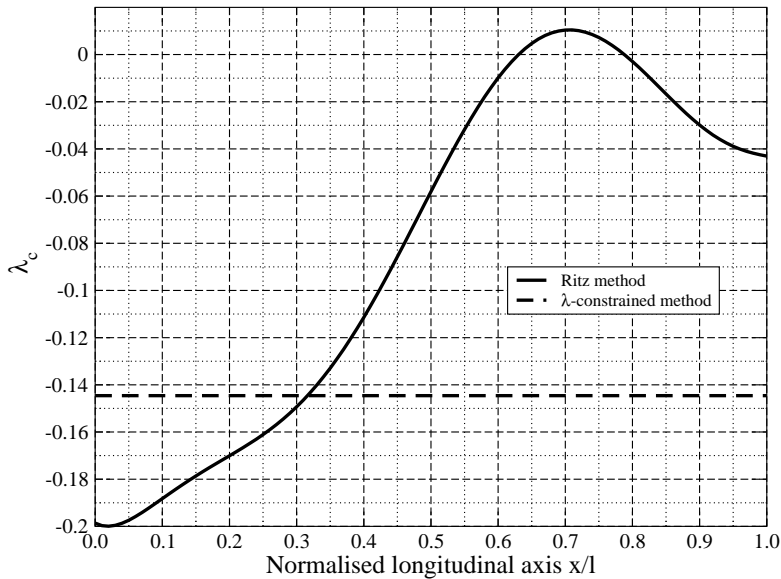
Figure 4. Ritz method for the variation of λ_c along the longitudinal axis of a propped cantilever beam supporting a uniform load. Geometric and material parameters: $l = 200\,\text{mm}$, $t = 5\,\text{mm}$, $c = 20\,\text{mm}$, $E_s = 16000\,\text{MPa}$, $G_s = 6154\,\text{MPa}$, $E_c = 100\,\text{MPa}$, and $G_c = 50\,\text{MPa}$.

$w_2 \approx -229.9(p/b)\,\text{mm}^3/\text{N}$, and $w_3 \approx 64.57(p/b)\,\text{mm}^3/\text{N}$. Such a solution highlights that for this case λ_c varies between a minimum value a little bit greater than $-t/c \equiv -0.2$ (which, as observed in Section 2.1, corresponds to an inefficient core if $\lambda_s \equiv 1$; see also [Allen 1969]) attained at the encastré ($x = 0$) and a maximum close to 0 in $x \approx 0.7l$ (see Figure 4). Even though λ_s varies within a quite limited range, as shown in Figure 5, its variation, too, has to be accounted for if one wants to be accurate in the stress computation. In fact, assuming λ_s constant (without changing the discretisation adopted for v and λ_c, so that the minimisation now depends on 12 weights) leads to an error on the reaction force R equal to 4.39%, producing a largely incorrect value of the moment M_0 at the encastré, which turns out to be underestimated by 24.4%. We have also verified that this discrepancy remains almost unaltered by improving the discretisations for v and λ_c while keeping λ_s constant (its value turns out to be $\lambda_s \approx 0.9915$). As it can be observed from Figures 4 and 5, the natural boundary conditions (5), in $x = l$, are approximately well met by the chosen discretisation (recall that we have a priori imposed the natural boundary conditions on $v(x)$ only).

Also the λ-constrained method to minimise the TPE provides a perhaps acceptable approximation of the deformed shape, but it is quite inaccurate in the reaction force computation. We note that an error of 7.16% on R leads to an underestimation of M_0 of about 40%, and, of course, this strongly and negatively affects the normal stress evaluation. This method gives in this case the stiffest response; this is confirmed by computing the estimate (8), by which the effective bending stiffness is larger than D by about 13%.

The actual inefficiency of the core at the encastré is confirmed in Figure 6, where, given a load $p = 1\,\text{N/mm}$ and a width $b = 50\,\text{mm}$, we report the contour of the normal stress σ_x obtained by means
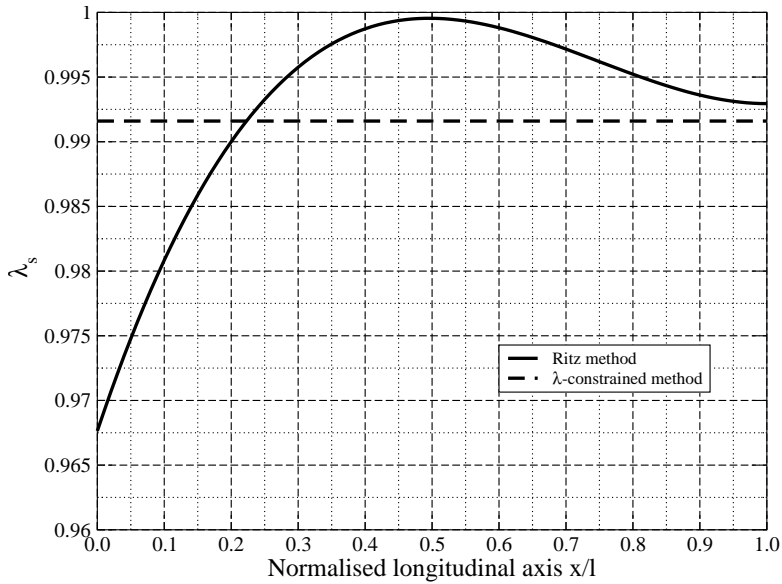
Figure 5. Ritz method for the variation of λ_s along the longitudinal axis of a propped cantilever beam supporting a uniform load. Geometric and material parameters: $l = 200\,\text{mm}$, $t = 5\,\text{mm}$, $c = 20\,\text{mm}$, $E_s = 16000\,\text{MPa}$, $G_s = 6154\,\text{MPa}$, $E_c = 100\,\text{MPa}$, and $G_c = 50\,\text{MPa}$.
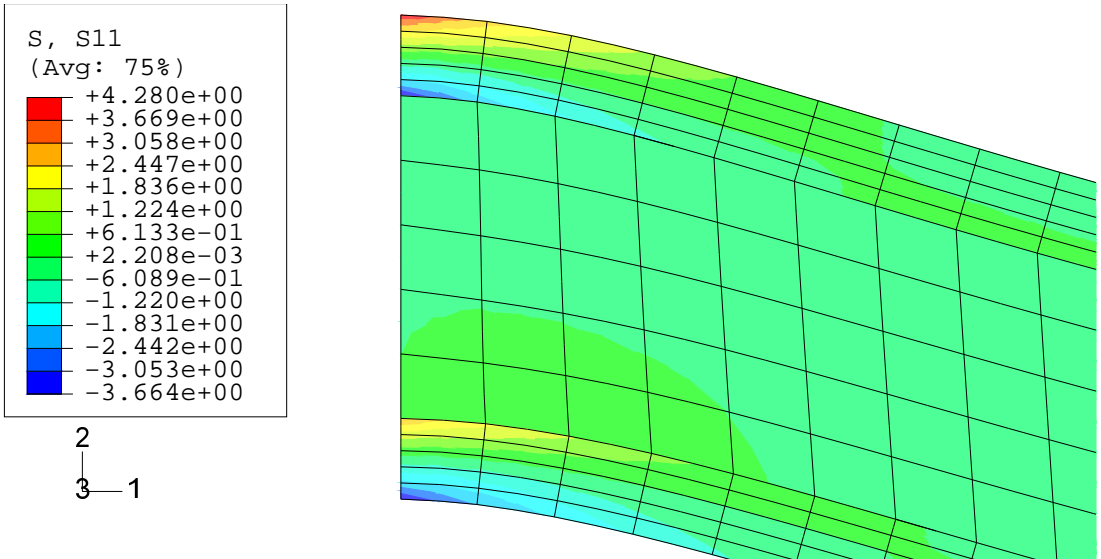

Figure 6. Finite element simulation of the deflection of a propped cantilever beam supporting a uniform load: normal stresses along the longitudinal axis at the encastré. The relevant data are $p = 1\,\text{N/mm}$, $l = 200\,\text{mm}$, $t = 5\,\text{mm}$, $c = 20\,\text{mm}$, $b = 50\,\text{mm}$, $E_s = 16000\,\text{MPa}$, $G_s = 6154\,\text{MPa}$, $E_c = 100\,\text{MPa}$, and $G_c = 50\,\text{MPa}$.

of the finite element analysis. Each skin mostly bends locally around its own midaxis parallel to z, both skins being subjected to substantial compression and tension in their lower and upper parts, respectively.

The foregoing observations imply that in this case the only procedure, among those presented, able to describe the stress distribution is the TPE minimisation accounting for the variations of both λ_c and λ_s. However, the chosen 15 parameter discretisation could be improved to obtain more accurate values for the stresses. In fact, for example, the normal stress in the skins is given by

$$\sigma_x = E_s\big[(\lambda_c' v' + \lambda_c'' v)c/2 + (\lambda_s' v' + \lambda_s'' v)(y - c/2)\big], \qquad y \in [-c/2 - t, -c/2] \cup [c/2, c/2 + t],$$

and, at the encastré, the employed discretisation allows one to predict, for both skins,

$$-2.23\,\text{MPa} \le \sigma_x \le +3.20\,\text{MPa},$$

to be compared with the contour of Figure 6; to this purpose, note that the maximum value reported in the legend is an approximated extrapolation, whereas the relevant maximum stress computed in a Gauss point is $\sigma_x = +3.54\,\text{MPa}$. We also note that computing the bending moment M_0 by evaluating Equation (2) in $x = 0$ leads to a value different by about 10% from $pl^2/2 - Rl$. Even though such a discrepancy diminishes as the discretisation is improved, in order to describe phenomena such as the slightly different bending behaviour of the two skins, due to the fact that in the finite element model the load is actually applied on the upper sandwich surface, one should also account for the core deformability along y (see, for example, [Krajcinovic 1971; Frostig et al. 1992]). On the other hand, one could obtain results closer to those predicted by the beam theory adopted if the distributed load were uniformly applied as a body force in the finite element simulation; in this case, for the normal stress computed at the Gauss points at the encastré section, we obtain $-2.73 \le \sigma_x \le +3.28\,\text{MPa}$, equally distributed on both skins.

Finally, we note that the FOSD order model based on Jourawsky's theory is much more accurate than Allen's superposition model, mostly concerning the support reaction force. In this regard, the accuracy of the Jourawsky approach is far better even than that obtained by means of the TPE λ-constrained method. The results of the scaled Reuss bound (the FOSD model described just before Section 3) are believed to be so good by chance, and are reported just for the sake of curiosity. The thin skin approximation fails badly, also because here the skins are quite thick.

4. Discussion and concluding remarks

We have considered various methods for computing the deflection $v(x)$ of sandwich beams, of identical skins, subjected to bending moment and shear, mostly aiming at finding insight on the reliability of FOSD models, that is, those making use of the standard formulae for displacements of the homogeneous Timoshenko beam.

A simple and often accurate FOSD method, put forward in [Bardella and Genna 2000] (see also [Bert 1973]), consists of estimating the shearing rigidity by means of an energy principle and the Jourawsky approximate treatment [Jourawsky 1856] of the shear problem for beams. The only difference between this Jourawsky approach and other FOSD theories, such as the well known method based on the approximation of thin skins and antiplane core [Allen 1969], lies in the evaluation of the shearing rigidity S. Instead, all these methods estimate the bending stiffness D by assuming that plane sandwich sections

remain plane during deformation, corresponding to a linear displacement field, whereas the estimation of S by means of Jourawsky's theory turns out to be based on a cubic displacement field.

The FOSD method based on the Jourawsky approach has been shown to furnish accurate results for the cases of three and four-point bending and for simply-supported beams subjected to uniform load [Gordaninejad and Bert 1989; Bardella and Genna 2000; 2001; Minelli 2007], all statically determinate, symmetrically loaded structures in which the bending moment does not change sign along the beam length. Concerning the interlaminar shear stress computation, Heller [1969] determined the conditions under which there is a satisfactory agreement between the results of Yu's model [1959] (based, as our TPE approach, on the kinematics of Figure 1) and those obtained by means of Jourawsky's formulae, still in sandwich beams whose shear force is statically determinate. In particular, Heller exploited the cases of a cantilever beam with a concentrated load at the free end and of a beam with both ends fixed, subjected to a uniform load. This allowed Heller to skip the crucial problem of choosing a FOSD model for the deflection evaluation. For such particular cases, Heller concluded that the Jourawsky theory is accurate enough if $n < 100$ or if $t/c \ll 1$ (see also [Allen 1969]).

Clearly, one of the advantages of any FOSD method consists of allowing the use of the classical formulae for the deflection of homogeneous beams to compute the deflection of sandwich beams, whereas both the Allen superposition method and the TPE approach may require, for every different set of boundary conditions, a new ad hoc integration that may be quite complicated.

The TPE approach is rigorously based on a suitable kinematics describing the warping. Here, we have considered the trilinear warping represented in Figure 1, known to provide an accurate description of the sandwich behaviour. Because of the chosen kinematics, hidden behind the minimisation of the TPE functional there has to be a bending stiffness lower than, and, probably, a shearing rigidity larger than those employed in the FOSD model based on the Jourawsky approach. We think that this is the main reason why it is a priori uncertain which of these methods provides more accurate results.

Moreover, the analytical minimisation of the TPE functional based on the trilinear kinematics of Figure 1 is unfeasible, even for the simplest sandwich structures. Bardella and Genna [2000] have found a closed-form solution based on the hypothesis that both the ratio between the rotations of the core and of the longitudinal axis, λ_c, and the ratio between the rotations of the skins and of the longitudinal axis, λ_s, are constant (or independent on the position along the longitudinal axis x). This hypothesis turns out to be appropriate for the cases mentioned above, in which the Jourawsky approach also exhibits good accuracy, often also in terms of stresses.

We have found that in the case of a propped cantilever beam supporting a uniform load, for a particular but not totally unrealistic choice of geometrical and material parameters, the direct numerical minimisation of the TPE functional (by a proper approximation of the unknown functions — v, λ_c, λ_s — involving 15 weights to be computed by imposing stationarity) is the only way, among those presented, to provide accurate results in terms of both displacement and bending moment, having also shown that the assumption of independence of both λ_c and λ_s upon x is inappropriate in this case. In particular, even though λ_s turns out to vary within a limited range ($\lambda_s \in (0.968, 1)$ in the benchmark considered), we have observed that assuming λ_s to be constant (in the literature it is even often set $\lambda_s = 1$) in the TPE minimisation can be acceptable for the deflection computation, but may lead to quite inaccurate values for the stresses.

Finally, based on all above, we put forward that the convenient FOSD method based on Jourawsky's theory should always be able to describe the deflection v when λ_c and λ_s turn out to be approximately constant over the sandwich length, which seems to happen mostly when the bending moment does not change sign along the sandwich length. Getting a better insight on this could be extremely useful for engineering practice.

References

[ABAQUS 2006] *ABAQUS User's and Theory Manuals*, ABAQUS Inc., Providence, RI, 2006.

[Allen 1969] H. G. Allen, *Analysis and design of structural sandwich panels*, Pergamon, Oxford, 1969.

[Bardella and Genna 2000] L. Bardella and F. Genna, "Approximate computation of the elastic shear stiffness of a sandwich beam", pp. 218–226 in *Proceedings of the XIII Italian Congress on Computational Mechanics* (Brescia, 2000), 2000. ISBN 88-86524-47-1.

[Bardella and Genna 2001] L. Bardella and F. Genna, "Elastic design of syntactic foamed sandwiches obtained by filling of three-dimensional sandwich-fabric panels", *Int. J. Solids Struct.* **38**:2 (2001), 307–333.

[Bert 1973] C. W. Bert, "Simplified analysis of static shear factors for beams of nonhomogeneous cross section", *J. Composite Materials* **7** (1973), 525–529.

[Bunn and Mottram 1993] P. Bunn and J. T. Mottram, "Manufacture and compression properties of syntactic foams", *Composites* **24**:7 (1993), 565–571.

[Frostig et al. 1992] Y. Frostig, M. Baruch, O. Vilnay, and I. Shelnman, "High-order theory for sandwich-beam behavior with transversely flexible core", *J. Eng. Mech.* **118**:5 (1992), 1026–1043.

[Ghugal and Shimpi 2001] Y. M. Ghugal and R. P. Shimpi, "A review of refined shear deformation theories for isotropic and anisotropic laminated beams", *J. Reinforced Plastics Composites* **20**:3 (2001), 255–272.

[Gordaninejad and Bert 1989] F. Gordaninejad and C. W. Bert, "A new theory for bending of thick sandwich beams", *Int. J. Mech. Sci.* **31**:11-12 (1989), 925–934.

[Heller 1969] R. A. Heller, "Interlaminar shear stress in sandwich beams", *Experimental Mechanics* **26** (1969), 413–418.

[Hutchinson 2001] J. R. Hutchinson, "Shear coefficients for Timoshenko beam theory", *J. Appl. Mech.* **68** (2001), 87–92.

[Jourawsky 1856] M. Jourawsky, "Sur la résistance d'un corps prismatiques et d'une pièce composée en bois ou en tôle de fer à une force perpendiculaire à leur longeur", *Annales des Ponts et Chaussées* **12** (1856), 328–351.

[Khdeir and Reddy 1997] A. A. Khdeir and J. N. Reddy, "An exact solution for the bending of thin and thick cross-ply laminated beams", *Composite Structures* **37** (1997), 195–203.

[Krajcinovic 1971] D. Krajcinovic, "Sandwich beam analysis", *J. Appl. Mech.* **39**:3 (1971), 773–778.

[Mai et al. 2007] S. P. Mai, N. A. Fleck, and T. J. Lu, "Optimal design of box-section sandwich beams in three-point bending", *Int. J. Solids Struct.* **44** (2007), 4742–4769.

[Minelli 2007] M. Minelli, *Deformabilità di travi sandwich soggette a flessione e taglio*, Laurea thesis, Universitá di Brescia, 2007.

[Pagano 1970] N. J. Pagano, "Exact solutions for rectangular bidirectional composites and sandwich plates", *Journal of Composite Materials* **4** (1970), 20–34.

[Renton 1991] J. D. Renton, "Generalized beam theory applied to shear stiffness", *Int. J. Solids Struct.* **27**:15 (1991), 1955–1967.

[Silverman 1980] I. K. Silverman, "Flexure of laminated beams", *Journal of the Structural Division, ASCE* **106** (1980), 711–725.

[Timoshenko 1921] S. P. Timoshenko, "On the correction for shear of the differential equation for transverse vibrations of prismatic bars", *Philos. Mag.* **38** (1921), 744–746.

[Timoshenko and Gere 1990] S. P. Timoshenko and J. M. Gere, *Mechanics of materials*, 3rd ed., PWS-KENT, Boston, 1990.

[Yu 1959] Y. Y. Yu, "A new theory of elastic sandwich plates: one dimensional case", *J. Appl. Mech.* **26**:3 (1959), 415–421.

[Yu et al. 2008] W. Yu, J.-S. Kim, D. H. Hodges, and M. Cho, "A critical evaluation of two Reissner-Mindlin type models for composite laminated plates", *Aerospace Science and Technology* (2008). to appear.

[Zenkert 1997] D. Zenkert, *An introduction to sandwich construction*, Chameleon, London, UK, 1997.

LORENZO BARDELLA: lorenzo.bardella@ing.unibs.it
DICATA, University of Brescia, Via Branze, 43, 25123 Brescia, Italy
http://dicata.ing.unibs.it/bardella/

PERIODIC CONTACT PROBLEMS IN PLANE ELASTICITY

JOSEPH M. BLOCK AND LEON M. KEER

Various methods for solving the partial contact of surfaces with regularly periodic profiles — which might arise in analyses of asperity level contact, serrated surfaces or even curved structures — have previously been employed for elastic materials. A new approach based upon the summation of evenly spaced Flamant solutions is presented here to analyze periodic contact problems in plane elasticity. The advantage is that solutions are derived in a straightforward manner without requiring extensive experience with advanced mathematical theory, which, as it will be shown, allows for the evaluation of new and more complicated problems. Much like the contact of a single indenter, the formulation produces coupled Cauchy singular integral equations of the second kind upon transforming variables. The integral equations of contact along with both the boundary and equilibrium conditions provide the necessary tools for calculating the surface tractions, often found in closed-form for regularly periodic surfaces. Various loading conditions are considered, such as frictionless contact, sliding contact, complete stick, and partial slip. Solutions for both elastically similar and dissimilar materials of the mating surfaces are evaluated assuming Coulomb friction.

1. Introduction

Understanding the microscopic interaction of real rough surfaces in contact is difficult. Mathematical solutions for the contact of real rough surfaces are complicated and closed form solutions are limited. One simplifying assumption is to approximate asperities or even smooth wavy surfaces as sinusoidal, which allows for greater analytic feasibility, assuming the wavelength is much larger than the amplitude of the wave. Physically, the sine wave represents the first term in a Fourier decomposition of an actual rough surface. Asperity contact and geometrically wavy surfaces are the centerpieces of tribological phenomena such as friction, wear and fracture. Other periodic geometries are of particular tribological and mechanical interest as well. In addition to the normal contact of periodic surfaces, other modes of contact such as sliding, partial slip, and complete stick of mating surfaces become increasingly important when studying different types of failure, such as fretting fatigue, creep failure, and crack nucleation.

The problem of smooth, elastic periodic surfaces in contact has been solved using various methods and in many different contexts; many of the contributions to the area of regularly wavy contact are described below. The first solution is credited to Westergaard [1939], who found a closed form solution for the contact problem of an elastic half-space with a wavy surface by utilizing complex stress functions for a sinusoidal normal pressure. Westergaard derived expressions for the surface tractions and the dependence of the contact area on applied pressure. He also showed that for light loading, that is, for a small area of contact, Hertzian contact of cylinders is recovered. England and Green [1963] also employed complex

potential functions to solve the problem of an infinite row of punches upon a half-space. Their formulation reduces to an integral of the Abel type to determine the extent of contact.

Using a stress function approach, Dundurs et al. [1973] solved an integral of the Abel type for two wavy surfaces with aligned peaks of the same amplitude. The mixed boundary conditions for the contact and stress free regions lead to a set of dual series equations [Sneddon 1966]. Exploiting the orthogonality of Legendre polynomials and the Mehler–Laplace integral yields closed form solutions for the extent of contact for a given level of loading and distribution of contact pressure. Johnson [1985b] obtained closed form asymptotic results for light loading and nearly complete contact of surfaces having orthogonal two-dimensional waves of equal amplitude and wavelength.

Two books on contact mechanics, [Hills et al. 1993] and [Johnson 1985b], dedicate entire chapters to periodic contact problems. Starting with the Flamant solution for a concentrated force on a half-space, both sources derive integral equations with a Hilbert kernel to determine surface stresses. Analytical solutions for periodic contact are limited in both books; they cite the Westergaard solution and then statistical and numerical methods for rough contact. A recent book by Cai and Lu [2000] extended Muskhelishvili's approach [Muskhelishvili 1992] to periodic plane elasticity. Expressed as Riemann–Hilbert boundary value problems, they are solved using complex variables and Hilbert kernels. Systematically, the authors work out solutions for periodic contact problems, crack problems, anisotropic surfaces, moving loads, and finally doubly periodic problems. Frictionless normal contact and sliding contact with Coulomb friction are worked out for flat, inclined, and circular punches.

Kryshtafovych and Martynyak [2000] considered frictional contact of elastic half-spaces with periodic surface relief for isotropic and anisotropic solid surfaces. The method of interface gaps reduces the problem to a singular integral equation, which is numerically solved. The authors also derived a cotangent kernel for periodic profiles in a general form, which is reduced to a Hilbert kernel. A closed form solution was obtained for an anisotropic half-plane in contact with a rigid wavy body [Krishtafovich et al. 1994]. A series of papers by Kuznetsov on periodic contact with friction [Kuznetsov 1975], with a fluid lubricant [Kuznetsov 1985], for a polymeric material [Kuznetsov and Gorokhovsky 1978], and with depth-varying Poisson's ratio [Kuznetsov 1983] have been published, in which he utilizes the theory of automorphic functions. Panek [1975] solved the normal contact of an elastic, regularly wavy strip pressed between flat surfaces by reposing the problem as an infinite, straight strip indented by regularly wavy surfaces. He determined the local contact stress and heat conduction of the wavy strip by means of dual series equations and a Fredholm integral equation of the second kind.

Nosonovsky and Adams [2000] studied the dry, steady-state frictional sliding of elastic, wavy bodies in two dimensions. A Cauchy singular integral equation of the second kind is derived from integral transforms and Fourier series and then numerically solved using Jacobi polynomials. Based on Staierman's general solutions for periodic contact [Schtaierman 1949], Ciavarella [1998a; 1998b] provided Cattaneo–Mindlin partial slip results for a few periodic geometries with two bodies of the same material. Ciavarella assumes that the periodic profiles chosen demonstrate self-similarity and thus the correction term in the shear traction is of the same form as the normal traction. He also explains why flat punches must either completely stick or slip entirely and cannot undergo partial slip for elastically similar materials. Manners [1998] analyzed more complicated periodic half-space profiles in partial contact with a flat rigid plane. The crux of the analysis is based on a cotangent transform, which allows for a simple method of finding the surface pressure for wavy surfaces with a finite number of harmonics. Manners later extended his

analytical method to a numerical one for random rough profiles in order to determine the extent of contact, which is not known a priori [Manners 2003].

Carbone and Mangialardi [2004] recently published a paper on the adhesion and friction between an elastic half-plane and a rigid wavy surface which has application to tire-road contact. By imposing a sliding velocity that is much smaller than the sound velocity in the solids, an eccentricity, e, is created. The authors also require the large-scale viscoelastic behavior to be neglected so that linear elasticity theory can be employed. The eccentricity gives rise to an antisymmetric contribution to the surface stress. The adhesion is modeled by superposing Koiter's solution for an infinite row of collinear cracks with the contact problem, as was first performed by Johnson [1995]. Linear elastic fracture mechanics provides equilibrium values for the eccentricity and contact region of the adhered surfaces. Friction coefficients and conditions for the surfaces to jump in and out of contact are evaluated. Carbone and Decuzzi [2004] solved the solution for an infinitely long elastic beam adhered to a wavy foundation. It was found that the surface energy, amplitude, and thickness of the beam are the main contributors to the deformation of the strip. Adams [2004] considered the adhesive contact of two elastic wavy surfaces assuming Maugis' model of adhesion [Maugis 2000]. Papkovich–Neuber potentials transform the boundary conditions into a triple series, which leads to a singular integral equation that is solved numerically. A loading cycle is developed, which is characterized by discontinuities in the form of a hysteresis.

As shown above, periodic contact problems have received much attention and analysis. At the same time, many rather simple periodic problems in plane elasticity remain unsolved. This fact is partly due to the complicated nature of the mathematical techniques previously used and partly due to a misunderstanding of the capability of the Flamant solution. It will be shown here that for periodic contact, a summation of periodically spaced Flamant solutions must be used. The resulting integral equations result in a cotangent kernel, which can be transformed to a Hilbert kernel by a simple change of variables. This cotangent kernel was first derived by Schtaierman [1949] for a very general case of periodic contact and later by Schmueser and Comninou [1979] for a periodic array of interface cracks. The advantage of this formulation is that solutions can be solved in a closed form in a rather straightforward manner and reduced to the single contact solution in the limit as the period approaches infinity. Moreover, the formulation has a simple physical explanation, as opposed to a gap function [Kryshtafovych and Martynyak 2000], Riemann–Hilbert approach [Cai and Lu 2000] or complex potential approach [England and Green 1963].

The governing equations of elastic contact mechanics and assumptions used are discussed. A periodic array of Flamant solutions on a half-space is used to derive a cotangent kernel for periodic contact problems. Following the general nomenclature and methodology outlined by Hills et al. [1993], an integral equation approach for periodic contact problems is developed. A modification to the kernel to ensure moment equilibrium is introduced and finally the governing equations for periodic plane elasticity are laid out.

Numerous periodic contact problems are solved. A few known solutions are corroborated from the coupled integral equations in order to demonstrate the method. New and more complicated solutions are derived for various periodic profiles, elastically dissimilar materials and types of contact, such as sliding, partial slip and complete stick.

2. Theory of periodic contact in plane elasticity

Assumptions. It will be assumed throughout that the bodies involved are linear elastic, isotropic mate-
rials. For isotropic bodies, Poisson's ratio ν and shear modulus μ are used. A small strain theory of
elasticity is assumed, where the contact area is significantly smaller than the radii of curvature of the
undeformed surfaces. Under these assumptions, the stresses of each surface can be calculated with good
accuracy by treating each contacting body as a semiinfinite body bounded by a plane surface, also called
a half-space. Such an idealization was first introduced by Hertz [1881].

Contact mechanics. For a distribution of normal and shear tractions — $p(x)$ and $q(x)$ respectively —
on a half-space's free surface and depicted in Figure 1, it was shown in [Johnson 1985b] that a pair of
coupled integral equations result:

$$\frac{1}{A}\frac{\partial h}{\partial x} = \frac{1}{\pi}\int\frac{p(\xi)}{x-\xi}d\xi - \beta q(x), \tag{1}$$

$$\frac{1}{A}\frac{\partial g}{\partial x} = \frac{1}{\pi}\int\frac{q(\xi)}{x-\xi}d\xi + \beta p(x), \tag{2}$$

where $h(x) = v_1(x) - v_2(x)$ and $g(x) = u_1(x) - u_2(x)$ are the differences in displacements between the
upper and lower surfaces, represented by the subscripts 1 and 2 respectively. The integral equations were
derived using the Flamant solution. Also, the mismatch in material parameters between the two surfaces
couples the two integral equations and results in

$$A = \frac{\kappa_1 + 1}{4\mu_1} + \frac{\kappa_2 + 1}{4\mu_2}, \qquad \beta = \frac{\Gamma(\kappa_1 - 1) - (\kappa_2 - 1)}{\Gamma(\kappa_1 + 1) + (\kappa_2 + 1)}, \tag{3}$$

where A is the compliance between the bodies, β is Dundur's parameter representing the elastic mismatch,
and $\Gamma = \mu_2/\mu_1$, as defined in [Hills et al. 1993]. The bulk modulus, κ, is defined as $\kappa = 3 - 4\nu$ for
plane strain and $\kappa = (3 - \nu)/(1 + \nu)$ for plain stress, with subscripts for the respective surfaces. When
both bodies are of the same materials, Dundur's parameter is zero. When one body is rigid, it becomes
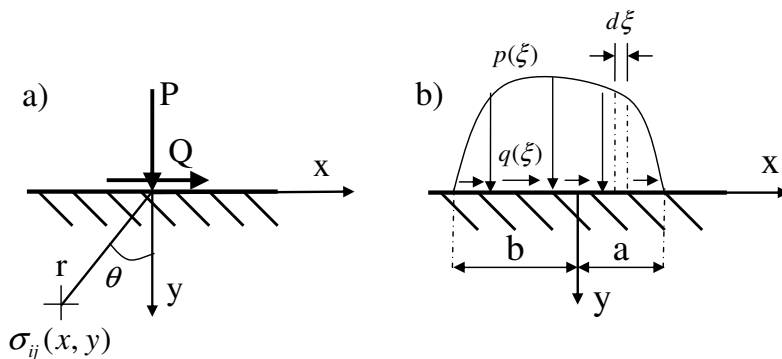$\beta = (1 - 2\nu)/2(1 - \nu)$.

Figure 1. An elastic half-space (a) under a concentrated normal and tangential line force
and (b) under an arbitrary distributed normal and tangential pressure.

Lastly, equilibrium of the external forces, P and Q, needs to be ensured and is done so with

$$P = \int p(\xi)\,d\xi, \qquad Q = \int q(\xi)\,d\xi.$$

Equations (1) and (2) are the foundations of plane elastic contact mechanics. Many well-known solutions are obtained using them; see [Hills et al. 1993] and [Johnson 1985b].

Periodic contact mechanics. The solution for periodic regions of distributed normal and shear tractions can be derived in a similar fashion to that of a single region. Taking the Flamant solution as the starting point, consider infinitely many evenly-spaced concentrated normal, compressive forces on a half-space's free surface depicted in Figure 2a. On the free surface, the normal displacements in Cartesian coordinates are

$$v(x) = -P\left(\frac{\kappa+1}{4\pi\mu}\right)\ln|x| - \sum_{n=1}^{\infty} P\left(\frac{\kappa+1}{4\pi\mu}\right)\ln|nL+x| - \sum_{n=1}^{\infty} P\left(\frac{\kappa+1}{4\pi\mu}\right)\ln|nL-x| + \frac{C_2}{2\mu}, \quad (4)$$

where C_2 is an arbitrary rigid body displacement. Taking the derivative of (4) to remove C_2 gives

$$\frac{dv(x)}{dx} = -P\left(\frac{\kappa+1}{4\pi\mu}\right)\frac{1}{x} - \sum_{n=1}^{\infty} P\left(\frac{\kappa+1}{4\pi\mu}\right)\frac{1}{nL+x} - \sum_{n=1}^{\infty} P\left(\frac{\kappa+1}{4\pi\mu}\right)\frac{1}{nL-x}. \quad (5)$$

Using the identity

$$\sum_{n=-\infty}^{\infty} \frac{1}{x+nL} = \frac{\pi}{L}\cot\frac{\pi x}{L},$$
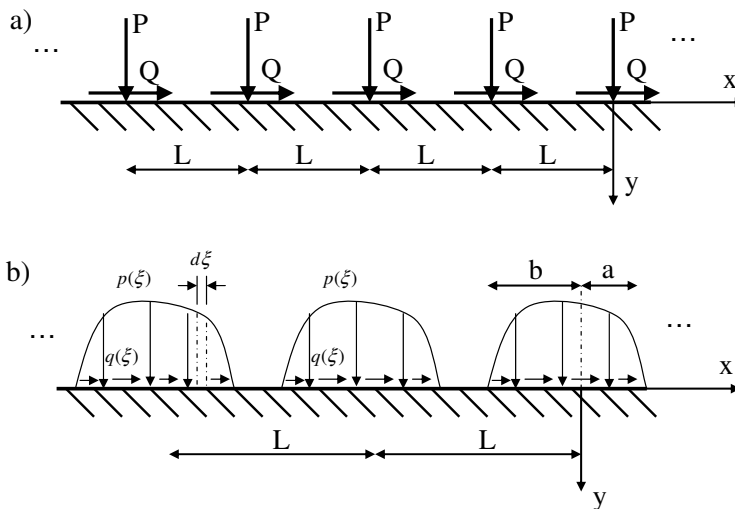

Figure 2. A half-space loaded by (a) an array of evenly spaced concentrated normal and tangential line forces and (b) periodic distributions of normal and shear surface tractions.

allows the displacement derivative in (5) to be rewritten as

$$\frac{dv(x)}{dx} = -P\left(\frac{\kappa+1}{4L\mu}\right)\cot\frac{\pi x}{L}. \tag{6}$$

Equation (6) gives the normal displacement due to evenly spaced concentrated forces on a half-space. This result can now be extended to periodic regions of distributed normal and shear tractions on the half-space's flat free surface, as shown in Figure 2b. The resulting integral equations for contact are

$$\frac{dv(x)}{dx} = \frac{\kappa+1}{4L\mu}\int p(\xi)\cot\left(\frac{\pi}{L}(x-\xi)\right)d\xi - \frac{\kappa-1}{4\mu}q(x), \tag{7}$$

$$\frac{du(x)}{dx} = \frac{\kappa+1}{4L\mu}\int q(\xi)\cot\left(\frac{\pi}{L}(x-\xi)\right)d\xi + \frac{\kappa-1}{4\mu}p(x), \tag{8}$$

where the following result was used for the displacements normal to the surface in order to determine the second term in the right hand side of (7),

$$\frac{dv(x)}{dx} = -\frac{\kappa-1}{4\mu}\sum_{n=-\infty}^{\infty}\int q(\xi)\delta(x-\xi+nL)d\xi = -\frac{\kappa-1}{4\mu}q(x),$$

and similarly for the tangential displacements in (8). If the relative difference in displacements between two elastic bodies in contact is considered, the integral equations become

$$\frac{1}{A}\frac{\partial h}{\partial x} = \frac{1}{2\pi}\int_b^a p(\xi)\cot\frac{x-\xi}{2}d\xi - \beta q(x), \tag{9}$$

$$\frac{1}{A}\frac{\partial g}{\partial x} = \frac{1}{2\pi}\int_b^a q(\xi)\cot\frac{x-\xi}{2}d\xi + \beta p(x), \tag{10}$$

where $L = 2\pi$ has been chosen for simplicity. The integral is taken over only a single contact region, $[b, a]$, since the periodicity of the problem guarantees that each period will produce the same result. The equations are easily modified for an arbitrary period, so long as the amplitude of the contacting surface is small compared to the wavelength, L, an assumption critical to the elasticity theory approximation.

Equations (9) and (10) are the foundations of elastic periodic contact mechanics in Cartesian coordinates; accordingly, the equations and their cotangent kernel will be referred to regularly and taken as the starting point of the physical problem to be solved. Before solving specific problems, a few comments should be made. The periodic integral equations resemble those for a single region of contact, (1) and (2), except that the kernel is now a cotangent kernel instead of a Hilbert kernel, whose solutions and transforms have been studied extensively. However, an appropriate change of variables transforms the cotangent kernel into a Hilbert kernel. That is, let

$$u = \tan\xi/2, \quad v = \tan x/2, \quad \text{and} \quad \alpha = \tan a/2. \tag{11}$$

Note that for the rest of the paper, u and v will only be used to represent these transformations and not the normal and tangential displacements defined above. Then (9) becomes

$$\frac{1}{A}\frac{\partial h}{\partial x} = \frac{1}{\pi}\int_{-\alpha}^{\alpha}\frac{p(u)(1+uv)}{(v-u)(1+u^2)}du - \beta q(v), \tag{12}$$

where the contact region has been centered on the interval $[-a, a]$. The derivative displacement term is kept in terms of x, but typically needs to be changed to the transformed variables to solve for the surface tractions. The change of variables in (11) will be used and referred to regularly. To simplify the integral in (12) and the corresponding one for the tangential displacements, add and subtract u^2 in the numerator to get

$$\frac{1}{A}\frac{\partial h}{\partial x} = \frac{1}{\pi}\int_{-\alpha}^{\alpha}\frac{p(u)}{v-u}du + \frac{1}{\pi}\int_{-\alpha}^{\alpha}\frac{up(u)}{1+u^2}du - \beta q(v),\tag{13}$$

$$\frac{1}{A}\frac{\partial g}{\partial x} = \frac{1}{\pi}\int_{-\alpha}^{\alpha}\frac{q(u)}{v-u}du + \frac{1}{\pi}\int_{-\alpha}^{\alpha}\frac{uq(u)}{1+u^2}du + \beta p(v).\tag{14}$$

The first integral on the right-hand side is a Cauchy singular integral and will also be referred to as the Hilbert kernel. The second integral is a constant which represents physically the moment on the surface due to periodic tractions, $p(u)$, given by

$$M = \frac{1}{L}\int_{-a}^{a}p(x)\tan\frac{\pi x}{L}dx = \frac{1}{\pi}\int_{-\alpha}^{\alpha}\frac{up(u)}{1+u^2}du.$$

When $p(u)$ is symmetric, it is seen that $M = 0$ and only the Hilbert kernel integral remains in (13). If $p(u)$ is asymmetric however, $M \neq 0$ and the cotangent kernel can sometimes be modified to eliminate the unprescribed moment on the surface. The shear tractions however cannot produce a moment and must therefore be removed. This issue is discussed by Cai and Lu [2000, pp. 57–60], who comment that an extra term must be included in the kernel

$$\frac{1}{A}\frac{\partial h}{\partial x} = \frac{1}{2\pi}\int_{b}^{a}p(\xi)\left(\cot\frac{x-\xi}{2} - \tan\frac{\xi}{2}\right)d\xi - \beta q(x),\tag{15}$$

$$\frac{1}{A}\frac{\partial g}{\partial x} = \frac{1}{2\pi}\int_{b}^{a}q(\xi)\left(\cot\frac{x-\xi}{2} - \tan\frac{\xi}{2}\right)d\xi + \beta p(x).\tag{16}$$

It is seen that the change of variables from (11) removes the moment term. Thus, (15) and (16) will sometimes be the starting point for solving problems when equilibrium requires removing the unwanted moment. Furthermore, equilibrium is achieved by balancing the total normal and tangential loads

$$P = \int_{-a}^{a}p(x)dx = \int_{-\alpha}^{\alpha}\frac{2p(u)}{1+u^2}du,\tag{17}$$

$$Q = \int_{-a}^{a}q(x)dx = \int_{-\alpha}^{\alpha}\frac{2q(u)}{1+u^2}du.\tag{18}$$

The integral equations (15)–(16) and the conditions (17)–(18) form the basis of solving periodic contact problems. Using the change of variables (11), some well-known solutions will be derived in simpler ways and new solutions will be solved in a closed form in the next sections.

3. Problems in periodic contact: frictionless contact

Normal frictionless contact of periodic profiles. The simplest problems in contact mechanics are indentations without friction in normal contact with the free surface of a half-space. The no-friction

assumption decouples the integral equations of periodic contact, thus increasing the availability of closed-form solutions. In this section, various periodic profiles, such as periodic flat punches and sinusoids, are considered. The surface geometry provides the necessary boundary conditions to solve the mixed boundary value problem in order to determine the surface stresses.

Sinusoids: Westergaard's solution. The solution of a wavy surface in contact with a flat surface, as shown in Figure 3, has practical importance in tribology and solid mechanics. The first mathematical solution was credited to Westergaard [1939], who used complex stress functions to obtain the contact stress. Later, Dundurs et al. [1973] employed a stress function approach, which required solving a set of dual series equations. Using the approach delineated in the previous section, the Westergaard solution is rederived here.

The surface profile for a sinusoidal surface with period 2π is

$$h(x) = \delta - \Delta(1 - \cos x), \tag{19}$$

where $h(x)$ is the difference in the normal displacements, δ is the approach and Δ is the amplitude of the undeformed surface profile. Physically, $h(x)$ represents the amount of interpenetration of the bodies and is a geometrical constraint condition. Differentiating Equation (19) to remove the rigid body displacement gives

$$\frac{\partial h(x)}{\partial x} = \Delta \sin x. \tag{20}$$

Transforming (20) using (11) and then substituting into (13) yields

$$\frac{\Delta}{A} \frac{2v}{1 + v^2} = \frac{1}{\pi} \int_{-\alpha}^{\alpha} \frac{p(u)}{v - u} du + \frac{1}{\pi} \int_{-\alpha}^{\alpha} \frac{u p(u)}{1 + u^2} du - \beta q(v).$$

It should be noted that the axes are positioned at the center of the contact region to exploit symmetry; this assumption will be employed throughout the paper unless otherwise specified. For frictionless contact or contact of smooth surfaces, $q(x) = 0$, and the integral equations are uncoupled. For two bodies with elastically similar materials, $\beta = 0$, which also removes the coupling term. The symmetry of the problem removes the second integral term on the right-hand side (since $p(u)$ is even) and gives

$$\frac{2\Delta}{A} \frac{v}{1 + v^2} = \frac{1}{\pi} \int_{-\alpha}^{\alpha} \frac{p(u)}{v - u} du,$$
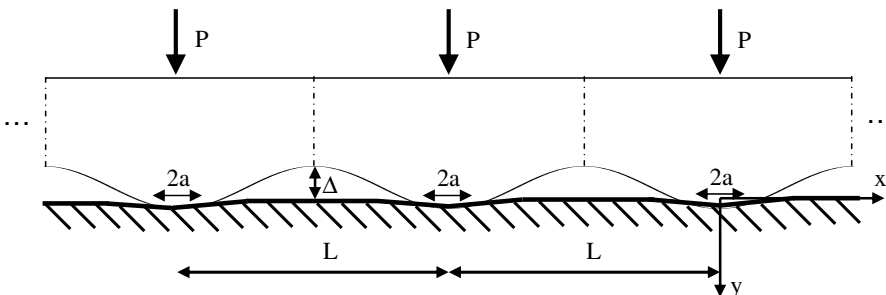

Figure 3. Normal contact of a sinusoidal profile without friction.

which is a Cauchy singular integral equation of the first kind for determining $p(u)$. Section A.1 provides inversion that is nonsingular at both endpoints,

$$p(u) = \frac{2\Delta}{\pi A} \sqrt{\alpha^2 - u^2} \int_{-a}^{\alpha} \frac{v}{1+v^2} \frac{1}{\sqrt{\alpha^2 - v^2}} \frac{1}{v-u} \, dv.$$

Using partial fractions and evaluating the resulting integrals gives

$$p(u) = -\frac{2\Delta}{A} \frac{\sqrt{\alpha^2 - u^2}}{(1+u^2)\sqrt{1+\alpha^2}}.$$

Reverting to original variables produces

$$p(x) = -\frac{\sqrt{2}\Delta}{A} \cos\frac{x}{2} \sqrt{\cos x - \cos a}. \tag{21}$$

If one requires the solution for an arbitrary period L instead of 2π, Equation (21) becomes

$$p(x) = -\frac{2\sqrt{2}\Delta\pi}{AL} \cos\frac{\pi x}{L} \sqrt{\cos\frac{2\pi x}{L} - \cos\frac{2\pi a}{L}}.$$

It is sometimes convenient to express the normal traction in terms of a peak pressure, p_0, in order to find the contact length, a. Let $p_0 = 2\Delta/A$ and invoking equilibrium from (18) gives

$$P = \frac{2p_0}{\sqrt{1+\alpha^2}} \int_{-\alpha}^{\alpha} \frac{\sqrt{\alpha^2 - u^2}}{(1+u^2)^2} \, du.$$

Evaluating the integral results in

$$p_0 = \frac{P(1+\alpha^2)}{\pi\alpha^2} = \frac{2\Delta}{A}. \tag{22}$$

In original variables,

$$p(x) = -\frac{P\sqrt{2}\cos(x/2)\sqrt{\cos x - \cos a}}{2\pi \sin^2(a/2)},$$

which reproduces the Westergaard solution with $\bar{p} = P/2\pi$. It has been previously shown [Dundurs et al. 1973] that, for light loading, the Hertz line contact solution is recovered.

Periodic inclined punches. The problem of evenly spaced indenters on a half-space, shown in Figure 4, was originally studied by England and Green [1963] using complex potential functions. A general result for symmetric and/or antisymmetric loading was developed and the particular case of inclined flat punches was solved. The problem was later solved by Cai and Lu [2000]. Their solution is rederived here using the method of the previous section. As the slope of the punches approaches zero, the result for periodic flat punches is recovered.

For an inclined punch, the derivative of the surface profile is given by

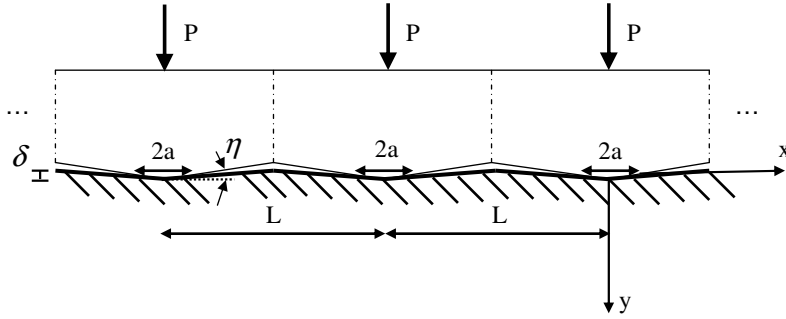$$\frac{\partial h(x)}{\partial x} = \varepsilon, \tag{23}$$

Figure 4. Frictionless normal contact of evenly spaced blunt wedges.

where ε is the slope of the punch. Substituting Equation (23) into (13) for frictionless contact ($q(u) = 0$) where now $p(u)$ is not symmetric gives

$$\frac{\varepsilon}{A} = \frac{1}{\pi} \int_{-\alpha}^{\alpha} \frac{p(u)}{(v-u)} \, du + \frac{1}{\pi} \int_{-\alpha}^{\alpha} \frac{up(u)}{(1+u^2)} \, du.$$

[Söhngen 1954] suggested solving this type of integral equation by decomposing $p(u)$ into a homogeneous part, $p_h(u)$, and an inhomogeneous part, $p_i(u)$, which results in two integral equations

$$\frac{1}{2\pi} \int_{-\alpha}^{\alpha} \frac{p_h(u)}{v-u} \, du = 0, \tag{24}$$

$$\frac{1}{\pi} \int_{-\alpha}^{\alpha} \frac{p_i(u)}{v-u} \, du + \frac{1}{\pi} \int_{-\alpha}^{\alpha} \frac{up_i(u)}{1+u^2} \, du = \frac{\varepsilon}{A}. \tag{25}$$

The first integral is recognized as the periodic flat punch solution, or the homogenous case of the integral equation. The second integral represents the contribution due to the slope of the indenter. Inverting (24) according to the appropriate formula in Section A.1 (with singularities at both endpoints) gives

$$p_h(u) = \frac{C}{\sqrt{1 - (u/\alpha)^2}}. \tag{26}$$

The equilibrium (18) gives

$$C = -\frac{P\sqrt{1+\alpha^2}}{2\alpha\pi}. \tag{27}$$

Putting (27) into (26) gives the solution for the complete contact of periodic flat punches on an elastic half-space without friction

$$p_h(x) = -\frac{P\sqrt{2}\cos(x/2)}{2\pi\sqrt{\cos x - \cos a}}, \qquad |x| < a. \tag{28}$$

Refer to (25) for the inhomogeneous solution and let $C_1 = \varepsilon/A - C_2$. Recognizing that the second integral only produces a constant

$$\frac{1}{\pi} \int_{-\alpha}^{\alpha} \frac{up_i(u)}{1+u^2} \, du = C_2,$$

then the integral equation is rewritten as

$$\frac{1}{\pi} \int_{-\alpha}^{\alpha} \frac{p_i(u)}{v-u} du = C_1.$$

Inverting for $p_i(u)$ (see Section A.1) produces

$$p_i(u) = \frac{C_1}{\pi \sqrt{\alpha^2 - u^2}} \int_{-\alpha}^{\alpha} \frac{\sqrt{\alpha^2 - s^2}}{u-s} ds = -\frac{C_1 u}{\pi \sqrt{\alpha^2 - u^2}}.$$

To solve for C_1, insert $p_i(u)$ into (25), obtaining

$$C_1 = \frac{\pi \varepsilon}{A} \sqrt{\alpha^2 + 1}.$$

Returning to original variables gives

$$p(x) = p_i + p_h = -\frac{\varepsilon \sqrt{2} \sin(x/2)}{A \sqrt{\cos x - \cos a}} - \frac{P \sqrt{2} \cos(x/2)}{2\pi \sqrt{\cos x - \cos a}}, \tag{29}$$

which is the result in [England and Green 1963; Cai and Lu 2000]. It is seen that for $\varepsilon = 0$, (29) is the flat punch solution in (28). For incomplete penetration, the pressure must be positive, in which case it is required that for period L and contact length $2a$,

$$P \geq -\frac{L\varepsilon}{A} \tan \frac{\pi a}{L}.$$

Now that the method has been verified against some well-known solutions, new solutions in periodic contact are solved in the following sections.

Indentation by blunt periodic wedges. In Figure 4, the problem of a periodic array of wedges is shown. To ensure that the small strain assumption is valid, the wedge must be blunt, which means that the angle η is small. The normal displacement derivative is

$$\frac{\partial h(x)}{\partial x} = -\eta \operatorname{sgn}(\tan x/2).$$

The function changes sign as necessary for periodic wedges with period 2π. Anticipating a symmetric stress distribution, $p(u)$, the governing integral equation is

$$\frac{1}{\pi} \int_{-\alpha}^{\alpha} \frac{p(u)}{v-u} du = \frac{\eta}{A} \operatorname{sgn}(v). \tag{30}$$

This integral can be found in [Hills et al. 1993] with solution

$$p(u) = -\frac{2\eta}{\pi A} \cosh^{-1} \frac{\alpha}{|u|},$$

or in original variables with arbitrary period, L, is

$$p(x) = -\frac{2\eta}{A\pi} \cosh^{-1} \frac{\tan(\pi a/L)}{\tan(\pi |x|/L)}.$$
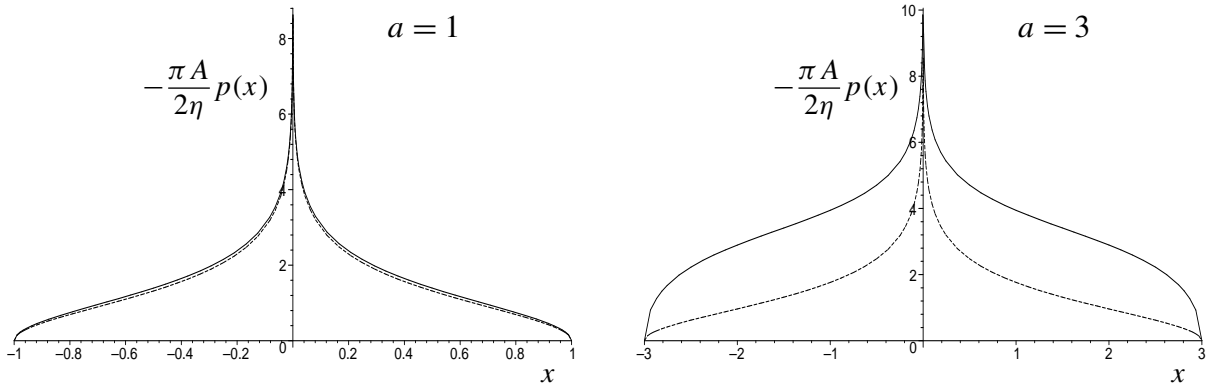
Figure 5. Normal surface tractions for single (dotted lines) and periodic (solid lines) blunt wedge indenters for wavelength $L = 2\pi$, for $a = 1$ and $a = 3$.

In the limit as $L \to \infty$, the solution for a single blunt wedge (see [Truman et al. 1995] for instance) is recovered. The normal surface tractions are plotted in Figure 5 to compare the single wedge to the periodic array of wedges. When the contact region is small compared to the wavelength, the two results are almost indistinguishable. As the contact length approaches the wavelength, the plots become noticeably different. The normalization factor is chosen for convenience, but could easily be adjusted in terms of the total load, P, by evaluating the equilibrium of surface tractions. The main feature of the blunt wedge indenter is the singularity at the tip due to the discontinuity in the displacement derivative.

4. Problems in periodic contact: sliding contact

Sliding contact of elastically dissimilar materials. It was assumed that either the bodies in contact were elastically similar or that the contact was frictionless. As a result, the integral equations were uncoupled and solved using standard techniques. In this section, the sliding contact of elastically dissimilar materials with friction is considered. The empirical Coulomb friction law is used here, which states:

(i) the frictional force is proportional to the normal force multiplied by the coefficient of friction;

(ii) the frictional force opposes the direction of relative motion;

(iii) neither the apparent contact area nor the velocity during gross sliding affects the magnitude of the frictional force;

(iv) the motion is assumed to be quasistatic.

While these observations typically apply to rigid bodies, it is reasonable to extend the model to the analysis of frictional elastic contacts in two dimensions. More complicated studies suggest a nonlinear relationship between normal loading and frictional force [Urbakh et al. 2004]; however only Coulomb friction will be considered here.

By assuming that the shear tractions are proportional to the normal force, limited everywhere by friction and independent of the speed, except for sign, one obtains

$$q(x) = -fp(x), \tag{31}$$

where f is the coefficient of friction. Substituting Equation (31) into (16) yields

$$\frac{1}{A}\frac{\partial h}{\partial x} = \frac{1}{2\pi}\int_b^a p(\xi)\left(\cot\frac{x-\xi}{2} - \tan\frac{\xi}{2}\right)d\xi + \beta f p(x), \tag{32}$$

which is a Cauchy singular integral equation of the second kind, where the solution technique is outlined in Section A.2. Another consequence of introducing friction is that the contact patch, $2a$, is no longer expected to be centered. Instead, an eccentricity, e, is introduced into the displacement derivative, which corresponds to the rotation due to the sliding of elastically dissimilar materials. Equation (32) is used as the starting point for much of the problems solved below.

Sliding contact of periodic flat punches. For periodic flat punches sliding on an elastic half-space, the derivative of the surface profile is proportional to a constant, which represents a rotation due to the sliding of elastically dissimilar materials. However, the problem has more practical relevance when the periodic punches are rigid, which means that the punch is not free to rotate and the resulting boundary condition becomes

$$\frac{\partial h(x)}{\partial x} = 0. \tag{33}$$

Since there is no rotation, (32) must be used. Substituting (33) leads to

$$\frac{1}{\pi}\int_{-\alpha}^{\alpha}\frac{p(u)}{(v-u)}du + \beta p(v) = 0.$$

For a rigid punch in contact with an elastic half-space in plane strain contact, the Dundurs' parameter, β, is

$$\beta = \frac{1-2\nu}{2(1-\nu)},$$

although the definition in (3) can be still be used without much loss of generality. Returning to the Cauchy singular integral equation of the second kind, Section A.2 gives an inversion for $p(u)$ that is singular at both endpoints, namely $p(u) = C(\alpha - u)^{m-1}(\alpha + u)^{-m}$, where $\tan m\pi = 1/\beta f$ and $0 < m < 1$. To find C, equilibrium of the total load, (18), gives

$$P = 2C\int_{-\alpha}^{\alpha}\frac{(\alpha - u)^{m-1}(\alpha + u)^{-m}}{1 + u^2}du.$$

The integral is solved using complex variables and is given in Appendix B. Solving for C,

$$C = -\frac{P\sqrt{1+\alpha^2}\sin m\pi}{2\pi\sin[m\pi - \phi(2m-1)]},$$

where $\tan\phi = 1/\alpha$. Returning to original variables,

$$p(x) = -\frac{P\sin m\pi\left(\tan(a/2) - \tan(x/2)\right)^{m-1}\left(\tan(a/2) + \tan(x/2)\right)^{-m}}{2\pi\cos(a/2)\sin[m\pi - \phi(2m-1)]},$$

where $\tan\phi = \cot(a/2)$. When $m = 1/2$, the result for frictionless contact in Equation (28) is recovered. The equation is singular at both end points, $x = \pm a$, as expected for complete contact.
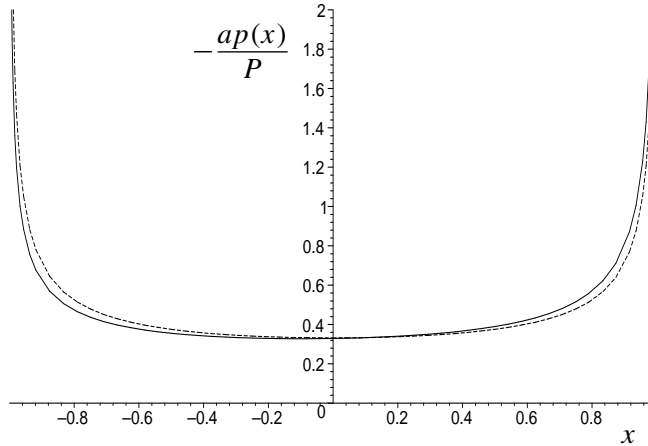
Figure 6. The surface pressure for a evenly spaced rigid flat punches with $f = 0.5$, $\nu = 0.3$ and $L = 2\pi$, for frictionless (dotted curve) and sliding (solid curve) contact for $a = 1$, sliding from left to right.

The normal tractions are no longer symmetric, as shown in Figure 6. However, the frictionless result is not very different from the sliding one for the given parameters. If however the punch were no longer rigid but elastic, the material mismatch would lead to greater discrepancy between the results, as would an increase in the coefficient of friction. It is also seen that the corners of the flat punch lead to singularities in the pressure distribution at the edge of the contact.

Sliding contact of sinusoids. The sliding of elastically dissimilar sinusoidal surfaces was studied by Nosonovsky and Adams [2000], who numerically solved the dry steady-state frictional sliding incorporating wave speeds, and later by Carbone and Mangialardi [2004], who used linear fracture mechanics to determine the coefficient of friction due to the adhesive forces.

For a given coefficient of friction, the sliding of elastically dissimilar sinusoids is solved here in a closed-form for the first time. This new result is compared to the frictionless case, except for an eccentricity, e, due to the dissimilar elastic constants. The difference of the displacement derivatives for two wavy surfaces is

$$\frac{\partial h(x)}{\partial x} = \Delta \sin(x - e), \tag{34}$$

where e represents the phase shift due to sliding and Δ is a function of the gap and amplitude(s) to ensure that the displacements are continuous at the edge of the contact region. Substituting (34) into (32) with the usual change of variables (and with an eye toward the integrals in Appendix B) yields

$$\frac{1}{\pi} \int_{-\alpha}^{\alpha} \frac{p(u)}{v - u} \, du + \beta p(v) = \frac{\Delta}{A} w(v), \tag{35}$$

where $e_1 = \cos e$, $e_2 = \sin e$ and $w(v) = \left(e_1 \frac{2v}{1 + v^2} - e_2 \frac{1 - v^2}{1 + v^2} \right)$; this determines the eccentricity, e, from the consistency condition

$$\int_{-\alpha}^{\alpha} w(v)(\alpha - v)^{-m}(\alpha + v)^{m-1} \, dv = 0.$$

This integral may seem different from those in Appendix B with respect to their powers; however, setting $m = 1 - n$ transforms the powers to the desired form. The eccentricity is found to be

$$e = \tan^{-1}\left(\frac{\cos \lambda}{\sin \lambda - \alpha^2 \sqrt{1 + \alpha^2} m(1 - m)}\right),$$

where $\lambda = (m\pi - \phi(2m - 1))$ and $\tan \phi = 1/\alpha$. For $m = 1/2$ the eccentricity vanishes, as expected from the absence of sliding.

The integral equation in Equation (35) is now inverted for $p(u)$ according to the appropriate formula in Section A.2 as

$$p(u) = \frac{\Delta}{A}\left[\beta f w(u) - \frac{1}{\pi}\int_{-\alpha}^{\alpha} w(v)\frac{(\alpha - v)^{-m}(\alpha + v)^{m-1}}{v - u}\,dv\right](\alpha - v)^m(\alpha + v)^{1-m}.$$

Using partial fractions and evaluating the Cauchy integrals which cancel with the βf terms above results in

$$p(u) = -\frac{2\Delta}{A\pi(1 + u^2)}(\alpha - v)^m(\alpha + v)^{1-m}\int_{-\alpha}^{\alpha}\left(e_1(1 - uv) + e_2(v + u)\right)\frac{(\alpha - v)^{-m}(\alpha + v)^{m-1}}{1 + v^2}\,dv.$$

Calculating the integrals according to Appendix B, the surface stress is

$$p(u) = -\frac{2\Delta}{A(1 + u^2)}\frac{1}{\sqrt{1 + \alpha^2}}\frac{\left[\sin(\lambda + e) - u\cos(\lambda + e)\right]}{\sin \pi m}(\alpha - v)^m(\alpha + v)^{1-m}.$$

In dimensional variables, the final result for the normal surface tractions is

$$p(x) = -\frac{2\Delta}{A}\frac{\cos(a/2)\cos(x/2)}{\sin \pi m}\sin\left[\lambda + e - \frac{x}{2}\right]\left(\tan\frac{a}{2} - \tan\frac{x}{2}\right)^m\left(\tan\frac{a}{2} + \tan\frac{x}{2}\right)^{1-m}. \tag{36}$$

The surface stress can also be expressed in terms of the total load, P, by substituting (31) into the equilibrium equation in (17) and exploiting the solutions given in Appendix B. For $m = 1/2$, (36) reduces to the frictionless contact of sinusoids given in (21) as expected.

Equation (36) is the first closed form solution for the sliding of an elastic wavy surface. It may prove useful in analyzing real rough surface whose average amplitude and wavelength have been evaluated in order to obtain pressure approximations or even to back-out the coefficient of friction of the mating surfaces.

The Coulomb friction again causes the sliding result to be asymmetric, but it is only slightly different from the frictionless result; see Figure 7. The friction reduces the pressure at the front edge of the indenter but increases it at the rear. The plots become more disparate by considering two elastic bodies or increasing the coefficient of friction. The smooth nature of the wavy profiles does not produce singularities in the surface stress and vanishes at the edge of the contact.

5. Problems in periodic contact: partial slip contact of similar materials

Partial slip contact: similar materials. In the previous section, sliding contact problems of various periodic geometries — in which the entire surface of the indenter moves in the same direction — were solved in a closed-form. The elastically dissimilar materials produced asymmetry in the solutions.

A different type of contact is considered in this section, namely partial slip contact of elastically similar materials. Typically in partial slip problems, the normal load is held fixed and the tangential load
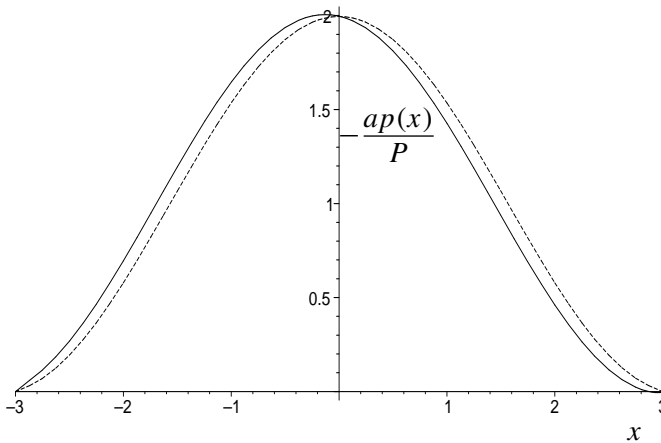
Figure 7. The surface pressure for a rigid wavy surface with $f = 0.5$, $\nu = 0.3$ and $L = 2\pi$ for frictionless (dotted curve) and sliding (solid curve) contact for $a = 3$.

is increased from zero causing two types of contact regions. One region consists of a contact area that is a stick region, and the other region of the contact area slips such that, shear tractions remain bounded. This requires the region to undergo "microslip." Partial slip analyses are particularly useful for analyzing fretting fatigue problems [Hills and Nowell 1994].

A comprehensive examination of partial slip theory and problems for similar materials was undertaken by Ciavarella [1998a; 1998b], who based his analysis on Cattaneo and Mindlin's solution. Their method was to write the shear tractions, $q(x)$, in the contact region as a linear combination of the normal traction and a correction term, that is,

$$q(x) = -fp(x) + q^*(x), \tag{37}$$

where f is the coefficient of friction, $p(x)$ is the normal traction, and $q^*(x)$ is a correction to the shear traction to ensure a finite coefficient of friction at the edge of contact. It should be noted that $q^*(x)$ is zero in the slip zones, meaning the shear traction is simply given by Coulomb's friction law.

Based on this approach, Ciavarella derived closed form solutions for many indenter geometries, including a few involving periodic indenters. More importantly, he summarized his findings on the theory in a few rules which are quoted exactly below:

(1) If the indenter profile is symmetric and *self-similar*, the corrective solution is of the same shape as the normal pressure in the contact area for any load.

(2) No partial slip solution can be predicted where the stick zone lies entirely within a flat region of the punch; in other words, flat regions are either entirely in full stick or are in full slip conditions.

(3) If in normal indentation there is no change of relative rotation, then the points that come into contact last are the first to slip.

(4) If the indenter profile has discontinuities, these affect the tangential load, stick area dimension relation in the same was as they affect the normal load, contact area dimension.

When solving periodic problems, Ciavarella does not differentiate between a single indenter and periodic indenters; he presupposes that the shear correction term has the same form as the normal pressure
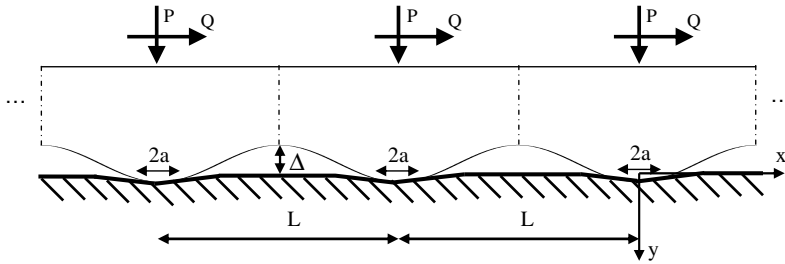
Figure 8. Partial slip contact of a sinusoidal profile for elastically similar materials.

solution. In (1) above, surfaces are assumed self-similar. Periodic solutions are not necessarily self-similar, because they have a wavelength which introduces a length scale.

In this section Ciavarella's solution for periodic contact of similar materials will be derived using the previous technique. The standard change of variables changes the periodic problem to a single contact patch.

Sinusoids in partial slip. Since elastically similar bodies are considered here, it means that the governing integral equations are uncoupled ($\beta = 0$). As opposed to the sliding contact problems in the previous section, symmetric surface tractions are once again expected, as shown in Figure 8.

For a sinusoidal indenter, the stick zone is anticipated at the center of the contact, since the loading, geometry and material properties are symmetric about the x and y axes. The slip zones occur at the edges of contact region and are the points which are last to come into contact. The shear tractions can be expressed by (37) in the stick zone and (31) in the slip zone and the governing integral equation for the shear tractions is

$$\frac{1}{2\pi} \int_{-a}^{a} q(\xi) \cot \frac{x-\xi}{2} d\xi = \frac{1}{A} \frac{\partial g(x)}{\partial x}, \qquad |x| < b, \tag{38}$$

which is (10) for similar materials. Also, since the relative tangential displacements due to the normal load, P, are constant, it follows that $\partial g(x)/\partial x = 0$ in the stick zone. Thus, substituting (37) into (38) gives

$$\frac{1}{2\pi} \int_{-b}^{b} q^*(\xi) \cot \frac{x-\xi}{2} d\xi = \frac{f}{2\pi} \int_{-a}^{a} p(\xi) \cot \frac{x-\xi}{2} d\xi, \qquad |x| < b, \tag{39}$$

where $p(x)$ is the Westergaard solution found in Equation (21). In order to solve for the shear correction term in (39), the change of variables in (28) is used as well as $\gamma = \tan(b/2)$ to get

$$\frac{1}{\pi} \int_{-\gamma}^{\gamma} \frac{q^*(u)}{v-u} du + \frac{1}{\pi} \int_{-\gamma}^{\gamma} \frac{uq'(u)}{1+u^2} du = -\frac{2f\Delta}{A\pi} \int_{-\alpha}^{\alpha} \frac{(1+uv)\sqrt{\alpha^2-u^2}}{(1+u^2)^2(v-u)\sqrt{1+\alpha^2}}, \qquad |v| < \gamma. \tag{40}$$

Noting the symmetry of $q^*(x)$ eliminates the second term on the left-hand side of (40). The right-hand side is simplified by first adding and subtracting v^2 in the numerator and yields

$$\frac{1}{\pi} \int_{-\gamma}^{\gamma} \frac{q^*(u)}{v-u} du = -\frac{2f\Delta}{A\pi\sqrt{1+\alpha^2}} \left((1+v^2) \int_{-\alpha}^{\alpha} \frac{\sqrt{\alpha^2-u^2}}{(1+u^2)^2(v-u)} du + v \int_{-\alpha}^{\alpha} \frac{\sqrt{\alpha^2-u^2}}{(1+u^2)^2} du \right), \quad |v| < \gamma. \tag{41}$$

The second term on the right-hand side of (41) is easily evaluated. The remaining term on the right-hand side is simplified by using partial fractions, which gives

$$\frac{1}{\pi} \int_{-\gamma}^{\gamma} \frac{q^*(u)}{v - u} du = -\frac{2f\Delta}{A} \frac{v}{1 + v^2}, \qquad |v| < \gamma.$$

Inverting for $q^*(x)$ (Section A.1) and again using partial fractions results in

$$q^*(u) = -\frac{2f\Delta\sqrt{\gamma^2 - u^2}}{A(1 + u^2)\sqrt{1 + \gamma^2}}, \qquad |u| < \gamma.$$

Reverting to original variables gives the final result for the shear correction term

$$q^*(x) = -\frac{\sqrt{2}f\Delta}{A} \cos\frac{x}{2}\sqrt{\cos x - \cos b}. \tag{42}$$

It is seen that indeed the shear correction term (42) has the same form as the normal tractions, (21), which is also revealed upon inspection of (39). But it has been shown that it indeed has the same form for regularly periodic indenters. Lastly, satisfying equilibrium requires that

$$Q^* = \frac{2q_0^*}{\sqrt{1 + \gamma^2}} \int_{-\gamma}^{\gamma} \frac{\sqrt{\gamma^2 - u^2}}{(1 + u^2)^2} du.$$

Evaluating the integral results in

$$q_0^* = \frac{Q(1 + \gamma^2)}{\pi\gamma^2} = -\frac{\sqrt{2}f\Delta}{A}. \tag{43}$$

Combining (22) with (43) gives the result in a convenient form to determine the stick zone

$$\frac{Q}{fP} = 1 - \frac{\sin^2(\pi b/L)}{\sin^2(\pi a/L)}, \tag{44}$$

which is the result in [Ciavarella 1998b] for sinusoidal indenters. The result is expressed in terms of period, L, for practicality. Here, Q and P are understood to be the total normal and shear loads.

Other periodic profiles under partial slip. Other new results can be obtained for various periodic indenter profiles. For instance, Ciavarella [1998b] provides the result for a single wedge, power-law or polynomial punch

$$\frac{Q}{fP} = 1 - \left(\frac{b}{a}\right)^k, \tag{45}$$

where $k = 1, 2, 4, 6$ is a power representing a wedge, parabolic (Hertzian) and high-order polynomial indenters respectively. His method is easily extended to periodic indenters as well. Starting with Equation (9) with $\beta = 0$,

$$\frac{1}{A}\frac{\partial h}{\partial x} = \frac{1}{2\pi} \int_{-a}^{a} p(\xi) \cot\frac{x - \xi}{2} d\xi. \tag{46}$$

Changing variables and inverting for $p(u)$ gives

$$p(u) = \frac{1}{\pi A}\sqrt{\alpha^2 - u^2} \int_{-\alpha}^{\alpha} \frac{h'(x)}{\sqrt{\alpha^2 - v^2}(v - u)} dv, \qquad |u| < \alpha, \tag{47}$$

where $h'(t) = \partial h/\partial x$ is the derivative of the indenter profile in terms of the original variable x. Substituting (47) into the equilibrium equation, (30), gives the total load, P as

$$P = -\frac{1}{A\pi} \int_{-\alpha}^{\alpha} \frac{h'(x)}{\sqrt{\alpha^2 - v^2}} dv \int_{-\alpha}^{\alpha} \frac{\sqrt{\alpha^2 - u^2}}{(1+u^2)(v-u)} du.$$

Interchanging the order of integration and then using partial fractions results in

$$P = -\frac{\sqrt{1+\alpha^2}}{A} \int_{-\alpha}^{\alpha} \frac{vh'(x)}{\sqrt{\alpha^2 - v^2}(1+v^2)} dv. \tag{48}$$

Equation (48) directly relates the surface profile to the total load. A similar calculation is done for the shear correction load, Q^*, by first substituting (46) into (39) to get

$$\frac{1}{2\pi} \int_{-b}^{b} \frac{q^*(\xi)}{f} \cot \frac{x-\xi}{2} d\xi = \frac{1}{A} \frac{\partial h(x)}{\partial x}. \tag{49}$$

Inverting (49) for $q^*(u)$ with changed variables, invoking equilibrium and finally solving for Q^* gives

$$Q^*/f = \frac{\sqrt{1+\gamma^2}}{A} \int_{-\gamma}^{\gamma} \frac{vh'(x)}{\sqrt{\gamma^2 - v^2}(1+v^2)} dv. \tag{50}$$

Integrating (37) over the contact region and substituting (50) yields

$$Q = fP + \frac{f\sqrt{1+\gamma^2}}{A} \int_{-\gamma}^{\gamma} \frac{vh'(x)}{\sqrt{\gamma^2 - v^2}(1+v^2)} dv. \tag{51}$$

Combining (51) with (48) produces the final result for the ratio of the shear load to the normal load for periodic indenters

$$\frac{Q}{fP} = 1 - \frac{\sqrt{1+\gamma^2} \int_{-\gamma}^{\gamma} \dfrac{vh'(x)}{\sqrt{\gamma^2 - v^2}(1+v^2)} dv}{\sqrt{1+\alpha^2} \int_{-\alpha}^{\alpha} \dfrac{vh'(x)}{\sqrt{\alpha^2 - v^2}(1+v^2)} dv}. \tag{52}$$

Depending on the nature of $h'(x)$, other closed-form solutions for periodic indenters can be derived from Equation (52). For instance, the partial slip of periodic blunt wedges is solved by first noting

$$h'(x) = \eta \, \mathrm{sgn}(x). \tag{53}$$

Substituting (53) into (52) and integrating yields

$$\frac{Q}{fP} = 1 - \frac{\tanh^{-1}\left(\gamma/\sqrt{1+\gamma^2}\right)}{\tanh^{-1}\left(\alpha/\sqrt{1+\alpha^2}\right)} = 1 - \frac{\tanh^{-1} \sin(\pi b/L)}{\tanh^{-1} \sin(\pi a/L)}, \tag{54}$$

where L is the period of the indenters. For a small contact region, $a/L \ll 1$, (54) reduces to (45) for $k=1$ as anticipated. For a general power-law profile, the displacement derivative is

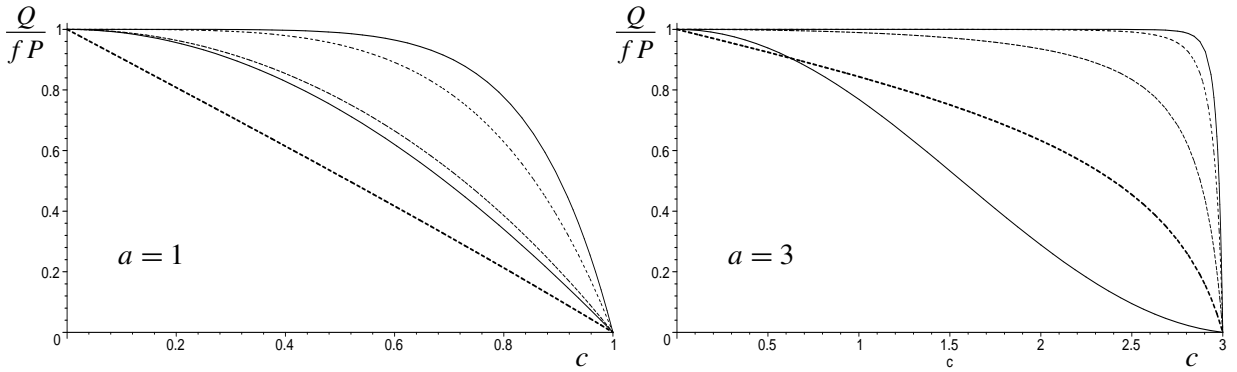$$h'(x) = -\eta k |x|^{k-1} \, \mathrm{sgn}(x). \tag{55}$$

Figure 9. Ratio of shear force to normal load as a function of slip zone, c, for $a = 1, 3$ and various power-law profiles. Curves from top to bottom: $k = 6$ profile, quadratic profile, parabolic profile, wedge profile, simple profile.

For $k = 2$, which physically corresponds to evenly spaced Hertzian indenters, the ratio of shear to normal loads is

$$\frac{Q}{fP} = 1 - \frac{\sqrt{\gamma^2 + 1} - 1}{\sqrt{\alpha^2 + 1} - 1}. \tag{56}$$

Returning to original variables with period, L, changes (56) into

$$\frac{Q}{fP} = 1 - \frac{\cos(\pi a/L)}{\cos(\pi b/L)} \frac{1 - \cos(\pi b/L)}{1 - \cos(\pi a/L)}.$$

When the contact region is small, $a/L \ll 1$, the result for $k = 2$ in (54) is recovered. In a similar fashion, higher order power-law and polynomial indenter profiles can be solved. For $k = 4$ in (55), the ratio of the transmitted forces is found to be

$$\frac{Q}{fP} = 1 - \frac{\cos(\pi a/L)}{\cos(\pi b/L)} \frac{\left(\tan^2(\pi b/L) + 2\cos(\pi b/L) - 2\right)}{\left(\tan^2(\pi a/L) + 2\cos(\pi a/L) - 2\right)}.$$

For $k = 6$, the solution is

$$\frac{Q}{fP} = 1 - \frac{\cos(\pi a/L)}{\cos(\pi b/L)} \frac{\left(3\tan^4(\pi b/L) - 4\tan^2(\pi b/L) - 8\cos(\pi b/L) + 8\right)}{\left(3\tan^4(\pi a/L) - 4\tan^2(\pi a/L) - 8\cos(\pi a/L) + 8\right)}.$$

Further higher-order power-law indenters can be calculated in a similar manner. The results for the partial slip of elastically similar profiles are plotted below in Figure 9. As the power of the profile increases, the slip zone size varies weakly under small loads and strongly under larger loads, which is the same observation made in [Ciavarella 1998b]. The higher order polynomial indenters are close to a flat punch profile, which must either completely stick or slip and is discussed next.

Another solution of interest is the partial slip of evenly spaced flat punches on a half-space of similar material. Ciavarella notes that elastically similar flat punches must either completely slip or completely

stick. The shear tractions are always proportional to the normal tractions, which are given by

$$q(x) = -\frac{Q\sqrt{2}\cos(\pi x/L)}{L\sqrt{\cos(2\pi x/L) - \cos(2\pi a/L)}}, \qquad |x| < a. \tag{57}$$

It should not be surprising then that Equation (57) resembles (28), which is the frictionless normal contact solution for flat punches. When $|Q| = fP$, full slip occurs throughout the contact region. The solution is singular at the edge of the contact area, as expected for flat punch indenters.

6. Problems in periodic contact: partial contact of dissimilar materials

Partial slip contact: dissimilar materials. The partial slip contact of elastically dissimilar materials is considered here, which means that the governing integral equations are coupled. Before solving the partial slip problem, which is mathematically complicated, the no slip or complete stick problem is solved for periodic profiles. Physically, complete stick occurs when the friction force is large enough to prevent any slip. Even though the integral equations are still coupled for complete stick, some closed-form solutions are calculated in this section.

One simplifying assumption to uncouple the integral equations is to assume the effect of the shear tractions on the normal displacements is negligible, the Goodman approximation [Goodman 1962]. This simplification removes the coupling in (15). The advantage is that the normal contact solutions are known and as a first approximation can then be substituted into the shear traction (16). Solutions for flat punches and sinusoidal profiles are worked out for this type of analysis.

Lastly, partial slip solutions for elastically dissimilar periodic flat punches and sinusoids are solved based upon the procedure of Spence [1973], who used a self-similarity argument when evaluating the displacement derivatives. In light of the previous section, it is now known that even though regularly periodic profiles are not self-similar, the appropriate transformation of variables changes the problem to a single contact patch which *is* self-similar; then the solution techniques for a single indenter can be exploited. Although the materials are dissimilar, the removal of the coupling term ensures that the normal tractions are symmetric for symmetric indenters, which in turn causes the shear tractions to also be symmetric about the centerline of the contact region. The stick region is anticipated in the center of the contact region with slip regions at the edges.

No slip contact of periodic flat punches: coupled. In this section, the problem of elastically dissimilar flat punches in contact with an elastic half-space is solved for the completely coupled case. It may be more practical to assume that the flat punches are rigid, but the solution here is solved more generally in terms of Dundur's parameter. For flat punches, the displacement derivates are

$$\frac{\partial h(x)}{\partial x} = \frac{\partial g(x)}{\partial x} = 0. \tag{58}$$

This reduces the integral equations of contact, (15)–(16), in changed variables to

$$\frac{1}{\pi}\int_{-\alpha}^{\alpha}\frac{p(u)}{(v-u)}du - \beta q(v) = 0, \qquad \frac{1}{\pi}\int_{-\alpha}^{\alpha}\frac{q(u)}{(v-u)}du + \beta p(v) = 0.$$

The solution technique for the above coupled integral equations is described in [Johnson 1985b], where the solution is

$$F(v) = -\frac{\lambda}{\sqrt{1-\lambda^2}} \frac{C}{\pi \sqrt{\alpha^2 - v^2}} \left(\frac{\alpha - v}{\alpha + v}\right)^{i\eta}, \tag{59}$$

where $F(u) = p(u) + iq(u)$, $i = \sqrt{-1}$, $\lambda = -i/\beta$, and

$$\eta = \frac{1}{2\pi} \ln \frac{1 + \beta}{1 - \beta}.$$

Note that η is a constant based on the material parameter β here and not the slope for a blunt wedge used above. The constant, C, in (59) is determined from the equilibrium equation

$$\int_{-\alpha}^{\alpha} \frac{2F(v)}{1 + v^2} dv = P + iQ.$$

The final result for the surface tractions in terms of the original variable is

$$p(x) + iq(x) = \frac{P + iQ}{\sqrt{1 - \beta^2}} \frac{\sqrt{2}\cos(x/2)}{2\pi \sqrt{\cos x - \cos a}} \left(\frac{\tan(a/2) + \tan(x/2)}{\tan(a/2) - \tan(x/2)}\right)^{i\eta}. \tag{60}$$

It is seen that the singularities at $x = \pm a$ are complex for the completely coupled case. As the wavelength of the periodic punches becomes infinite, the result for a single flat indenter given in [Johnson 1985b] is recovered. When $P = 0$, (57) for the shear tractions due to a tangential force, Q, is recovered.

No slip contact of periodic flat punches: approximation. Because of the limited availability of closed-form solutions for the completely coupled integral equations, it is often convenient to introduce the Goodman approximation, which neglects the contributions of the shear stress on the normal displacements. The advantage is that the frictionless normal contact solutions developed in previous section can be used to derive the shear tractions without much loss of accuracy. Recalling the solution for frictionless normal contact of a flat punch

$$p(x) = -\frac{P\sqrt{2}\cos(x/2)}{2\pi \sqrt{\cos x - \cos a}},$$

and using Equation (58) causes the integral equation for the shear traction, (14), to be

$$\frac{1}{\pi} \int_{-\alpha}^{\alpha} \frac{q(u)}{(v - u)} du - \frac{\beta P \sqrt{1 + \alpha^2}}{2\pi \sqrt{\alpha^2 - v^2}} = 0. \tag{61}$$

Inverting (61) for $q(u)$ according to the formula in Section A.1 with singularities at both endpoints gives

$$q(u) = \frac{\beta P \sqrt{1 + \alpha^2}}{2\pi^2 \sqrt{\alpha^2 - u^2}} \int_{-\alpha}^{\alpha} \frac{dv}{v - u} + \frac{Q\sqrt{2}\sqrt{1 + \alpha^2}}{2\pi \sqrt{\alpha^2 - u^2}}, \tag{62}$$

where the second term corresponds to the shear traction solution for a flat punch, (57). Evaluating the integral in (62) yields

$$q(u) = \frac{\beta P \sqrt{1 + \alpha^2}}{2\pi^2 \sqrt{\alpha^2 - u^2}} \ln\left(\frac{\alpha + u}{\alpha - u}\right) + \frac{Q\sqrt{2}\sqrt{1 + \alpha^2}}{2\pi \sqrt{\alpha^2 - u^2}}.$$
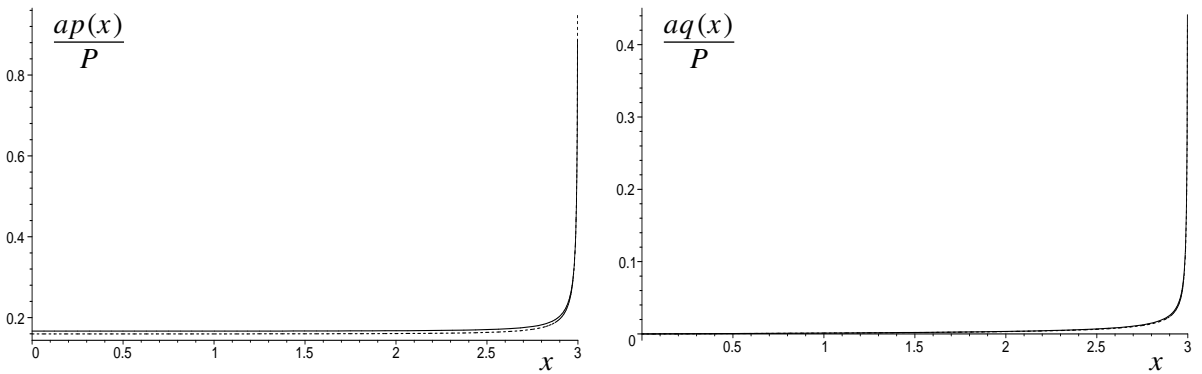
Figure 10. Normal (left) and tangential (right) tractions for the slipless contact of periodic rigid flat punches, for $\nu = 0.3$, $f = 0.215$, $L = 2\pi$, and $a = 3$. On the left, the solid curves is for the coupled normal force and the dashed curve for the frictionless normal force. On the right panel, the curves for the coupled tangential force and the Goodman tangential force are confounded.

Returning to original variables, the shear traction with the Goodman approximation is

$$q(x) = -\frac{\beta P \sqrt{2} \cos(x/2)}{2\pi^2 \sqrt{\cos x - \cos a}} \ln \frac{\tan(a/2) + \tan(x/2)}{\tan(a/2) - \tan(x/2)} + \frac{Q\sqrt{2} \cos(x/2)}{2\pi \sqrt{\cos x - \cos a}}. \tag{63}$$

As the period goes to infinity, the result for a single flat indenter is recovered. The coupled normal and shear traction solutions in the previous section, (60), are compared below with the frictionless, (28), and Goodman approximation, (63), respectively.

Figure 10 demonstrates that the Goodman approximation is not very different than that for the coupled case, even as the contact length approaches the period. In fact, the shear tractions are essentially indistinguishable. One interesting thing to note about the solution is the symmetry about the origin. Because of the symmetric normal tractions and symmetric indenter, the shear tractions are also symmetric about the center line of the contact region, although the materials are dissimilar. This is a consequence of neglecting the coupling term in the normal displacement governing integral equation, which was not done in the sliding contact solutions.

No slip contact of sinusoids: Goodman approximation. The no slip problem for a sinusoidal surface in contact with an elastic half-space is developed in a similar manner to the flat punch solution. However, the tangential displacement derivative is

$$\frac{\partial g(x)}{\partial x} = C\Delta |\sin x|,$$

where C is an unknown constant to be determined. The absolute value function comes from the self-similarity argument made by Spence [1973]. The premise is that the stick zone is proportional to the slip zone; see (44). Thus, as the shear load is steadily increased from zero, the particles entering the stick zone undergo a prestrain that is proportional to $|\sin x|$, which is the absolute distance from the center of the contact region. For a single indenter, the prestrain is proportional to x, which is recovered for small

x (or large L) in the periodic problem. It is also noted that the tangential displacement derivative must be an even function in order to ensure the symmetry of the solution.

Recalling from (21) the normal tractions for a sinusoidal profile, the integral (18) upon changing variables becomes

$$\frac{1}{\pi} \int_{-\alpha}^{\alpha} \frac{q(u)}{(v-u)} du - \frac{\beta p_0 \sqrt{\alpha^2 - v^2}}{\sqrt{1+\alpha^2}(1+v^2)} = \frac{2\Delta C}{A} \frac{|v|}{1+v^2}, \qquad |v| < \alpha. \tag{64}$$

Inverting (64) for $q(u)$ with no singularities at the endpoints gives

$$q(u) = \frac{\sqrt{\alpha^2 - u^2}}{\pi} \int_{-\alpha}^{\alpha} \frac{F(v)}{\sqrt{\alpha^2 - v^2}(v-u)} dv, \tag{65}$$

with consistency condition

$$\int_{-\alpha}^{\alpha} \frac{F(v)}{\sqrt{\alpha^2 - v^2}} dv = 0,$$

where

$$F(v) = \frac{\beta p_0 \sqrt{\alpha^2 - v^2}}{\sqrt{1+\alpha^2}(1+v^2)} + \frac{2\Delta C}{A} \frac{|v|}{1+v^2}.$$

The consistency condition is evaluated, and it is found that

$$C = \frac{-p_0 \beta A}{2\Delta} \frac{\tan^{-1}(\alpha)}{\tanh^{-1}(\alpha/\sqrt{1+\alpha^2})}.$$

The integral equation, (65), is solved using partial fractions. After some work, the result is

$$q(u) = \frac{p_0 \beta}{\pi(1+u^2)} \left[\frac{\sqrt{\alpha^2 - u^2}}{\sqrt{1+\alpha^2}} \ln\left|\frac{\alpha+u}{\alpha-u}\right| + \frac{u \tan^{-1}(\alpha)}{\tanh^{-1}(\alpha/\sqrt{1+\alpha^2})} \ln\left(\frac{\alpha + \sqrt{\alpha^2 - u^2}}{\alpha - \sqrt{\alpha^2 - u^2}}\right) \right], \tag{66}$$

where $\alpha = \tan(a/2)$ and $u = \tan(x/2)$ are in terms of the original variables. The solution for a single Hertzian indenter is provided by Johnson [1985b] and corresponds to when the period between the sinusoids approaches infinity and the contact region is small in the above solution.

Partial slip contact of periodic flat punches: Goodman approximation. The next step is to evaluate the partial slip solution with the Goodman approximation. This type of partial slip analysis with the Goodman approximation was first done for a single flat indenter [Spence 1973] and then Hertz contact [Spence 1975; Hills and Sackfield 1985]. The main difference from the complete stick analyses above are that the shear tractions are now split into stick and slip regions with

$$\int_{-\alpha}^{\alpha} \frac{q(u)}{(v-u)} du = 2f \int_{\gamma}^{\alpha} \frac{up(u)}{v^2 - u^2} du + 2 \int_0^{\gamma} \frac{uq(u)}{v^2 - u^2} du, \tag{67}$$

where $\gamma = \tan(b/2)$ and $q(u) = f p(u) \operatorname{sgn}(\beta u)$ in the slip region but is unknown within the stick region. The symmetry about the centerline has also been exploited. For periodic flat punches, Equation (67) is substituted into (66) to get

$$\frac{2}{\pi} \int_0^{\gamma} \frac{uq(u)}{v^2 - u^2} du = G(v), \qquad |v| < \gamma, \tag{68}$$

where

$$G(v) = \frac{2fp_0\sqrt{1+\alpha^2}}{\pi} \int_\gamma^\alpha \frac{u\,du}{(v^2-u^2)\sqrt{\alpha^2-v^2}} + \frac{\beta p_0\sqrt{1+\alpha^2}}{\sqrt{\alpha^2-v^2}}, \tag{69}$$

which has the flat punch solution, (28), substituted for $p(u)$ with $p_0 = P/2\pi$. Inverting (68) for $q(u)$ gives

$$q(u) = \frac{2u}{\pi\sqrt{\gamma^2-u^2}} \int_0^\gamma \frac{\sqrt{\gamma^2-v^2}G(v)}{u^2-v^2}\,dv. \tag{70}$$

Upon substituting (69) into (70) and interchanging the order of integration in the first term, $q(u)$ becomes

$$q(u) = \frac{2u\sqrt{1+\alpha^2}}{\pi\sqrt{\gamma^2-u^2}} \left[fp_0 \int_\gamma^\alpha \frac{\sqrt{v^2-\gamma^2}}{(v^2-u^2)\sqrt{\alpha^2-v^2}}\,dv - \beta p_0 \int_0^\gamma \frac{\sqrt{\gamma^2-v^2}}{(u^2-v^2)\sqrt{\alpha^2-v^2}}\,dv \right].$$

It is necessary that $q(u)$ be bounded at $u = \gamma$, which requires that

$$fK'\left(\frac{\gamma}{\alpha}\right) = \beta K\left(\frac{\gamma}{\alpha}\right), \tag{71}$$

which relates the friction coefficient, f, to the elastic mismatch, β, through the complete elliptic integrals of the first kind, which are defined in Appendix B. The $'$ notation on $K'(\gamma/\alpha)$ refers to the complementary argument, which means replacing γ/α with $\sqrt{1-(\gamma/\alpha)^2}$. Once the singularity at $u = \gamma$ is removed by assuming (71), the integral (68) can be inverted according to the formula in Section A.1 for nonsingular endpoints. After some lengthy calculations, the shear tractions in the stick region are found to be

$$q(x) = \frac{fP\sqrt{2}\cos(x/2)}{2\pi\sqrt{\cos x - \cos a}} \frac{F\left(\sin^{-1}\frac{\tan(x/2)}{\tan(b/2)}, \frac{\tan(b/2)}{\tan(a/2)}\right)}{K\left(\frac{\tan(b/2)}{\tan(a/2)}\right)} \operatorname{sgn}\left(\beta \tan\frac{x}{2}\right), \qquad |x| < \tan\frac{b}{2}, \tag{72}$$

where $F(\phi, k)$ is an incomplete elliptic integral of first kind, which is defined in Appendix B.

The shear tractions for the partial slip of evenly spaced rigid flat punches are plotted in Figure 11. For aesthetics, the coefficient of friction is chosen to be $f = 0.215$, so that $b \approx 0.5$, which is half of the entire contact length. The shear tractions are symmetric about the center of the contact region and transition from the partial slip result, Equation (72), in the stick region to Coulomb friction, (28), in the slip region at $x = b$, producing a discontinuity in the shear tractions. It is interesting to note the continuity of the plot despite the abrupt change from stick to slip at $x = b$; that is because the partial slip solution contains the normal traction solution, but is corrected by the elliptic functions, the coefficient of friction and the sign function.

As another interesting side note, it turns out that (71) is valid for all regularly periodic profiles that display self-similarity in a single contact patch, that is, in a single period.

Partial slip contact of sinusoids: Goodman approximation. In this section, the partial slip problem for elastically dissimilar wavy surfaces with Coulomb friction is solved with the Goodman approximation.
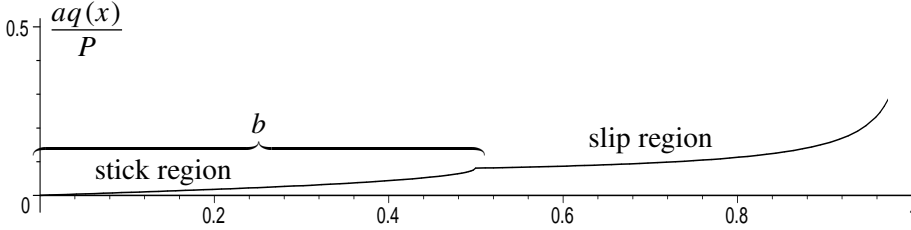
Figure 11. Partial slip of a periodic rigid flat punch with $f = 0.215$, $\nu = 0.3$, $L = 2\pi$ for $a = 1$.

The shear tractions are again divided into stick and slip regions. Thus, substituting (67) into (64) for a sinusoidal profile gives

$$\frac{2}{\pi} \int_0^\gamma \frac{uq(u)}{v^2 - u^2} du = G(v), \qquad |v| < \gamma, \tag{73}$$

with consistency condition

$$\int_0^\gamma \frac{G(v)}{\sqrt{\gamma^2 - v^2}} dv = 0, \tag{74}$$

where

$$G(v) = \frac{2fp_0}{\pi\sqrt{1+\alpha^2}} \int_\gamma^\alpha \frac{u\sqrt{\alpha^2 - u^2}}{(1+u^2)(v^2 - u^2)} du + \frac{\beta p_0 \sqrt{\alpha^2 - v^2}}{\sqrt{1+\alpha^2}(1+v^2)} + \frac{2\Delta C}{A} \frac{|v|}{1+v^2}, \tag{75}$$

and C is an unknown constant. To solve for C, change the order of integration

$$\int_\gamma^\alpha \frac{s\sqrt{\alpha^2 - s^2} ds}{(1+s^2)} \int_0^\gamma \frac{dv}{(v^2 - s^2)\sqrt{\gamma^2 - v^2}} = -\frac{\pi}{2} \int_\gamma^\alpha \frac{\sqrt{\alpha^2 - s^2} ds}{(1+s^2)\sqrt{s^2 - \gamma^2}}. \tag{76}$$

Equation (75) is then substituted into (74) in light of (76), resulting in

$$\frac{fp_0}{\sqrt{1+\alpha^2}} \int_\gamma^\alpha \frac{\sqrt{\alpha^2 - v^2} dv}{(1+v^2)\sqrt{v^2 - \gamma^2}} - \frac{\beta p_0}{\sqrt{1+\alpha^2}} \int_0^\gamma \frac{\sqrt{\alpha^2 - v^2} dv}{(1+v^2)\sqrt{\gamma^2 - v^2}} + \frac{2C\Delta}{A} \int_0^\gamma \frac{v dv}{(1+v^2)\sqrt{\gamma^2 - v^2}} = 0. \tag{77}$$

The integrals in (77) can now all be evaluated analytically. Returning now to the integral equation, the shear tractions are found by first substituting (75) into (73). Then, using partial fractions and (77), $q(u)$ becomes

$$q(u) = -\frac{2u}{\pi} \frac{\sqrt{\gamma^2 - u^2}}{(1+u^2)} \left[\frac{-fp_0}{\sqrt{1+\alpha^2}} \int_\gamma^\alpha \frac{\sqrt{\alpha^2 - v^2} dv}{(v^2 - u^2)\sqrt{v^2 - \gamma^2}} \right.$$
$$\left. + \frac{\beta p_0}{\sqrt{1+\alpha^2}} \int_0^\gamma \frac{\sqrt{\alpha^2 - v^2} dv}{(v^2 - u^2)\sqrt{\gamma^2 - v^2}} + \frac{2\Delta C}{A} \int_0^\gamma \frac{v dv}{(v^2 - u^2)\sqrt{\gamma^2 - v^2}} \right].$$

Evaluating the integrals gives

$$q(u) = \left[\frac{fp_0}{(1+u^2)} \frac{\sqrt{\alpha^2 - u^2}}{\sqrt{1+\alpha^2}} \frac{F(\phi, \gamma/\alpha)}{K(\gamma/\alpha)} + \frac{\Delta C u}{\pi A(1+u^2)} \ln\left(\frac{\alpha + \sqrt{\alpha^2 - u^2}}{\alpha - \sqrt{\alpha^2 - u^2}} \right) \right] \text{sgn}(\beta u),$$
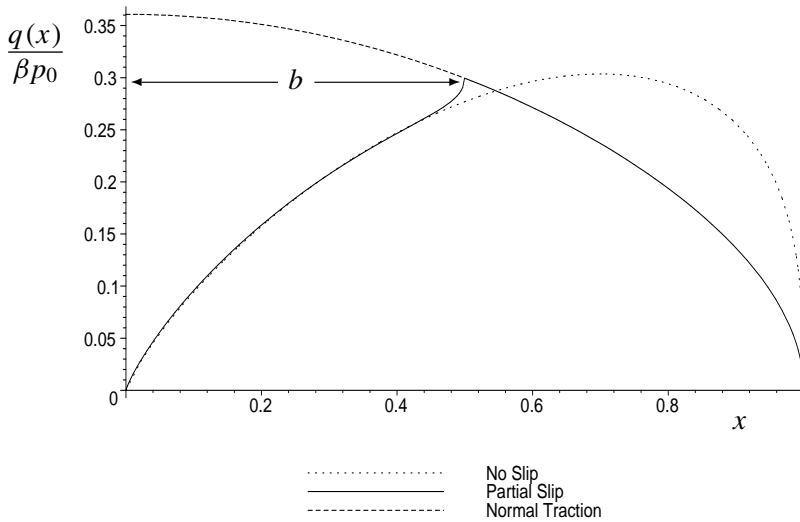
Figure 12. Partial slip of a sinusoidal surface on an elastic half-space for $a = 1$ with $f = 0.215$, $v = 0.3$, and $L = 2\pi$.

where $\phi = \sin^{-1}(u/\gamma)$ and $F(\phi, k)$ is an incomplete elliptic integral of first kind. Returning to original variables, the shear tractions are

$$q(x) = \left(\frac{fp_0}{\sqrt{2}} \cos\frac{x}{2} \sqrt{\cos x - \cos a} \; \frac{F\big(\phi, \, \tan(b/2)/\tan(a/2)\big)}{K\big(\tan(b/2)/\tan(a/2)\big)} \right.$$

$$\left. + \frac{Cp_0 \sin(x/2)}{2\pi} \ln \frac{\tan(b/2) + \sqrt{\tan(b/2)^2 - \tan(x/2)^2}}{\tan(b/2) - \sqrt{\tan(b/2)^2 - \tan(x/2)^2}} \right) \mathrm{sgn}\!\left(\beta \tan\frac{x}{2} \right), \quad |x| < \tan\frac{b}{2},$$

where C is determined from (77) with (71) and $\phi = \sin^{-1}(\tan(x/2)/\tan(b/2))$.

The partial slip contact of an elastically dissimilar wavy surface and a half-space is compared with the complete stick solution, (61), and normal traction solution, (21), in Figure 12. Again, the coefficient of friction is chosen such that the stick and slip regions are equal. The dotted line above represents the normal traction solution multiplied by the coefficient of friction, meaning Coulomb friction, whereas the dash-dot line represents the no-slip solution.

For the partial slip solution, the transition of the shear traction from the stick region to the slip region is much more drastic than that for the flat punch for the same parameters. When the contact length approaches the wavelength, the Goodman approximation is no longer valid. Not surprisingly, increasing the coefficient of friction can also have the same effect, since greater shear tractions are required to maintain the large contact region. The no slip solution is indistinguishable from the partial slip curve initially, but later overshoots the normal traction plot, as was the case for the single indenter [Johnson 1985b]. The complete stick solution however does not violate the Coulomb friction law as the contact region approaches the wavelength, although the curve no longer is approximately equivalent to the partial slip curve for small x.

Conclusion

The contact mechanics solutions derived in the paper may prove useful for validating computational approaches and are convenient for benchmarking numerical calculations or analyzing experimental results. Because of the systematic nature of the theory presented, more complicated problems can also be solved starting with the fundamental integral equations of contact.

The findings of the paper are summarized below:

(1) Based on a periodic array of Flamant solutions, the contact integral equations were derived. The equilibrium equations were also provided for periodic profiles.

(2) Previously known solutions for the frictionless contact of a sinusoidal profile, flat punch and inclined punch were derived from the integral equations of contact in order to demonstrate the validity of the method.

(3) New closed-form results for sliding contact with Coulomb friction for evenly-spaced flat punches and sinusoidal profiles were derived.

(4) Partial slip results for elastically similar materials were rederived using the contact integral equations and extended to periodic power law indenters.

(5) The first solution for the complete stick of periodic flat punches using the coupled integral equation was derived; the Goodman approximation was applied to complete stick and partial slip problems for both periodic flat punches and a sinusoidal profile to obtain new closed-form solutions and its applicability commented upon.

7. Acknowledgments

Appendix A: Integral equation inversions

Hills et al. [1993] provide straightforward solutions of Cauchy singular integral equations of the first and second kind. Since these solution techniques are regularly used throughout the paper and in view of the limited availability of the book, the results are reproduced exactly in this appendix, for the reader's convenience.

A.1 *Cauchy singular integral equations of the first kind*

Equation to be solved:
$$\frac{1}{\pi} \int_{-a}^{a} \frac{f(s)}{x-s} ds = g(x), \qquad |x| < a$$

Solution:
$$f(x) = -\frac{w(x)}{\pi} \int_{-a}^{a} \frac{g(s)}{w(s)(s-x)} ds + Cw(x),$$

where the solution is required to have the following characteristics:

Singular at both ends: $w(x) = 1/\sqrt{a^2 - x^2}, \; C \neq 0$

Nonsingular at $x = a$: $w(x) = \sqrt{(a-x)/(a+x)}, \; C \neq 0$

Nonsingular at $x = -a$: $w(x) = \sqrt{(a+x)/(a-x)}, \; C = 0$

Nonsingular at $x = \pm a$: $w(x) = \sqrt{a^2 - x^2}, \; C = 0$, with the consistency condition $\displaystyle\int_{-a}^{a} \frac{g(s)}{w(s)} ds = 0$

A.2   *Cauchy singular integral equations of the second kind*

Equation to be solved: $Rf(x) + \dfrac{P}{\pi} \displaystyle\int_{-a}^{a} \dfrac{f(s)}{s-x} ds = g(x), \qquad |x| < a$

Solution: $f(x) = \dfrac{1}{R^2 + P^2} \left(Rg(x) - \dfrac{P}{\pi} w(x) \displaystyle\int_{-a}^{a} \dfrac{g(s)}{w(s)(s-x)} ds \right) + Cw(x),$

assuming the functions involved are wholly real and that $\tan \pi B = -P/R$.

The solution is required to have the following characteristics:

Singular at both ends: $w(x) = (a-x)^{B-1}(a+x)^{-B}, \; C \neq 0$

Nonsingular at $x = a$: $w(x) = (a-x)^{B}(a+x)^{-B}, \; C = 0$

Nonsingular at $x = -a$: $w(x) = (a-x)^{B-1}(a+x)^{1-B}, \; C = 0$

Nonsingular at $x = \pm a$: $w(x) = (a-x)^{B}(a+x)^{1-B}, \; C = 0$, with consistency condition $\displaystyle\int_{-a}^{a} \frac{g(s)}{w(s)} ds = 0$

Appendix B: Integrals of importance

Below are a few of the complex integrals that were derived to solve periodic problems in plane elasticity. Elliptic integrals are also provided since their solutions prove useful as well.

Complex integrals for $0 < m < 1$ and $\tan \phi = 1/a$

$$\int_{-a}^{a} \frac{(a-u)^{m-1}(a+u)^{-m}}{1+u^2} du = \frac{\pi}{\sqrt{1+\alpha^2}} \frac{\sin[\pi m - \phi(2m-1)]}{\sin \pi m}$$

$$\int_{-a}^{a} \frac{u(a-u)^{m-1}(a+u)^{-m}}{1+u^2} du = \frac{\pi}{\sqrt{1+\alpha^2}} \frac{\cos[\pi m - \phi(2m-1)]}{\sin \pi m}$$

$$\int_{-a}^{a} \frac{(a-u)^{m}(a+u)^{1-m}}{1+u^2} du = \frac{\pi}{\sin \pi m} \{\sqrt{1+a^2} \sin[\pi m - \phi(2m-1)] - 1\}$$

$$\int_{-a}^{a} \frac{u(a-u)^{m}(a+u)^{1-m}}{1+u^2} du = \frac{\pi}{\sin \pi m} \{\sqrt{1+a^2} \cos[\pi m - \phi(2m-1)] - a(2m-1)\}$$

$$\int_{-a}^{a} \frac{(a-u)^{m}(a+u)^{1-m}}{(1+u^2)^2} du = \frac{\alpha\pi(2m-1)\sqrt{1+a^2}}{\sin \pi m} \cos[\pi m - \phi(2m-1)]$$

$$\int_{-a}^{a} \frac{u(a-u)^{m}(a+u)^{1-m}}{(1+u^2)^2} du = -\frac{\pi\sqrt{1+a^2}}{\sin \pi m} \cos[\pi m - \phi(2m-1)]$$

Elliptic integrals of the first, second and third kinds

<u>Incomplete integrals:</u>

$$F(\phi, k) = \int_0^\phi \frac{d\theta}{\sqrt{1 - k^2 \sin^2 \theta}} \quad E(\phi, k) = \int_0^\phi \sqrt{1 - k^2 \sin^2 \theta} \, d\theta \quad \Pi(n; \phi, k) = \int_0^\phi \frac{d\theta}{(1 - n^2 \theta)\sqrt{1 - k^2 \sin^2 \theta}}$$

<u>Complete integrals:</u> $\quad K(k) = F(\pi/2, k) \quad E(k) = E(\pi/2, k) \quad \Pi(n, k) = \Pi(n; \pi/2, k)$

References

[Adams 2004] G. G. Adams, "Adhesion at the wavy contact interface between two elastic bodies", *J. Appl. Mech. Trans. ASME* **71** (2004), 851–856.

[Cai and Lu 2000] H. Cai and J. Lu, *Mathematical theory in periodic plane elasticity*, vol. 4, edited by C. Yang, Asian Mathematics Series, Gordon and Breach Science Publishers, Amsterdam, 2000.

[Carbone and Decuzzi 2004] G. Carbone and P. Decuzzi, "Elastic beam over an adhesive wavy foundation", *Journal of Applied Physics* **95** (2004), 4476–4482.

[Carbone and Mangialardi 2004] G. Carbone and L. Mangialardi, "Adhesion and friction of an elastic half-space in contact with a slightly wavy rigid surface", *Journal of the Mechanics and Physics of Solids* **52** (2004), 1267–1287.

[Ciavarella 1998a] M. Ciavarella, "The generalized Cattaneo partial slip plane contact problem, I: Theory", *International Journal of Solids and Structures* **35** (1998), 2349–2362.

[Ciavarella 1998b] M. Ciavarella, "The generalized Cattaneo partial slip plane contact problem, II: Examples", *International Journal of Solids and Structures* **35** (1998), 2363–2378.

[Dundurs et al. 1973] J. Dundurs, K. C. Tsai, and L. M. Keer, "Contact between elastic bodies with wavy surfaces", *Journal of Elasticity* **3** (1973), 109–115.

[England and Green 1963] A. H. England and A. E. Green, "Some 2-dimensional punch and crack problems in classical elasticity", pp. 489–500 in *Proceedings of the Cambridge Philosophical Society*, vol. 59, 1963.

[Goodman 1962] L. E. Goodman, "Contact stress analysis of normally loaded rough spheres", *J. Appl. Mech. Trans. ASME* **29** (1962), 515–522.

[Hertz 1881] H. Hertz, "On the contact of elastic solids", *J. Reine Angew. Math.* **92** (1881), 156–171.

[Hills and Nowell 1994] D. A. Hills and D. Nowell, "Mechanics of fretting fatigue", in *Solid Mechanics and its Applications*, vol. 30, edited by G. M. L. Gladwell, Kluwer, Dordrecht, 1994.

[Hills and Sackfield 1985] D. A. Hills and A. Sackfield, "Sliding contact between dissimilar elastic cylinders", *J. Tribology Trans. ASME* **107** (1985), 463–466.

[Hills et al. 1993] D. A. Hills, D. Nowell, and A. Sackfield, *Mechanics of elastic contacts*, Butterworth-Heinemann Ltd., Oxford, 1993.

[Johnson 1985b] K. L. Johnson, *Contact mechanics*, Crambridge University Press, Cambridge, 1985b.

[Johnson 1995] K. L. Johnson, "The adhesion of two elastic bodies with slightly wavy surfaces", *International Journal of Solids and Structures* **32**:3-4 (1995), 423–430.

[Krishtafovich et al. 1994] A. A. Krishtafovich, R. M. Martynyak, and R. N. Shvets, "Contact between anisotropic half-lan and rigid body with regular microrelief", *Journal of Friction and Wear* **15** (1994), 15–21.

[Kryshtafovych and Martynyak 2000] A. A. Kryshtafovych and R. M. Martynyak, "Friction contact of two elastic half-planes with wavy surfaces", *Journal of Friction and Wear* **21** (2000), 1–8.

[Kuznetsov 1975] Y. A. Kuznetsov, "Periodic contact problem for half-plane allowing for forces of friction", *Internation. Applied Mechanics* **12** (1975), 1014–1019.

[Kuznetsov 1983] Y. A. Kuznetsov, "Plane contact problem for a half-space with a poisson's Ratio that varies with depth", *Wear* **92** (1983), 171–196.

[Kuznetsov 1985] Y. A. Kuznetsov, "Effect of fluid lubricant on the contact characteristics of rough elastic bodies in compression", *Wear* **102** (1985), 177–194.

[Kuznetsov and Gorokhovsky 1978] Y. A. Kuznetsov and G. A. Gorokhovsky, "Stress distribution in a polymeric material subjected to action of a rough-surface indenter", *Wear* **51** (1978), 299–308.

[Manners 1998] W. Manners, "Partial contact between elastic surfaces with periodic profiles", *Proceedings of the Royal Society of London* **454** (1998), 3203–3221.

[Manners 2003] W. Manners, "Methods for analysing partial contact between surfaces", *International Journal of Mechanical Sciences* **45**:6-7 (2003), 1181–1199.

[Maugis 2000] D. Maugis, "Contact, adhesion and rupture of elastic solids", in *Solid-State Sciences*, vol. 130, edited by M. E. A. Cardona, Springer, Berlin, 2000.

[Muskhelishvili 1992] N. I. Muskhelishvili, "Singular integral equations", (1992).

[Nosonovsky and Adams 2000] M. Nosonovsky and G. G. Adams, "Steady-state frictional sliding of two elastic bodies with a wavy contact interface", *J. Tribology Trans. ASME* **122** (2000), 490–495.

[Panek 1975] C. F. Panek, "Study of contact problems with heat conduction or in connection with beam theories", in *Theoretical and Applied Mechanics* (Northwestern University: Evanston), 1975.

[Schmueser and Comninou 1979] D. Schmueser and M. Comninou, "Periodic array of interface cracks and their interaction", *International Journal of Solids and Structures* **15** (1979), 927–934.

[Schtaierman 1949] I. Y. Schtaierman, Контактная задача теории упругости, Gostekhizdat, Moscow, 1949.

[Sneddon 1966] I. N. Sneddon, *Mixed boundary value problems in potential theory*, John Wiley, New York, 1966.

[Söhngen 1954] H. Söhngen, "Zur theorie der endlichen Hilbert transformation", *Math. Zeitschrift* **60** (1954), 31–51.

[Spence 1973] D. A. Spence, "Eigenvalue problem for elastic contact with finite friction", pp. 249–268 in *Proceedings of the Cambridge Philosophical Society*, vol. 73, 1973.

[Spence 1975] D. A. Spence, "Hertz contact problem with finite friction", *Journal of Elasticity* **5**:3-4 (1975), 297–319.

[Truman et al. 1995] C. E. Truman, A. Sackfield, and D. A. Hills, "Contact mechanics of wedge and cone indenters", *International Journal of Mechanical Sciences* **37** (1995), 261–275.

[Urbakh et al. 2004] M. Urbakh, J. Klafter, D. Gourdon, and J. Israelachvili, "The nonlinear nature of friction", *Nature* **430** (2004), 525–528.

[Westergaard 1939] H. M. Westergaard, "Bearing pressures and cracks", *Trans. ASME, J. Appl. Mech* **6** (1939), 49–53.

JOSEPH M. BLOCK: gnomeattic@gmail.com
2143 Kerwood Ave., Los Angeles, CA 90025, United States

LEON M. KEER: l-keer@northwestern.edu
Department of Mechanical Engineering, 2145 Sheridan Rd., Evanston, IL 60208-3100, United States

DETERMINATION OF MODE I STRESS INTENSITY FACTORS OF COMPLEX CONFIGURATIONS USING STRAIN GAGES

S. SWAMY, M. V. SRIKANTH, K. S. R. K. MURTHY AND P. S. ROBI

Among techniques for the determination of the mode I stress intensity factors (SIFs), strain gage procedures are the simplest and most straightforward. We report here on an experimental investigation of the determination of opening mode stress intensity factors using the single strain gage method. Our approach overcomes certain drawbacks and greatly widens the applicability of strain gage methods in the determination of static SIFs of complex configurations. The approach was tested through experiments on specimens of finite width and finite height edge-cracked plates (fully finite plates) subjected to tensile stress. We compared the experimentally determined mode I stress intensity factors of fully finite plates with the computed values using finite element analysis, obtaining good agreement between the present approach and computed values.

1. Introduction

Cracks frequently initiate and grow at stress concentration zones such as notches, holes, reentrant corners and welded joints in structural components. Because such elements occur frequently in structural components, understanding the severity of cracks is important in the development of static strength, fatigue crack growth and fatigue life prediction methodologies. The stress intensity factor (SIF) is the key parameter in linear elastic fracture mechanics (LEFM) for quantifying the severity of cracks. It reflects the effect of loading, crack size, crack shape and component geometry in life and strength prediction methods.

An accurate knowledge of the stress intensity factor is essential for the prevention of brittle fractures arising from cracks; in particular, the use of the LEFM principles in preventing the fracture of engineering components depends largely on the availability of accurate SIFs. As a result, analytical, numerical and experimental methods for SIF determination in cracked bodies have been developed for several decades [Sanford 2003]. Analytical methods are limited to simple configurations due to mathematical difficulties, and one must resort to numerical or experimental methods for more complex situations. The experimental determination of stress intensity factors is also needed as a way to validate theoretical and numerical results, and provides a valuable aid to their application. Approaches include the compliance method [Bonesteel et al. 1978; Jr 1981], photoelasticity [Gdoutos and Theocaris 1978; Hyde and Warrior 1990], caustics [Theocaris 1970; Konsta-Gdoutos 1996] and strain gage methods [Dally and Berger 1993].

Of all these techniques, the most straightforward is the use of electrical resistance strain gages [Sanford 2003]. It has received much attention because it can measure surface strains accurately and directly within strain gradient zones, allowing the subsequent determination of SIFs. Irwin [1957] first suggested the use of strain gages to determine SIFs; however, the local yielding effect at the crack tip of metallic materials, high strain gradients, the three-dimensional state of stress at the crack tips and the finite size of the strain

gages are the primary issues for establishing a valid approach for accurate measurement of SIFs using the strain gage techniques. Earlier attempts to measure SIFs using strain gages were reported in [Broek 1982].

A practical method to tackle the issues mentioned in the previous paragraph, providing an effective strain gage technique for measuring the static opening mode stress intensity factor (K_I) in two-dimensional bodies, was first proposed by Dally and Sanford [1987] for linear elastic isotropic materials. In this method the strains are represented by three/four parameter series. The generalized Westergaard approach [Sanford 1979] is employed to determine the strain series and subsequently K_I. The chief advantage of the Dally–Sanford approach is that only a single strain gage is sufficient to determine the mode I SIF, which can be placed at distances far away from the crack tip. Their numerical results reveal that the zone of three-parameter strain series is sufficiently large. Further, an analysis of the error due to strain gradient effects was presented, to suggest possible locations for the finite-sized strain gages. Experiments were conducted on aluminum compact tension (CT) specimens with small strain gages (active grid size $0.76 \times 0.76\,\text{mm}^2$) at different distant radial locations from the crack tip. The authors noticed that the gage readings at all locations were affected by the formation of a plastic zone and the subsequent redistribution of stresses and strains. A methodology has been suggested based on Irwin's method of shifting the elastic field [Sanford 2003] by a distance equal to the plastic zone radius r_y to correct the measured strains, and hence the SIFs. However, a major limitation of this approach is that one should know the exact SIF of the selected configuration a priori in order to calculate the plastic zone size.

Parnas and Bilir [1996] employed the Dally–Sanford single strain gage method to determine the SIFs of CT specimens made of steel and aluminum. Their investigation included the effect of plate thickness. The accuracy of the measured SIFs was observed to depend on the thickness of the specimen. The results clearly show that in the case of thin plates the linearity between applied load and measured strain is not achieved at all loads: beyond a certain load the relationship is found to be nonlinear. However, the linear relation is observed for thick plates. Parnas and Bilir attributed these effects to the formation of plastic zones in the specimens.

Other strain gage methods designed specifically for measuring static mode I SIFs have been proposed by Wei and Zhao [1997] and Kuang and Chen [1995]. Unlike Dally and Sanford, Wei and Zhao used two strain gages, and adopted Williams' [1957] eigenfunction expansion to determine the truncated strain series. These authors tested their theory on three-point bend steel (TPBS) specimens using $0.5 \times 0.5\,\text{mm}^2$ active-grid strain gages and reported inaccuracies in the measured SIFs due to the formation of plastic zones. However, the locations of the strain gages were suggested empirically and require knowing a priori knowledge about the plastic zone size, which depends on the unknown exact stress intensity factor of the configuration.

Kuang and Chen [1995], in contrast, approached the problem using near-field strain equations and asymptotic strain expressions. They suggested that strain gages can be placed at distances greater than half the thickness of the specimen from the crack tip despite the fact that at distances larger from the crack tip, the measured strains cannot be accurately represented by asymptotic terms alone. They conducted experiments on steel CT specimens using strip gages containing 10 strain sensors each of $0.5 \times 0.5\,\text{mm}^2$ active grid size. Contrary to theoretical predictions, the normalized mode I SIF was found to be a function of the applied loads and the thickness of the specimen. The measured SIF was also found to

depend on the angular position relative to the crack axis. However these authors demonstrated that highly inaccurate SIF results are obtained if the strain gages are placed at distances below half the thickness of the specimen. Their measurements at locations away from the crack tip are also affected by plasticity effects. Corrections to the measured strains were suggested, in a manner similar to that of [Dally and Sanford 1987], but contrary to earlier works, no improvement of the measured SIFs was accomplished, even after incorporating plastic zone corrections.

Of these various strain gage methods for measuring opening mode static SIFs, the procedure of Dally and Sanford enjoys the greatest practicability and a solid mathematical background. By contrast, very large numbers of strain gages are needed to measure opening mode SIFs in the overdetermined method proposed by Berger and Dally [1988]. Dally and Sanford's technique has been extended to mixed mode cases [Dally and Berger 1986], which requires four strain gages for determination of the SIFs. A proportional extrapolation technique for determining mixed mode SIFs using strain gages has also been proposed [Itoh et al. 1988]. However, a special strain gage pattern is needed in this technique.

An advantage of strain gage techniques is that they can be employed directly on metallic engineering components to determine the SIF of their configurations. Also important is that numerical and analytical solutions of static SIFs of complex domains can be corroborated via strain gage procedures to provide reliability of the results/methods. For example, many researchers have reported on the application of photoelastic methods [Marloff et al. 1971; Chan and Chow 1979; Amir et al. 1989; Nurse et al. 1994] and caustics [Biak et al. 1995; Lee and Hong 1993] to the determination of static SIFs or the corroboration of analytical and numerical solutions for important configurations. Such application investigations using existing procedures are useful in establishing the experimental methods and make them into a viable alternative in real design situations of great complexity.

In spite of these important applications of strain gage methods, no work has been reported to date on the application of the Dally–Sanford single strain gage procedure to the validation of accurate mode I static SIFs of the complex configurations, so as to establish the usefulness of this technique in real design situations. This is true also of the other strain gage methods.

A critical review of earlier work [Dally and Sanford 1987; Parnas and Bilir 1996; Wei and Zhao 1997; Kuang and Chen 1995] in this field discloses the various drawbacks that prevented further utilization of these methods in the determination of SIFs for important complex configurations: (a) the normalized SIF is found to be function of thickness of the specimen and the applied loads which is obstinate to the theory; (b) the measured strains are severely affected by plastic zone formation and subsequent strain redistribution; (c) while certain approximate procedures have been proposed to correct the measured strains (and hence SIFs), these procedures depend on the unknown exact stress intensity factor of the configuration; (d) there are indications that at times no significant improvements can be achieved even after plastic zone corrections are applied. The last three works referenced at the start of this paragraph employed theoretical values of SIFs for CT and TPBS specimens to correct measured SIFs for plasticity effects. Clearly such corrections are not possible in the case of configurations for which no SIF solutions are available.

These difficulties arise mainly from the use of the metallic specimens in strain gage procedures, although the SIF is independent of the material. The preparation of complex configurations, particularly of cracked specimens, is relatively difficult with metallic materials; great care has to be exercised in creating

sharp natural cracks with intricate orientations. Thus methods such as Dally and Sanford's, which have a sound mathematical basis, may be more effectively exploited by using materials other than metals.

The fact that the SIF is independent of the material is exploited in photoelastic and other experimental methods [Gdoutos 1990; Dally and Riley 1991]. As is well known, polymethylmethacrylate (PMMA), known commercially as Perspex or Plexiglas, is a homogeneous, isotropic and brittle material at room temperatures [Maccagno and Knott 1989]. This material has long been used in studies of many aspects of linear elastic fracture mechanics [Maccagno and Knott 1989; Mukherjee and Burns 1972; Katsamanis and Delides 1988; Xu et al. 2004]. One advantage it offers is that it is relatively easy to introduce sharp natural cracks by pressing a razor blade into the bottom of a notch. PMMA is also inexpensive and easy to fabricate in complex cracked configurations, making it an excellent model material for experimental fracture mechanics. (See [Maccagno and Knott 1989] for details and a historical account of the use of PMMA for this purpose.)

In view of the shortcomings arising to the use of metallic specimens in strain gage procedures and of the availability of excellent strain gage technology, we suggest that the use of the specimens made of PMMA material will greatly broaden the applications of these methods. All of aforesaid drawbacks of use of the metallic specimens can be overcome with the use of this material. However, to the best of our knowledge no published report is available on use of the PMMA in conjunction with strain gage methods, in particular with the single gage technique of Dally and Sanford.

The proximity of component boundaries to the crack tip has an effect on SIFs [Sanford 2003; Gdoutos 1990]. In general, as the boundaries come close to the crack tip, the magnitude of the SIF increases. An edge-cracked plate subjected to uniform tensile stress is a widely used benchmark problem [Pang 1993]. Analytical and numerical solutions for the mode I SIF of this configuration are available only for finite width plates [Murakami 1987; Tada et al. 2000], that is, for large values of a/w and $h/w \geq 1$, where a is the crack length, w is the width of the plate and h is the height of the plate from the crack axis. However, to our knowledge no report in the open literature, whether using analytical, experimental or numerical methods, is available on SIFs for edge-cracked plates of finite width and finite height (large a/w and $h/w \leq 1$) subjected to uniform tension. In this situation both the width and the height of the plate are close to the crack tip. We call such plates *fully finite*.

In this work we investigate the feasibility of experimental determination of accurate opening mode stress intensity factors using the Dally–Sanford method and cracked polymethylmethacrylate (PMMA) specimens. In the Dally–Sanford procedure, gages can be placed at low strain gradient zones; as a consequence larger gages can be employed. In contrast with [Dally and Sanford 1987; Wei and Zhao 1997; Kuang and Chen 1995], our work attempts to measure accurate SIFs using relatively large strain gages (active gage length 3 mm) and monotonically increasing loads with continuous measurement of the strain. Our goal is to accurately determine opening mode SIFs of fully finite edge-cracked plates subject to uniform tension. To validate the proposed method for the determination of SIFs, we compare our experimental results with computer-calculated values obtained using ANSYS finite-element software.

2. Theoretical background

In the Dally and Sanford method [1987], the strain field adjacent to a crack tip is represented by an infinite series solution. The area around a crack tip can be divided into three regions (Figure 1) to identify valid
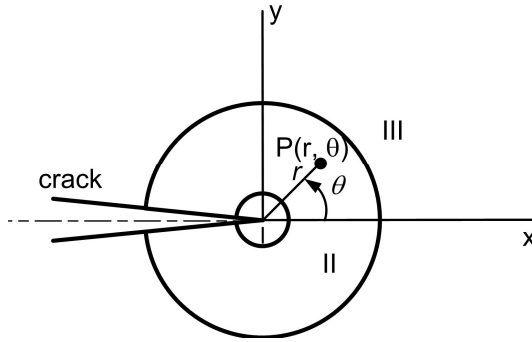
Figure 1. Different regions at the crack tip.

locations for accurate strain measurements. The very near field region (region I in Figure 1) is the zone where the singular term in the series or asymptotic expression is sufficient to represent this region. This is a singularity dominated zone. Due to yielding of material and three-dimensional nature of stress state, this is not a valid region for accurate strain measurements.

Region II is the near-field region, defined as the area beyond region I where the strain field can be represented within a specified accuracy by a small number of series terms, both singular and nonsingular. Region III, the far-field region, corresponds to large values of the radial distance r from the crack tip; in that region a very large number of unknowns are needed in the series for an accurate representation of the strain field, so strain measurements are not appropriate there. Thus region II is the optimum zone for accurate strain measurements: it can be represented by few terms and is sufficiently away from the crack tip. Dally and Sanford [1987] adopted a three-parameter approach; that is, they assumed that the strain field in region II can be represented with sufficient accuracy by three series terms. The strain field in this region for plane stress conditions is then written as (see also [Sanford 2003])

$$E\varepsilon_{xx} = A_0 r^{-1/2} \cos\frac{\theta}{2}\Big((1-v)-(1+v)\sin\frac{\theta}{2}\sin\frac{3\theta}{2}\Big) + 2B_0 + A_1 r^{1/2} \cos\frac{\theta}{2}\Big((1-v)-(1+v)\sin^2\frac{\theta}{2}\Big),$$

$$E\varepsilon_{yy} = A_0 r^{-1/2} \cos\frac{\theta}{2}\Big((1-v)-(1+v)\sin\frac{\theta}{2}\sin\frac{3\theta}{2}\Big) - 2vB_0 + A_1 r^{1/2} \cos\frac{\theta}{2}\Big((1-v)-(1+v)\sin^2\frac{\theta}{2}\Big),$$

$$2G\gamma_{xy} = A_0 r^{-1/2}\Big(\sin\theta\cos\frac{3\theta}{2}\Big) - A_1 r^{1/2}\Big(\sin\theta\cos\frac{\theta}{2}\Big),$$

where A_0, A_1 and B_0 are unknown coefficients that can be determined using the geometry of the specimen and the boundary conditions. Using the definition of K_I one can easily show that it is related to A_0 by

$$K_I = \sqrt{2\pi}\,A_0. \tag{2}$$

A single strain gage is sufficient to measure the constant A_0 (hence K_I) by placing and orienting the strain gage as given below. Using the strain transformation equations, the strain component $\varepsilon_{x'x'}$ at the point P located by r and θ (Figure 2) is given by

$$2G\varepsilon_{x'x'} = A_0 r^{-1/2}\Big(k\cos\frac{\theta}{2} - \frac{1}{2}\sin\theta\sin\frac{3\theta}{2}\cos 2\alpha + \frac{1}{2}\sin\theta\cos\frac{3\theta}{2}\sin 2\alpha\Big)$$
$$+ B_0(k+\cos 2\alpha) + A_1 r^{1/2}\cos\frac{\theta}{2}\Big(k+\sin^2\frac{\theta}{2}\cos 2\alpha - \frac{1}{2}\sin\theta\sin 2\alpha\Big), \tag{3}$$

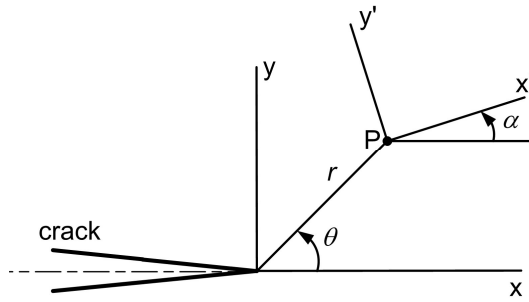where $\kappa = \dfrac{1-v}{1+v}$.

Figure 2. Strain gage location and orientation.

The coefficient B_0 term in (3) can be eliminated by selecting the angle α so that

$$\cos 2\alpha = -\kappa = -\frac{1-\nu}{1+\nu}. \tag{4}$$

The coefficient A_1 can also be made zero if the angle θ is selected so that

$$\tan \frac{\theta}{2} = -\cot 2\alpha. \tag{5}$$

Thus by placing a single strain gage (Figure 2) with α and θ as defined by (4) and (5) one can measure the strain $\varepsilon_{x'x'}$, which in turn is related to K_I by

$$2G\varepsilon_{x'x'} = \frac{K_I}{\sqrt{2\pi r}}\left(k\cos\frac{\theta}{2} - \frac{1}{2}\sin\theta\sin\frac{3\theta}{2}\cos 2\alpha + \frac{1}{2}\sin\theta\cos\frac{3\theta}{2}\sin 2\alpha\right). \tag{6}$$

The angles α and θ depend only on the Poisson's ratio of the specimen material. The selection of the radius r for locating the strain gage can be obtained by considering strain gradient effects, as explained in [Dally and Sanford 1987]. Since the gages can be located far from high strain gradient zones, the measurements can be taken with relatively large, hence inexpensive, strain gages.

3. Numerical evaluation of the SIFs of fully finite edge-cracked plates

The SIFs of finite width and finite height edge-cracked plates is given by

$$K_I = \sigma\sqrt{\pi a}\, F_I\left(\frac{a}{w}, \frac{h}{w}\right), \tag{7}$$

where $F_I\left(\frac{a}{w}, \frac{h}{w}\right)$ is the configuration factor or normalized SIF, which shows the effect of geometry of the body on the SIF [Sanford 2003; Gdoutos 1990].

Finite element analyses using ANSYS 9.0 were carried out to determine accurate opening mode SIFs of fully finite edge-cracked plates (with various values of a/w and h/w) subject to uniform tension (Figure 3). The displacement extrapolation method of ANSYS [2005] was employed to compute the normalized opening mode SIFs. It is known (see [Swain 2007]) that this method is consistent and yields very accurate SIFs. In our investigation we chose two values of a/w, 0.3 and 0.5, and values of h/w ranging from 0.2 to 1.1 in steps of 0.1. It is well known that semi-infinite plates can be represented approximately by $h/w \geq 1$, while $h/w < 1$ represents fully finite edge-cracked configurations.
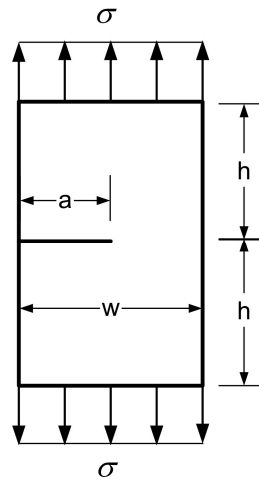
Figure 3. Problem domain: Edge cracked plate subjected to uniform tension.

Natural isoparametric quadratic triangular elements (T6) and the corresponding quarter point singular elements [Barsoum 1976; Freese and Tracey 1976] were used. We assume plane stress conditions, $\sigma = 1.0$ MPa, a Young's modulus $E = 10000$ MPa and a Poisson's ratio of 0.3. Because of symmetry, only half the plate was considered in the analysis. Figure 4 shows a typical unstructured mesh pattern (without gradation) used in the determination of the normalized SIFs. Such meshes were used for all values of a/w and h/w. No significant improvements in the SIFs were observed when the meshes were refined further [Swamy 2007].

The computed normalized opening mode SIFs for different values of a/w and h/w are presented in Table 1. As expected, the SIF increases as the a/w ratio increases and the h/w ratio decreases, that is,
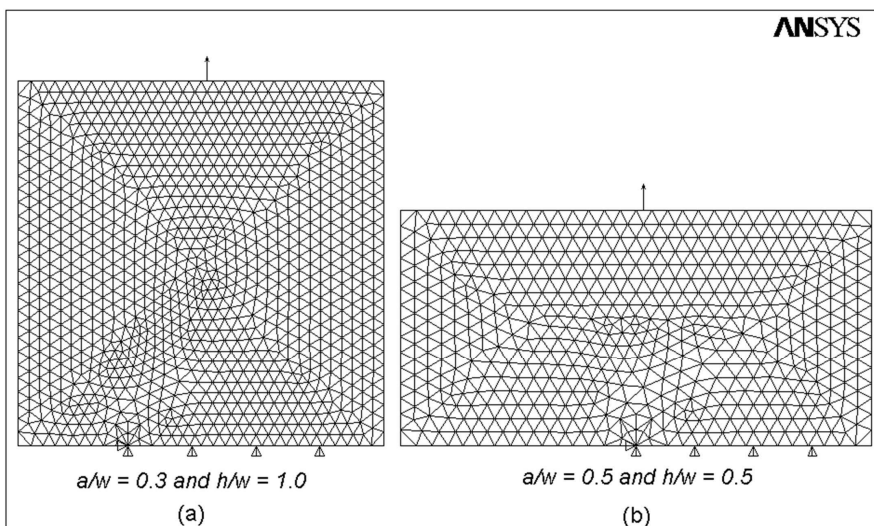

Figure 4. Typical meshes for SIF determination for the problem domain.

| h/w | $F_I = K_I/\sigma\sqrt{\pi a}$ | | h/w | $F_I = K_I/\sigma\sqrt{\pi a}$ | |
	$a/w = 0.3$	$a/w = 0.5$		$a/w = 0.3$	$a/w = 0.5$
0.2	3.5979	6.0343	0.7	1.6938	2.8514
0.3	2.5390	4.0308	0.8	1.6733	2.8342
0.4	2.0736	3.2898	0.9	1.6649	2.8277
0.5	1.8496	3.0060	1.0	1.6622	2.8250
0.6	1.7420	2.8954	1.1	1.6613	2.8249

Table 1. FE-computed normalized SIFs of semi-infinite and finite edge-cracked plates.

when the surrounding boundaries approach the crack tip. It may also be noticed from Table 1 that F_I remains almost constant for $h/w \geq 0.9$, indicating semi-infinite cases.

4. Experimental details

As stated, our goal was to determine the SIFs of fully finite edge-cracked panels with the shape shown in Figure 3, using the single strain gage technique of [Dally and Sanford 1987]. The configuration of the experimental specimens representing the problem domain is shown in Figure 5. The specimens were made from commercially available PMMA (Perspex sheet) with a thickness of 6 mm. Plane stress condition is anticipated in the specimens. The width of all the specimens was kept at $w = 150$ mm, while the crack length a and the height h of the specimen were varied to create semi-infinite and fully finite edge-cracked specimens.
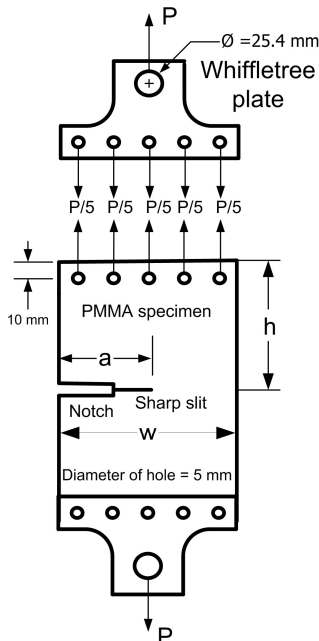

Figure 5. Details of the experimental PMMA specimen.

All specimens were monotonically loaded with a closed loop, servohydraulic INSTRON 8801 machine (100 kN capacity) under displacement control with actuator speed 0.05 mm/min. The whiffletree technique (Figure 5) was employed to transform the point load from the INSTRON to a uniformly distributed load on the specimen. The whiffletree plates were made from mild steel, and mild steel pins were used to connect them with the specimens. Five holes were used to connect each whiffletree to the corresponding specimen. As shown in Figure 5, each hole lies 10 mm from the top or bottom edge of the specimen. It was assumed that the point load applied by the machine is equally divided between the five holes as shown in Figure 5.

To imitate the sharp crack form the model (Figure 3), we made a 3 mm wide notch with a jigsaw, of length $(a-2)$ mm, and further created a fine slit, 2 mm long, by means of a razor blade. Very sharp cracks can be made in this way: the crack tip root radius is less than 0.0035 mm (see [Srikanth 2006]). Two a/w ratios (0.3 and 0.5) and four h/w ratios (0.3, 0.5, 0.7 and 1.0) were chosen for the experimental study. Only one specimen each was tested for $a/w = 0.3$ and various values of h/w, and two specimens each for $a/w = 0.5$ and various h/w. Strain measurements on the loaded specimens were carried out using a single electrical strain gage (HBM type 1-LY11-3/120) with an active grid of 3×1.4 mm^2. A Young's modulus of 2300 MPa and Poisson's ratio of 0.37 have been measured for the PMMA material in a tensile test [Swamy 2007]. Thus α and θ in (4) and (5) equal respectively 58.69° and 54.76°. The radial position of the strain gage $r = 10$ mm was chosen in all experiments based on the strain gradient analysis presented in [Dally and Sanford 1987].

The measured strains were processed and digitized using a National Instruments Data Acquisition Board (PXI 1052) and an eight-channel universal strain gage module (SCXI 1520). Continuous strain measurements was made by interfacing the INSTRON machine's load cell with a NI Data Acquisition Board (DAQ). Figure 6 depicts a specimen attached to the INSTRON with whiffletree plates.
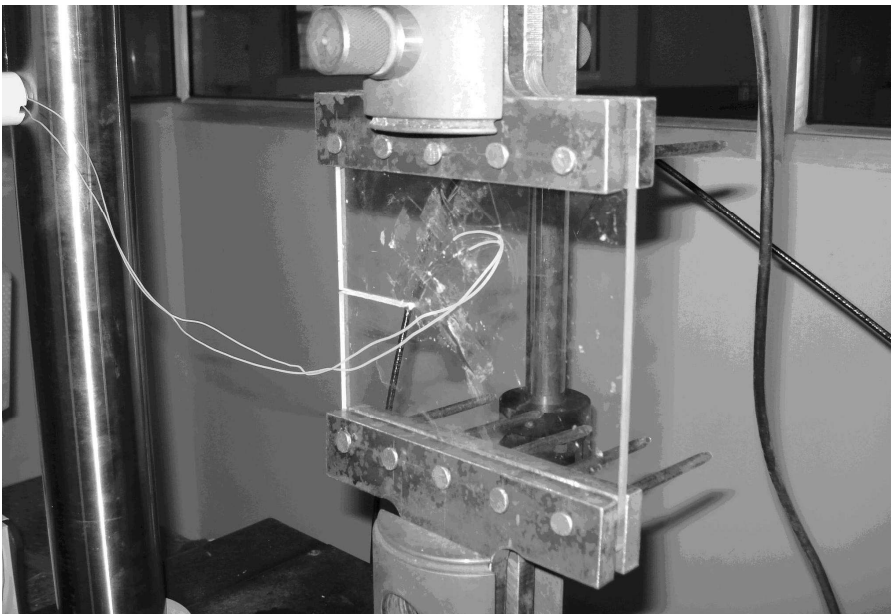

Figure 6. A typical PMMA specimen with whiffletree plates.

5. Finite element simulation of the experimental specimens

Since the experimental specimen (Figure 5) differs from the original problem domain (Figure 3) especially in the matter of loading, a finite element simulation of the experimental specimen with assumed magnitude of point loads at the five holes was carried out using ANSYS. Such simulations before the experiments are vital in establishing whether or not the selected configuration of the experimental specimen mimics the actual problem domain. The specimens were modeled with T6 elements and quarter-point singular elements were placed at the crack tips. Figure 7 shows a representative mesh with loading and boundary conditions employed in the numerical simulation studies.
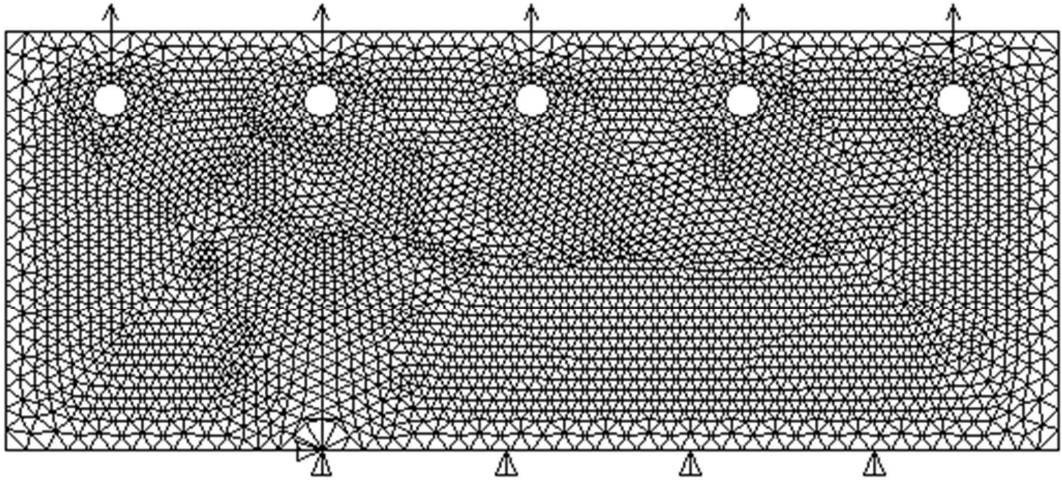

Figure 7. Typical mesh of an experimental specimen, computed by ANSYS.

A few results of computed SIFs of the experimental specimens and that of original problem domain are presented in Table 2. It also presents the percent relative error (in absolute value) considering SIFs in Table 1 as exact values. It may be noticed from table that, the expected SIFs from the specimens are in very good agreement with the SIFs of the original problem (Figure 3). Although not presented here, similar simulations were carried out for other values of h/w and exceptional agreement between the two set of SIFs was observed [Swamy 2007]. Thus the numerical results clearly indicate that experimental specimen as designed in Figure 5 can accurately imitate the original problem (Figure 3).

h/w	0.4	0.6	1.0
speciment F_I (Figure 5)	2.0652	1.7427	1.6655
problem domain F_I (Figure 3)	2.0736	1.7420	1.6622
relative error	0.41%	0.04%	0.20%

Table 2. Experimental and computed normalized SIFs for $a/w = 0.3$ and selected values of h/w.
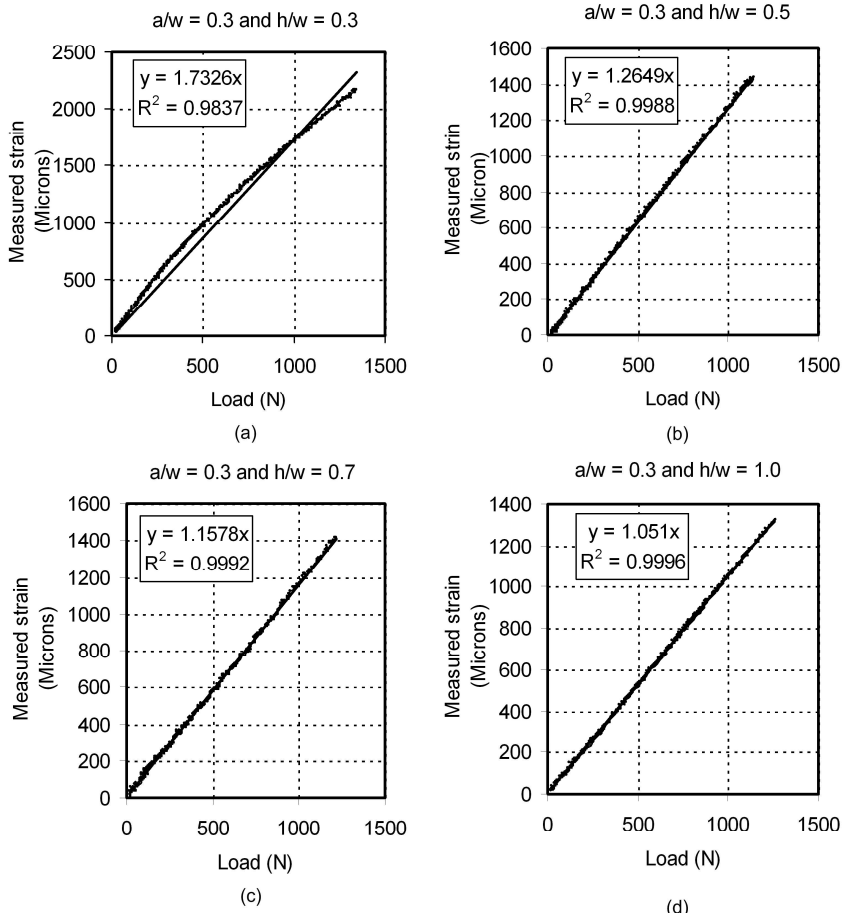
Figure 8. Variation of the measured strain with applied load for $a/w = 0.3$.

6. Experimental results and discussion

Figure 8 shows the experimentally measured strain data on PMMA specimens as a function of the applied load for $a/w = 0.3$ and $h/w = 0.3, 0.5, 0.7, 1.0$. A linear fit was made to the data points of all the specimens. A very good linear relationship can be noticed between the measured strain and the applied load in the figure for all four specimens. The coefficient of determination R^2 in all the graphs is also close to unity, indicating good fits. A slight deviation from linearity in Figure 8(a) is probably due to the improper settlement of the pins in the holes of the whiffletree. From the linear equations presented in each of the four graphs, measured strains were calculated at different loads. Subsequently, using the computed strains the opening mode SIFs were determined using (6) at different values of applied load.

Table 3 presents the measured opening mode SIFs (K_I) at different loads for semi-infinite and fully finite edge-cracked plates of $a/w = 0.3$. The experimental results of Table 3 are presented in graphical form in Figure 9 to show the dependency of K_I on the applied load and proximity to the boundaries. Since the measured strains are linearly proportional to the applied load so are the measured SIFs. Besides
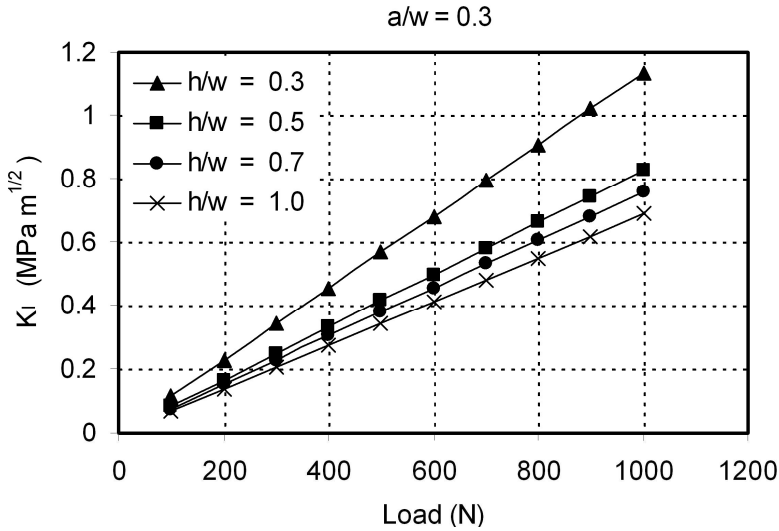
Figure 9. Variation of the measured K_I with applied load for $a/w = 0.3$.

this, the trend that the magnitude of the measured SIF is increasing with the increase in load is also in agreement with the theoretical predictions [Sanford 2003; Gdoutos 1990]. Further, the magnitude of SIF increases with decreasing h/w. Table 3 also provides normalized SIFs (F_I), which are found to be independent of applied loads. Therefore a single value corresponding to a configuration is presented in the table.

Plots of the measured strain data as a function of the applied load for $a/w = 0.5$ and $h/w = 0.3$, 0.5, 0.7, 1.0 were found to be very similar to the case of $a/w = 0.3$, and the corresponding averaged

Load (N)	K_I (MPa $\sqrt{m}$)			
	$a/w = 0.3$	$a/w = 0.5$	$a/w = 0.7$	$a/w = 1.0$
100	0.1132	0.0827	0.0757	0.0687
200	0.2265	0.1653	0.1513	0.1374
300	0.3397	0.2480	0.2270	0.2061
400	0.4529	0.3307	0.3027	0.2748
500	0.5662	0.4133	0.3783	0.3434
600	0.6794	0.4960	0.4540	0.4121
700	0.7926	0.5787	0.5297	0.4808
800	0.9059	0.6613	0.6053	0.5495
900	1.0191	0.7440	0.6810	0.6182
1000	1.1323	0.8267	0.7567	0.6869
F_I	2.7098	1.9783	1.8108	1.6438

Table 3. Measured K_I values at different loads for $a/w = 0.3$, and load-independent normalized SIFs (last row).
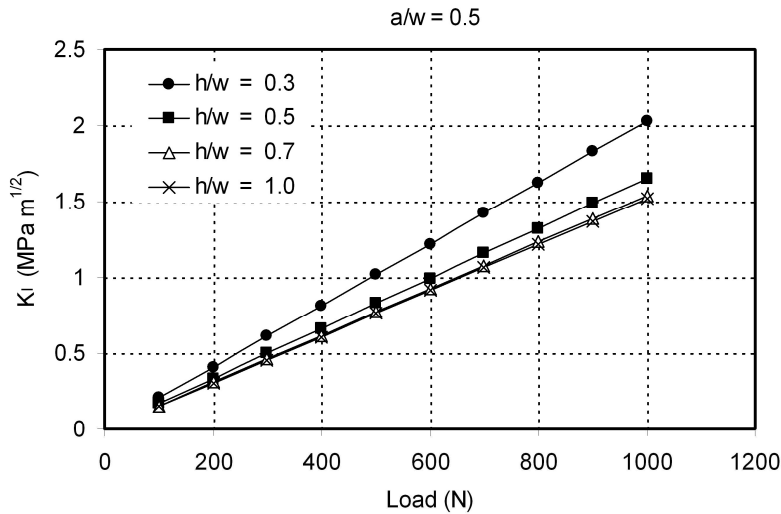
Figure 10. Variation of the measured K_I with applied load for $a/w = 0.5$.

measured SIFs at different applied loads are shown in Table 4. Figure 10 shows the graph of averaged measured SIFs as function of the applied load. As in the case of $a/w = 0.3$, the increase of the SIF with decreasing h/w and increasing values of the applied loads are in line with the theory. The normalized SIFs for $h/w = 0.3$, 0.5, 0.7, and 1.0 also appear in Table 4.

The measured F_I using strain gages and the computed normalized SIFs using FEA of semi-infinite and fully finite edge-cracked plate appear in Table 5. For comparison, the table also shows the analytical values of normalized SIFs [Tada et al. 2000] for semi-infinite plates ($h/w = 1.0$). The discrepancy between

| Load (N) | K_I (MPa $\sqrt{m}$) | | | |
	$a/w = 0.3$	$a/w = 0.5$	$a/w = 0.7$	$a/w = 1.0$
100	0.2031	0.1654	0.1540	0.1520
200	0.4063	0.3308	0.3081	0.3040
300	0.6094	0.4962	0.4621	0.4560
400	0.8126	0.6616	0.6162	0.6080
500	1.0157	0.8270	0.7702	0.7600
600	1.2189	0.9923	0.9242	0.9120
700	1.4220	1.1577	1.0783	1.0639
800	1.6252	1.3231	1.2323	1.2159
900	1.8283	1.4885	1.3864	1.3679
1000	2.0315	1.6539	1.5404	1.5199
F_I	3.7666	3.0665	2.8561	2.8181

Table 4. Measured K_I values at different loads for $a/w = 0.5$, and load-independent normalized SIFs (last row).

h/w	F_I $(a/w = 0.3)$			F_I $(a/w = 0.5)$		
	numerical	experimental	analytic	numerical	experimental	analytic
0.3	2.5390	2.7098 (6.7%)	——	4.0308	3.7666 (6.6%)	——
0.5	1.8486	1.9783 (7.0%)	——	3.0060	3.0665 (2.0%)	——
0.7	1.6938	1.8108 (6.9%)	——	2.8514	2.8561 (0.2%)	——
1.0	1.6622	1.6438 (1.1%)	1.6624	2.8250	2.8181 (0.2%)	2.8291

Table 5. FE-computed, experimentally measured, and (where available) analytic values of F_I for edge-cracked plate and two choices of a/w. Bracketed values are absolute values of relative error. Analytic solutions are from [Tada et al. 2000].

the experimentally determined and FE-computed values, ranging from 0.2% to 7%, shows (assuming the FE-computed values to be exact) that the experimental method is substantially accurate in spite of the relatively large gage (3 mm active length). Excellent agreement is also observed between the measured and the theoretical normalized SIFs of semi-infinite plates.

Probable reasons for the somewhat larger errors (up to 7%) appearing in Table 5 are: (a) In all cases the cracks (fine slits) were made by pressing a razor blade through a distance of 2 mm; although great care was taken, it is difficult to control this length precisely. (b) When the razor blade is employed, the crack front at times is not precisely normal to the sheet surface. Similar observations were made in [Williams and Ewing 1972].

The measured and computed SIFs are shown in Figure 11, in order to assess the usefulness of the strain gage method of Dally and Sanford [1987] in combination with PMMA specimens for measuring the accurate SIFs. We see that either the results of Table 1 or the graphs in Figure 11 may be employed for SIFs of finite width and finite height edge-cracked plates subject to uniform tension.
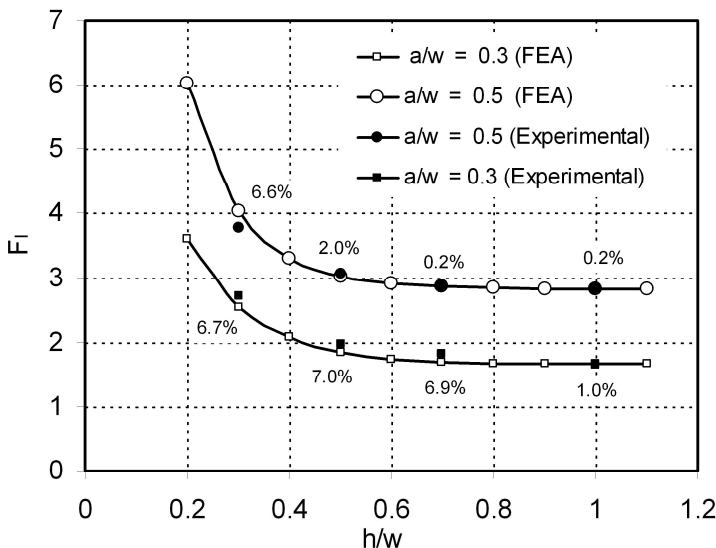

Figure 11. Comparison of measured and computed values of the normalized SIF.

7. Conclusions

The present investigation outlines various reasons which prevented the extensive application of the strain gage methods in determination of the accurate mode I SIFs. An experimental program is devised which includes the use of PMMA specimens so as to make the single strain gage method of [Dally and Sanford 1987] a more powerful and attractive experimental technique. The effectiveness of use of PMMA specimens in conjunction with the Dally and Sanford technique in measuring accurate opening mode stress intensity factors was demonstrated in the present investigation. Monotonically increasing load experiments were performed on the finite width and finite height PMMA edge-cracked specimens and strains were measured using 3 mm active length strain gages. Various trends of the experimental results are in excellent agreement with the LEFM theory. Moreover, a good agreement has also been observed between computed SIFs using FEA and the measured SIFs using the relatively large strain gages. The present investigation attempts to suggest accurate SIFs of the fully finite edge-cracked plates and subjected to uniform tension. The results of the present work clearly demonstrate that the single strain gage technique of Dally and Sanford can be used more effectively in combination with the PMMA specimens and can become a very useful tool for measurement of accurate opening mode SIFs of the complex configurations yet with relatively large gages.

Acknowledgement

References

[Amir et al. 1989] A. D. K. Amir, N. S. Murthy, and N. G. Raju, "Stress intensity factor determination of radially cracked circular rings subjected to tension using photoelastic technique", *Engng. Fract. Mech.* **32** (1989), 403–408.

[ANSYS 2005] "ANSYS POST1-crack analysis", in *Theory reference manual*, ANSYS, Inc., 2005.

[Barsoum 1976] R. S. Barsoum, "On the use of isoparametric finite elements in linear fracture mechanics", *Int. J. Num. Meth. Engng.* **10** (1976), 25–37.

[Berger and Dally 1988] J. R. Berger and J. W. Dally, "An overdeterministic approach for measuring using strain gages", *Exp. Mech.* **28** (1988), 142–145.

[Biak et al. 1995] M. C. Biak, S. H. Choi, J. S. Hawong, and J. D. Kwon, "Determination of stress-intensity factors by the method of caustics in anisotropic materials", *Exp. Mech.* **35** (1995), 137–143.

[Bonesteel et al. 1978] R. M. Bonesteel, D. E. Pipers, and A. T. Davinroy, "Compliance and calibration of double cantilever beam (DCB) specimens", *Engng. Fract. Mech.* **10** (1978), 425–428.

[Broek 1982] D. Broek, *Elementary engineering fracture mechanics*, The Hague, 1982.

[Chan and Chow 1979] W. Y. Chan and C. L. Chow, "Photoelastic stress intensity determination of circular-sector crack in rectangular plate", in *Proceedings of the Society for Experimental Stress Analysis Spring meeting* (San Francisco, 1979), 1979.

[Dally and Berger 1986] J. W. Dally and J. R. Berger, "A strain gage method for determining and in a mixed mode stress field", in *Proceedings of the SEM spring conference on experimental mechanics* (New Orleans, LA, 1986), Society for Experimental Mechanics, Bethel, CT, 1986.

[Dally and Berger 1993] J. W. Dally and J. R. Berger, "The role of the electrical resistance strain gauge in fracture research", pp. 1–39 in *Experimental techniques in fracture mechanics*, edited by J. S. Epstein, VCH, New York, 1993.

[Dally and Riley 1991] J. W. Dally and W. F. Riley, "Experimental stress analysis", *McGraw-Hill* (1991).

[Dally and Sanford 1987] J. W. Dally and R. J. Sanford, "Strain gage methods for measuring the opening mode stress intensity factor", *Exp. Mech.* **27** (1987), 381–388.

[Freese and Tracey 1976] C. E. Freese and D. M. Tracey, "The natural isoparametric triangle versus collapsed quadrilateral for elastic crack analysis", *Int. J. Fract.* **12** (1976), R767–R770.

[Gdoutos 1990] E. E. Gdoutos, *Fracture mechanics criteria and applications*, Dordrecht, 1990.

[Gdoutos and Theocaris 1978] E. E. Gdoutos and P. S. Theocaris, "A photoelastic determination of mixed-mode stress intensity factors", *Exp. Mech.* **18** (1978), 87–96.

[Hyde and Warrior 1990] T. H. Hyde and N. A. Warrior, "An improved method for determination of photoelastic stress intensity factors using the Westergaard stress function", *Int. J. Mech. Sci.* **32** (1990), 265–273.

[Irwin 1957] G. R. Irwin, "Analysis of stresses and strains near the end of a crack traversing a plate", *J. Appl. Mech.* **24** (1957), 361–364.

[Itoh et al. 1988] Y. Z. Itoh, T. Murakami, and H. Kashiwaya, "Proportional extrapolation techniques for determining stress intensity factors", *Engng. Fract. Mech.* **31** (1988), 297–308.

[Jr 1981] J. C. N. Jr, "Stress-intensity factors and crack-opening displacements for round compact specimens", *Int. J. Fract.* **17** (1981), 567–578.

[Katsamanis and Delides 1988] F. G. Katsamanis and C. G. Delides, "Fracture surface energy measurements of PMMA: A new experimental approach", *J. Phys. D Appl. Phys.* **21** (1988), 79–86.

[Konsta-Gdoutos 1996] M. Konsta-Gdoutos, "Limitations in mixed-mode stress intensity factor evaluation by the method of caustics", *Engng. Fract. Mech.* **55** (1996), 371–382.

[Kuang and Chen 1995] J. H. Kuang and L. S. Chen, "A single strain gage method for measurement", *Engng. Fract. Mech.* **51** (1995), 871–878.

[Lee and Hong 1993] O. S. Lee and S. K. Hong, "Determination of stress intensity factors and J-integrals using the method of caustics", *Engng. Fract. Mech.* **44** (1993), 981–989.

[Maccagno and Knott 1989] T. M. Maccagno and J. F. Knott, "The fracture behaviour of PMMA in mixed modes I and II", *Engng. Fract. Mech.* **34** (1989), 65–86.

[Marloff et al. 1971] R. H. Marloff, M. M. Leven, T. N. Ringler, and R. L. Johnson, "Photoelastic determination of stress-intensity factors", *Exp. Mech.* **11** (1971), 529–539.

[Mukherjee and Burns 1972] B. Mukherjee and D. J. Burns, "Growth of part-through thickness fatigue cracks in sheet Poly-methylmethacrylate", *Engng. Fract. Mech.* **4** (1972), 675–685.

[Murakami 1987] Y. Murakami (editor), *Stress intensity factors handbook*, vol. 1, Pergamon, Oxford, 1987.

[Nurse et al. 1994] A. D. Nurse, E. W. O'Brien, and E. A. Patterson, "Stress intensity factors for cracks at fastener holes", *Fatigue Fract. Eng. Mater. Struct.* **17** (1994), 791–799.

[Pang 1993] H. L. J. Pang, "Linear elastic fracture mechanics benchmarks: 2D finite element test cases", *Engng. Fract. Mech.* **44** (1993), 741–751.

[Parnas and Bilir 1996] L. Parnas and O. G. Bilir, "Strain gage methods for measurement of opening mode stress intensity factor", *Engng. Fract. Mech.* **55** (1996), 485–492.

[Sanford 1979] R. J. Sanford, "A critical re-examination of the Westergaard method for solving opening-mode crack problems", *Mech. Res. Comm.* **6** (1979), 289–294.

[Sanford 2003] R. J. Sanford, *Principles of fracture mechanics*, Upper Saddle River, NJ, 2003.

[Srikanth 2006] M. V. Srikanth, *Experimental determination of mode I and mixed mode stress intensity factors using strain gage technique*, Dissertation, Indian Institute of Technology Guwahati, 2006.

[Swain 2007] P. K. Swain, *Comparison between various displacement based stress intensity factor computation techniques*, Dissertation, Indian Institute of Technology Guwahati, 2007.

[Swamy 2007] S. Swamy, *Experimental determination of mode I stress intensity factors using strain gage technique*, Dissertation, Indian Institute of Technology Guwahati, 2007.

[Tada et al. 2000] H. Tada, P. C. Paris, and G. R. Irwin (editors), *The stress analysis of cracks handbook*, ASME, New York, 2000.

[Theocaris 1970] P. S. Theocaris, "Local yielding around a crack tip in Plexiglas", *J. Appl. Mech.* **37** (1970), 409–415.

[Wei and Zhao 1997] J. Wei and J. H. Zhao, "A two-strain-gage technique for determining mode I stress-intensity factor", *Theor. Appl. Fract. Mech.* **28** (1997), 135–140.

[Williams 1957] M. L. Williams, "On the stress distribution at the base of a stationary crack", *J. Appl. Mech.* **24** (1957), 109–114.

[Williams and Ewing 1972] J. G. Williams and P. D. Ewing, "Fracture under complex stress: the angle crack problem", *Int. J. Fract.* **8** (1972), 441–446.

[Xu et al. 2004] W. Xu, X. F. Yao, M. Q. Xu, G. C. Jin, and Y. H. Yeh, "Fracture characterizations of V-notch tip in PMMA polymer material", *Poly. Test.* **23** (2004), 509–515.

S. SWAMY: s.swamy@iitg.ernet.in
Mahindra and Mahindra Limited, Pune, India

M. V. SRIKANTH: venkatasrikanth.manda@wipro.com
Wipro Technologies, Cyber City, Hyderabad, India

K. S. R. K. MURTHY: ksrkm@iitg.ernet.in
Department of Mechanical Engineering, Indian Institute of Technology, Guwahati 781 039, Assam, India

P. S. ROBI: psr@iitg.ernet.in
Department of Mechanical Engineering, Indian Institute of Technology, Guwahati 781 039, Assam, India

PLASTIC YIELD AND COLLAPSE MECHANISM OF PLANAR LATTICE STRUCTURES

YIHUI ZHANG, ZHENYU XUE, XINMING QIU AND DAINING FANG

Lattice structures possess a huge potential for energy absorbing applications, and the postinitial collapse region should be analyzed with respect to design principles in such cases. This paper presents an analytical method to calculate the ultimate yield surfaces of statically indeterminate planar lattice structures, based on the assessment of static equilibrium of the unit cell before and after initial yielding. The material of the unit cell wall is assumed to be elastic, perfectly plastic. Three statically indeterminate planar lattice structures: the diamond cross cell, the statically-indeterminate square cell (SI-square cell), the new Kagome cell (N-Kagome), are analyzed. The parametric studies reveal the roles of various geometrical parameters on the performance of each structure. The SI-square cell is utilized as an example to demonstrate the evolution of structural yielding, thus providing an insight into the collapse mode of lattice structures. Furthermore, the stress-strain relationships of the SI-square and N-Kagome cells are also calculated, and the effective constitutive relations of both lattices are found to be linearly hardening, which is validated by finite element (FE) simulations.

1. Introduction

Recently, lightweight structures, including metal foams, metallic sandwiches with various core topologies, and lattice structures, have been widely used in engineering applications [Gibson and Ashby 1997; Ashby et al. 2000; Smith et al. 2001; Xue and Hutchinson 2003; 2004; 2006; Hutchinson and Xue 2005] for their superior properties of high specific stiffness and strength, most effective energy absorption, shock mitigation, and heat insulation. A lattice structure consists of periodically patterned trusses or sheets which provide large interstructural spaces, thus significantly enhancing the mechanical performance of the structure compared with the equivalent solid plate of same weight. Furthermore, the periodic cellular structures possess far superior specific strengths compared with disordered structures such as Voronoi honeycombs [Fazekas et al. 2002] or less ordered open or closed cell metallic foams [Doyoyo and Wierzbicki 2003]. Two-dimensional lattice structures possess configurations with regular and periodic microstructures in a plane and remain the same along the normal direction of the plane. Because two-dimensional lattice structures are attractive for use as cores in lightweight sandwich beams or plates, for load carrying, energy-absorption, and packaging applications, various aspects of their mechanical and thermal behaviors have received significant attention [Gibson and Ashby 1997; Chen et al. 1999; Evans et al. 2001; Hayes et al. 2004; Fleck and Qiu 2007].

Yielding is generally premonitory of structural collapse for lattice structures, and so a comprehensive understanding of lattice yielding behavior is indispensable for engineering applications. Previous studies on yielding behavior of cellular structures were mainly focused on the yielding criterion and the continuum constitutive relations, and employed the phenomenological and micromechanics methods in the analysis of the periodic unit cell. Deshpande and Fleck [2000] proposed two phenomenological isotropic constitutive models for the plastic behavior of metallic foams, and good agreement was found between their experimental results and analytical predictions. Xue et al. [2005] presented a phenomenological plastic constitutive model for compressible orthotropic materials and extended the model for applications to metal core structures in sandwich plates. This plastic constitutive model was also implemented in a finite element program to study the dynamic mechanical behavior of metal cores [Vaziri and Xue 2007]. From investigations of the representative periodic units, Gibson and Ashby [1997] presented basic mechanical results about ideal and commercial hexagonal honeycombs. Mohr [2005] suggested a mechanism-based multisurface plasticity model for ideal truss lattice materials. Standard homogenization techniques were employed to develop a general micromechanics-based finite-strain constitutive model for truss lattice materials. Wang and McDowell [2005] systematically calculated the initial yield surfaces of five different types of planar lattice patterns by analysis of the periodic unit cells, considering both the in-plane and triaxial stress states. Doyoyo and Mohr [2003] experimentally investigated the microstructural response of aluminum honeycomb under combined normal and shear out-of-plane loading. Zhang et al. [2008] designed two novel statically indeterminate planar lattice structures and calculated their initial yield surfaces and buckling surfaces.

It should be noted that the previous studies about yield surfaces of lattice structures were mainly based on numerical or experimental methods. These methods are commonly complicated and often cannot provide simple explicit results which are more convenient for engineering applications. However, it must be noted that high accuracy results can be obtained by utilizing these methods, especially for the case where buckling of the microstructure is evident. For most stretching dominated structures composed of moderately flexible struts (that is, when the relative density is larger than 0.06), comparison of the yield strengths and elastic strengths indicates that elastic buckling generally does not occur before yielding [Wang and McDowell 2004; Zhang et al. 2008]. In this case, the analytical method based on the micromechanics method, through analysis of the periodic unit cell, is capable of deriving explicit yield surface results with enough accuracy. Since the statically indeterminate lattice structure is still dominated by stretching after the initial yielding, it can still sustain comparatively large additional load after initial yielding. Besides, this category of lattices is expected to possess higher specific strengths than that of statically determinate lattices such as the triangular and Kagome lattices. Therefore, for practical applications of the statically indeterminate lattice structures in engineering conditions, it is crucial to investigate their ultimate yield behavior in detail. The results concerning the ultimate yielding of statically indeterminate cells have not been reported so far.

In this paper, a simple analytical method based on analysis of the equilibrium of the periodic unit cell before and after initial yielding is put forward to calculate the ultimate yield equations of planar lattice structures whose degree of static indeterminacy are one, which is introduced in Section 2.

In Section 3, the ultimate yield surfaces of three statically indeterminate planar lattices are calculated using this method. Comparison of yield strengths among these lattice structures are made in Section 4.

Finally, in Section 5, the whole stress-strain relationships of two statically indeterminate lattice structures in the principal directions are analyzed.

2. Formulation of ultimate yield surface

We consider a representative statically indeterminate lattice structure so that its periodic unit cell, comprised of eight struts fastened to each other, has a parallelogram shape as depicted in Figure 1. The structure undergoes in-plane deformation under multiaxial stressing. The applied normal stresses in the x_1 and x_2 directions are denoted as σ_1 and σ_2, respectively, and the shear stress is τ_{12}. It is noted that the pair of struts having the same orientation must exhibit identical mechanical behavior, so analyzing only one strut is sufficient for each pair. For convenience, each selected strut in the four pairs is numbered by ith, $i = 1, \ldots, 4$ respectively and the length of the ith strut is l_i.

The onsets of yielding of the four pairs of struts are generally not concurrent. As the applied stresses increase up to a set of particular values, a certain pair of struts starts to yield. This state is considered the *initial yielding* of the lattice structure. After initial yielding, the unit cell of the structure is still capable of withstanding further loading. Continuously increasing the loads results in at least one more pair of struts also yielding. Consequently, the structural unit cell will become a mechanism and eventually collapse. We name such behavior the *ultimate yielding* of the lattice structure. After the initial yielding of the statically indeterminate lattice structure, the load is mainly supported by the original configuration (excluding the initially yielding struts) although the initial yielding struts still increase in strength to some extent when the material possesses a strain hardening effect. The strain hardening effect of the parent material will make the solution of the ultimate yielding equation very complicated. Therefore, all struts are assumed to be made of elastic, perfectly plastic material in this paper. Basically, once the ultimate yielding occurs, the structure cannot bear additional loads any more in this case. It is also possible that
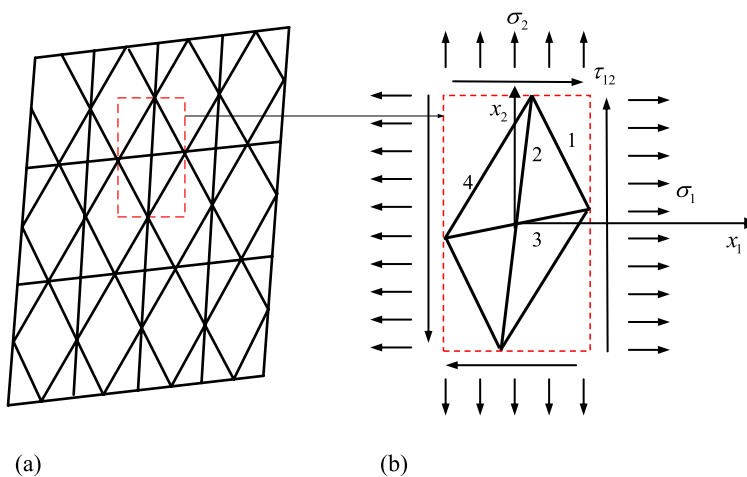

(a) (b)

Figure 1. Sketch of a representative statically indeterminate lattice structure (a) and its unit cell (b).

two or more pairs of struts simultaneously start to yield, in which case we consider that the structure is undergoing the ultimate yielding without experiencing the initial yielding. The evolution of structural yielding will be addressed again later, while the emphasis in this section is to establish the equations for identifying the initial and ultimate yielding conditions of the structure.

According to the criteria proposed by Deshpande et al. [2001], the lattice pattern in Figure 1 is a stretching dominated structure. Furthermore, the unit cell in Figure 1 without one pair of struts is still statically determinate, and each strut still undergoes mainly stretching or compressing; that is to say, the structure is still stretching dominant after initial yielding. Therefore, the deformation of the lattice structure is still very small compared with the dimension of the lattice unit cell. The analytical results in Section 5 also demonstrate that the effective ultimate yielding strain of the lattice structures are both within $5\varepsilon_{ys}$, where ε_{ys} denotes the strain of the solid material. For the typical value of $\varepsilon_{ys} = 0.001$, for a metal material, the effective ultimate yielding strain of the lattice structure is only 0.005. Therefore, the assumption of "small deformation" is still reasonable after initial yield. The agreement of the analytical and Finite Element (FE) results on the stress-strain relationships of the SI-square and N-Kagome cells in Section 5 also demonstrate that the "small deformation" assumption can be accepted. Besides, the bending deformation of each strut in the lattice structure is still small enough so that they cannot contact each other. The results of finite element method (FEM) calculations also support this statement. As shown in Figure 2, when ultimate yielding in the SI-square lattice structure occurs under uniaxial loading in the x_1 and diagonal directions, the bending deformations and rotational angles of each strut are both comparatively small. Therefore, the assumption that the structural elements do not contact each other is precise for describing the deformation mode before the ultimate yielding of the lattice structure, and the equilibrium equations established on the original configuration of the lattice are also accurate enough.

Due to the dominance of cell wall stretching, the internal force of the ith strut is proportional to each applied stress component, thus the initial yielding condition of the ith strut can be written in nondimensional terms as

$$|N_i/(\sigma_{ys}bt)| = |p_i\sigma_1^\circ/\sigma_{ys} + q_i\sigma_2^\circ/\sigma_{ys} + r_i\tau_{12}^\circ/\sigma_{ys}| = 1, \qquad i = 1, \ldots, 4, \tag{1}$$

where N_i denotes the internal force of the ith strut, and σ_{ys} is the yield strength of strut material; b and t are the in-plane wall thickness and out-of-plane dimensions, respectively; σ_1°, σ_2° and τ_{12}° are the applied stresses leading to initial yielding of the unit cell. The coefficients p_i, q_i, and r_i can be considered as the contributing fraction of each stress component to the internal force of the ith strut, depending on the
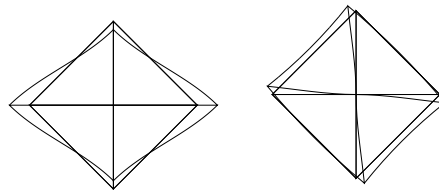

Figure 2. The deformation sketches of the SI-square cell under uniaxial loading in the x_1 and diagonal directions with the deformations magnified by 100 times.

initial structural geometry. For the case in which a single stress component exists (that is, σ_1), the related coefficient (that is, p_i) can be determined straightforwardly (that is, $p_i = N_i/(\sigma_1 bt)$).

It is noted that after initial yielding (that is, the ith strut is yielding), the structure is still stretching dominant. Assuming that the jth ($j = 1, \ldots, 4$, $j \neq i$) strut yields subsequently after the ith strut, then the corresponding ultimate yield equation of the unit cell can be given by

$$
\begin{aligned}
|N_j^{(i)}/(\sigma_{ys}bt)| &= |(N_j^{(i)\circ} + \Delta N_j^{(i)})/\sigma_{ys}bt| \\
&= \left| \begin{array}{l} p_j \sigma_1^\circ/\sigma_{ys} + q_j \sigma_2^\circ/\sigma_{ys} \\ + r_j \tau_{12}^\circ/\sigma_{ys} + P_j^{(i)} \Delta\sigma_1/\sigma_{ys} \\ + Q_j^{(i)} \Delta\sigma_2/\sigma_{ys} + R_j^{(i)} \Delta\tau_{12}/\sigma_{ys} \end{array} \right| = 1, \qquad i, j = 1, \ldots, 4, \; j \neq i,
\end{aligned}
\tag{2}
$$

where $N_j^{(i)\circ}$ denotes the internal force of the jth strut at the onset of initial yielding of the ith strut. $\Delta N_j^{(i)}$ denotes the additional internal force within the jth strut thereafter, and correspondingly $\Delta\sigma_1$, $\Delta\sigma_2$, and $\Delta\tau_{12}$ are the additional applied stresses thereafter. By definition, the additional stresses can be written by

$$
\Delta\sigma_1 = \sigma_1 - \sigma_1^\circ, \tag{3}
$$

$$
\Delta\sigma_2 = \sigma_2 - \sigma_2^\circ, \tag{4}
$$

$$
\Delta\tau_{12} = \tau_{12} - \tau_{12}^\circ, \tag{5}
$$

where σ_1, σ_2, and τ_{12} are the final applied stresses. Analogous to p_i, q_i, and r_i, the coefficients $P_j^{(i)}$, $Q_j^{(i)}$, and $R_j^{(i)}$ can be considered as the contribution fraction of each stress component increment to the additional internal force of the jth strut after the initial yielding of the structure. They are determined by the geometrical configuration, which excludes the initially yielding struts (the ith strut), and this configuration is named the postyielding configuration. Assuming that an additional stress is exerted to such postyielding configuration, ($\Delta\sigma_1$), the related coefficients (that is, $P_j^{(i)}$) can be determined straight-forwardly ($P_j^{(i)} = N_j^{(i)}/(\Delta\sigma_1 bt)$).

Substituting Equation (3) into (2) gives

$$
\left| \begin{array}{l} (p_j - P_j^{(i)})\sigma_1^\circ/\sigma_{ys} + (q_j - Q_j^{(i)})\sigma_2^\circ/\sigma_{ys} \\ + (r_j - R_j^{(i)})\tau_{12}^\circ/\sigma_{ys} + P_j^{(i)}\sigma_1/\sigma_{ys} \\ + Q_j^{(i)}\sigma_2/\sigma_{ys} + R_j^{(i)}\tau_{12}/\sigma_{ys} \end{array} \right| = 1, \qquad i, j = 1, \ldots, 4, \; j \neq i.
\tag{6}
$$

Through analyzing, in detail, the equilibrium of the structural unit cell under the specified uniaxial stress-ing, we find that the parameters $(p_j - P_j^{(i)})$, $(q_j - Q_j^{(i)})$, $(r_j - R_j^{(i)})$, and p_i, q_i, r_i satisfy the following generalized relation:

$$
\frac{p_j - P_j^{(i)}}{p_i} = \frac{q_j - Q_j^{(i)}}{q_i} = \frac{r_j - R_j^{(i)}}{r_i} = s_j^{(i)}, \qquad (i, j = 1, \ldots, 4, \; i \neq j),
\tag{7}
$$

where $s_j^{(i)}$ is introduced as the scale parameter, depending only on the geometry of the unit cell. The details of the procedure for getting Equation (7) will be given in Appendix A. For the special structure depicted in Figure 1, the parameter $s_j^{(i)}$ can be further related to the length ratios. By introducing the effective lengths, defined as $l_1' = l_1$, $l_2' = 2l_2$, $l_3' = 2l_3$, and $l_4' = l_4$, $s_j^{(i)}$ can be simply written in a generalized form as

$$s_j^{(i)} = \begin{cases} l_j'/l_i' & i + j = 5, \\ -l_j'/l_i' & i + j \neq 5, \end{cases} \qquad (i, j = 1, \ldots, 4, \ i \neq j). \tag{8}$$

The term $|(p_j - P_j^{(i)})\sigma_1^{\circ}/\sigma_{ys} + (q_j - Q_j^{(i)})\sigma_2^{\circ}/\sigma_{ys} + (r_j - R_j^{(i)})\tau_{12}^{\circ}/\sigma_{ys}|$ can be simplified by combining Equations (1) and (7), that is,

$$\left|(p_j - P_j^{(i)})\sigma_1^{\circ}/\sigma_{ys} + (q_j - Q_j^{(i)})\sigma_2^{\circ}/\sigma_{ys} + (r_j - R_j^{(i)})\tau_{12}^{\circ}/\sigma_{ys}\right| = |s_j^{(i)}|. \tag{9}$$

Substituting (9) into (6), the ultimate yield equation is written as:

$$\max_{i,j=1,\ldots,4, i \neq j}\{|s_j^{(i)} + P_j^{(i)}\sigma_1/\sigma_{ys} + Q_j^{(i)}\sigma_2/\sigma_{ys} + R_j^{(i)}\tau_{12}/\sigma_{ys}|\} = 1$$
$$\left(\text{when } \max_{i=1,\ldots,4}\{p_i\sigma_1/\sigma_{ys} + q_i\sigma_2/\sigma_{ys} + r_i\tau_{12}/\sigma_{ys}\} \geq 1, \quad i = 1, \ldots, 4\right), \tag{10a}$$

$$\max_{i,j=1,\ldots,4, i \neq j}\{|-s_j^{(i)} + P_j^{(i)}\sigma_1/\sigma_{ys} + Q_j^{(i)}\sigma_2/\sigma_{ys} + R_j^{(i)}\tau_{12}/\sigma_{ys}|\} = 1$$
$$\left(\text{when } \min_{i=1,\ldots,4}\{p_i\sigma_1/\sigma_{ys} + q_i\sigma_2/\sigma_{ys} + r_i\tau_{12}/\sigma_{ys}\} \leq -1, \quad i = 1, \ldots, 4\right). \tag{10b}$$

Equation (10a) is related to the ith strut's initial yielding under tension, while Equation (10b) is related to its initial yielding under compression. It should be pointed out that the above equations are applicable for any kind of statically indeterminate structures whose degrees of static indeterminacy are one even though their derivation is based on the particular configuration shown in Figure 1.

Here we make a simple comparison of the present analytical method with the methods adopted in the previous investigations on the yield surfaces of the lattice structures. Xue et al. [2005] proposed a phenomenological ellipsoidal yield surface for lattice materials based on the six initial yield strengths in the orthotropic axes. This kind of closed-form yield surface is advantageous in establishing the hardening rule and the plastic constitutive relations similar to that of the isotropic metal material. The deformation of each strut within the lattice cell is not detailed analyzed in this model, so this phenomenological method is not capable of presenting an explicit ultimate yielding equation beyond the initial yielding. Mohr [2005] suggested a mechanism-based multisurface plasticity model for ideal truss lattice materials. Standard homogenization techniques were employed to develop a general micromechanics-based finite-strain constitutive model for truss lattice materials. In their integration algorithm, an iterative numerical method needs to be adopted to check the yield condition and calculate the plastic strain step by step, and thus an explicit analytical ultimate equation also cannot be obtained using their method.

3. Ultimate yield surfaces of three types of lattice structures

Utilizing the equations presented in Section 2, we explore the ultimate yield surfaces of several lattice structures, including the diamond cross cell, SI-square cell and N-Kagome cell. The configurations of
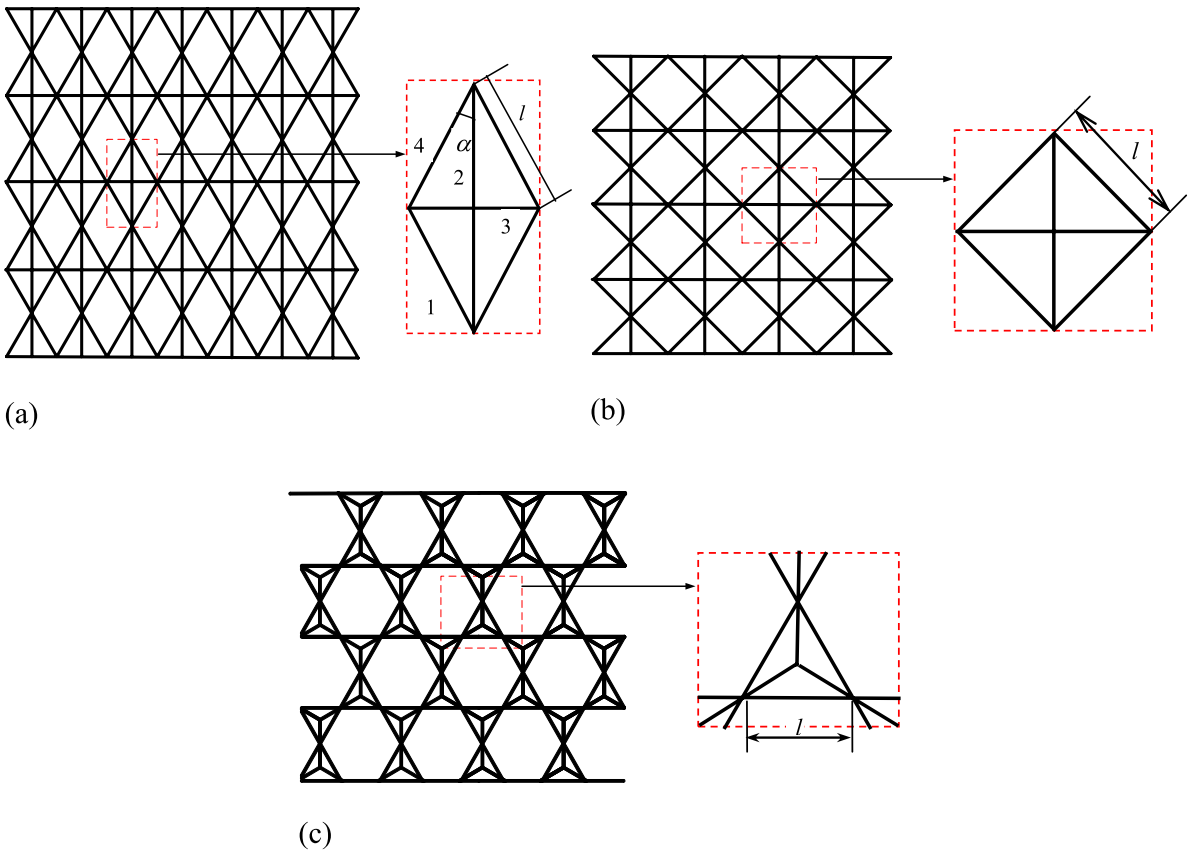
Figure 3. Configurations of the diamond cross (a), the SI-square (b), and the N-Kagome (c) lattice structures.

these lattice structures are shown in Figure 3. Figure 3(a) presents a diamond cross cell having a half top angle of α, which can be specified by setting the lengths of all four outside struts of the unit cell structure shown in Figure 1 to be equal. The statically indeterminate square (SI-square) cell, as shown in Figure 3(b), is considered to be a special diamond cross cell having the half top angle of $\alpha = \pi/4$. The N-Kagome cell, proposed by Zhang et al. [2008], is presented in Figure 3(c). Compared with the original Kagome cell, the N-Kagome cell has three short struts inside the triangle. Zhang et al. [2008] indicated that, for a given relative density and wall thickness, the N-Kagome cell has larger hexagon cavities, which are convenient for oil storage, disposal of heat exchanger, battery deploying and for other functions..

In this section, the procedure of gaining the ultimate yield surfaces is explained in detail by exemplifying that of the diamond cross cell. The similar descriptions for the SI-square and N-Kagome cells are omitted and only the results of the ultimate yield surfaces for these two cells are listed in Appendix B. By employing an energy method, the statically indeterminate problem of the diamond cross cell under a general stress state can be solved, and the internal forces of each strut can be expressed in terms of the applied stress components. Then the initial yield equation of the diamond cross cell is obtained as

follows:

$$\max \begin{bmatrix} \frac{l}{t\sigma_{ys}} \left| \frac{\sin 2\alpha(\sigma_1 \sin\alpha + \sigma_2 \cos\alpha)}{1+2\sin^3\alpha+2\cos^3\alpha} - \tau_{12} \right| - 1 \\ \frac{l}{t\sigma_{ys}} \left| \frac{-\sigma_1 \sin^2 2\alpha + 2\sigma_2 \sin\alpha(1+2\sin^3\alpha)}{1+2\sin^3\alpha+2\cos^3\alpha} \right| - 1 \\ \frac{l}{t\sigma_{ys}} \left| \frac{2\sigma_1 \cos\alpha(1+2\cos^3\alpha) - \sigma_2 \sin^2 2\alpha}{1+2\sin^3\alpha+2\cos^3\alpha} \right| - 1 \\ \frac{l}{t\sigma_{ys}} \left| \frac{\sin 2\alpha(\sigma_1 \sin\alpha + \sigma_2 \cos\alpha)}{1+2\sin^3\alpha+2\cos^3\alpha} + \tau_{12} \right| - 1 \end{bmatrix} = 0. \tag{11}$$

According to Equation (8), the values of $s_j^{(i)}$ are calculated and written in form of an array as following,

$$\left[s_j^{(i)} \right] = \begin{bmatrix} / & -2\cos\alpha & -2\sin\alpha & 1 \\ -\frac{1}{2\cos\alpha} & / & \frac{\sin\alpha}{\cos\alpha} & -\frac{1}{2\cos\alpha} \\ -\frac{1}{2\sin\alpha} & \frac{\cos\alpha}{\sin\alpha} & / & -\frac{1}{2\sin\alpha} \\ 1 & -2\cos\alpha & -2\sin\alpha & / \end{bmatrix}, \tag{12}$$

where i and j are the row index and column index, respectively and $i \neq j$.

Based on the methods briefed in the previous section, the parameters, $P_j^{(i)}$, $Q_j^{(i)}$, and $R_j^{(i)}$, are identified by

$$\left[P_j^{(i)} \right] = \begin{bmatrix} / & 0 & 2bl\cos\alpha & 0 \\ 0 & / & 2bl\cos\alpha & 0 \\ bl\frac{\cos\alpha}{\sin\alpha} & -2bl\frac{\cos^2\alpha}{\sin\alpha} & / & bl\frac{\cos\alpha}{\sin\alpha} \\ 0 & 0 & 2bl\cos\alpha & / \end{bmatrix}, \quad \left[Q_j^{(i)} \right] = \begin{bmatrix} / & 2bl\sin\alpha & 0 & 0 \\ bl\frac{\sin\alpha}{\cos\alpha} & / & -2bl\frac{\sin^2\alpha}{\cos\alpha} & 0 \\ 0 & 2bl\sin\alpha & / & 0 \\ 0 & 2bl\sin\alpha & 0 & / \end{bmatrix},$$

$$\left[R_j^{(i)} \right] = \begin{bmatrix} / & 0 & -2bl\cos\alpha & -2bl\cos\alpha \\ -bl & / & 2bl\cos\alpha & bl \\ -bl & 0 & / & bl \\ -2bl & 2bl\cos\alpha & 2bl\sin\alpha & / \end{bmatrix}. \tag{13}$$

Substituting Equations (11), (12) and (13) into Equations (10a) and (10b) gives the ultimate yield equations of the diamond cross cell, that is,

$$
\max \begin{bmatrix}
2\frac{l}{t\sigma_{ys}}|-\sin\alpha+\sigma_1\cos\alpha\pm\tau_{12}\sin\alpha|-1 \\[6pt]
2\frac{l}{t\sigma_{ys}}|-\cos\alpha+\sigma_2\sin\alpha\pm\tau_{12}\cos\alpha|-1 \\[6pt]
\frac{l}{t\sigma_{ys}}|1\pm2\tau_{12}\cos\alpha|-1 \\[6pt]
\frac{l}{t\sigma_{ys}}\left|\frac{\sin\alpha}{\cos\alpha}+2\sigma_1\cos\alpha-2\sigma_2\frac{\sin^2\alpha}{\cos\alpha}\right|-1 \\[6pt]
\frac{l}{t\sigma_{ys}}\left|\frac{\cos\alpha}{\sin\alpha}-2\sigma_1\frac{\cos^2\alpha}{\sin\alpha}+2\sigma_2\sin\alpha\right|-1
\end{bmatrix}=0, \quad \text{when}
$$

$$
\max \begin{bmatrix}
\frac{l}{t\sigma_{ys}}\frac{\sin2\alpha(\sigma_1\sin\alpha+\sigma_2\cos\alpha)}{1+2\sin^3\alpha+2\cos^3\alpha}-\tau_{12}-1 \\[6pt]
\frac{l}{t\sigma_{ys}}\frac{-\sigma_1\sin^2 2\alpha+2\sigma_2\sin\alpha(1+2\sin^3\alpha)}{1+2\sin^3\alpha+2\cos^3\alpha}-1 \\[6pt]
\frac{l}{t\sigma_{ys}}\frac{2\sigma_1\cos\alpha(1+2\cos^3\alpha)-\sigma_2\sin^2 2\alpha}{1+2\sin^3\alpha+2\cos^3\alpha}-1 \\[6pt]
\frac{l}{t\sigma_{ys}}\frac{\sin2\alpha(\sigma_1\sin\alpha+\sigma_2\cos\alpha)}{1+2\sin^3\alpha+2\cos^3\alpha}+\tau_{12}-1
\end{bmatrix}>0, \quad (14a)
$$

$$
\max \begin{bmatrix}
2\frac{l}{t\sigma_{ys}}|\sin\alpha+\sigma_1\cos\alpha\pm\tau_{12}\sin\alpha|-1 \\[6pt]
2\frac{l}{t\sigma_{ys}}|\cos\alpha+\sigma_2\sin\alpha\pm\tau_{12}\cos\alpha|-1 \\[6pt]
\frac{l}{t\sigma_{ys}}|-1\pm2\tau_{12}\cos\alpha|-1 \\[6pt]
\frac{l}{t\sigma_{ys}}\left|-\frac{\sin\alpha}{\cos\alpha}+2\sigma_1\cos\alpha-2\sigma_2\frac{\sin^2\alpha}{\cos\alpha}\right|-1 \\[6pt]
\frac{l}{t\sigma_{ys}}\left|-\frac{\cos\alpha}{\sin\alpha}-2\sigma_1\frac{\cos^2\alpha}{\sin\alpha}+2\sigma_2\sin\alpha\right|-1
\end{bmatrix}=0, \quad \text{when}
$$

$$
\min \begin{bmatrix}
-\frac{l}{t\sigma_{ys}}\frac{\sin2\alpha(\sigma_1\sin\alpha+\sigma_2\cos\alpha)}{1+2\sin^3\alpha+2\cos^3\alpha}-\tau_{12}+1 \\[6pt]
-\frac{l}{t\sigma_{ys}}\frac{-\sigma_1\sin^2 2\alpha+2\sigma_2\sin\alpha(1+2\sin^3\alpha)}{1+2\sin^3\alpha+2\cos^3\alpha}+1 \\[6pt]
-\frac{l}{t\sigma_{ys}}\frac{2\sigma_1\cos\alpha(1+2\cos^3\alpha)-\sigma_2\sin^2 2\alpha}{1+2\sin^3\alpha+2\cos^3\alpha}+1 \\[6pt]
-\frac{l}{t\sigma_{ys}}\frac{\sin2\alpha(\sigma_1\sin\alpha+\sigma_2\cos\alpha)}{1+2\sin^3\alpha+2\cos^3\alpha}+\tau_{12}+1
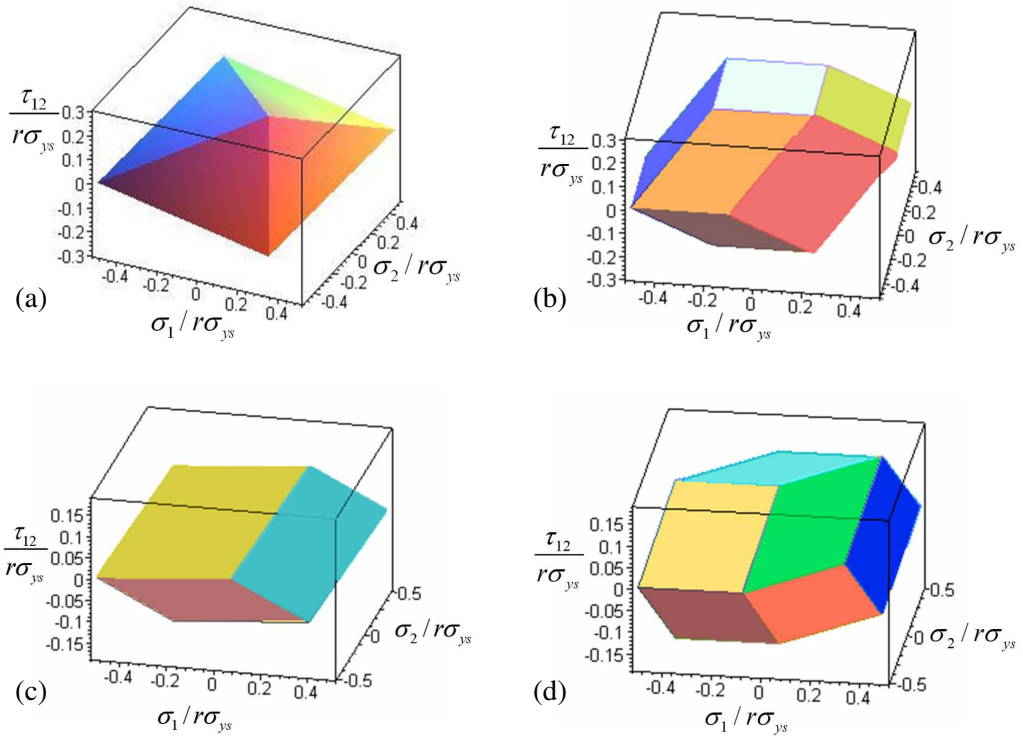\end{bmatrix}<0. \quad (14b)
$$

Figure 4. The initial (a) and ultimate (b) yield surfaces of the SI-square cell, and the initial (c) and ultimate (d) yield surfaces of the N-Kagome cell.

Since the SI-square lattice structure can be considered as a special diamond cross lattice structure, only the results for the SI-square and N-Kagome lattice structures are discussed herein. Figures 4(a) and 4(b) show the initial and ultimate yield surfaces of the SI-square cell in the space of normalized effective stresses respectively, while Figures 4(c) and 4(d) are corresponding to the N-Kagome cell. All four yield surfaces are closed, convex, and anisotropic. By comparison, the ultimate yield surfaces of both structures are entirely outside their initial yield surfaces, indicating that the structures still have capabilities of bearing extra loads after the onset of initial yielding. It is also demonstrated that the magnitude of the residual carrying capacity depends on the loading conditions. The initial and ultimate yield surfaces consist of only planar facets. This is the common feature of the stretching dominated structures.

Representations of yield surfaces in the stress spaces of σ_1 and σ_2, σ_1 and τ_{12}, and σ_2 and τ_{12} are illustrated in Figures 5(a), (b) and (c) respectively. In all three stress spaces, the ultimate yield surfaces of the SI-square cell embrace those of the N-Kagome cell with a large extra area, although the sizes of their initial yield surfaces are comparative with those of the N-Kagome cell. Therefore, we may draw a conclusion that the SI-square cell has much larger ultimate load-carrying capacity than the N-Kagome cell.
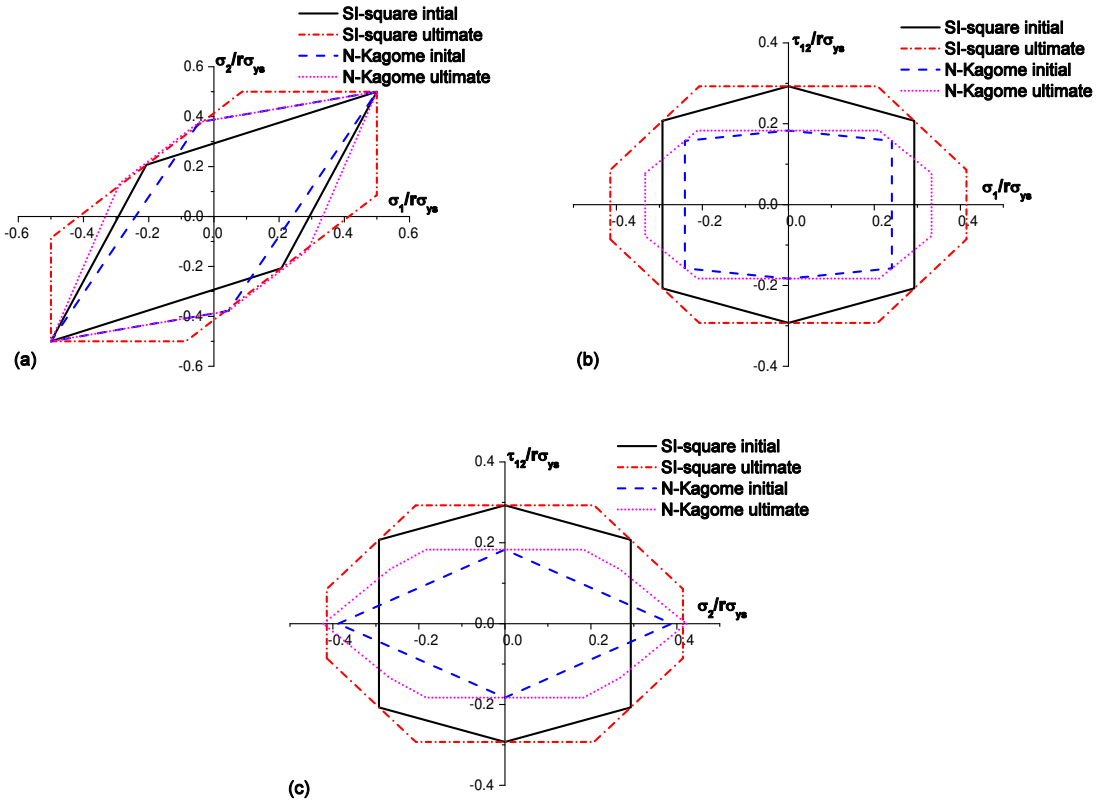
Figure 5. The initial and ultimate yield surfaces of the SI-square cell and N-Kagome cell in the stress spaces of σ_1, σ_2 (a), σ_1, τ_{12} (b) and σ_2, τ_{12} (c).

4. Yielding responses of the lattice structures under uniaxial loading

In order to estimate the structural load carrying capacity, we analyze the ultimate yield strength of each aforementioned lattice patterns subjected to uniaxial loads. Assume that the angle between the loading direction and x_1 direction is θ ($0 \leq \theta < \pi$). The resultant stress can be decomposed into two normal stress components and a shear stress component such that

$$\sigma_1 = \sigma \cos^2 \theta, \qquad \sigma_2 = \sigma \sin^2 \theta, \qquad \tau_{12} = \sigma \sin \theta \cos \theta. \qquad (15)$$

Thus, the ultimate yield equations obtained before can be easily exploited to calculate the yielding responses of the structures to given stresses in any loading directions.

4.1. *The ultimate yield strengths of three lattice structures under uniaxial loading.* From (14a), (14b), and (15), the ultimate yield strength of the diamond cross cell related to the loading direction of θ is

obtained as

$$
\frac{\sigma_{ut}^*(\theta)}{\sigma_{ys}} = \min \begin{bmatrix} \left| \frac{\sin\alpha + \cos\alpha}{2\cos^2\theta\cos^2\alpha - 2\sin^2\theta\sin^2\alpha} \frac{t}{l} \right| \\[2ex] \left| \frac{1}{\sin\theta\cos\theta} \frac{t}{l} \right| \\[2ex] \left| \frac{1 + 2\sin\alpha}{2\cos\theta\cos(\alpha\pm\theta)} \frac{t}{l} \right| \\[2ex] \left| \frac{1 + 2\cos\alpha}{2\sin\theta\cos(\alpha\pm\theta)} \frac{t}{l} \right| \end{bmatrix}. \tag{16}
$$

For the SI-square cell, its ultimate yield strength as a function of θ is given by

$$
\frac{\sigma_{ut}^*(\theta)}{\sigma_{ys}} = \begin{cases} \frac{\sqrt{2}-1}{\cos 2\theta} r & (0 \le \theta \le 0.0541\pi), \\[2ex] \frac{1}{2\cos\theta(\sin\theta + \cos\theta)} r & (0.0541\pi \le \theta \le \frac{\pi}{4}). \end{cases} \tag{17}
$$

where r is the relative density of the lattice structure. Furthermore, the values of the maximum and minimum ultimate yield strengths for the SI-square cell are as follows,

$$
\frac{\sigma_{ut\,\max}^*}{\sigma_{ys}} = 0.5r, \quad \left(\theta = \frac{n\pi}{2} \pm \frac{\pi}{4},\ n = 1, \ldots, 4\right), \tag{18a}
$$

$$
\frac{\sigma_{ut\,\min}^*}{\sigma_{ys}} = 0.414r, \quad \left(\theta = \frac{n\pi}{2},\ n = 1, \ldots, 4\right). \tag{18b}
$$

For the N-Kagome cell, the relationship between the ultimate strength and the loading direction is calculated according to the ultimate yield equation (Equation (A.4)), that is,

$$
\frac{\sigma_{ut}^*(\theta)}{\sigma_{ys}} = \begin{cases} \frac{r}{4\cos^2\theta - 1} & \left(0 \le \theta < \frac{\pi}{12}\right), \\[2ex] \frac{(\sqrt{3}-1)r}{\sqrt{3}\cos 2\theta + \sin 2\theta} & \left(\frac{\pi}{12} \le \theta < \frac{\pi}{6}\right), \\[2ex] 0.388r & \left(\theta = \frac{\pi}{6}\right). \end{cases} \tag{19}
$$

Its maximum and minimum values of normalized ultimate strengths are given by

$$
\frac{\sigma_{ut\,\max}^*}{\sigma_{ys}} = 0.423r, \qquad \theta = \frac{n\pi}{3} + \frac{\pi}{6}(n = 0, \ldots, 5), \tag{20a}
$$

$$
\frac{\sigma_{ut\,\min}^*}{\sigma_{ys}} = 0.333r, \qquad \theta = \frac{n\pi}{3} + \frac{\pi}{3}(n = 0, \ldots, 5). \tag{20b}
$$

4.2. *Comparison of yield strength for various cell patterns.* The yield strengths of four types of cell patterns, including the diamond, Kagome, SI-square, and diamond cross cells, are compared in Figure 6. Among them, the former two, as representatives of the statically determinate lattice structures, are excellent structures for high specific stiffness and specific strength [Wang and McDowell 2004; 2005]. Different from the SI-square and diamond cross cells, they are not able to sustain further load after initial yielding. Therefore, their initial yield strengths are adopted to identify their maximum load-carrying capability. For the latter two statically indeterminate structures, the SI-square and diamond cross cells, the
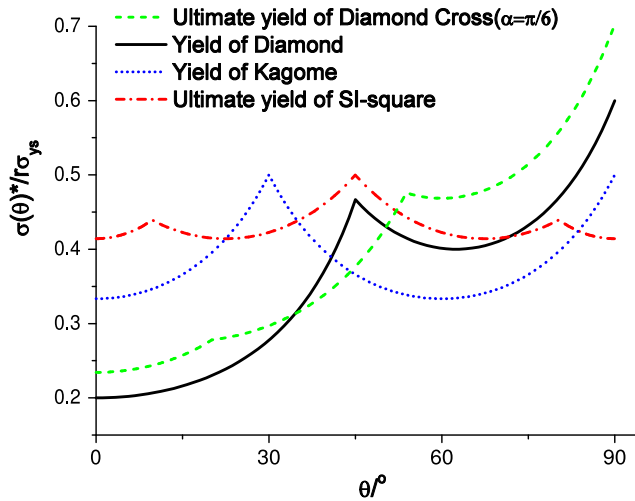
Figure 6. Comparison of yield strength among four different cell patterns.

ultimate yield strengths are employed to weigh their maximum load-carrying capabilities. The diamond cross cell that we analyze has the half top angle of $\alpha = \pi/6$. Basically, the yield strengths of the structures vary as the loading direction changes. The ultimate yield strength of the SI-square cell stays at a higher level relative to that of the Kagome cell over almost the whole range of loading directions, indicating that the SI-square cell has an advantage with respect to withstanding loads. For both the diamond and diamond cross cells, their strengths depend on the applied loading direction. The minimum yield strengths of both patterns occur when $\theta = 0°$ while the maximum values are higher than 0.6 at $\theta = 90°$. On the whole, the ultimate yield strengths of the diamond cross cell ($\alpha = \pi/6$) are slightly higher than that of the diamond cell. It is usual in estimation of the structural performance to adopt the worst case scenario so that the structure is considered to be a better one if it is able to survive relatively longer under any loading conditions. By comparison, the SI-square cell, the minimum yield strength of which is much higher than the others, is recommended as the best two-dimensional lattice structure for its superior load carrying capability among those aforementioned lattice patterns.

For the diamond cross cell with different half top angle α, the uniaxial ultimate yield strength is also calculated and plotted in Figure 7. It is noted that if rotated an angle of $\pi/2$, the diamond cross cell of the half top angle α will be the same as that of the half top angle $\pi/2 - \alpha$. Therefore, the top angle considered in the analysis is restricted in the range of $0 < \alpha \leq \pi/4$. As shown in Figure 7, as the half top angle decreases from $\pi/7$, the maximum yield strength is elevated and the minimum yield strength is lowered slightly. Therefore, the structure exhibits more obvious anisotropy. When the half top angle α is less than $\pi/6$, each of the corresponding curves is composed of three segments, and value of the normalized strength $(\sigma_{ut}^*(\theta)/\sigma_y)(1/r)$ increases with load direction θ. For α in the range of $\pi/6 < \alpha < \pi/4$, the corresponding curve consists of four parts. It is noted that the anisotropy of the structural response is not always a disadvantage. Particularly, for the case where the applied load is fixed at a determined direction, the half top angle of the structure can be well designed to ensure that its corresponding yield strength is as high as possible. The structure with the half top angle of $\pi/4$ evolves into the SI-square one, which displays a more isotropic yielding behavior.
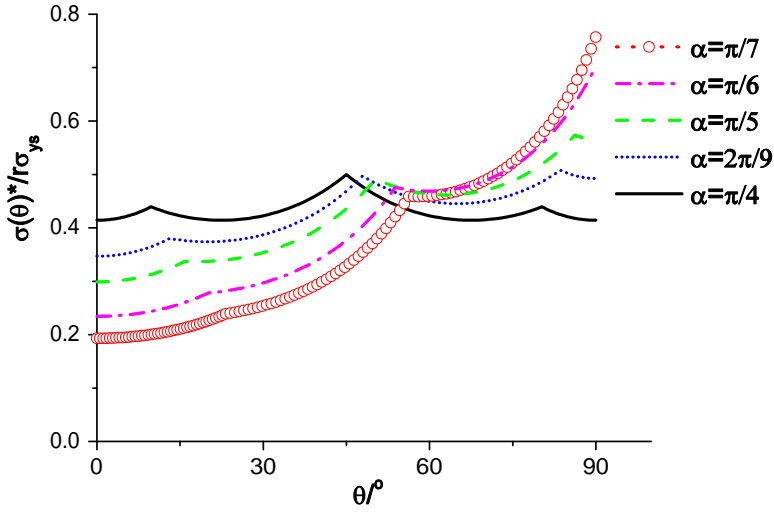
Figure 7. The ultimate yield strength of the diamond cross cells with different half top angles.

4.3. *Evolution of the yield modes for the SI-square cell.* As discussed before, the SI-square cell, as a statically indeterminate structure, undergoes initial yielding followed by the ultimate yielding. Its initial yield strength and ultimate yield strength are presented in Figure 8 as a function of θ. As the loading direction θ varies, both the initial yield strength and the ultimate yield strength are changed. It is seen that there exist several sharp peaks on the curves. Careful analysis exposes that each sharp peak actually corresponds to the transition of the yielding modes from one to another. Corresponding to each marked point on the curves, the yield modes are demonstrated in Figure 8. The curved segment between A and E on the initial yield curve arises from the fact that the horizontal struts experience yielding; the curved segment between E and F is related to the case where the inclined struts yield first. Initial yielding of a pair of struts usually does not mark the limit of its load-carrying resistance. Rather, it signifies a change in the way in which the structure responds to further loads. The structural unit cell does not collapse until additional plastic yielding struts have formed to convert it into a mechanism. The collapse modes are different for different loading directions. For $\theta = 0°$, after the horizontal struts yield initially, the vertical struts will yield finally as the applied effective stress increases up to $\sigma^*(\theta)/r\sigma_{ys} = 0.414$. For either $\theta = 9.7°$ or $\theta = 45°$, three pairs of struts, including the horizontal, the vertical, and the inclined struts, all yield together once the applied load increases beyond the corresponding values of the ultimate yield strength. It is also noted that at $\theta = 27.3°$ the horizontal and inclined struts will yield simultaneously, resulting in direct structural collapse without initial yielding. The maximum load carrying capacity of the SI-square structure occurs when the load is applied to the unit cell along the angle of $\theta = 45°$, while the structure is relatively weaker to the horizontally applied load.

5. Stiffness analysis under uniaxial loading

For the struts made of the elastic, perfectly plastic material, the stress-strain relationships and stiffness characteristics of the SI-square and N-Kagome cells are also solved analytically and presented in this section.
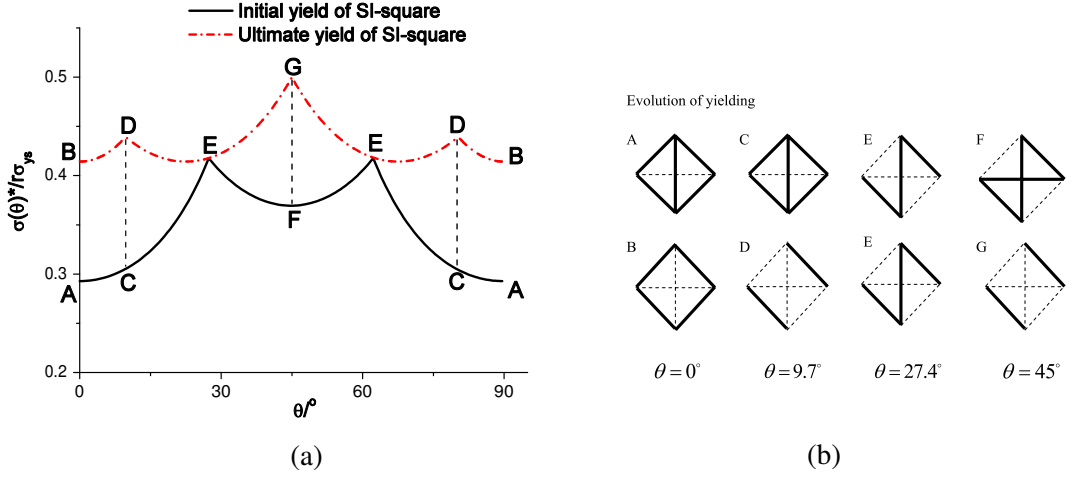
Figure 8. The initial and ultimate yield strength of the SI-square cell (a) along with the evolution of the yielding mode (b).

Considering the stress-strain relationship of the SI-square cell loaded in the x_1 direction ($\theta = 0°$), with increase of the effective stress, σ_1, from zero to the initial yield strength, the effective stress is proportional to the effective strain, with the slope just equal to the effective modulus. If the stress still increases after the initial yielding, the horizontal strut will yield (see yielding mode A in Figure 8), and the additional stress, $\Delta\sigma_1$, will be proportional to the additional strain $\Delta\varepsilon_1$. In this case, the stress is still linearly dependent on the strain, while the slope becomes the effective modulus of the unit cell without the horizontal strut. This is presented in Figure 9. The second pair of struts will occur yielding when the stress reaches the ultimate yield strength. After onset of the ultimate yielding, the unit cell is not able to support additional stress any more. The effective modulus and initial yield strength of the SI-square cell have been obtained by Zhang et al. [2008]. The effective stiffness of the unit cell without the initial yielding strut can also be easily calculated, thus the normalized stress-strain relationship can be gained, that is,

$$\frac{\sigma_1}{r\sigma_{ys}} = \begin{cases} \frac{2-\sqrt{2}}{2}\frac{\varepsilon_1}{\varepsilon_{ys}}, & 0 \leq \frac{\varepsilon_1}{\varepsilon_{ys}} \leq 1, \\ \frac{2-\sqrt{2}}{2} + \frac{3-2\sqrt{2}}{2}\left(\frac{\varepsilon_1}{\varepsilon_{ys}} - 1\right), & 1 < \frac{\varepsilon_1}{\varepsilon_{ys}} \leq \sqrt{2}+1, \\ \sqrt{2}-1, & \frac{\varepsilon_1}{\varepsilon_{ys}} > \sqrt{2}+1, \end{cases} \tag{21}$$

where ε_{ys} is the yield strain of the material, and the stiffness of the material is $E_s = \sigma_{ys}/\varepsilon_{ys}$. Similarly, the normalized stress-strain relationship of the SI-square cell in the diagonal direction can also be obtained,

$$\frac{\sigma_{diag}}{r\sigma_{ys}} = \begin{cases} \frac{4-\sqrt{2}}{7}\frac{\varepsilon_{diag}}{\varepsilon_{ys}}, & 0 \leq \frac{\varepsilon_{diag}}{\varepsilon_{ys}} \leq 1, \\ \frac{4-\sqrt{2}}{7} + \frac{5\sqrt{2}-6}{14}\left(\frac{\varepsilon_{diag}}{\varepsilon_{ys}} - 1\right), & 1 < \frac{\varepsilon_{diag}}{\varepsilon_{ys}} \leq \frac{4+\sqrt{2}}{2}, \\ \frac{1}{2} & \frac{\varepsilon_{diag}}{\varepsilon_{ys}} > \frac{4+\sqrt{2}}{2}. \end{cases} \tag{22}$$
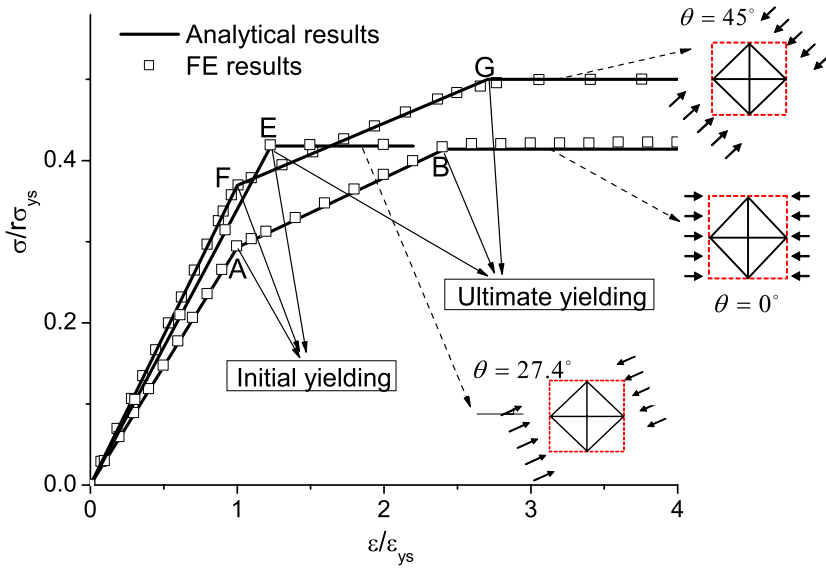
Figure 9. The stress-strain relationships of the SI-square cell in the three typical directions.

The normalized stress-strain relationship of the N-Kagome cell in the x_1 and x_2 directions could also be calculated,

$$\frac{\sigma_1}{r\sigma_{ys}} = \begin{cases} \frac{9-2\sqrt{3}}{23}\frac{\varepsilon_1}{\varepsilon_{ys}}, & 0 \leq \frac{\varepsilon_1}{\varepsilon_{ys}} \leq 1, \\ \frac{9-2\sqrt{3}}{23} + \frac{11\sqrt{3}-15}{138}\left(\frac{\varepsilon_1}{\varepsilon_{ys}}-1\right), & 1 < \frac{\varepsilon_1}{\varepsilon_{ys}} \leq \frac{9+2\sqrt{3}}{3}, \\ \frac{1}{3}, & \frac{\varepsilon_1}{\varepsilon_{ys}} > \frac{9+2\sqrt{3}}{3}. \end{cases} \tag{23}$$

$$\frac{\sigma_2}{r\sigma_{ys}} = \begin{cases} \frac{9-2\sqrt{3}}{23}\frac{\varepsilon_2}{\varepsilon_{ys}}, & 0 \leq \frac{\varepsilon_2}{\varepsilon_{ys}} \leq \frac{16+\sqrt{3}}{11}, \\ \frac{6-\sqrt{3}}{11} + \frac{111-45\sqrt{3}}{694}\frac{\varepsilon_2}{\varepsilon_{ys}}, & \frac{16+\sqrt{3}}{11} < \frac{\varepsilon_2}{\varepsilon_{ys}} \leq 2.345, \\ \frac{3-\sqrt{3}}{3}, & \frac{\varepsilon_2}{\varepsilon_{ys}} > 2.345. \end{cases} \tag{24}$$

According to Equations (21)–(24), the normalized stress-normalized strain curves are plotted in Figures 9 and 10 for the SI-square and the N-Kagome cells respectively. Each change in slope corresponds to the formation of plastic struts which produces progressive *flexibility* of the structure. In Figure 9, each marked transition point is corresponding to the yielding mode marked with the same letter in Figure 8. Collapse occurs when enough struts have undergone plastic yielding to transform the structure into a mechanism with no inherent stiffness, corresponding to the final horizontal segments of the curves.

Corresponding FE simulations are performed to verify the analytical stress-strain relations. In the calculation, the material is linear elastic with linear hardening plasticity. A small linearly hardening coefficient, $E'/E = 0.001$, is adopted for the cell wall material, where E and E' are the elastic modulus
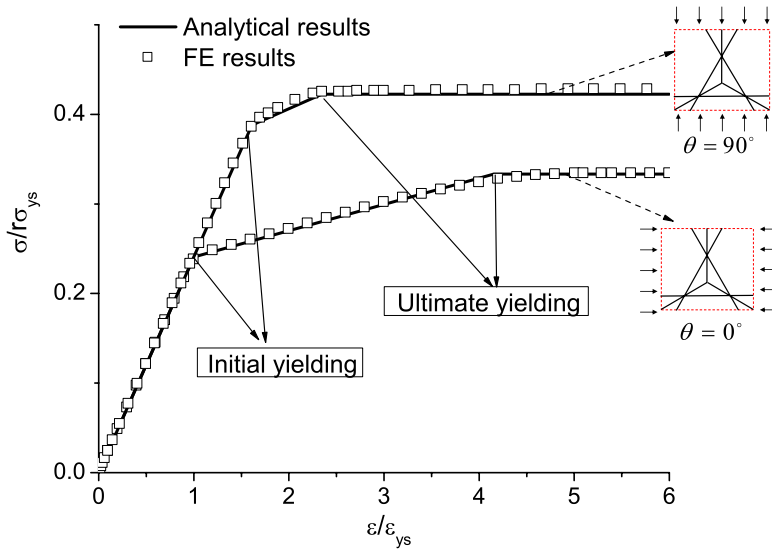
Figure 10. The stress-strain relationships of the N-Kagome cell in the principle directions.

and the tangential modulus. As shown in Figures 9 and 10, good agreements are found between the FE results and the analytical stress-strain predictions, thus verifying the analytical solutions.

6. Concluding remarks

Based on the analysis of the equilibrium of a unit cell before and after initial yielding, a simple analytical method is put forward to calculate the ultimate yield equation of statically indeterminate planar lattice structures for the elastic, perfectly plastic parent material. The ultimate yield surfaces and yield strengths of several indeterminate unit cells are assessed using the proposed method, and the residual loading capacity after the onset of initial yielding can be quantitatively predicted. The stress-strain relationships of the SI-square and N-Kagome cells are also calculated for the elastic, perfectly plastic materials, and the effective constitutive relations of both lattices are found to be linearly hardening, which is validated by finite element (FE) simulations. Comparison of the initial and ultimate yield surfaces indicates that these lattice structures possess considerable residual loading capacities which depend on the loading conditions. It is found that the ultimate yield strength of the SI-square cell is nearly isotropic, possesses a higher ultimate yield strength, and therefore is an excellent lightweight structure for load carrying. The ultimate yield strengths of the diamond cross cell ($\alpha = \pi/6$) are slightly higher than that of the diamond cell on the whole.

Appendix A: the deduction of the relationship given by Equation (7)

In order to obtain the relationships between the parameters $(p_j - P_j^{(i)})$, $(q_j - Q_j^{(i)})$, $(r_j - R_j^{(i)})$, and p_i, q_i, r_i, the equilibrium of the unit cell is analyzed. The anticlockwise angle of the ith strut and the x_1 direction is assumed to be θ_i. For the case where the first strut yields first, that is, $i = 1$, we simply take the values of applied stresses to be unit, that is, $\sigma_1 = 1$ or $\Delta\sigma_1 = 1$, which can be equivalent to two

concentrated loads exerted on the connecting nodes of the struts, P_A and P_B, as shown in Figure 11. (We note that the stress quantities σ and $\Delta\sigma$ are reference stresses that can be chosen arbitrarily; they are simply scaling factors.) The equilibrium equations of points A and B before initial yielding are

$$
\begin{aligned}
-p_1 \cos\theta_1 + p_3 \cos\theta_3 + p_4 \cos\theta_4 &= P_A/bt, \\
-p_1 \sin\theta_1 + p_3 \sin\theta_3 + p_4 \sin\theta_4 &= 0, \\
p_1 \sin\theta_1 + p_2 \sin\theta_2 + p_4 \sin\theta_4 &= 0, \\
p_1 \cos\theta_1 + p_2 \cos\theta_2 + p_4 \cos\theta_4 &= -P_B/bt.
\end{aligned}
\tag{A.1}
$$

The equilibrium equations of points A and B after initial yielding are:

$$
\begin{aligned}
P_3^{(1)} \cos\theta_3 + P_4^{(1)} \cos\theta_4 &= P_A/bt, \\
P_3^{(1)} \sin\theta_3 + P_4^{(1)} \sin\theta_4 &= 0, \\
P_2^{(1)} \sin\theta_2 + P_4^{(1)} \sin\theta_4 &= 0, \\
P_2^{(1)} \cos\theta_2 + P_4^{(1)} \cos\theta_4 &= -P_B/bt.
\end{aligned}
\tag{A.2}
$$

Subtracting each equation of Equation (A.2) from Equation (A.1) gives:

$$
\begin{aligned}
(p_3 - P_3^{(1)}) \cos\theta_3 + (p_4 - P_4^{(1)}) \cos\theta_4 &= p_1 \cos\theta_1, \\
(p_3 - P_3^{(1)}) \sin\theta_3 + (p_4 - P_4^{(1)}) \sin\theta_4 &= p_1 \sin\theta_1, \\
(p_2 - P_2^{(1)}) \sin\theta_2 + (p_4 - P_4^{(1)}) \sin\theta_4 &= -p_1 \sin\theta_1, \\
(p_2 - P_2^{(1)}) \cos\theta_2 + (p_4 - P_4^{(1)}) \cos\theta_4 &= -p_1 \cos\theta_1.
\end{aligned}
\tag{A.3}
$$

Taking these parameters, $(p_2 - P_2^{(1)})$, $(p_3 - P_3^{(1)})$, $(p_4 - P_4^{(1)})$ and p_1, as unknown quantities, the rank of the coefficient matrix of Equation (A.3) is three, which indicates that those four equations in Equation (A.3) are not independent, and the value of $\frac{p_j - P_j^{(1)}}{p_1}$ ($j = 2, 3, 4$) can be uniquely determined as follows,

$$
\frac{p_2 - P_2^{(1)}}{p_1} = \frac{\sin(\theta_4 - \theta_1)}{\sin(\theta_2 - \theta_4)}, \qquad
\frac{p_3 - P_3^{(1)}}{p_1} = \frac{\sin(\theta_4 - \theta_1)}{\sin(\theta_4 - \theta_3)}, \qquad
\frac{p_4 - P_4^{(1)}}{p_1} = \frac{\sin(\theta_1 - \theta_3)}{\sin(\theta_4 - \theta_3)}.
\tag{A.4}
$$

Analogously, if the first strut yields first, and only the unit applied stress $\sigma_2 = 1$ or $\tau_{12} = 1$ exists, the following relationships can be obtained:

$$
\frac{q_2 - Q_2^{(1)}}{q_1} = \frac{\sin(\theta_4 - \theta_1)}{\sin(\theta_2 - \theta_4)}, \qquad
\frac{q_3 - Q_3^{(1)}}{q_1} = \frac{\sin(\theta_4 - \theta_1)}{\sin(\theta_4 - \theta_3)}, \qquad
\frac{q_4 - Q_4^{(1)}}{q_1} = \frac{\sin(\theta_1 - \theta_3)}{\sin(\theta_4 - \theta_3)},
\tag{A.5}
$$

$$
\frac{r_2 - R_2^{(1)}}{r_1} = \frac{\sin(\theta_4 - \theta_1)}{\sin(\theta_2 - \theta_4)}, \qquad
\frac{r_3 - R_3^{(1)}}{r_1} = \frac{\sin(\theta_4 - \theta_1)}{\sin(\theta_4 - \theta_3)}, \qquad
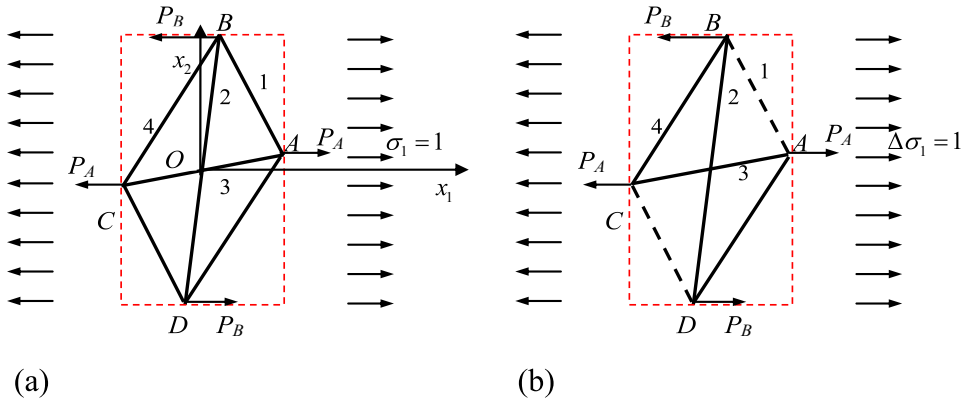\frac{r_4 - R_4^{(1)}}{r_1} = \frac{\sin(\theta_1 - \theta_3)}{\sin(\theta_4 - \theta_3)}.
\tag{A.6}
$$

Figure 11. The unit cell under uniaxial compression in the x_1 direction (a) before and (b) after the initial yield of the first strut.

Similar deduction can be performed for the cases that the second, third, and fourth struts yield first by using the same method, and the results can be concluded as:

$$\frac{p_j - P_j^{(i)}}{p_i} = \frac{q_j - Q_j^{(i)}}{q_i} = \frac{r_j - R_j^{(i)}}{r_i} = s_j^{(i)} = \begin{cases} l'_j/l'_i & i+j=5, \\ -l'_j/l'_i & i+j \neq 5, \end{cases} \qquad (i,j=1,\ldots,4,\ i \neq j), \quad (A.7)$$

where the definition of $s_j^{(i)}$ and l'_i can be seen in Section 2.

Appendix B: the initial and ultimate yield equations of the SI-square and N-Kagome lattice structures

The SI-square cell can be considered as a special diamond cross cell having the half top angle of $\alpha = \pi/4$. By taking $\alpha = \pi/4$ in Equation (11) and Equation (14), the initial and ultimate yield equations of the SI-square cell are respectively given by

$$\max \begin{bmatrix} (|(\sigma_1/r\sigma_{ys} + \sigma_2/r\sigma_{ys}) - (2+\sqrt{2})(\tau_{12}/r\sigma_{ys})| - 1), \\ (|-\sqrt{2}\sigma_1/r\sigma_{ys} + (2+\sqrt{2})(\sigma_2/r\sigma_{ys})| - 1), \\ (|(\sigma_1/r\sigma_{ys} + \sigma_2/r\sigma_{ys}) + (2+\sqrt{2})(\tau_{12}/r\sigma_{ys})| - 1), \\ (|(2+\sqrt{2})(\sigma_1/r\sigma_{ys}) - \sqrt{2}(\sigma_2/r\sigma_{ys})| - 1) \end{bmatrix} = 0, \qquad (A.1)$$

$$
\max \begin{bmatrix} \left|2\left(\frac{\sigma_1}{r\sigma_{ys}} + \frac{\tau_{12}}{r\sigma_{ys}}\right)\right| - 1 = 0, \\ \left|2\left(\frac{\sigma_1}{r\sigma_{ys}} - \frac{\tau_{12}}{r\sigma_{ys}}\right)\right| - 1 = 0, \\ \left|(\sqrt{2}+1)\left(\frac{\sigma_1}{r\sigma_{ys}} - \frac{\sigma_2}{r\sigma_{ys}}\right)\right| - 1 = 0, \\ \left|2\left(\frac{\sigma_2}{r\sigma_{ys}} + \frac{\tau_{12}}{r\sigma_{ys}}\right)\right| - 1 = 0, \\ \left|2\left(\frac{\sigma_2}{r\sigma_{ys}} - \frac{\tau_{12}}{r\sigma_{ys}}\right)\right| - 1 = 0, \\ \left|(\sqrt{2}+2)\frac{\tau_{12}}{r\sigma_{ys}}\right| - 1 = 0 \end{bmatrix} = 0, \tag{A.2}
$$

where r is the relative density of the SI-square lattice, that is, $r = (2 + \sqrt{2})t/l$.

Exploiting the method introduced in Section 2, the initial and ultimate yield equations of the N-Kagome cell are respectively obtained as follows:

$$
\max \begin{bmatrix} \left|-\frac{\sqrt{3}}{3}\frac{\sigma_1}{r\sigma_{ys}} + \frac{6+\sqrt{3}}{3}\frac{\sigma_2}{r\sigma_{ys}} - 2(1+\sqrt{3})\frac{\tau_{12}}{r\sigma_{ys}}\right| - 1 \\ \left|-\frac{\sqrt{3}}{3}\frac{\sigma_1}{r\sigma_{ys}} + \frac{6+\sqrt{3}}{3}\frac{\sigma_2}{r\sigma_{ys}} + 2(1+\sqrt{3})\frac{\tau_{12}}{r\sigma_{ys}}\right| - 1 \\ \left|\frac{9+2\sqrt{3}}{3}\frac{\sigma_1}{r\sigma_{ys}} - \frac{3+2\sqrt{3}}{3}\frac{\sigma_2}{r\sigma_{ys}}\right| - 1 \end{bmatrix} = 0, \tag{A.3}
$$

$$
\max \begin{bmatrix} \left|2\frac{\sigma_2}{r\sigma_{ys}} - 2\sqrt{3}\frac{\tau_{12}}{r\sigma_{ys}}\right| - 1 \\ \left|2\frac{\sigma_2}{r\sigma_{ys}} + 2\sqrt{3}\frac{\tau_{12}}{r\sigma_{ys}}\right| - 1 \\ 2(\sqrt{3}+1)\left|\frac{\tau_{12}}{r\sigma_{ys}}\right| - 1 \\ \left|-3\frac{\sigma_1}{r\sigma_{ys}} + \frac{\sigma_2}{r\sigma_{ys}}\right| - 1 \\ \frac{\sqrt{3}+1}{2}\left|\sqrt{3}\left(-\frac{\sigma_1}{r\sigma_{ys}} + \frac{\sigma_2}{r\sigma_{ys}}\right) - 2\frac{\tau_{12}}{r\sigma_{ys}}\right| - 1 \\ \frac{\sqrt{3}+1}{2}\left|\sqrt{3}\left(-\frac{\sigma_1}{r\sigma_{ys}} + \frac{\sigma_2}{r\sigma_{ys}}\right) + 2\frac{\tau_{12}}{r\sigma_{ys}}\right| - 1 \end{bmatrix} = 0, \tag{A.4}
$$

where the relative density of the N-Kagome cell is $r = (\sqrt{3} + 1)\frac{t}{l}$.

References

[Ashby et al. 2000] M. F. Ashby, A. G. Evans, N. A. Fleck, L. J. Gibson, J. W. Hutchinson, and H. N. G. Wadley, *Metal foams: a design guide*, Butterworth Heinemann, Boston, 2000.

[Chen et al. 1999] C. Chen, T. J. Lu, and N. A. Fleck, "Effect of imperfections on the yielding of two-dimensional foams", *J. Mech. Phys. Solids* **47** (1999), 2235–2272.

[Deshpande and Fleck 2000] V. S. Deshpande and N. A. Fleck, "Isotropic constitutive models for metallic foams", *J. Mech. Phys. Solids* **48** (2000), 1253–1283.

[Deshpande et al. 2001] V. S. Deshpande, M. F. Ashby, and N. A. Fleck, "Foam topology bending versus stretching dominated architectures", *Acta Mater.* **49** (2001), 1035–1040.

[Doyoyo and Mohr 2003] M. Doyoyo and D. Mohr, "Microstructural response of aluminum honeycomb to combined out-of-plane loading", *Mech. Mater.* **35** (2003), 865–876.

[Doyoyo and Wierzbicki 2003] M. Doyoyo and T. Wierzbicki, "Experimental studies on the yield behavior of ductile and brittle aluminum foams", *Int. J. Plast.* **19** (2003), 1195–1214.

[Evans et al. 2001] A. G. Evans, J. W. Hutchinson, N. A. Fleck, M. F. Ashby, and H. N. G. Wadley, "The topological design of multifunctional cellular metals", *Prog. Mater. Sci.* **46** (2001), 309–327.

[Fazekas et al. 2002] A. Fazekas, R. Dendievel, L. Salvo, and Y. Brechet, "Effect of microstructural topology upon the stiffness and strength of 2D cellular structures", *Int. J. Mech. Sci.* **44** (2002), 2047–2066.

[Fleck and Qiu 2007] N. A. Fleck and X. M. Qiu, "The damage tolerance of elastic-brittle, two-dimensional isotropic lattices", *J. Mech. Phys. Solids* **55** (2007), 562–588.

[Gibson and Ashby 1997] L. J. Gibson and M. F. Ashby, *Cellular solids: structure and properties*, 2nd Edition ed., Cambridge Uni. Press, Cambridge, 1997.

[Hayes et al. 2004] A. M. Hayes, A. Wang, B. M. Dempsey, and D. L. McDowell, "Mechanics of linear cellular alloys", *Mech. Mater.* **36** (2004), 691–713.

[Hutchinson and Xue 2005] J. W. Hutchinson and Z. Xue, "Metal sandwich plates optimized for pressure impulses", *Int. J. Mech. Sci.* **47** (2005), 545–569.

[Mohr 2005] D. Mohr, "Mechanism-based multi-surface plasticity model for ideal truss lattice materials", *Int. J. Solids Struct.* **42** (2005), 3235–3260.

[Smith et al. 2001] H. B. Smith, J. W. Hutchinson, and A. G. Evans, "Measurement and analysis of the structural performance of cellular mental sandwich construction", *Int. J. Mech. Sci.* **43** (2001), 1945–1963.

[Vaziri and Xue 2007] A. Vaziri and Z. Xue, "Mechanical behavior and constitutive modeling of metal cores", *J. Mech. Mater. Struct.* **2** (2007), 1743–1760.

[Wang and McDowell 2004] A. J. Wang and D. L. McDowell, "In-plane stiffness and yield strength of periodic metal honeycombs", *J. Eng. Mater. Technol. (Trans. ASME)* **126** (2004), 137–156.

[Wang and McDowell 2005] A. J. Wang and D. L. McDowell, "Yield surfaces of various periodic metal honeycombs at intermediate relative density", *Int. J. Plast.* **21** (2005), 285–320.

[Xue and Hutchinson 2003] Z. Xue and J. W. Hutchinson, "Preliminary assessment of sandwich plates subject to blast loads", *Int. J. Mech. Sci.* **45** (2003), 687–705.

[Xue and Hutchinson 2004] Z. Xue and J. W. Hutchinson, "A comparative study of impulse-resistant metal sandwich plates", *Int. J. Impact Eng.* **30** (2004), 1283–1305.

[Xue and Hutchinson 2006] Z. Xue and J. W. Hutchinson, "Crush dynamics of square honeycomb sandwich cores", *Int. J. Numer. Methods Eng.* **65** (2006), 2221–2245.

[Xue et al. 2005] Z. Xue, A. Vaziri, and J. W. Hutchinson, "Non-uniform hardening constitutive model for compressible orthotropic materials with application to sandwich plate cores", *Comput. Model. Eng. Sci.* **10** (2005), 79–95.

[Zhang et al. 2008] Y. H. Zhang, X. M. Qiu, and D. N. Fang, "Mechanical properties of two novel planar lattice structures", *Int. J. Solids Struct.* **45** (2008), 3751–3768.

YIHUI ZHANG: zhang-yh06@mails.tsinghua.edu.cn
Department of Engineering Mechanics FML, Tsinghua University, Beijing, 100084, China

ZHENYU XUE: xue@seas.harvard.edu
Department of Engineering Mechanics FML, Tsinghua University, Beijing, 100084, China

XINMING QIU: qxm@mail.tsinghua.edu.cn
Department of Engineering Mechanics FML, Tsinghua University, Beijing, 100084, China

DAINING FANG: fangdn@mail.tsinghua.edu.cn
Department of Engineering Mechanics FML, Tsinghua University, Beijing, 100084, China

NUMERICAL CHARACTERIZATION OF MATERIAL ELASTIC PROPERTIES FOR RANDOM FIBER COMPOSITES

LUCIAN IORGA, YI PAN AND ASSIMINA PELEGRI

This paper presents a numerical investigation of the material elastic properties for short-length mostly in-plane random fiber composites, based on microscale geometrical modeling. The particular case considered is that of materials in which the majority of fibers' orientations are contained or slightly deviate from a dominant plane. Representative volume elements for two types of random fiber composite material geometries with different fiber aspect ratios and volume fractions are generated using a novel technique. The elastic properties of the equivalent homogeneous material are determined using direct three-dimensional finite element analysis. A windowing-type analysis is employed to investigate the influence of the fiber distribution homogeneity on the homogenized elastic properties. The results are compared and validated using two alternative approaches — first, by orientation averaging of the stiffness tensor of the equivalent unidirectional composite determined by direct FEM analysis and, second, by employing the laminated random strand method.

1. Introduction

With the maturing of the preforming technologies, random fiber composites have received increased attention in recent years as potential replacements for traditional structural materials, especially steel, given the significant weight savings they offer. Already, such materials, particularly chopped glass fiber composites, have been adopted in the automotive industry for manufacturing nonstructural components [Dahl et al. 2005], and a significant effort is under way towards the utilization of carbon reinforced random composites, which offer weight savings of 50–70% relative to steel.

The utilization of such novel materials for safety critical applications requires, first, reliable estimates of the overall material properties following a homogenization process that allows for efficient analysis of large scale structures and, second, good predictions of the microlevel properties for predefined macroscale loadings.

The traditional approach in composite continuum micromechanics analysis is to employ a mean field model which, for the case of random fiber composites can be used together with an orientation averaging procedure to account for the fiber orientation randomness. Mean field models allow the estimation of material properties based on Eshelby's field solution for single ellipsoidal inclusions in an infinite medium (matrix) [Eshelby 1957]. Despite their approximate nature, given the specific assumptions, such methods offer the advantage of analytical or semianalytical results which require only a reduced

computational effort. The extension to the family of effective field methods based on the original work by Mori and Tanaka [1973] has enjoyed substantial interest, particularly following the clarifications offered by Benveniste [1987]. The Mori–Tanaka approach is based on the fundamental assumption that within a concentrated composite with many identical inclusions, that is, fibers, each inclusion experiences a far-field strain equal to the average matrix strain. This allows the determination of the Mori–Tanaka strain concentration tensor as a function of the Eshelby's strain concentration tensor obtained for the dilute case.

A substantially different approach consists in evaluating highly resolved fields for specific micro-geometries representing the analyzed material. A volume element has to be generated and must be sufficiently large to statistically represent the material and completely characterized in the microgeometry sense. The microlevel stress and strain fields due to a macroscopic loading are resolved using numerical analysis, for example, using an FEM approach.

For the case of mostly in-plane oriented random fiber composites, only relatively few studies based on direct numerical analysis can be documented in the literature [Gusev et al. 2002; Duschlbauer et al. 2006]. In this study we propose to investigate the elastic properties of two composite materials consisting of an epoxy matrix reinforced by short glass fibers. First, we investigate the corresponding representative volume elements via a homogenization scheme based on the direct three-dimensional FEM solution of the stress and strain fields. Second, we investigate the material homogeneity for relatively large structures, meaning at the macroscopic scale, in order to evaluate the applicability of the representative volume element (RVE) based homogenized model.

2. Microscale geometry generation

The microscale geometry generation algorithm used in this work is essentially a random sequential ad-sorption (RSA) technique, widely used in the literature for studies of particle reinforced composites. Various particle shapes have been considered for this type of geometry generation, including spherical or spherocylindrical particles [Coelho et al. 1997; Williams and Philipse 2003] or cylindrical rods [Williams and Philipse 2003; Duschlbauer et al. 2006; Kari et al. 2007; Pan et al. 2007]. The specific algorithm's application and implementation on random chopped fiber composites are described in detail elsewhere [Pan et al. 2007] and we will only briefly outline it here, for the sake of completeness.

The RSA technique for generating a RVE geometry implies iteratively adding cylinders in the pre-scribed rectangular parallelepiped volume occupied by the RVE. In the current approximation, each cylinder represents the volume occupied by one fiber bundle. The center point $C(x)$, the in-plane orientation angle ϕ, and the out-of-plane orientation angle θ (see Figure 1) of each newly generated cylinder are chosen randomly. The orientation angle selection can be done with a probability defined by a fiber orientation distribution function, $f(\phi, \theta)$. Following the definition of a new cylinder, an intersection test, based on the algorithm presented by Eberly [2001], is carried out to determine any possible intersections with the cylinders previously accepted in the configuration. No intersection between two cylinders is accepted, with the minimum distance between cylinders being set to 5% of the cylinder radius, to avoid both the generation of excessively steep stress gradients and meshing difficulties. An investigation of the influence of the minimum distance on the local stress fields is detailed in [Pan et al. 2007].
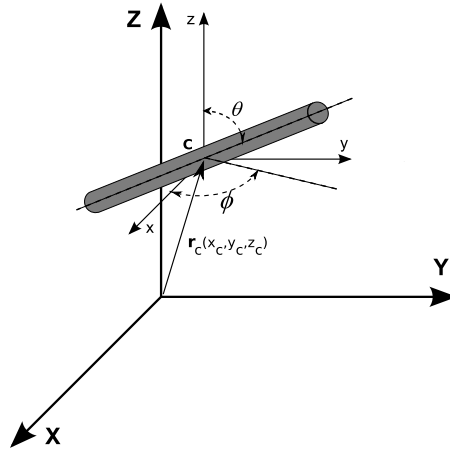
Figure 1. Fiber bundle location and orientation definition.

A provision is made in the current algorithm for the generation of periodic RVE geometries, that is, fiber arrangements that ensure material continuity across the boundaries when multiple RVEs are aggregated for the generation of a macrostructure. Specifically, when a newly generated cylinder intersects the boundaries of the RVE parallelepiped, a *clone* cylinder with the same orientation angles ϕ and θ is created on the opposite side of the parallelepiped in order to ensure geometry periodicity. This amounts to the inclusion of the volume of a full cylinder but doubles the number of intersection checks required. The flowchart of the RSA is shown in Figure 2.

Figure 2. Random sequential adsorption flowchart.

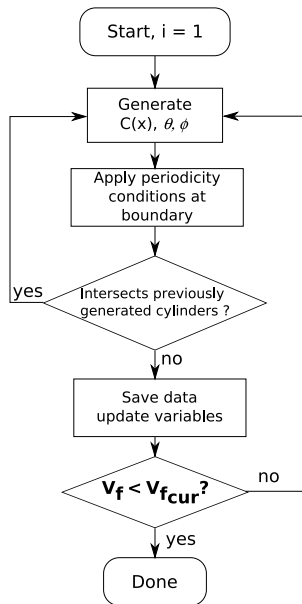We consider in this study two random glass-fiber material configurations and the associated micro-geometries, with predominantly in-plane fiber distributions. The configurations qualitatively represent a composite panel manufactured using the programmable powdered preform process. As such, no fiber intersections are accepted with the upper and lower parallelepiped surfaces, which correspond to the panel surfaces. However we do not account for variations in fiber length, fiber contact and fiber agglomerations observed to occur in practice, which help significantly increase the maximum achievable fiber volume fraction up to 35%–40%.

The first configuration is that of a short fiber composite with fiber aspect ratio $AR = 10$ and fiber volume fraction of $v_f = 15\%$. Geometry periodicity conditions are enforced and the out-of-plane fiber orientation angle is limited to $\pm 10°$ ($\theta \in [80°, 100°]$), while the in-plane angle ϕ is selected with uniform probability in the full-circle interval, $\phi \in [0°, 360°]$, per fabrication restrictions. The second geometry configuration considers fibers with aspect ratio $AR = 20$ and fiber volume fraction $v_f = 20\%$ but with the out-of-plane orientation angle limited to $\pm 5°$ ($\theta \in [85°, 95°]$), while uniform probability in-plane orientation is maintained.

The RVEs generated using the RSA technique will be named, for the remainder of the paper, RVE1 and RVE2, for the first ($v_f = 15\%$) and the second ($v_f = 20\%$) configuration respectively. They are defined using 124 and 227 cylinders, respectively, contained in cuboids of dimensions $3.00 \times 3.00 \times 0.60$ and $2.00 \times 2.00 \times 0.40$, where the dimensions are normalized to the fiber length. The cylinder arrangements are shown in Figure 3.

The statistics of the fiber orientation for the two RVEs are presented in terms of the probability density distribution of the orientation angles ϕ and θ. Figure 4 shows the RVE1 cylinder probability distributions for the in-plane orientation angle ϕ in 5° intervals and for the out-of-plane orientation angle θ in intervals of 2°. The corresponding results for RVE2 are shown in Figure 5, where the probability distribution for θ is given in 1° intervals. We note that a certain tendency towards fiber aggregation on preferred orientations can be noticed for both RVEs, being more evident in the case of RVE2. This can be explained through the natural tendency towards fiber aggregation in high fiber volume fraction composites and is a phenomenon also noticed in other studies such as [Duschlbauer et al. 2006]. However, we note that the imposition of the geometry periodicity requirements in the RSA generation algorithm usually tends to exacerbate this tendency.
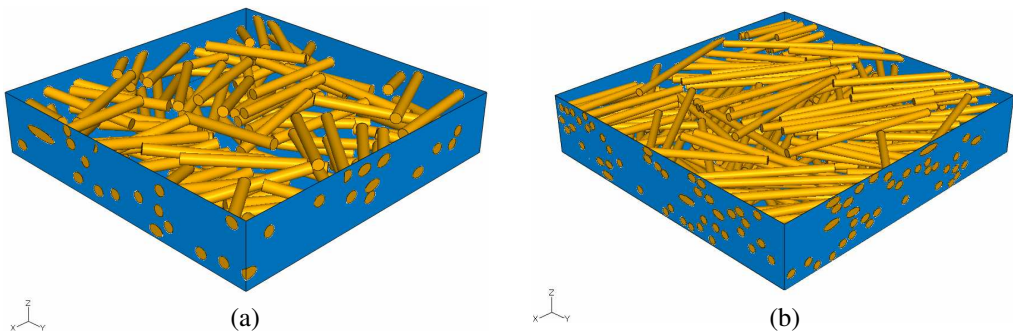

Figure 3. RVE microscale geometries for (a) RVE1 ($v_f = 15\%$, $AR = 10$) and (b) RVE2 ($v_f = 20\%$, $AR = 20$).
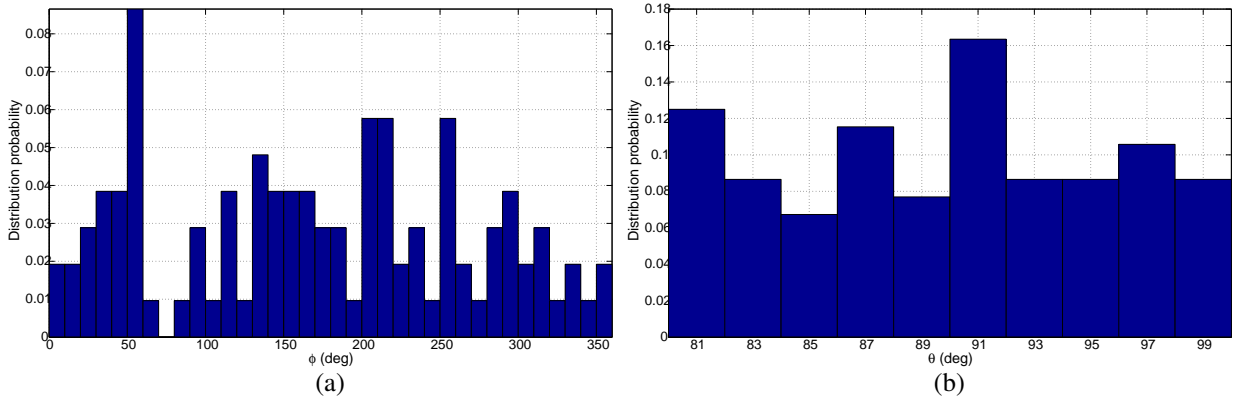
Figure 4. RVE 1: Cylinder orientation distribution (a) in-plane angle ϕ and (b) out-of-plane angle θ.

The two material models considered in this paper will be analyzed using the two generated RVEs and following the approach outlined in the next section.

3. Homogenization scheme

Homogenization approach. The basics of the homogenization procedure are briefly reviewed. In order to determine the properties of an equivalent homogeneous medium that accurately represents, at the macroscopic level (that is, the RVE volume, in this study), the response of the microscopically heterogeneous one, we consider the equivalent macro stress and strain, $\overline{\sigma}$ and $\overline{\epsilon}$, defined as the mean values of the respective fields in the RVE [Sun 2006],

$$\overline{\sigma}_{ij} = \frac{1}{V} \int_V \sigma_{ij}(\boldsymbol{x}) \, dV, \qquad \overline{\epsilon}_{ij} = \frac{1}{V} \int_V \epsilon_{ij}(\boldsymbol{x}) \, dV, \qquad i, j = 1, 2, 3, \quad \boldsymbol{x} \in V. \tag{1}$$
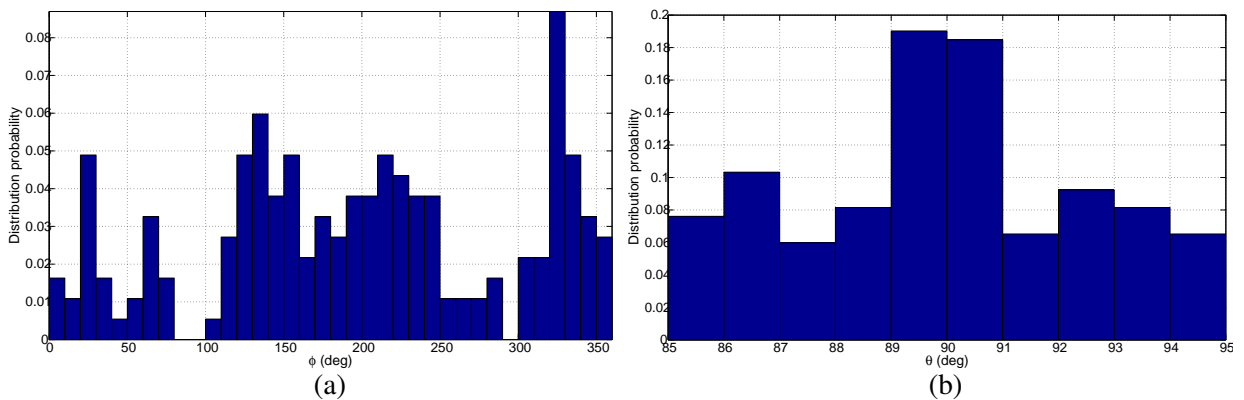

Figure 5. RVE 2: Cylinder orientation distribution (a) in-plane angle ϕ and (b) out-of-plane angle θ.

The effective elastic constants of the homogeneous material can then be defined by the linear constitutive equation,

$$\overline{\sigma}_{ij} = \overline{C}_{ijkl}\overline{\epsilon}_{kl}. \tag{2}$$

We note that the equivalence of the strain energy between the random composite material and the homogeneous one is ensured through the Hill condition [Hill 1971],

$$\frac{1}{2V}\int_V \sigma_{ij}\epsilon_{ij}\, dV = \frac{1}{2}\overline{\sigma}_{ij}\overline{\epsilon}_{ij}.$$

Boundary conditions. The components of the stiffness tensor of the equivalent homogeneous material, $\overline{C}_{ijkl}$, can be completely determined by solving the state equilibrium solution for six independent loading cases. To this end, we employ kinematic boundary conditions [Sanchez-Palencia and Zaoui 1985; Kanit et al. 2006] that correspond to three pure axial and three pure shear deformations of the RVE. The boundary conditions are specified by imposing a displacement $\boldsymbol{u}$ at a point $\boldsymbol{x}$ on the boundary ∂V, such that $u_i = \epsilon_{ij}^0 x_j$, $\forall \boldsymbol{x} \in \partial V$, where the second order tensor ϵ^0 is independent of $\boldsymbol{x}$ and represents, in effect, a uniformly applied strain. The six loading cases considered here correspond to specifying the nonzero elements of ϵ^0 as follows: $\epsilon_{11}^0 = 10^{-5}$, $\epsilon_{22}^0 = 10^{-5}$, $\epsilon_{33}^0 = 10^{-5}$, $\epsilon_{12}^0 = 10^{-5}$, $\epsilon_{13}^0 = 10^{-5}$ and $\epsilon_{23}^0 = 10^{-5}$.

We note here that kinematic uniform boundary conditions lead to upper estimates of the stiffness tensors [Hazanov and Huet 1994]. It must also be noted that although the boundary conditions imposed in this study are of the uniform strain type, the rationale for the generation of periodic geometries is to provide the means for a future comparison of the numerical results obtained through the imposition of periodic and homogeneous boundary conditions.

Following the simulation of the material response under the load due to the above values of the uniform strain, the average stress and strain in the RVE can be computed using Equation (1). Thus, the use of (2) for each of the loading cases will yield the system of 36 equations from which the values of the stiffness tensor C can be readily determined. The symmetry requirements for the stiffness tensor, which effectively reduce the number of unknowns to 21, are used solely to verify the correctness of the numerical results.

An alternative approach is to directly estimate the average stress in the RVE via an elementary mechanics of materials definition of stress,

$$\overline{\sigma}_{ij} = F_i^j / A, \tag{3}$$

where F_i^j is the i-direction component of the reaction force on the boundary face of area A, which develops in the loading case j (for shear-loading cases $j = 4, 5, 6$, the force is tangential to the face A). Despite its simplicity this approach yields results of comparable accuracy to the actual application of (1), while proving to be significantly faster. The practical aspects of direct FEM implementation and alternative solution approaches employed for validating the direct numerical simulation results are discussed next.

4. RVE numerical simulations

The modeling approach towards solving the six static problems corresponding to the loading cases required for the determination of tensor $\overline{C}$, as well as the alternative approaches used for comparison of

results, namely an orientation averaging approach and the laminated random strand (LRS) method are discussed next.

For the purpose of this work, the fiber and matrix materials for the two composite configurations are considered as E-glass and epoxy, respectively. No particular production composite is analyzed, but the procedure and results are considered to be representative for the material design and selection phase. For E-glass, the Young's modulus and Poisson ratio values used are $E_f = 70\,\text{GPa}$ and $\nu_f = 0.2$, while for the matrix material, $E_m = 3\,\text{GPa}$ and $\nu_m = 0.35$. Furthermore, the E-glass fibers and matrix are isotropic.

4.1. *Finite element modeling.* A three-dimensional solid model is built in the commercial FEA package ABAQUS (version 6.7) by importing the fiber positions and orientation angles. The RVEs are meshed with linear C3D4 4-node tetrahedral elements, with total node counts of approximately 250,000 for RVE1 and 750,000 for RVE2. Node sharing at the fiber-matrix interface is ensured by modeling the RVE as a single part solid. The FEA discretization is restricted primarily by the memory limitations on the available computers. The evaluation of the average stress and strain in the RVEs (see Equation (1)) can be performed approximately using the ABAQUS feature of returning the value of the volume associated with the element integration node. Thus, volume integration of functions can be performed by summing the function values at the integration points, multiplied by the respective elemental volumes. The application of Equation (3) is carried out directly by summation of the nodal reaction forces on the boundary surfaces.

4.2. *Validation approaches.* In order to validate the three-dimensional FEM analysis, two alternative approaches are considered. First, we rely on the orientation averaging scheme of Advani and Tucker [1987] to determine the elastic constants of the random composite based on those of the equivalent material with fully aligned fibers. Second, we employ the LRS method recently proposed by Ionita and Weitsman [2006] as a way of rapidly evaluating the properties of large numbers of fiber arrangements.

Orientation averaging. This approach was validated by Gusev et al. [2002] by an analysis of composites with 15% fiber volume fraction, for different orientation states, which led to the conclusion that orientation averaging offers good engineering predictions. We follow here a similar approach, first constructing RVEs with perfectly aligned, but randomly positioned, cylindrical fibers, and determining by direct FEM analysis their respective stiffness tensor. Next, orientation averaging is performed to obtain an estimate of the equivalent composite with randomly oriented fibers. We will briefly present here the basic concepts of the method.

The orientation of a fiber is fully described by the direction unit vector $\boldsymbol{p}$, that is

$$p_1 = \sin(\theta)\cos(\phi) \qquad p_2 = \sin(\theta)\sin(\phi) \qquad p_3 = \cos(\theta),$$

while the orientation of a whole set of fibers is defined by an infinite series of orientation tensors, $\boldsymbol{a}$. Since the fiber orientation is periodic, meaning a fiber oriented at angles (ϕ, θ) is indistinguishable from one with angles $(\phi + \pi, \pi - \theta)$, due to symmetry considerations, only the even second and fourth order

tensors $\boldsymbol{a}_2$, $\boldsymbol{a}_4$ are relevant. These are defined as

$$a_{ij} = \langle p_i p_j \rangle = \int_0^{2\pi} \int_0^\pi p_i p_j \psi(\phi, \theta) \sin(\theta) \, d\theta d\phi,$$

$$a_{ijkl} = \langle p_i p_j p_k p_l \rangle = \int_0^{2\pi} \int_0^\pi p_i p_j p_k p_l \psi(\phi, \theta) \sin(\theta) \, d\theta d\phi,$$

where $\psi(\phi, \theta)$ is the probability distribution function characterizing the fiber orientations in the composite. For the cases of mostly in-plane fiber orientations considered in this work, the probability distribution function $\psi(\phi, \theta)$ can be written as

$$\psi(\phi, \theta) = \frac{1}{n} \big[H(\theta - \theta_1) - H(\theta - \theta_2) \big],$$

where $H(\theta)$ denotes the Heaviside step-function and θ_1 and θ_2 are the limits of the interval of variation for the out-of-plane angle θ, that is, $\theta_1 = 80°$, $\theta_2 = 100°$ and $\theta_1 = 85°$, $\theta_2 = 95°$ for RVE1 and RVE2, respectively. The scalar n is a scaling factor such that

$$\int_0^{2\pi} \int_0^\pi \psi(\phi, \theta) \sin(\theta) \, d\theta d\phi = 1.$$

As mentioned, due to symmetry considerations, the orientation averaged stiffness tensor $\overline{\boldsymbol{C}}'$ can be completely determined only in terms of the tensors $\boldsymbol{a}_2$ and $\boldsymbol{a}_4$ and the five elastic constants B corresponding to the stiffness tensor of the aligned composite

$$\overline{C}'_{ijkl} = B_1 a_{ijkl} + B_2(a_{ij}\delta_{kl} + a_{kl}\delta_{ij}) + B_3(a_{ik}\delta_{jl} + a_{il}\delta_{jk} + a_{jk}\delta_{il} + a_{jl}\delta_{ik}) + B_4\delta_{ij}\delta_{kl} + B_5(\delta_{ik}\delta_{jl} + \delta_{il}\delta_{jk}),$$

where δ_{ij} denotes the Kronecker delta function and the constants B are given by:

$$B_1 = C_{1111} + C_{2222} - 2C_{1122} - 4C_{1212}, \qquad B_2 = C_{1122} - C_{2233},$$

$$B_3 = C_{1212} + \tfrac{1}{2}(C_{2233} - C_{2222}), \qquad B_4 = C_{2233},$$

$$B_5 = \tfrac{1}{2}(C_{2222} - C_{2233}).$$

Unidirectional composite analysis. Two alternate unidirectional RVEs, namely RVE1 and RVE2, are generated using the RSA procedure, with constraints $\phi = 0°$ and $\theta = 90°$. RVE1a, which corresponds to the composite configuration with fiber aspect ratio $AR = 10$ and volume fraction $v_f = 15.13\%$, is composed of 128 cylinders enclosed in a cuboid of dimensions $3l_f \times 3l_f \times 0.6l_f$, where l_f is the fiber length. Similarly, for the configuration with fiber aspect ratio $AR = 20$ and volume fraction $v_f = 20\%$, RVE2a has dimensions $1.5l_f \times 1.5l_f \times 0.4l_f$ and includes a total of 132 cylinders. For both RVE1a and RVE2a, a geometry periodicity requirement was imposed on the parallelepiped faces normal to the fiber directions. As in the aforementioned random orientation cases, both RVEs are meshed using 4-node tetrahedron elements, with mesh densities similar to those used for RVE1 and RVE2.

The laminated random strand method. The laminated random strand (LRS) method was recently proposed by Ionita and Weitsman [2006] as an alternative, approximate, approach that allows for the rapid evaluation of a large number of fiber arrangements in a mostly in-plane random fiber orientation. Based

on the composite laminate theory, and approximating the geometry as a series of pseudolayers of randomly oriented strands, the method does not account explicitly for out-of-plane fiber orientations or for strand overlaps. However, it does account for the strand stiffness reduction due to *kinks* at contact points, by statistically determining the average number of contact points and kink size and considering the corresponding average strand stiffness reduction.

The LRS method is, essentially, a windowing-type method. Windowing methods seek to determine lower and upper property estimates as well as bounds through varying the analysis window size [Jiang et al. 2001]. In the LRS method, a rectangular window of size L is selected and in each pseudolayer, N strands are considered such that $\sum_{i=1}^{N} A_i = L^2$, where $A_i = l_i w_i$ is the area covered by the i-th strand in the sampling window, of width w_i and length l_i. Since the elastic properties of the strand, Q_{ij}, as well as the orientation of each strand are known, the transformed properties $\overline{Q}_{ij}$ can be computed in the reference system attached to the sample window. The contribution of each strand stiffness to the total stiffness of the layer in which it is contained is considered proportional to the area ratio $\mu_i = A_i/L^2$. This allows for immediate evaluation of the individual layer stiffnesses and, in turn, the total *random laminate* elastic properties can be readily estimated using the classical laminate theory.

The evaluation of strand elastic properties is done using the well-known Halpin–Tsai equations. Although initially derived for long-fiber composites, and semiempirical in nature, they are based, as pointed out by Hine et al. [2002] on the self-consistent ideas of Hill [1971]. In this work, the parameter ξ in the Halpin–Tsai equations was assigned the widely used value $\xi = 2$, which is known to correctly predict the transverse modulus, while slightly overestimating the Poisson ratio [Hine et al. 2002].

In the present study, a number of 4 pseudolayers was considered for the case of the $v_f = 15.13\%$, $AR = 10$ composite, while 7 pseudolayers were considered for the $v_f = 20\%$, $AR = 20$ material. For the first material, the evaluation is performed for 50 different windows sizes chosen in the interval $[0.5l_f, 7.5l_f]$. The windows are chosen randomly from a $9l_f \times 9l_f \times 0.6l_f$ box, and 50 strand configurations are analyzed for each window size. Similarly, for the second material, sets of 50 strand configurations are analyzed for each of the 50 sampling windows considered for the second material. In this case, the sampling windows are selected randomly from a $9l_f \times 9l_f \times 0.4l_f$ box.

Numerical results. The static analyses corresponding for the loading cases and the homogenization procedure described in Section 3 are performed for RVE1 and RVE2. For RVE1 ($v_f = 15.13\%$, $AR = 10$), the direct three-dimensional numerical analysis yields the stiffness tensor (in contracted notation, in GPa)

$$\overline{C} = \begin{bmatrix} 7.95 & 3.59 & 3.20 & 0 & 0 & 0 \\ 3.59 & 7.41 & 3.16 & 0 & 0 & 0 \\ 3.20 & 3.16 & 5.93 & 0 & 0 & 0 \\ 0 & 0 & 0 & 1.55 & 0 & 0 \\ 0 & 0 & 0 & 0 & 1.55 & 0 \\ 0 & 0 & 0 & 0 & 0 & 2.14 \end{bmatrix}, \tag{4}$$

while for the unidirectional composite characterized by RVE1a,

$$C = \begin{bmatrix} 10.58 & 3.07 & 2.95 & 0 & 0 & 0 \\ 3.07 & 5.94 & 3.10 & 0 & 0 & 0 \\ 2.95 & 3.10 & 5.97 & 0 & 0 & 0 \\ 0 & 0 & 0 & 1.56 & 0 & 0 \\ 0 & 0 & 0 & 0 & 1.56 & 0 \\ 0 & 0 & 0 & 0 & 0 & 1.45 \end{bmatrix}, \tag{5}$$

which, after orientation averaging yields

$$\overline{C}' = \begin{bmatrix} 7.74 & 3.65 & 3.10 & 0 & 0 & 0 \\ 3.65 & 7.54 & 3.10 & 0 & 0 & 0 \\ 3.10 & 3.10 & 5.94 & 0 & 0 & 0 \\ 0 & 0 & 0 & 1.51 & 0 & 0 \\ 0 & 0 & 0 & 0 & 1.52 & 0 \\ 0 & 0 & 0 & 0 & 0 & 2.14 \end{bmatrix}. \tag{6}$$

We note that in Equations (4)–(6) the null entries correspond to nonzero numerical results. These are, however, three or four orders of magnitude lower than the nonzero ones and, for all practical reasons, can be taken as null. The relative error between the components of the stiffness tensor for the three-dimensional FEM simulation, (4), and the one obtained by orientation averaging, (6), are presented in Figure 6.

We note that the results obtained from RVE1, by direct three-dimensional FEM analysis, indicate that the material approaches a transversely isotropic one, with the axis of symmetry in the 3-direction, as expected. Transverse isotropy requires that $C_{11} = C_{22}$, $C_{44} = C_{55}$, and $C_{66} = (C_{11} - C_{12})/2$. Consequently, the following departures from transverse isotropy are computed,

$$2\frac{C_{11} - C_{22}}{C_{11} + C_{22}} = 0.7\%, \qquad 2\frac{C_{11} - C_{12} - 2C_{66}}{C_{11} - C_{12} + 2C_{66}} = 8.7\%,$$

$$C_{44} = C_{55}, \qquad 2\frac{C_{13} - C_{23}}{C_{13} + C_{23}} = 1\%,$$

and are considered small for all practical purposes.

For RVE2 ($v_f = 20\%$, $AR = 20$), the stiffness tensor results are

$$\overline{C} = \begin{bmatrix} 9.52 & 4.49 & 3.32 & 0 & 0 & 0 \\ 4.49 & 10.04 & 3.33 & 0 & 0 & 0 \\ 3.32 & 3.33 & 6.41 & 0 & 0 & 0 \\ 0 & 0 & 0 & 1.67 & 0 & 0 \\ 0 & 0 & 0 & 0 & 1.67 & 0 \\ 0 & 0 & 0 & 0 & 0 & 3.02 \end{bmatrix},$$
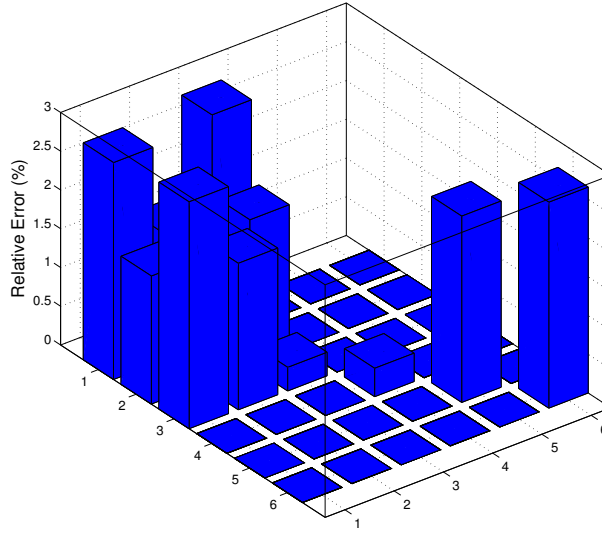
Figure 6. Relative error of stiffness tensor components: RVE1 three-dimensional simulation compared to orientation averaging, $\|\overline{C}_{ij} - \overline{C}'_{ij}\|/\overline{C}'_{ij}$.

while for RVE2a we obtain

$$C = \begin{bmatrix} 15.82 & 3.20 & 3.15 & 0 & 0 & 0 \\ 3.20 & 6.48 & 3.21 & 0 & 0 & 0 \\ 3.15 & 3.21 & 6.60 & 0 & 0 & 0 \\ 0 & 0 & 0 & 1.64 & 0 & 0 \\ 0 & 0 & 0 & 0 & 1.63 & 0 \\ 0 & 0 & 0 & 0 & 0 & 1.47 \end{bmatrix}.$$

The orientation averaged stiffness tensor, for the orientation state characterized by a_2 and a_4 is

$$\overline{C}' = \begin{bmatrix} 9.62 & 4.65 & 3.21 & 0 & 0 & 0 \\ 4.65 & 9.72 & 3.21 & 0 & 0 & 0 \\ 3.21 & 3.21 & 6.48 & 0 & 0 & 0 \\ 0 & 0 & 0 & 1.64 & 0 & 0 \\ 0 & 0 & 0 & 0 & 1.64 & 0 \\ 0 & 0 & 0 & 0 & 0 & 2.99 \end{bmatrix}.$$

The results of the departure from transverse isotropy tests,

$$2\frac{C_{11} - C_{22}}{C_{11} + C_{22}} = 5.34\%, \qquad 2\frac{\frac{1}{2}(C_{11} + C_{22}) - C_{12} - 2C_{66}}{\frac{1}{2}(C_{11} + C_{22}) - C_{12} + 2C_{66}} = 13.29\%,$$

$$C_{44} = C_{55}, \qquad\qquad\qquad C_{13} = C_{23},$$

display the significant effect of the preferred fiber orientations on the values of C_{11}, C_{22}, and C_{12}. Figure 7 shows the relative error between the components of the stiffness tensor for the two approaches considered.
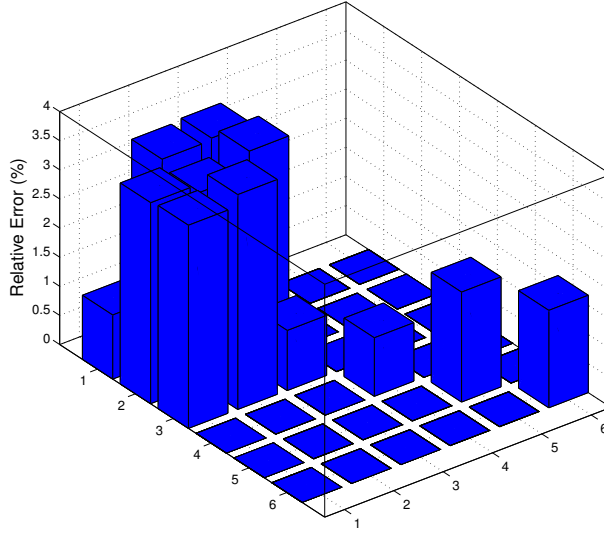
Figure 7. Relative error of stiffness tensor components: RVE2 three-dimensional simulation compared to orientation averaging, $\|\overline{C}_{ij} - \overline{C}'_{ij}\|/\overline{C}'_{ij}$.

5. Automated FEM analysis

With the solution of the RVE geometry and analysis procedure in place, we are interested in the material properties variations that occur locally in a large structure, due to the microscale inhomogeneities — particularly the variation of the fiber volume fraction, caused by fiber aggregation. Consequently, we generate the microgeometry for large panels for each of the materials considered in this study, glass/epoxy $AR = 10$ and $AR = 20$, and we employ a windowing-type analysis. For several sizes of the selected window, a parallelepiped is selected at a random location in the plate. The process is repeated 10 times for each window size and the three-dimensional FEM analysis described earlier is performed for each case. The process, including window selection, meshing and postprocessing of the results, is fully automated and is implemented in ABAQUS via the Python scripting interface. A flowchart of the whole process is illustrated in Figure 8. We note that due to the completely automated nature of the analysis meshing may fail in regions of high geometric complexity, which requires that the model is also automatically checked for complete meshing of all components, as well as for the existence of distorted elements, as shown by the *failed meshing* check block in Figure 8.

In order to analyze the transverse isotropy of the material we consider a measure similar to the one adopted by Ionita and Weitsman [2006]:

$$\Delta = \sqrt{\Delta_1^2 + \Delta_2^2},$$

where

$$\Delta_1 = \frac{2(C_{11} - C_{22})}{C_{11} + C_{22}} \quad \text{and} \quad \Delta_2 = \frac{2(C_{11} - C_{12} - 2C_{66})}{C_{11} + C_{22} + 2C_{66}}.$$
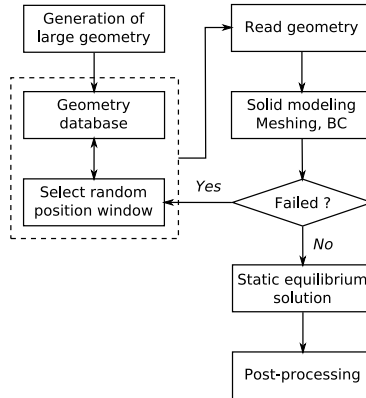
Figure 8. Flowchart of automated three-dimensional FEM windowing analysis.

We also propose a measure of statistical inhomogeneity in the material,

$$\Lambda = \frac{\|\boldsymbol{C}^M - \boldsymbol{C}^K\|}{\|\boldsymbol{C}\|},$$

where M and K, $M \neq K$, denote two nonidentical realizations of a window with the same size, and $\|\cdot\|$ is the matrix 2-norm of the tensor $\boldsymbol{C}$ computed by orientation averaging for an ideally random fiber distribution.

For the first material ($v_f = 15.13\%$), the windowing analysis is performed on a $9l_f \times 9l_f \times 0.6l_f$ box. A number of 20 window sizes L_w are considered in the interval $0.5l_f \leq L \leq 3l_f$ and 10 samples are selected for each value of L_w. The results for the Young's modulus and Poisson ratio are compared to those obtained from LRS in Figures 9 and 10. The departure from isotropy and the statistical inhomogeneity are shown in Figures 11 and 12. It can be noticed that the departure from isotropy becomes smaller with increasing window size, an effect also noticed by Ionita and Weitsman and is explained by the presence of a larger number of fibers in larger samples. An additional explanation lies in the increasing variations in fiber volume fractions, when reducing the sampling window size. This also justifies the larger average values of the Young's modulus for small values of L_w. We note that, while more consistent averages of E may be obtained by increasing the number of sampling windows, at the expense of increased computational time, the evolution of Δ and Λ indicates that, for the materials considered, the use of RVEs of dimensions up to approximately $1.5l_f$ may not be representative.

For the second case analyzed ($v_f = 20\%$), the initial box has dimensions $4l_f \times 4l_f \times 0.4l_f$, limited by the very slow convergence of the generation algorithm at high fiber volume fraction and large dimensions. An analysis similar to the previous one is performed for 10 random samples selected for 16 windows sizes in the interval $[0.5l_f, 2l_f]$. The results for the Young's modulus, Poisson ratio, as well as for the two statistical measures Δ and Λ are shown in Figures 13–16. We note that, unlike in this case of $AR = 10$, while the statistical inhomogeneity Λ reduces with increasing window size, this tendency is not as pronounced for the departure of isotropy Δ. We explain this as an effect of the much smaller domain from which the sampling windows are chosen, which in effect leads to an increased probability of repeatedly including much of the same material subdomains in different analysis windows. We expect

Figure 9. Comparison of predicted equivalent in-plane Young's modulus E versus windows size normalized to strand length, $v_f = 15.13\%$.

Figure 10. Comparison of predicted in-plane Poisson ratio v_{12} versus window size normalized to strand length, $v_f = 15.13\%$.

Figure 11. Departure from isotropy Δ versus window size normalized to strand length, $v_f = 15.13\%$.

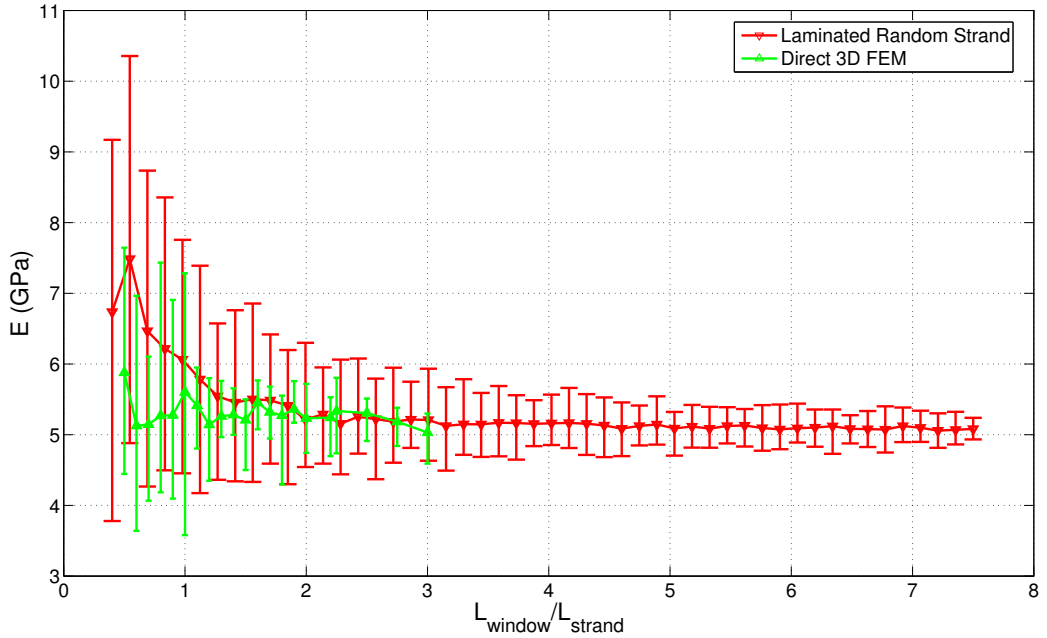**Figure 12.** Statistical inhomogeneity Λ versus window size normalized to strand length, $v_f = 15.13\%$.

Figure 13. Comparison of predicted equivalent in-plane Young's modulus E versus windows size normalized to strand length, $v_f = 20\%$.

that a steeper reduction can be observed if the dimensions of the initial box are increased, as well as following an increase in the number of samples for each window size. However, we believe the observed behavior of Δ underlines the significant variations in material property that can be observed at the local (micro) level. We also note that the results for the Poisson ratio show, for both LRS and FEM analysis, a remarkable independence with respect to the window size in an average sense. The higher average value in the case of the LRS is due primarily to the choice of the Halpin–Tsai parameter used in computing the strand stiffness.

6. Conclusions

We presented a micromechanical analysis for the determination of the elastic material properties for two types of composite materials with random cylindrical, mostly in-plane oriented short fibers. A random sequential adsorption algorithm was employed for the generation of the microscale geometries and a homogenization technique is employed to determine the equivalent macroscale material properties. The generated RVEs display a tendency towards fiber aggregation on preferred directions due to the geometry periodicity conditions imposed, an effect also noticed in other works. The primary effect is the deviation from the transverse isotropy expected in a composite with an ideally random fiber orientation state. While the RVEs are considered representative for all practical purposes, this emphasizes the difficulty of generating accurate random microscale geometries and the need for more sustained research in this field.
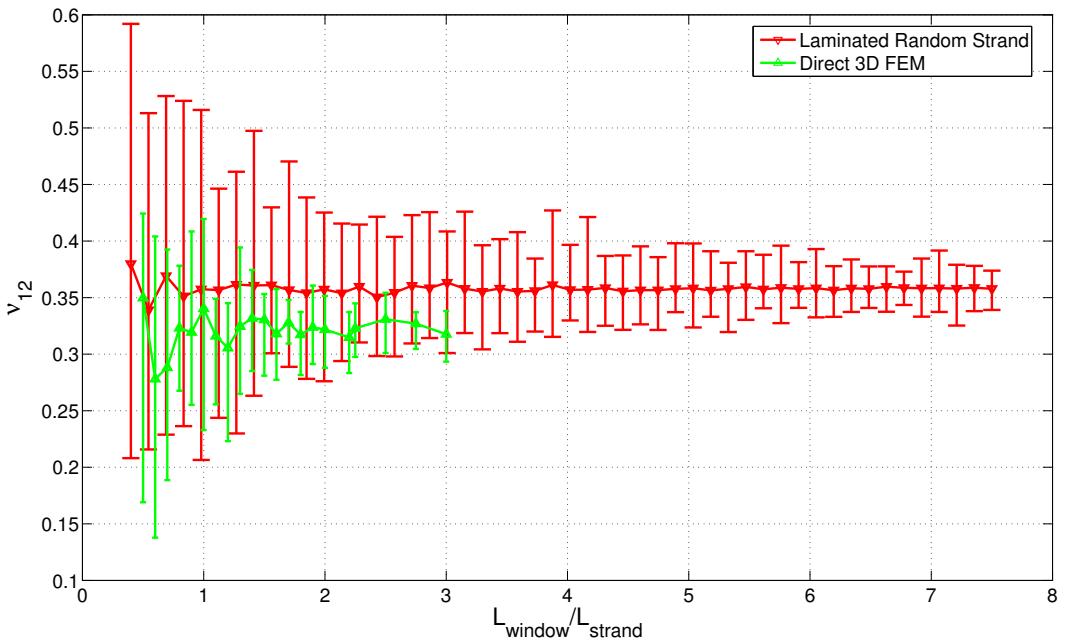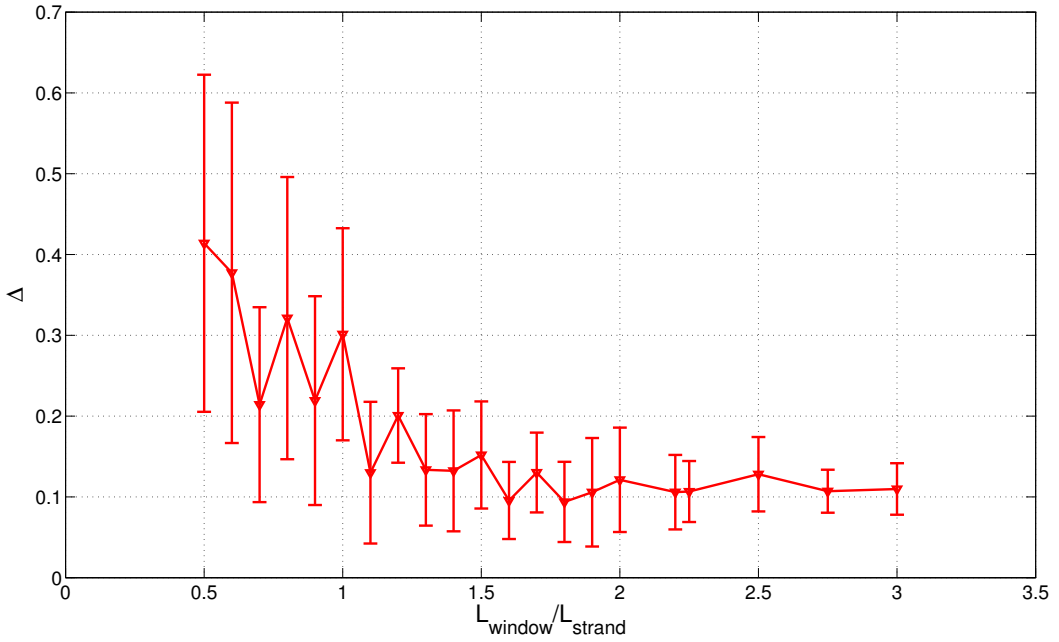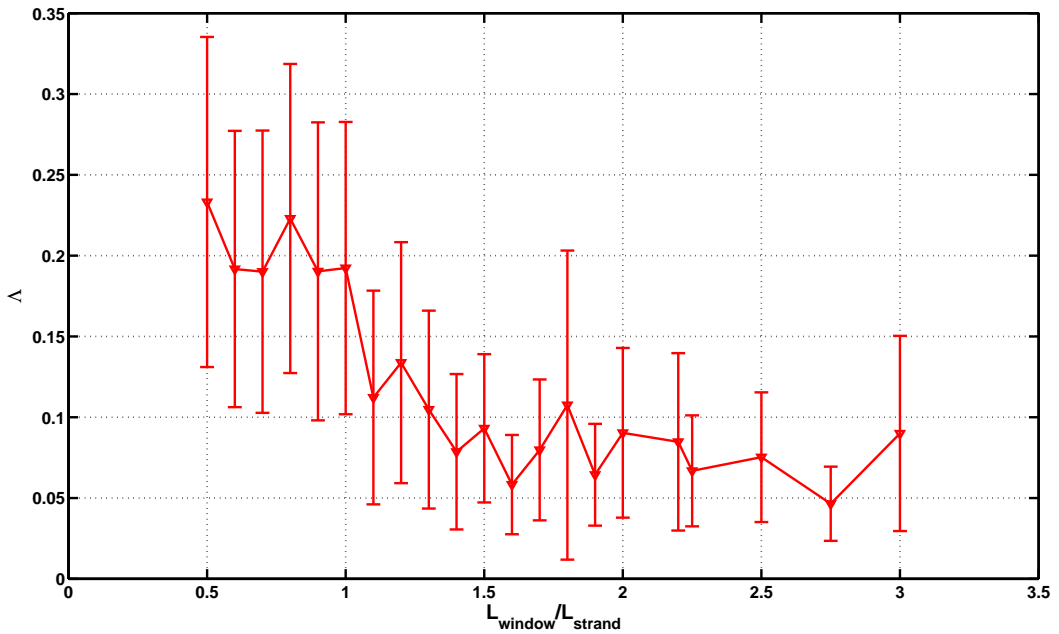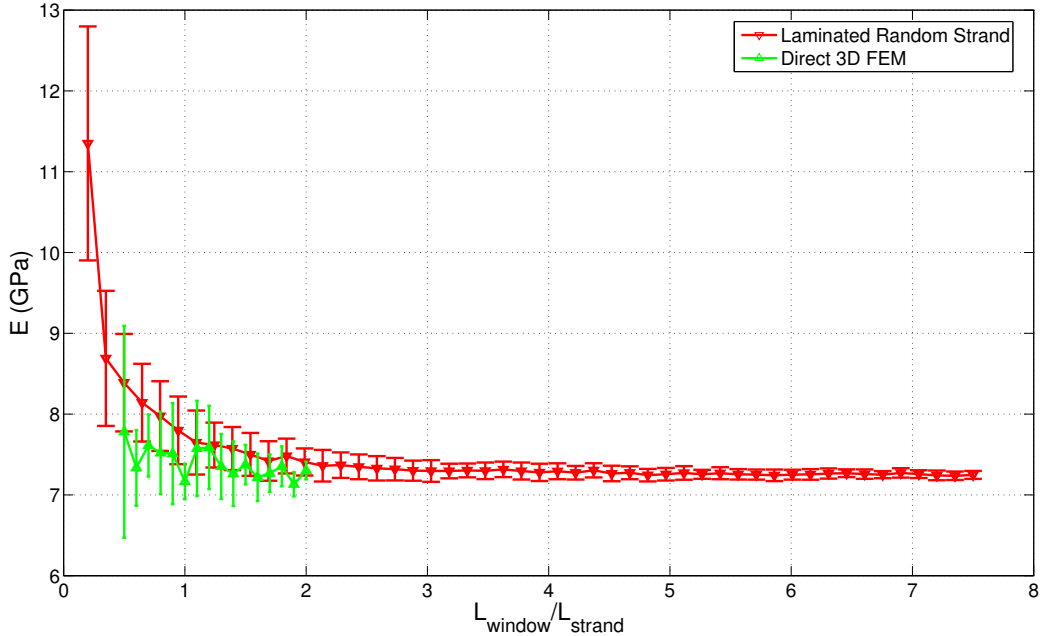
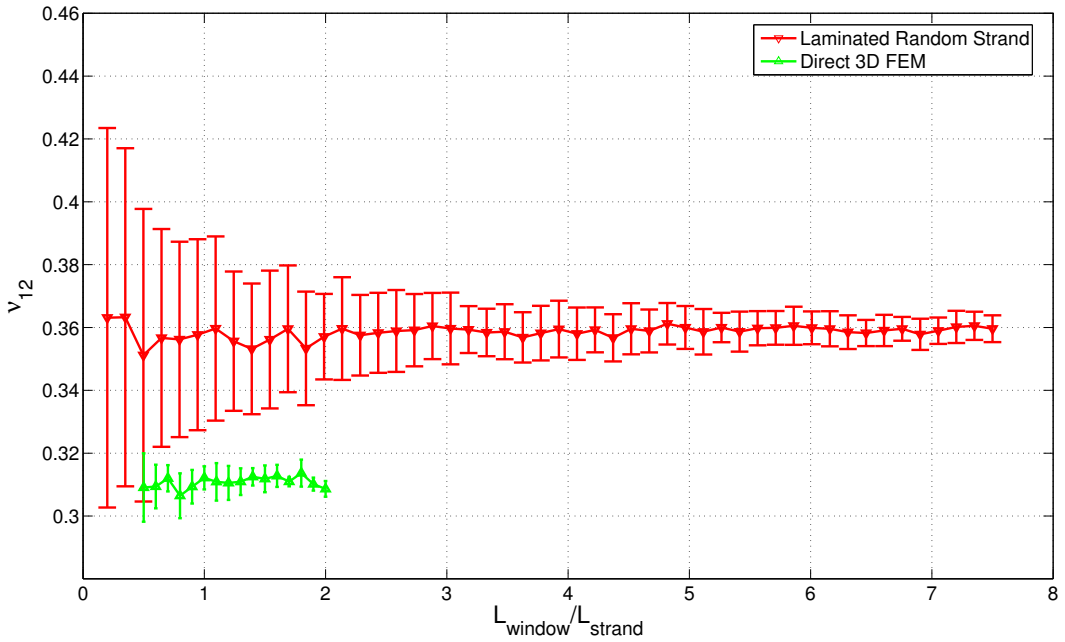**Figure 14.** Comparison of predicted in-plane Poisson ratio ν_{12} versus window size normalized to strand length, $v_f = 20\%$.
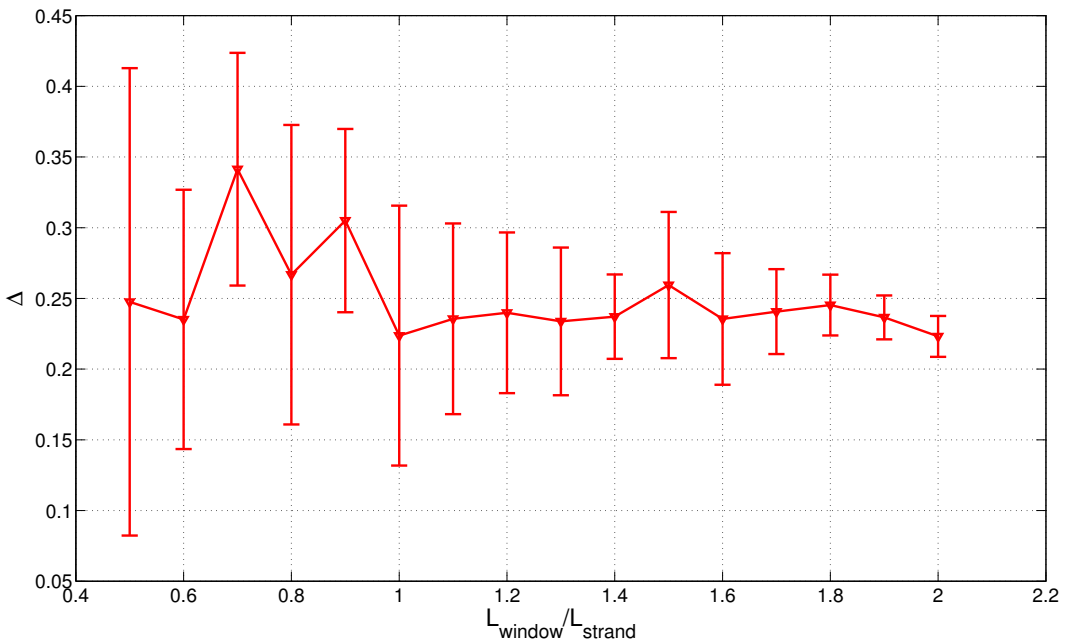
Figure 15. Departure from isotropy Δ versus window size normalized to strand length, $v_f = 20\%$.
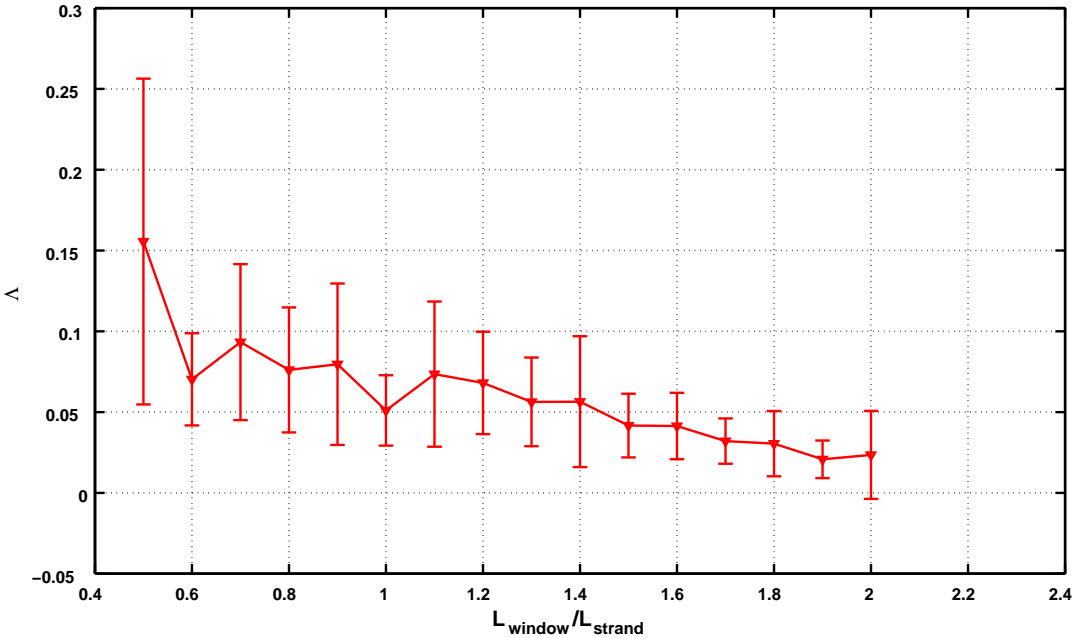
Figure 16. Statistical inhomogeneity Λ versus window size normalized to strand length, $v_f = 20\%$.

Moreover, an evaluation of the material homogeneity for large scale structures was performed. Relatively large plates were generated for the two materials considered and a windowing technique was employed to evaluate the local material properties for different analysis window sizes, using the homogenization technique employed earlier. Although somewhat limited by the reduced number of windows considered, due to the significant computational costs, this analysis indicates that representative volume elements with the side equal to one and a half fiber bundle lengths can be expected to reasonably approximate the homogeneous material properties. We note that the local departure from isotropy can be significant even at higher RVE dimensions, particularly at higher fiber volume fractions, due to the fiber aggregation behavior inherent to the geometry generation algorithm. However, we note that the variations in material properties at the local level, length scales smaller than $1.5l_f$, are significant, as indicated by the values of the departure from isotropy measure Δ and the statistical inhomogeneity Λ. While this can be justified by the already mentioned tendency for preferred fiber orientations, we must also note that no restriction on the *local* fiber volume fraction of the analysis windows has been imposed, leading to variations of the actual volume fraction in the analyzed windows. Thus, the analysis is indicative of an interval of confidence for the local material properties, offering designers an insight on the limits of applicability of the homogenized model and, implicitly, the choice of safety coefficients.

Acknowledgments

References

[Advani and Tucker 1987] S. G. Advani and C. L. Tucker, "The Use of Tensors to Describe and Predict Fiber Orientation in Short Fiber Composites", *Journal of Rheology* **31** (1987), 751–784.

[Benveniste 1987] Y. Benveniste, "A new approach to the application of Mori–Tanaka's theory in composite materials", *Mechanics of Materials* **6**:1 (1987), 147–157.

[Coelho et al. 1997] D. Coelho, J.-F. Thovert, and P. M. Adler, "Geometrical and transport properties of random packings of spheres and aspherical particles", *Physical Review E* **55**:2 (1997), 1959–1978.

[Dahl et al. 2005] J. S. Dahl, G. Smith, D. Houston, and L. Berger, "The influence of fiber tow size on the performance of chopped carbon fiber reinforced composites", *Materials and processing technologies for revolutionary applications, 37th ISTC,Washington* (2005).

[Duschlbauer et al. 2006] D. Duschlbauer, H. J. Böhm, and H. E. Pettermann, "Computational Simulation of Composites Reinforced by Planar Random Fibers: Homogenization and Localization by Unit Cell and Mean Field Approaches", *Journal of Composite Materials* **40**:24 (2006), 2217–2234.

[Eberly 2001] D. Eberly, "Intersection of Cylinders", http://www.geometrictools.com, 2001.

[Eshelby 1957] J. D. Eshelby, "The determination of the elastic field of an ellipsoidal inclusion, and related problems", *Proceedings of the Royal Society of London. Series A* **241**:1226 (1957), 376–396.

[Gusev et al. 2002] A. Gusev, M. Heggli, H. Lusti, and P. Hine, "Orientation Averaging for Stiffness and Thermal Expansion of Short Fiber Composites", *Advanced Engineering Materials* **4**:12 (2002), 931–933.

[Hazanov and Huet 1994] S. Hazanov and C. Huet, "Order relationships for boundary conditions effect in heterogeneous bodies smaller than the representative volume", *Journal of the Mechanics and Physics of Solids* **42**:12 (1994), 1995–2011.

[Hill 1971] R. Hill, "Elastic properties of reinforced solids: some theoretical principles", *Journal of the Mechanics and Physics of Solids* **11**:5 (1971), 357–372.

[Hine et al. 2002] P. J. Hine, H. R. Lusti, and A. A. Gusev, "Numerical simulation of the effects of volume fraction, aspect ratio and fibre length distribution on the elastic and thermoelastic properties of short fibre composites", *Composites science and technology* **62**:10-11 (2002), 1445–1453.

[Ionita and Weitsman 2006] A. Ionita and W. J. Weitsman, "On the mechanical response of randomly reinforced chopped-fibers composites: Data and model", *Composites Science and Technology* **66** (2006), 2566–2579.

[Jiang et al. 2001] M. Jiang, K. Alzebdeh, I. Jasiuk, and M. Ostoja-Starzewski, "Scale and boundary conditions effects in elastic properties of random composites", *Acta Mechanica* **vol.148** (2001), 63–78.

[Kanit et al. 2006] T. Kanit, F. N'Guyen, S. Forest, D. Jeulin, M. Reed, and S. Singleton, "Apparent and effective physical properties of heterogeneous materials: Representativity of samples of two materials from food industry", *Computer Methods in Applied Mechanics and Engineering* **195**:33-36 (July 2006), 3960–3982.

[Kari et al. 2007] S. Kari, H. Berger, and U. Gabbert, "Numerical evaluation of effective material properties of randomly distributed short cylindrical fibre composites", *Computational Materials Science* **39** (2007), 198–204.

[Mori and Tanaka 1973] T. Mori and K. Tanaka, "Average stress in matrix and average elastic energy of materials with misfitting inclusions", *Acta Metallurgica* **21** (1973), 571–574.

[Pan et al. 2007] Y. Pan, A. A. Pelegri, and L. Iorga, "Analysis of 3D random chopped fiber reinforced composite using the finite element method", *Accepted for publication in Computational Materials Science* (2007).

[Sanchez-Palencia and Zaoui 1985] E. Sanchez-Palencia and A. Zaoui (editors), *Homogenization techniques for composite media : Lectures delivered at the* CISM *International Center for Mechanical Science*, Lecture Notes in Physics, Springer-Verlag, 1985.

[Sun 2006] C. Sun, "Mechanics of Composite Materials and Laminates - Lecture Notes", 2006. unpublished.

[Williams and Philipse 2003] S. Williams and A. Philipse, "Random packings of spheres and spherocylinders simulated by mechanical contraction", *Physical Review E* **67**:5 (May 2003), 051301.

LUCIAN IORGA: liorga@rci.rutgers.edu
Mechanical and Aerospace Engineering, School of Engineering, Rutgers University, 98 Brett Road, Piscataway, NJ 08854-8058, United States

YI PAN: yipan@eden.rutgers.edu
Mechanical and Aerospace Engineering, School of Engineering, Rutgers University, 98 Brett Road, Piscataway, NJ 08854-8058, United States

ASSIMINA PELEGRI: pelegri@jove.rutgers.edu
Mechanical and Aerospace Engineering, School of Engineering, Rutgers University, 98 Brett Road, Piscataway, NJ 08854-8058, United States

VIBRATIONS OF HIGHLY INHOMOGENEOUS SHELLS OF REVOLUTION UNDER STATIC LOADING

ELENA BESPALOVA AND GALINA URUSOVA

An approach to determining natural frequencies of middle-thickness inhomogeneous shells of revolution acted upon by static axisymmetrical loads is proposed. The approach is based on application of the nonclassic shell model that takes into account transverse shears and reduction across the wall thickness. In solving the problem posed, decomposition into two interconnected problems is used. The first problem is related to determination of the initial stress-strain state of shells under static axisymmetrical loads. The second problem is related to determination of natural frequencies of shells relative to this state that appears in the form of parametric terms. To solve the problems, the numerical-analytical technique developed by the authors is used. The efficiency of allowance for reduction across the wall thickness is illustrated on the example of an inhomogeneous middle-thickness cylindrical shell under local loads. Analysis of natural frequencies of the shell having the form of a pneumatic tire is presented depending on the value of internal pressure.

1. Introduction

Shell structures in real conditions operate, as a rule, in the fields of static actions, such as heat or radioactive emanation, aggressive environment, mechanical loading, and so on. These fields cause in shells some initial stress-strain state. Allowance for this state makes it possible to study correctly more complex processes in shells such as processes of stationary and nonstationary dynamics, stability, contact interaction, and so on.

The present paper addresses the problem on small vibrations of middle-thickness essentially inhomogeneous across the thickness anisotropic shells of revolution with a meridian of arbitrary form acted upon by axisymmetric mechanical and heat loads of a general kind.

A large body of publications in this field deals with the study of free vibrations of shells of revolution without taking into account the initial stresses. In the case of thin shells, it can be judged by references of different years, for example, by [Xi et al. 1996; Tan 1998; Wang and Redekop 2005; Grigorenko et al. 2006]. Detailed analysis of studies on vibrations of some classes of thick shells of revolution is presented in [Redekop 2006; Kang 2007].

A number of works, where vibrations of shells of revolution have been studied with allowance for preliminary stresses, are rather limited. Only publications [Rao et al. 1974; Karmishin et al. 1975; Grigorenko et al. 1986; Bespalova et al. 1991; Sivadas 1995; Lam and Hua 1997; 1998; 2000; Hua and Lam 2000; Wang et al. 1997; Yuan and Liu 2007] directly refer to the object of the given paper. These works mostly consider, based on the Love model, homogeneous across the thickness isotropic

and orthotropic shells acted upon by initial pressure. In [Lam and Hua 1997; 1998; 2000; Hua and Lam 2000], initial pressure in rotating cylindrical and conical shells is caused by centrifugal forces and coriolis accelerations. The effect of boundary conditions, geometrical parameters, and rotating speeds on frequency characteristics of shells was studied. Inhomogeneous across the thickness orthotropic shells of revolution are addressed in [Karmishin et al. 1975] using the same Love model. Such classes of inhomogeneous shells of revolution and classes of cylindrical shells with arbitrary cross-section have been considered in [Grigorenko et al. 1986; Bespalova et al. 1991] based on the classic and Timoshenko–Reissner–Mindlin shear models. The purely shear first-order model has been used in [Sivadas 1995] to analyze vibrations of thick cones.

It should be noted that the distinguishing features of the class of shells being considered here are characterized by such factors as thick-walledness, essential inhomogeneity across the thickness (particularly, lamination), a complex pattern of distribution of the initial stresses caused by static loads of general form (particularly, localized ones). Owing to these complicating factors, vibrations of such shells should be studied based on the three-dimensional statement of the elasticity theory or on the shell models, taking into account all the kinds of transverse strain.

The present paper employs the nonclassic shell model with allowance for transverse shears and reduction. This makes it possible, in contrast to purely shear shell models, to take into account spatial effects of the chosen class of shells without increasing, in contrast to three-dimensional statement, the dimensionality of appropriate boundary-value problems. The last fact is rather important at the stage of realization of the chosen model of deformation, since the order of the resolving system of equations (algebraic or ordinary differential ones) rises by the power law with the problem dimensionality.

Note that the present-day tendency in analysis of compound deformable systems is connected in the majority of cases with employing finite-element and boundary-element methods. Allowing for the peculiarity of the class of shells under consideration, the authors propose the semianalytical approach, which is based on the accurate reduction of the dimensionality of an initial two-dimensional problem by analytical means and on the numerical solution of one-dimensional problems that makes it possible to obtain results with high accuracy.

2. The problem formulation and initial guidelines

Let us consider the class of inhomogeneous middle-thickness shells, which can be referred to the some surface of revolution. This surface in a general case is chosen by informal way and is known as a coordinate or reference surface (in particular, it is a median surface) [Ambartsumyan 1961]. Let this surface be generated by rotation of a some plane piecewise-smooth curve about the Oz-axis. It is convenient to describe the shell geometry in a spatial curvilinear orthogonal system of coordinates α, β, and γ, where the coordinate α changes along the generatrix (meridian), β is the angle in the cross-sectional plane $\alpha = $ const, and γ varies across the shell thickness and is reckoned from the coordinate surface $\gamma = 0$ (see Figure 1a and b).

In the general case, the shell is inhomogeneous across the thickness and may be composed of an arbitrary number M of layers with constant or variable thickness along the α-axis. The interface of the adjacent mth and $(m + 1)$th layers is specified by the equation $\gamma = \gamma_m(\alpha)$ $(m = \overline{1, M - 1})$ (see Figure 1c and d). The material of each of the layers may be both isotropic or anisotropic with three planes of
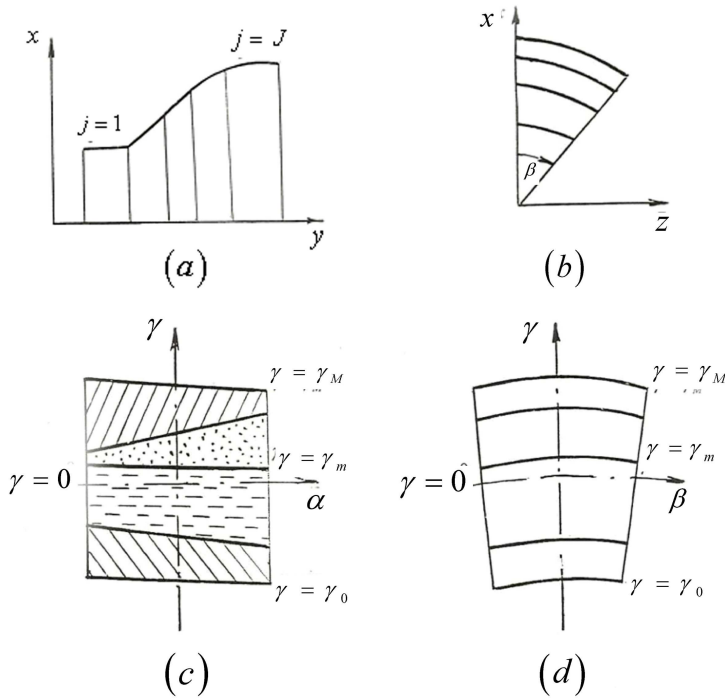
Figure 1. Schematic drawing of a laminated shell of revolution: (a) the overall view of the generatrix in the section $\beta = $ const; (b) the view of the shell in the section $\alpha = $ const; (c), (d) the structure of the shell across the thickness in the sections $\beta = $ const and $\alpha = $ const, respectively.

elastic symmetry and with principal directions of elastic symmetry coinciding with the lines of principal curvatures $\alpha = $ const and $\beta = $ const.

To describe the given class of shells, we divide their generatrix into J segments (see Figure 1a). Within the limits of each of the segments, geometrical parameters, values of the thickness, and physical-mechanical properties of the material are specified by smooth functions of the variable α. Besides, any kinds of boundary conditions, which take into account the character of loading and displacement of a contour, are admitted at the shell ends $\alpha = \alpha_0$ and $\alpha = \alpha_J$.

The static axisymmetrical fields imposed on the shell can be caused by the following actions: the normal $q_\gamma(\alpha)$ and meridional $q_\alpha(\alpha)$ loads applied at the points of the coordinate surface $\gamma = 0$; contour forces-moments, which act at the ends $\alpha = \alpha_0$ and $\alpha = \alpha_J$; concentrated forces-moments applied at the meridional sections $\alpha = \alpha_j = $ const ($j = \overline{1, J-1}$); and heating, which is described by the function $T = T(\alpha, \gamma)$.

To study vibrations of the prestressed shells, we will use the following assumptions:

(a) The problem on vibrations of statically loaded shells is formulated based on the geometrically non-linear theory in the quadratic approximation [Mushtari and Galimov 1957; Grigorenko and Mukoed 1983].

(b) Vibrations of the shells are treated as small perturbations relative to the initial state caused by the static loading.

(c) Material of the layers is linearly elastic and obeys the generalized Hooke's law within the whole range of applied loads.

(d) Separation and sliding of the shell layers are absent.

(e) The nonclassic deformation model taking into account transverse shears and reduction in linear approximation of all components of a displacement vector across the thickness is adopted for the whole package of layers [Grigorenko et al. 1987] in the form

$$u_\alpha^m(\alpha, \beta, \gamma, t) = u(\alpha, \beta, t) + \gamma \psi_\alpha(\alpha, \beta, t),$$
$$u_\beta^m(\alpha, \beta, \gamma, t) = v(\alpha, \beta, t) + \gamma \psi_\beta(\alpha, \beta, t) \qquad (m = \overline{1, M}),$$
$$u_\gamma^m(\alpha, \beta, \gamma, t) = w(\alpha, \beta, t) + \gamma \psi_\gamma(\alpha, \beta, t),$$

where u_α^m, u_β^m, and u_γ^m are the displacements of points of the mth layer, u, v, and w are the displacements of points of the coordinate surface $\gamma = 0$ in the directions α, β, and γ, respectively, ψ_α and ψ_β are the total rotation angles of a straight element, ψ_γ is the transverse normal strain, and t is the time variable.

(f) The inertial forces related to the shell translation, rotation of the straight element and its reduction are taken into account.

(g) Temperature actions are allowed for based on the Duhamel–Neumann hypothesis.

According to the assumptions adopted, the following basic relations are used:

• Motion equations

$$\frac{\partial(BN_\alpha)}{\partial\alpha} - \frac{\partial B}{\partial\alpha}N_\beta + \frac{\partial(AN_{\beta\alpha})}{\partial\beta} + ABk_1Q_\alpha + AB\Big(q_\alpha - I_0\frac{\partial^2 u}{\partial t^2} - I_1\frac{\partial^2 \psi_\alpha}{\partial t^2}\Big) = 0,$$

$$\frac{\partial(BN_{\alpha\beta})}{\partial\alpha} + \frac{\partial(AN_\beta)}{\partial\beta} + \frac{\partial B}{\partial\alpha}N_{\beta\alpha} + ABk_2Q_\beta + AB\Big(q_\beta - I_0\frac{\partial^2 v}{\partial t^2} - I_1\frac{\partial^2 \psi_\beta}{\partial t^2}\Big) = 0,$$

$$\frac{\partial(BQ_\alpha)}{\partial\alpha} + \frac{\partial(AQ_\beta)}{\partial\beta} - ABk_1N_\alpha - ABk_2N_\beta + AB\Big(q_\gamma - I_0\frac{\partial^2 w}{\partial t^2} - I_1\frac{\partial^2 \psi_\gamma}{\partial t^2}\Big) = 0,$$

$$\frac{\partial(BM_\alpha)}{\partial\alpha} - \frac{\partial B}{\partial\alpha}M_\beta + \frac{\partial(AM_{\beta\alpha})}{\partial\beta} - ABQ_\alpha - AB\big[(N_\alpha + k_1M_\alpha)\vartheta_\alpha + N_{\alpha\beta}\vartheta_\beta\big]$$
$$- AB\Big(-m_\alpha + I_1\frac{\partial^2 u}{\partial t^2} + I_2\frac{\partial^2 \psi_\alpha}{\partial t^2}\Big) = 0,$$

$$\frac{\partial(BM_{\alpha\beta})}{\partial\alpha} + \frac{\partial(AM_\beta)}{\partial\beta} + \frac{\partial B}{\partial\alpha}M_{\beta\alpha} - ABQ_\beta - AB\big[(N_\beta + k_2M_\beta)\vartheta_\beta + N_{\beta\alpha}\vartheta_\alpha\big]$$
$$- AB\Big(-m_\beta + I_1\frac{\partial^2 v}{\partial t^2} + I_2\frac{\partial^2 \psi_\beta}{\partial t^2}\Big) = 0,$$

$$\frac{\partial(BP_\alpha)}{\partial\alpha} + \frac{\partial(AP_\beta)}{\partial\beta} - ABk_1M_\alpha - ABk_2M_\beta - AB(C_{13}\varepsilon_\alpha + C_{23}\varepsilon_\beta + C_{33}\psi_\gamma + K_{13}\kappa_\alpha + K_{23}\kappa_\beta - N_{\gamma T})$$
$$- AB\Big(-\gamma_M q_\gamma^+ - \gamma_0 q_\gamma^- + I_1\frac{\partial^2 w}{\partial t^2} + I_2\frac{\partial^2 \psi_\gamma}{\partial t^2}\Big) = 0. \quad (1)$$

- Expressions for strains in terms of displacements

$$\varepsilon_\alpha = \frac{1}{A}\frac{\partial u}{\partial \alpha} + k_1 w + \frac{1}{2}\vartheta_\alpha^2, \qquad\qquad \varepsilon_\beta = \frac{1}{B}\frac{\partial v}{\partial \beta} + \frac{1}{AB}\frac{\partial B}{\partial \alpha}u + k_2 w + \frac{1}{2}\vartheta_\beta^2,$$

$$\varepsilon_{\alpha\beta} = \frac{1}{B}\frac{\partial u}{\partial \beta} - \frac{1}{AB}\frac{\partial B}{\partial \alpha}v + \frac{1}{A}\frac{\partial v}{\partial \alpha} + \vartheta_\alpha\vartheta_\beta, \qquad \kappa_\alpha = \frac{1}{A}\frac{\partial \psi_\alpha}{\partial \alpha} + k_1(\psi_\gamma - \varepsilon_\alpha),$$

$$\kappa_\beta = \frac{1}{B}\frac{\partial \psi_\beta}{\partial \beta} + \frac{1}{AB}\frac{\partial B}{\partial \alpha}\psi_\alpha + k_2(\psi_\gamma - \varepsilon_\beta),$$

$$2\kappa_{\alpha\beta} = \frac{1}{A}\frac{\partial \psi_\beta}{\partial \alpha} + \frac{1}{B}\frac{\partial \psi_\alpha}{\partial \beta} - \frac{1}{AB}\frac{\partial B}{\partial \alpha}\psi_\beta - k_1\frac{1}{A}\frac{\partial v}{\partial \alpha} - k_2(\frac{1}{B}\frac{\partial u}{\partial \beta} - \frac{1}{AB}\frac{\partial B}{\partial \alpha}v),$$

$$\varphi_\alpha = \psi_\alpha - \vartheta_\alpha, \qquad\qquad \varphi_\beta = \psi_\beta - \vartheta_\beta,$$

$$\vartheta_\alpha = -\frac{1}{A}\frac{\partial w}{\partial \alpha} + k_1 u, \qquad \vartheta_\beta = -\frac{1}{B}\frac{\partial w}{\partial \beta} + k_2 v. \tag{2}$$

- Elasticity relations

$$N_\alpha = C_{11}\varepsilon_\alpha + C_{12}\varepsilon_\beta + C_{13}\psi_\gamma + K_{11}\kappa_\alpha + K_{12}\kappa_\beta - N_{\alpha T},$$

$$N_\beta = C_{12}\varepsilon_\alpha + C_{22}\varepsilon_\beta + C_{23}\psi_\gamma + K_{11}\kappa_\alpha + K_{12}\kappa_\beta - N_{\beta T},$$

$$N_{\alpha\beta} = C_{66}\varepsilon_{\alpha\beta} + K_{66}2\kappa_{\alpha\beta} + k_2(K_{66}\varepsilon_{\alpha\beta} + D_{66}2\kappa_{\alpha\beta}) - N_{\alpha\beta T},$$

$$N_{\beta\alpha} = C_{66}\varepsilon_{\alpha\beta} + K_{66}2\kappa_{\alpha\beta} + k_1(K_{66}\varepsilon_{\alpha\beta} + D_{66}2\kappa_{\alpha\beta}) - N_{\beta\alpha T},$$

$$M_\alpha = K_{11}\varepsilon_\alpha + K_{12}\varepsilon_\beta + K_{13}\psi_\gamma + D_{11}\kappa_\alpha + D_{12}\kappa_\beta - M_{\alpha T},$$

$$M_\beta = K_{12}\varepsilon_\alpha + K_{22}\varepsilon_\beta + K_{23}\psi_\gamma + D_{12}\kappa_\alpha + D_{22}\kappa_\beta - M_{\beta T},$$

$$M_{\alpha\beta} = M_{\beta\alpha} = K_{66}\varepsilon_{\alpha\beta} + D_{66}2\kappa_{\alpha\beta} - M_{\alpha\beta T},$$

$$N_\gamma = C_{13}\varepsilon_\alpha + C_{23}\varepsilon_\beta + C_{33}\psi_\gamma + K_{13}\kappa_\alpha + K_{23}\kappa_\beta - N_{\gamma T},$$

$$Q_\alpha = K_1\varphi_\alpha + D_1\frac{1}{A}\frac{\partial \psi_\gamma}{\partial \alpha} - Q_{\alpha T}, \qquad Q_\beta = K_2\varphi_\beta + D_2\frac{1}{B}\frac{\partial \psi_\gamma}{\partial \beta} - Q_{\beta T},$$

$$P_\alpha = D_1\varphi_\alpha + C_1\frac{1}{A}\frac{\partial \psi_\gamma}{\partial \alpha} - P_{\alpha T}, \qquad P_\beta = D_2\varphi_\beta + C_2\frac{1}{B}\frac{\partial \psi_\gamma}{\partial \beta} - P_{\beta T}. \tag{3}$$

Here A and B and k_1 and k_2 are the coefficients of the first quadratic form and the principal curvatures of the chosen coordinate surface, N_α, $N_{\alpha\beta}$, and Q_α are the normal, shearing, and transverse forces in the section $\alpha = \text{const}$, M_α and $M_{\alpha\beta}$ are the bending and twisting moments, P_α is the first-order moment caused by the tangential stress of transverse shear in the same section, N_β, $N_{\beta\alpha}$, Q_β, M_β, $M_{\beta\alpha}$, and P_β are the same factors in the section $\beta = \text{const}$, $q_\alpha, q_\beta, q_\gamma, m_\alpha$, and m_β are the components of the intensity of the distributed load and bending moments statically equivalent to the body forces and forces, which are applied to the bounding surfaces $\gamma = \gamma_0$ and $\gamma = \gamma_M$, q_γ^+ and q_γ^- are the intensities of the normal force on outer and inner shell surfaces, ε_α, ε_β, and $\varepsilon_{\alpha\beta}$ are the tensile and shear strains of the coordinate surface, κ_α, κ_β, and $2\kappa_{\alpha\beta}$ are the bending and twisting strains, ϑ_α and ϑ_β are the rotation angles of the normal in the planes $\alpha = \text{const}$ and $\beta = \text{const}$, φ_α and φ_β are the rotation angles attributed to the transverse shears, $N_{\alpha T}, N_{\beta T}, \ldots, P_{\beta T}$ are the integral characteristics of the temperature field $T = T(\alpha, \beta)$, I_k ($k = 0, 1, 2$)

are the kth-order moments of the material density, and $C_{11}, \ldots, K_{11}, \ldots, D_{66}, K_1, \ldots, D_1, \ldots, C_2$ are the integral characteristics of the shell stiffness determined in terms of the thickness of layers and their elastic properties, for example

$$C_{11} = \sum_{m=1}^{M} \int_{\gamma_{m-1}}^{\gamma_m} \frac{E_\alpha}{1 - \nu_\alpha \nu_\beta} d\gamma, \; \ldots, \; K_{11} = \sum_{m=1}^{M} \int_{\gamma_{m-1}}^{\gamma_m} \frac{E_\alpha}{1 - \nu_\alpha \nu_\beta} \gamma \, d\gamma, \; \ldots, \; D_{66} = \sum_{m=1}^{M} \int_{\gamma_{m-1}}^{\gamma_m} G_{\alpha\beta} \gamma^2 d\gamma,$$

$$K_1 = \sum_{m-1}^{M} \int_{\gamma_{m-1}}^{\gamma_m} G_{\beta\gamma}(1 - k_1\gamma) d\gamma, \; \ldots, \; D_1 = \sum_{m-1}^{M} \int_{\gamma_{m-1}}^{\gamma_m} G_{\beta\gamma} \gamma \, d\gamma, \; \ldots, \; C_2 = \sum_{m-1}^{M} \int_{\gamma_{m-1}}^{\gamma_m} G_{\alpha\gamma} \gamma^2 d\gamma.$$

In these expressions, E_α, E_β and E_γ are the elastic moduli in the directions α, β and γ, respectively, $G_{\beta\gamma}$, $G_{\alpha\gamma}$, and $G_{\alpha\beta}$ are the shear moduli for the planes parallel to the coordinate surfaces $\alpha = \text{const}$, $\beta = \text{const}$, and $\gamma = \text{const}$, and ν_α and ν_β are Poisson's ratios.

Relations (1)–(3) make it possible to describe the shell state under consideration in the form of a two-dimensional nonlinear boundary-value problem. In the given paper, components of a vector-function $N = \{N_n(\alpha, \beta, t), n = \overline{1, 12}\} = \{Q, U\}$ are chosen as basic unknowns. They include static,

$$Q = \{N_\alpha, N_{\alpha\beta}, Q_\alpha, M_\alpha, M_{\alpha\beta}, P_\alpha\}^T, \tag{4}$$

and kinematic,

$$U = \{u, v, w, \psi_\beta, \psi_\beta, \psi_\gamma\}^T, \tag{5}$$

characteristics of the stress state [Grigorenko et al. 1987]. Then, expressing the functions N_β, M_β, ε_α, κ_α, $\varepsilon_{\alpha\beta}$, and $2\kappa_{\alpha\beta}$ with the help of Equations (2) and (3) through the functions N_α, M_α, $M_{\alpha\beta}$, ε_β, κ_β, and ψ_γ and the functions ψ_α, $\partial \psi_\gamma / \partial \alpha$, Q_β, and P_β through the functions Q_α, P_α, ψ_β, and $\partial \psi_\gamma / \partial \beta$, after linear but sufficiently cumbersome transformations, we arrive at the formulation of a two-dimensional problem in the form

$$\frac{\partial N}{\partial \alpha} = \mathbf{L}N + G + q^0 + \mathbf{C}\frac{\partial^2 N}{\partial t^2}, \qquad \alpha \in (\alpha_{j-1}, \alpha_j) \quad (j = \overline{1, J}), \qquad \beta \in [0, 2\pi],$$

$$\mathbf{S}_j N = \mathbf{S}_{j+1} N + F_j^0, \qquad\qquad \alpha = \alpha_j \qquad\quad (j = \overline{1, J-1}),$$

$$\mathbf{B}_j N = b_j^0, \qquad\qquad\qquad\quad \alpha = \alpha_j \qquad\quad (j = 0; J),$$

$$N(\alpha, \beta + 2\pi, t) = N(\alpha, \beta, t). \tag{6}$$

Here

$$\mathbf{L} = \left\{ l_{m,n} = \frac{1}{A}\left(A_{m,n}^0 + A_{m,n}^1 \frac{\partial}{\partial \beta} + A_{m,n}^2 \frac{\partial^2}{\partial \beta^2} \right) \right\} \qquad (m, n = \overline{1, 12}),$$

is the matrix differential second-order operator with respect to the variable β, constructed with the help of relations (1)–(3) of the deformation model adopted. Components of the vector $G = \{g_m\}$ are the quadratic functions of the components of the stress-strain state according to the geometrically nonlinear shell theory in the quadratic approximation; $\mathbf{C}$ is the matrix whose elements characterize the inertial properties of the shell; $\mathbf{S}_j$ and $\mathbf{B}_j$ are the matrices allowing for the discontinuities in representation of physical-mechanical and geometrical parameters of the shell in the section $\alpha = \alpha_j$ ($j = \overline{1, J-1}$), as well as the type of boundary conditions at the contour $\alpha = \alpha_j$ ($j = 0; J$); and q^0, F_j^0, and b_j^0 are the vectors

characterizing the axisymmetrical distributed loads and temperature fields, concentrated forces-moments in the section $\alpha = \alpha_j$ $(j = \overline{1, J-1})$ and contour actions at $\alpha = \alpha_j$ $(j = 0; J)$.

Note that choice of unknowns in Equations (4) and (5) makes it possible to formulate arbitrary boundary conditions at edges $\alpha = \alpha_0$ and $\alpha = \alpha_J$ in the simplest form.

According to assumption (b), the state of the shell being analyzed can be presented as

$$N = N^{\mathrm{st}} + N^{\mathrm{d}} \qquad \left(|N^{\mathrm{d}}| \ll |N^{\mathrm{st}}|\right),$$

where the vector-function N^{st} characterizes the stress-strain state of the shell under static actions (initial state), and N^{d} are the small undamping vibrations about this state. Correspondingly, initial nonlinear problem (6) is reduced to the following two coupled problems:

(i) The problem on deformation of a shell under specified axisymmetrical loads; this is formulated relative to the vector N^{st} as

$$\begin{aligned}
\frac{dN^{\mathrm{st}}}{d\alpha} &= \mathbf{L}^0 N^{\mathrm{st}} + G(\alpha, N^{\mathrm{st}}, \ldots) + q^0, & \alpha &\in (\alpha_{j-1}, \alpha_j) & (j &= \overline{1, J}), \\
\mathbf{S}_j N^{\mathrm{st}} &= \mathbf{S}_{j+1} N^{\mathrm{st}} + F_j^0, & \alpha &= \alpha_j & (j &= \overline{1, J-1}), \\
\mathbf{B}_j N^{\mathrm{st}} &= b_j^0, & \alpha &= \alpha_j & (j &= 0; J),
\end{aligned}$$

(7)

(here $\mathbf{L}^0$ is the matrix zeroth-order differential operator).

(ii) The problem on vibrations of a prestressed shell; this is formulated relative to the vector N^{d} as

$$\begin{aligned}
\frac{\partial N^d}{\partial \alpha} &= \widetilde{\mathbf{L}} N^{\mathrm{d}} + \mathbf{C} \frac{\partial^2 N^{\mathrm{d}}}{\partial t^2}, & \alpha &\in (\alpha_{j-1}, \alpha_j) & (j &= \overline{1, J}), & \beta &\in [0, 2\pi], \\
\mathbf{S}_j N^{\mathrm{d}} &= \mathbf{S}_{j+1} N^{\mathrm{d}}, & \alpha &= \alpha_j & (j &= \overline{1, J-1}), \\
\mathbf{B}_j N^{\mathrm{d}} &= 0, & \alpha &= \alpha_j & (j &= 0; J),
\end{aligned}$$

$$N^{\mathrm{d}}(\alpha, \beta + 2\pi, t) = N^{\mathrm{d}}(\alpha, \beta, t).$$

(8)

Here $\widetilde{\mathbf{L}}$ is the matrix differential operator corresponding to the operator $\mathbf{L}$ in (6). It was obtained as the result of linearization of the function G relative to the vector N^{d} and includes components of the vector N^{st} as parametric terms.

3. Problem-solving technique

Problems (7) and (8) methodically may be considered as two successive stages of solving the initial problem. At the first stage, we determine the stress-strain state of a shell under specified axisymmetrical loads. In the case of finite strains, the one-dimensional problem is nonlinear, and for its solving we can employ methods of quasilinearization or simple iteration [Bellman and Kalaba 1965]. One-dimensional linearized problems are solved numerically. In the present work, the study is limited by loads which cause small strains. For this reason problem (7) can be considered in the linear formulation. To solve it, we will use the numerical orthogonal-sweep method [Godunov 1961]. This method proved itself to be effective in solving the stationary problems of the shell theory by using different deformation models

[Grigorenko et al. 1986; 1987]. Detailed description of this method is presented in [Grigorenko and Rozhok 2003].

For the second stage, to solve the problem on small vibrations of the shell with allowance for the initial stress state N_d, we use a numerical-analytical approach. This approach includes the method of separation of variables, the method of reverse iterations with constructing the Rayleigh ratio, and numerical solving of one-dimensional boundary-value problems by the orthogonal-sweep method.

The first step in solving problem (8) is separation of the time multiplier $e^{i\omega t}$ for components of the vector-function N^{d} and their representation in the form of the single trigonometric Fourier series along the circumferential coordinate β by

$$N^{\mathrm{d}} = \left\{ N_n^d(\alpha, \beta, t) = \sum_{k=0}^{\infty} N_{nk}^d(\alpha) \begin{bmatrix} \sin k\beta \\ \cos k\beta \end{bmatrix} e^{i\omega t}, \quad n = \overline{1, 12} \right\}. \tag{9}$$

Here ω is the natural frequency of shell vibrations, k is the parameter characterizing the shape of a wave along the circumference (this parameter is equal to the number of waves, which go fully in this direction). The expression in square brackets indicates that one part of the components of the vector-function N^{d}, namely, $(N_\alpha^d, Q_\alpha^d, M_\alpha^d, P_\alpha^d, u^d, w^d, \psi_\alpha^d, \psi_\gamma^d)$ is represented in $\cos k\beta$, whereas the other part $(N_{\alpha\beta}^d, M_{\alpha\beta}^d, v^d, \psi_\beta^d)$ is represented in $\sin k\beta$. As a result, the two-dimensional problem (8) is reduced exactly to the following sequence of uncoupled single-parametric one-dimensional problems with respect to the functional coefficients $N_k^d = \{N_{nk}^d(\alpha), n = \overline{1, 12}\}$ in (9):

$$\begin{aligned}
\frac{dN_k^d}{d\alpha} &= (\mathbf{A}_k - \lambda\mathbf{C})N_k^d, & \alpha &\in (\alpha_{j-1}, \alpha_j) & (j = \overline{1, J}), \\
\mathbf{S}_j N_k^d &= \mathbf{S}_{j+1} N_k^d, & \alpha &= \alpha_j & (j = \overline{1, J-1}), \\
\mathbf{B}_j N_k^d &= 0, & \alpha &= \alpha_j & (j = 0; J) & (k = 0, 1, 2, \ldots),
\end{aligned} \tag{10}$$

where $\mathbf{A}_k$ is the squared 12th-order matrix defined by the operator $\widetilde{\mathbf{L}}$ in (8) in accordance with approximation (9), and $\lambda = \omega^2$ is the unknown numerical parameter. Expressions for elements of matrices $\mathbf{A}_k, \mathbf{S}_j, \mathbf{S}_{j+1}$ $(j = \overline{1, J-1})$, and $\mathbf{B}_j$ $(j = 0; J)$ are presented in [Grigorenko et al. 1987]. Nonzero elements of the matrix $\mathbf{C}$ are

$$c_{1,7} = c_{2,8} = c_{3,9} = I_0 = \sum_{m=1}^{M} \int_{\gamma_{m-1}}^{\gamma_m} \rho_m(\alpha, \gamma)\,d\gamma,$$

$$c_{1,10} = c_{2,11} = c_{3,12} = c_{4,7} = c_{5,8} = c_{6,9} = I_1 = \sum_{m=1}^{M} \int_{\gamma_{m-1}}^{\gamma_m} \rho_m(\alpha, \gamma)\gamma\,d\gamma, \tag{11}$$

$$c_{4,10} = c_{5,11} = c_{6,12} = I_2 = \sum_{m=1}^{M} \int_{\gamma_{m-1}}^{\gamma_m} \rho_m(\alpha, \gamma)\gamma^2\,d\gamma,$$

where $\rho_m(\alpha, \gamma)$ is the density of the mth layer.

To solve the eigenvalue problem (10), we employ the method of reverse iterations with the shift of the spectrum of eigenvalues [Kollatz 1963]. Application of this method to the problems of the given class

for the classic and Timoshenko–Mindlin type models is outlined in [Grigorenko et al. 1986; Bespalova et al. 1991].

According to the method of reverse iterations, the minimum eigenvalue of the shifted spectrum is determined as the limit of the numeric sequence λ_n constructed by the Rayleigh ratio

$$\lambda_n = \frac{\left(\boldsymbol{U}^{d,(n)}, \boldsymbol{C}^* \boldsymbol{U}^{d,(n-1)}\right)}{\left(\boldsymbol{U}^{d,(n)}, \boldsymbol{C}^* \boldsymbol{U}^{d,n}\right)}, \qquad n = 1, 2, \ldots, \tag{12}$$

where $\boldsymbol{U}^{d,(n)}$ is the vector of kinematic characteristics of the deformed state (5), $\boldsymbol{C}^*$ is the nonsingular matrix with elements (11), n is the iteration number, and $(\ldots, \ldots)$ is the scalar product. The vector-function $\boldsymbol{U}^{d,(n)}$ being the component of the vector-function $\boldsymbol{N}^{d,(n)}$ at each nth step of the iteration ($n = 1, 2, \ldots$) is determined from the solution of the nonuniform problem

$$
\begin{aligned}
\frac{d\boldsymbol{N}_k^{d,(n)}}{d\alpha} &= (\boldsymbol{A}_k - \tau \boldsymbol{C})\boldsymbol{N}_k^{d,(n)} - \boldsymbol{C}\boldsymbol{N}_k^{d,(n-1)}, & \alpha \in (\alpha_{j-1}, \alpha_j) \quad (j = \overline{1, J}), \\
\boldsymbol{S}_j \boldsymbol{N}_k^{d,(n)} &= \boldsymbol{S}_{j+1} \boldsymbol{N}_k^{d,(n)}, & \alpha = \alpha_j & \quad (j = \overline{1, J-1}), \\
\boldsymbol{B}_j \boldsymbol{N}_k^{d,(n)} &= 0, & \alpha = \alpha_j & \quad (j = 0; J) \quad (k = 0, 1, 2, \ldots).
\end{aligned}
\tag{13}
$$

According to [Kollatz 1963], the sequence of such problems ($n = 1, 2, \ldots$) is obtained from (10) by adding the term which characterizes the shift of a frequency spectrum of value τ, and by changing the term with the coefficient λ to $\boldsymbol{N}_k^{d,(n-1)}$. As in the first stage, problems (13) are solved numerically by the orthogonal-sweep method. If the sequence $\boldsymbol{N}_k^{d,(n)}$ ($n = 1, 2, \ldots$) converges, the vector-functions $\boldsymbol{U}_k^{d,(n)}$ will tend to the eigenvector-functions and the numerical sequence λ_n in (12) will tend to the sought for eigenvalue λ. Fulfillment of the condition $|1 - \lambda^{n+1}/\lambda^{(n)}| < \varepsilon$ is the natural criterion for the finish of the iterative process. The issue of the selection of the initial approximation and convergence of the process in the problems of the shell theory has been considered in [Grigorenko et al. 1986].

4. Vibration analysis of prestressed inhomogeneous shells

As an example of employment of the approach developed, we will solve two problems. The first one is a model problem and demonstrates the efficiency of the variant, in which reduction and transverse shear are taken into account, in contrast to the Kirchhoff–Love and Timoshenko–Mindlin theories. The second problem concerns analysis of natural frequencies of the shell similar to the real structure having the form of a pneumatic tire.

Problem 1. Here, using as an example a shell with a simple geometric shape which is homogeneous along the generatrix, we will estimate the validity of the technique depending on two factors: inhomogeneity of physical-mechanical properties across the thickness and localization of the acting load.

Let us consider a sandwich cylindrical shell of length $2l$ ($s \in [-l, l]$) with the radius of a median surface R_0 and general thickness h (s is the arc length of the generatrix). Layers of the shell are isotropic with different elastic properties and are placed symmetrically relative to the median surface. The elastic modulus and density of outer layers are $E = E_0$ and $\rho = \rho_0$, respectively, and Poisson's ratio is ν. These characteristics for the inner layer are $E = E_0/d$ and $\rho = \rho_0/d$ with the same Poisson's ratio. The volume of the inner layer is equal to that of two outer ones. The inhomogeneity of such laminated structures is

characterized by the parameters d or $\eta = \lg d$. The case $\eta = 0$ corresponds to a homogeneous isotropic shell made of a material of outer layers. Note that with η being varied, the velocity of propagation of elastic waves for the cylinder as a whole remains the same. The shell is under the action of the normal axisymmetrical load with intensity q. The load is applied on the circular ring of the length $2l^*$ with a center in the section $s = 0$ ($s \in [-l^*, l^*]$). To characterize the level of its localization, we will use the parameter $\delta = l^*/l$. As the limiting case of the load localization, we will consider the circular radial force Q_s (for $\delta = 0$) concentrated in the section $s = 0$. It is assumed that both cylinder ends $s = \pm l$ are hinged. In this case, the prestressed state is defined mainly by the circumferential force N_β.

Natural frequencies ω of the shell are analyzed depending on two parameters: the degree of the inhomogeneity across the thickness (parameter $\eta \in [0; 3]$) and the degree of the load localization (parameter $\delta \in [0; 0.2]$). We will compare the results obtained by different shell models using the load value q^*, for which the minimum frequency becomes equal to zero ($\omega_{min}(q) \simeq 0$). Note that in accordance with the dynamic criterion of the shell stability, the value q^* can be adopted as the upper quantity of a critical load.

To calculate the magnitudes of the critical load, we will employ the following shell models: the classic model (transverse strains are neglected), the Timoshenko–Mindlin type model (transverse shears are regarded), and nonclassic model (transverse shears and reduction across the wall thickness are regarded). Comparison of corresponding solutions makes it possible to evaluate the contribution of each type of the transverse strain into correction of the results obtained by the classic theory. These results are presented in Figure 2 for the relative value of the critical load $\chi = q^*(\eta)/q_c^*(0)$, where $q_c^*(0)$ is the q^* which is obtained for an homogeneous shell by the classic model.

The dependencies $\chi = \chi(\eta)$ are presented for the above-mentioned shell models and for different kinds of load localization $\delta = 0.2, 0.1$, and 0. Data accepted for calculations are $R_0 = 100l_0$, $2l/R_0 = 2$, and $h/R_0 = 1/5$, where l_0 is the typical linear dimension of the cylinder. It should be noted, that, as
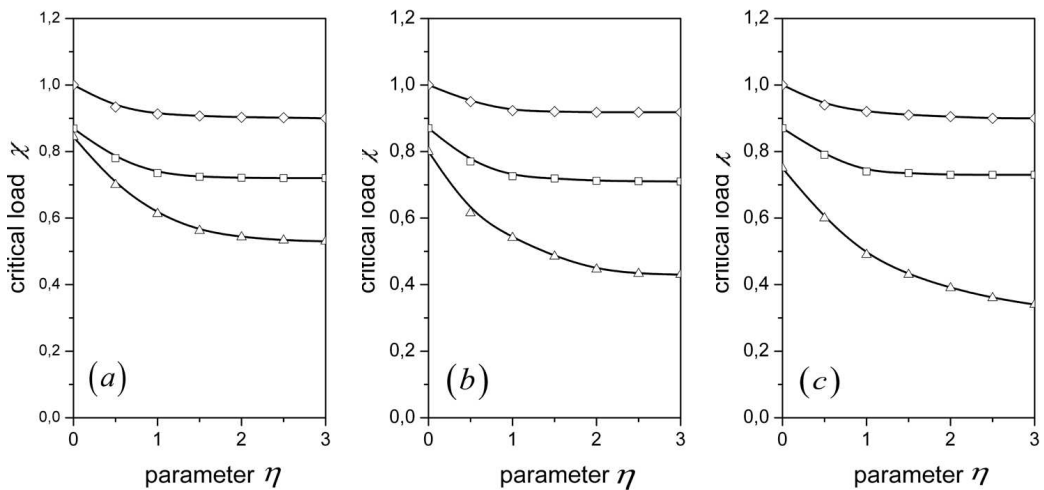

Figure 2. Dependency of the critical load $\chi = \chi(\eta)$ on the parameter of inhomogeneity η for different shell models: classic ($\diamond$), shear ($\square$), and with allowance for reduction ($\triangle$), and different values of the load localization: (a) $\delta = 0.2$; (b) $\delta = 0.1$; and (c) $\delta = 0$.

applied to these data, the calculation error, which takes place in determining the natural frequencies of unloaded shell by the nonclassic theory with reduction being taken into account, is not more then 2% in comparison with the results obtained by the three-dimensional theory [Bespalova and Urusova 2007].

Let us analyze in detail the dependencies $\chi = \chi(\eta)$.

In the case of a homogeneous shell ($\eta = 0$) and weak load localization (for example, at $\delta = 0.2$, see Figure 2a), the allowance for transverse shears makes it possible to refine the results obtained by the classic theory by 15%. The complementary allowance for the reduction does not result in any appreciable changes. For this reason, in the case of a homogeneous shell with small localization, we can limit ourselves to transverse shears only. The correct use of classic and purely shear models as applied to the inhomogeneous shells ($\eta > 0$) is possible only if $\eta < 1$ and ($d < 10$), that is, when the difference in properties of the material of layers is within the limit of one order.

When the inhomogeneity is considerable ($\eta > 1, d > 10$), both models do not depict variation in shell properties. The allowance for transverse shears yields only insignificant refinement (approximately for 20%) of results in comparison with a homogeneous shell. At the same time, the allowance for reduction results in considerable refinement for essentially inhomogeneous shells even if the localization of a load is insignificant. So, for $\eta = 3$, the magnitude of a critical load is refined by 40% compared with the classic theory and by 25% compared with the shear theory. With the localization increasing ($\delta = 0.1$, see Figure 2b) and especially in the limiting case of the point action ($\delta = 0$), the influence of allowance for reduction increases considerably. In the case of a concentrated load ($\delta = 0$, see Figure 2c) and homogeneous shell ($\eta = 0$), the effect of the allowance for transverse shears and reduction refines the magnitude of the critical load by 25% and reduction proper by 15%. For an inhomogeneous shell ($\eta = 3$) such refinement is more than 60% and 50%, respectively.

Thus, in determining the critical loads for essentially inhomogeneous shells ($\eta > 1$) and considerable localization of actions ($\delta < 0.2$), the allowance only for transverse shears may be inadequate. In these cases, for analysis to be correct, the shell models, which take into attention all kinds of the transverse strain including reduction, should be employed.

***Problem* 2.** As an example, let us determine natural frequencies of such standard shell construction as a pneumatic tire, which, as a preliminary, was loaded with internal pressure. This example in full measure represents the class of problems being considered. The shell has laminated structure and complicated geometric shape, variable thickness and inhomogeneous physical-mechanical properties both along the generatrix and across the thickness. These factors provoke the complex initial stress state even under the uniform action.

As the reference surface we will chose the inside surface of the shell. This surface has the shape of a torus with an elliptical cross-section, its half-axes are a and b, and distance to the axis of revolution is R_0. The shell can be divided conditionally into two segments with different thicknesses and different physical-mechanical properties: $\alpha \in [0, \alpha_1]$ and $\alpha \in [\alpha_1, \alpha_2]$, where the angle α characterizes the current position on the generatrix. On the first segment, the shell is composed of three layers. The inner layer with the thickness h_1 is made of orthotropic material with the characteristics $E_\alpha = 5.8E_0$, $E_\beta = E_\gamma = 0.12E_0$, $G_{\alpha\beta} = G_{\alpha\gamma} = 0.043E_0$, $G_{\beta\gamma} = 0.031E_0$, $\nu_\alpha = 0.42$, and $\rho = \rho_0$. The outer layer with the thickness h_3 is isotropic and has $E = 0.05E_0$, $\nu = 0.49$. The middle layer is composed of two orthotropic sublayers with the same thickness h_2, whose orthotropy axes in the sublayers are oriented relative to the shell generatrix

at angles of $\pm 70^0$. Its properties are $E_1 = 18.4E_0$, $E_2 = E_3 = 0.074E_0$, $G_{12} = G_{13} = 0.021E_0$, $G_{23} = 0.019E_0$, $\nu_{12} = 0.47$, and $\rho = 1.54\rho_0$, where indices 1 and 2 denote the principal elasticity directions of the orthotropic material. This layer as a whole is considered as structurally orthotropic and its characteristics are determined by the known formulas which are related to the turn of coordinate axes [Lechnitskii 1977]. In this case the rigidities connecting the tension-compression strains with twisting strains can be neglected due to the symmetric location of the orthotropic axes of the material in sublayers. The general thickness of the shell on this segment is $h = h_1 + 2h_2 + h_3$. On the second segment $\alpha \in [\alpha_1, \alpha_2]$, the shell is composed of one orthotropic layer with the thickness h_1 and characteristics $E_\alpha = 5.8E_0$, $E_\beta = E_\gamma = 0.12E_0$, $G_{\alpha\beta} = G_{\alpha\gamma} = 0.043E_0$, $G_{\beta\gamma} = 0.031E_0$, $\nu_\alpha = 0.42$, and $\rho = \rho_0$.

An initial stress-strain state of the shell is caused by the normal axisymmetric pressure of the intensity q.

Let us analyze the natural frequencies for the shell in the case of $R_0 = 217l_0$, $h_1 = 0.75l_0$, $h_2 = 1.4l_0$, $h_3 = 6.45l_0$, $\alpha_1 = 0.95\,\text{rad}$, $\alpha_2 = 2.168\,\text{rad}$ ($l_0 = 10^{-3}\,\text{m}$, $E_0 = 10^2\,\text{MPa}$, and $\rho_0 = 10^3\,\text{kg}\cdot\text{m}^{-3}$) as applied to the two following variants of geometric parameters: variant I, where $a = 84.6l_0$, and $b = 43.0l_0$ (elliptic-section torus), and variant II, where $a = b = 60.3l_0$ (circular-section torus).

The internal pressure causes in the shell the complex stress state. So, Figure 3a shows the distribution of dimensionless circumferential $\tilde{N}_\beta = N_\beta(\alpha)/g$ and meridional $\tilde{N}_\alpha = N_\alpha(\alpha)/g$ forces along the shell generatrix for two configurations (I, the elliptic cross-section, and II, the circular cross-section, $g = 10^3 q l_0$). In the case of an elliptic cross-section, the circumferential forces $\tilde{N}_\beta$ are dominating, moreover on the first segment they are two order higher then on the second one. At the point of the segment conjugation ($\alpha/\alpha_2 = 0.49$), we observe the jump attributed to the stepwise variation in the shell structure across

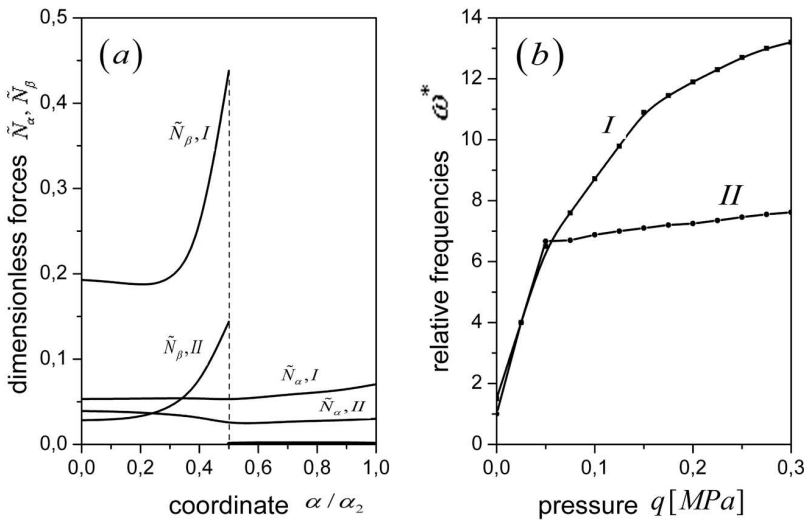**Figure 3.** Effect of the initial stress state on the natural frequencies of the toroidal shell. (a) The forces $\tilde{N}_\alpha$, I and $\tilde{N}_\beta$, I for an elliptic torus and the forces $\tilde{N}_\alpha$, II and $\tilde{N}_\beta$, II for a circular torus. (b) The dependency of minimum frequencies ω^* for elliptic ($i = \text{I}$) and circular ($i = \text{II}$) toruses on the internal pressure q.

the thickness. The meridional forces $\tilde{N}_\alpha$ are distributed along the generatrix nearly uniformly. The qualitative pattern of the force distribution for the circular torus is kept the same.

The natural frequencies of such a prestressed shell are determined depending on the value of the internal pressure q, which varies through the range [0; 0.3] MPa. The values of minimum frequencies for elliptic $\omega_{\mathrm{I}}(q)$ and circular $\omega_{\mathrm{II}}(q)$ toruses referred to the minimum frequency of the unloaded circular torus $\omega_{\mathrm{II}}(0)$ ($\omega^* = \omega_i(q)/\omega_{\mathrm{II}}(0)$, $i = \mathrm{I}$, II) are presented in Figure 3b.

For both variants of the geometry, the dependencies $\omega^* = \omega^*(q)$ are the monotonous piecewise smooth curves. Here inflection points correspond to the mode change at minimum frequency. If the internal pressure is low, difference in natural frequencies of both shells is negligibly small. With the pressure increasing ($q > 0.1$ MPa), difference in frequencies also increases and for $q = 0.3$ MPa frequencies of the elliptic torus exceed those for the circular one approximately by 70%.

5. Conclusions

The paper presents a numerical-analytical approach to the analysis of natural frequencies for middle-thickness inhomogeneous shells of revolution under axisymmetric loads. The approach includes the following points:

 (i) Formulation of the problem based on the nonclassic two-dimensional model of shells with allowance for transverse shears and reduction within the frame of the geometrically nonlinear theory.

 (ii) Decomposition of the problem into two interconnected problems: the problem on preliminary stresses in a shell under static loading and the problem on small shell vibrations with allowance for the preliminary stress-strain state.

(iii) Numerical-analytical technique for solving both problems using the following procedures:
  (a) Trigonometric Fourier series expansion along circumferential coordinate.
  (b) Inverse iterations method for solving eigenvalue problems.
  (c) Numerical orthogonal-sweep method for solving one-dimensional boundary-value problems.

The efficiency of the approach proposed is illustrated by the example of the inhomogeneous across the thickness nonthin cylindrical shell under localized loading in comparison with classical and shear models. It is shown that in analyzing the natural frequencies of a shell with the essential difference in physical-mechanical properties across the shell thickness (more than one order) and appreciable localization of static actions, it would be desirable to take into account not only transverse shears but also reduction.

We have analyzed the natural frequencies of a complicated pneumatic-tire shell system for two variants of cross-sectional configuration depending on the value of internal pressure. Calculation results are physically justified [Buchin 1988].

References

[Ambartsumyan 1961] S. A. Ambartsumyan, *The theory of anisotropic shells*, Nauka, 1961. In Russian.

[Bellman and Kalaba 1965] R. Bellman and R. Kalaba, *Quasi-linearization and nonlinear boundary-value problems*, Elsevier, 1965.

[Bespalova and Urusova 2007] E. I. Bespalova and G. P. Urusova, "Determining the natural frequencies of highly inhomogeneous shells of revolution with transverse strain", *Int. Appl. Mech.* **43**:5 (2007), 980–987.

[Bespalova et al. 1991] E. I. Bespalova, Y. M. Grigorenko, A. B. Kitaigorogskii, and A. I. Shinkar, "Free vibration of preloaded anisothropic shells of revolution", *Int. Applied Mechanics* **27**:5 (1991), 472–477.

[Buchin 1988] B. L. Buchin, *Introduction to mechanics of pneumatic tires*, Chimiya, 1988. In Russian.

[Godunov 1961] S. K. Godunov, "Numerical solution of boundary-value problems for systems of linear ordinary differential equations", *Uspekhi Mat. Nauk.* **16**:3 (1961), 171–174. In Russian.

[Grigorenko and Mukoed 1983] Y. M. Grigorenko and A. P. Mukoed, *Computer solution of nonlinear problems for shells*, Vyshcha Shkola, 1983. In Russian.

[Grigorenko and Rozhok 2003] Y. M. Grigorenko and L. S. Rozhok, "Discrete Fourier-series method in problems of bending of variable-thickness rectangular plates", *Journal of Engineering Mathematics* **46** (2003), 269–280.

[Grigorenko et al. 1986] Y. Grigorenko, E. I. Bespalova, A. B. Kitaigorodskii, and A. I. Shinkar, *Natural vibrations of elements in shell structures*, Naukova Dumka, Kiev, 1986. In Russian.

[Grigorenko et al. 1987] Y. M. Grigorenko, A. T. Vasilenko, and G. P. Golub, *Statics of anisotropic shells with finite shear stiffness*, Naukova Dumka, 1987. In Russian.

[Grigorenko et al. 2006] Y. M. Grigorenko, G. G. Vlaikov, and A. Y. Grigorenko, *Numerical-analytical solving the problems of shell mechanics on the basis of different models*, Akademperiodika, Kiev, 2006. In Russian.

[Hua and Lam 2000] L. Hua and K. Y. Lam, "The generalized differential quadrature method for frequency analysis of a rotating conical shell with initial pressure", *Int. J. for Numerical Methods in Engineering* **48**:12 (2000), 1703–1722.

[Kang 2007] J.-H. Kang, "Field equations, equations of motion, and energy functionals for thick shells of revolution with arbitrary curvature and variable thickness from a three-dimensional theory", *J. Acta Mechanica* **88**:1-2 (2007), 21–37.

[Karmishin et al. 1975] A. V. Karmishin, V. A. Lyaskovets, V. I. Myatchenkov, and A. N. Frolov, *Statics and dynamics of thin-walled shell structures*, Mashinostroenie, Moscow, 1975. In Russian.

[Kollatz 1963] L. Kollatz, *Eigenwertaufgaben mit technischen anwendungen*, Leipzig: Akademische Verlagsgesellschaft Geest und Portig K.–G., 1963.

[Lam and Hua 1997] K. Y. Lam and L. Hua, "Vibration analysis of a rotating truncated circular conical shell", *International Journal of Solids and Structures* **34**:17 (1997), 2183–2197.

[Lam and Hua 1998] K. Y. Lam and L. Hua, "Frequency characteristics of a thin rotating cylindrical shell using the generalized differential quadrature method", *International Journal of Mechanical Sciences* **40**:5 (1998), 443–459.

[Lam and Hua 2000] K. Y. Lam and L. Hua, "Influence of initial pressure on frequency characteristics of a rotating fruncated circular conical shell", *International Journal of Mechanical Sciences* **42**:2 (2000), 213–236.

[Lechnitskii 1977] S. G. Lechnitskii, *The theory of elasticity of anisotropic body*, Nauka, 1977. In Russian.

[Mushtari and Galimov 1957] K. M. Mushtari and K. Z. Galimov, *Nonlinear theory of elastic shells*, Tatknigoizdat, 1957. In Russian.

[Rao et al. 1974] G. V. Rao, V. Sundararamaiah, and I. S. Raju, "Finite element analysis of vibrations of initially stressed thin shells of revolution", *Journal of Sound and Vibration* **37**:1 (1974), 57–64.

[Redekop 2006] D. Redekop, "Three-dimensional free vibration analysis of inhomogeneous thick orthotropic shells of revolution using differential quadrature", *Journal of Sound and Vibration* **291**:3-5 (2006), 1029–1040.

[Sivadas 1995] K. R. Sivadas, "Vibration analysis of pre-stressed rotating thick circular conical shell", *Journal of Sound and Vibration* **186**:1 (1995), 99–109.

[Tan 1998] D.-Y. Tan, "Free vibration analysis of shells of revolution", *Journal of Sound and Vibration* **213**:1 (1998), 15–33.

[Wang and Redekop 2005] X. Wang and D. Redekop, "Natural frequencies and mode shapes of an orthotropic thin shell of revolution", *Thin-Walled Structures* **43**:5 (2005), 735–750.

[Wang et al. 1997] Y. Wang, X. Wang, and H. Song, "Nonlinear free vibration of orthotropic shallow shells of revolution under the static loads", *J. Appl. Mathematics and Mechanics* **18**:6 (1997), 585–591.

[Xi et al. 1996] Z. C. Xi, L. H. Lam, and T. Leung, "Semi-analytical study of free vibration of composite shells of revolution based on the Reissner–Mindlin assumption", *Int. J. of Solids and Structures* **33**:6 (1996), 851–863.

[Yuan and Liu 2007] H. Yuan and R.-H. Liu, "Nonlinear vibration of corrugated shallow shells under uniform load", *J. Appl. Mathemtics and Mechanics* **28**:5 (2007), 573–580.

ELENA BESPALOVA: Elena_Bespalova@ukr.net
Timoshenko Institute of Mechanics, National Academy of Sciences, 3, Nesterov str., Kiev 03057, Ukraine

GALINA URUSOVA: metod@inmech.kiev.ua
Timoshenko Institute of Mechanics, National Academy of Sciences, 3, Nesterov str., Kiev 03057, Ukraine

QUASISTATIC DEFORMATION AND FAILURE MODES OF COMPOSITE SQUARE HONEYCOMBS

BENJAMIN P. RUSSELL, VIKRAM S. DESHPANDE AND HAYDN N. G. WADLEY

Carbon fibre epoxy matrix composite honeycombs have been fabricated by slotting, assembling and adhesively bonding composite laminate sheets with various fibre architectures. Their out-of-plane compressive and in-plane shear responses were measured as a function of relative density, ratio of the cell height to width and the number of cells in the specimen. The measurements indicate that the response is relatively insensitive to the ratio of the cell height to cell width and number of cells in the specimen but is strongly dependent on the laminate type and fibre orientation. For example, the compressive strength of the honeycombs made from $0 - 90°$ laminates with fibres aligned with the compression direction was greater than that of honeycombs made from a woven material with fibres at $\pm 45°$. However, the shear strengths exhibited the opposite trend. These differences were attributed to a change in failure mode. In compression the honeycombs failed by either elastic buckling or plastic microbuckling while in shear the two main failure modes were elastic buckling or shear failure of the composite sheet material. Analytical models are derived for these collapse modes and used to predict the strength of the honeycomb structure. The predicted strengths are substantially higher than the measurements due to the presence of manufacturing imperfections in the honeycombs that are not accounted for in the analytical models. A limited finite element (FE) investigation is also reported to quantify the effects of imperfections on the compressive strength of the composite honeycombs. The measurements and analytical predictions reported here indicate that composite cellular materials such as honeycombs reside in a gap in the strength versus density material property space, providing new opportunities for lightweight, high strength structural design.

1. Introduction

The failure strength of sandwich panel structures depends upon many factors including the strength and thickness of the face sheets, the core topology and the parent material. A variety of polymeric foams and honeycombs are used for the cores of stiffness dominated designs. The need for higher strength, impact energy dissipating structures has stimulated the development of stronger metallic foams, see for example [Ashby et al. 2000]. These are mostly produced by the introduction of gas bubbles into the metal [Wadley 2002]. The bubble expansion process leads to random cellular structures, and minimization of surface energy leads to a low nodal connectivity, with typically three to four struts per joint. The resulting mechanical properties are far from optimal due to the fact that the cell walls deform by *local bending* [Deshpande et al. 2001a]. This led to a search for open-cell microstructures which have high nodal connectivities and deform by the *stretching* of constituent cell members, giving a much higher stiffness and strength per unit mass. These cellular solids, known as *lattice materials* — a term we define to

mean any micro-architectured cellular solid with straight webs or struts — have a stiffness and strength which scale linearly with relative density $\bar{\rho}$; in contrast, the Young's modulus and yield strength of metallic foams scale with $\bar{\rho}^2$ and $\bar{\rho}^{3/2}$, respectively. An example of a lattice material is the octet-truss structure with a face-centred cubic microstructure [Deshpande et al. 2001b]. Its joint connectivity is 12, and this spatially periodic material has the feature that the cell members deform by local stretching for all macroscopic loading states. Consequently, the specific mechanical properties (stiffness, strength, toughness and energy absorption) of the Octet-truss far exceed those of open-cell foams. Many variants of this structure have been explored and novel methods for their fabrication and multifunctional properties have been recently reviewed [Wadley 2006].

Examination of the modified Ashby material property chart [Ashby and Bréchet 2003] shown in Figure 1, indicates that aluminium foams and lattices occupy the low density region of material strength- density space. It also reveals a gap between the strength of existing lattice materials and the theoretical attainable material limit. Lattices fabricated from aluminium alloys have begun to extend the range of cellular materials into this gap in the material property space but it is clear that there remains much room for further improvements. Figure 1 illustrates how the combination of optimized lattice topology and parent
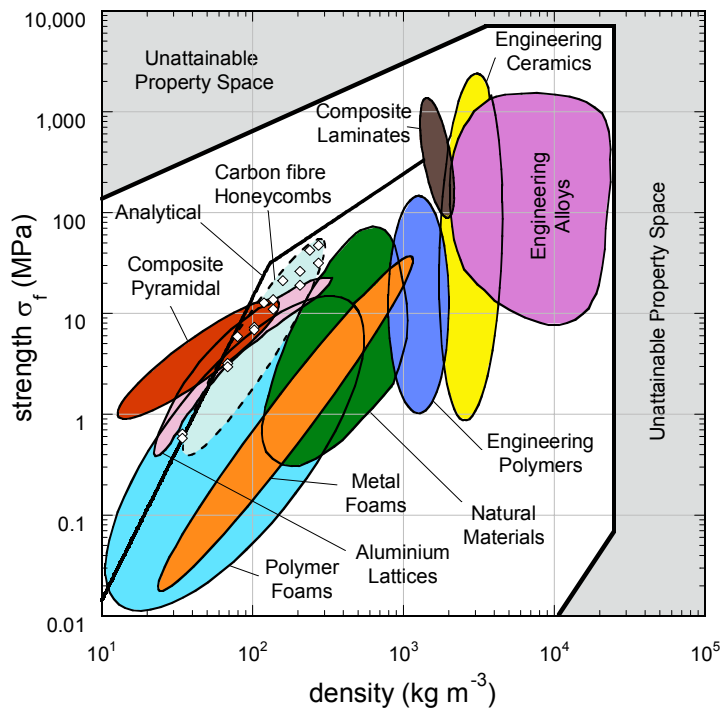

Figure 1. An Ashby material strength versus density map for engineering materials [Ashby and Bréchet 2003]. The map contains gaps between existing and unattainable materials. The maximum theoretical strength of composite square honeycombs is shown by the solid line marked *analytical*, which falls into the high specific strength gap at low densities. The measured properties of the composite honeycombs investigated here are also included.

material properties can be combined to expand material property space by creating new engineering materials or cellular structures. For instance, suppose composites containing fibres configured to provide high uniaxial specific strengths were used for the trusses or webs of a lattice structure. If buckling does not occur, the resulting lattice structures have anticipated compressive strengths that fill the gap in the strength versus density space for densities less than about $100 \, \mathrm{kg m^{-3}}$.

Continuous fibre polymer matrix composites such as carbon-epoxy systems have found extensive use as face-sheets in sandwich construction, particularly in aerospace and sports equipment applications. Typically carbon-epoxy laminate face-sheets are combined with an aluminium hexagonal honeycomb core: the high strength and stiffness per unit mass of carbon-fibre materials boost their ranking in face-sheet materials selection for light-weight structural applications. The use of composites as a core material is a natural progression for increasing the specific strength and stiffness of sandwich structures. The main examples include the Z-fiber and X-Cor[1] truss structures fabricated by angled carbon fibre rods embedded in a polymeric foam; and Nomex-phenolic resin honeycombs which find application in flooring panels for passenger aircraft. There exists little data on such sandwich core materials and that data suggests that the strength per unit mass of these sandwich cores is only marginally better than metallic structures [Marasco et al. 2006].

It is clear that topologically structuring composite materials shows promise for filling gaps in the strength versus density map of all known materials. The aim of the present study is to begin to investigate the expansion of *the strength – density material space* at low densities by using carbon fibre composites to build lattice materials. A related study explored the behaviour of carbon fibre composite lattice structures with an open cell pyramidal truss topology [Finnegan et al. 2007]. The measured peak compressive strengths from that study are included in Figure 1. Clearly the composite pyramidal lattices begin to fill a gap in the known material property space in that they have a strength greater than most known materials at densities less than $100 \, \mathrm{kg m^{-3}}$. However, the designs of the composite pyramidal cores in [Finnegan et al. 2007] do not achieve the full potential of composite lattice materials primarily due to the inefficient utilization of material in the nodes.

In general three classes of sandwich core architecture have been proposed: (i) prismatic cores, (ii) 3D trusses and (iii) honeycombs. The most suitable choice of sandwich core architecture depends upon the specific application. For example, trusses with their open celled architecture are ideal for multifunctional applications involving heat transfer in addition to load carrying capacity [Evans et al. 1998]. On the other hand, these sandwich cores have a low in-plane stretching strength. Thus, for panels subjected to large bending loads (where in in-plane core stretching is important), stretch resistant cores are superior to the truss cores. Traditionally, hexagonal honeycombs have been extensively employed in sandwich construction; see for example [Gibson and Ashby 1997]. However, hexagonal honeycombs also suffer from a low in-plane stretching strength. Square honeycombs overcome this drawback (at least for loadings along the directions of the cell walls) and thereby have promise for sandwich construction as demonstrated in a number of studies [Côté et al. 2004; Xue and Hutchinson 2004; Fleck and Deshpande 2004]. The out-of-plane compressive and shear deformation of carbon fibre composite square honeycombs is the focus of this study.

---

[1]Z-fiber and X-core are registered trademarks of Aztex Inc., Waltham, MA, USA.

The outline of the paper is as follows. First the composite sheet materials are described along with the route for fabricating the square-honeycombs cores from these materials. Second, the measured compressive and shear responses of the cores are detailed along with the observed failure modes. Analytical and finite element models are then developed for the elastic stiffness and collapse strengths of the composite honeycombs and these are compared with measurements. Finally, the measured strengths of the composite honeycombs are plotted on a map of density versus strength of all known materials in order to gauge the performance of these materials in terms of their strength to weight ratio.

2. Materials and manufacture

Square-honeycombs were manufactured from prefabricated composite sheet materials. The methodology follows closely that developed for metallic honeycombs by [Côté et al. 2004].

2.1. *Parent materials.* Two types of carbon fibre composite sheet material with an average sheet thickness $t = 0.355$ mm were employed in this study. One was a $\pm 45°$, 2×2 twill weave (3.7 tows per centimetre and 6000 fibres per tow) panel and the second was a laminate with a 4-ply symmetric balanced $[0°, 90°]$ lay-up. These two types of materials are referred to as the woven and laminate materials, respectively. In both cases, the composite sheets were made from T300-6k fibres (6–7.5 μm fibre diameter) and a high-heat resistant epoxy matrix (Fiberite 934). The as-fabricated densities of the woven and laminate composites were 1370 kgm^{-3} and 1590 kgm^{-3}, respectively.

2.2. *Manufacturing route.* Square-honeycombs were manufactured from composite sheets with a thickness $t = 0.355$ mm using a procedure similar to that developed for metallic honeycombs by [Côté et al. 2004]. The sheets were cropped into rectangles of height H in the range 26.0 to 124.8 mm and length of 37.8 mm to 256.2 mm. Cross-slots (Figure 2) of width $\Delta t = 0.40$ mm and spacing L in the range 5.2 mm to 41.6 mm, were cut using a 2-axis micromill with a mill head capable of cutting slots widths $\Delta t \geq 200$ μm. The 45 μm difference between sheet thickness and slot width facilitated assembly while providing a sufficiently tight fit to assure stability. The slotted rectangles were assembled into the square-honeycomb configuration (Figure 2) and adhesively bonded using a low viscosity epoxy resin (Opti-tec 5001[2]). The assembly was then cured at 65° C for 1 hour. Mild steel face sheets of thickness 3 mm were finally bonded to the top and bottom faces of the honeycomb using a nylon backed film epoxy (Redux 319[3] with an areal density 400 gm^{-2}) and the entire assembly again oven cured at 175° C for 1 hour.

The relative density $\bar{\rho}$ of the square-honeycomb is to first order given by

$$\bar{\rho} = \frac{2t}{L},\tag{1}$$

and honeycomb specimens of different densities were manufactured by varying the cell size L while keeping the wall thickness always fixed at the sheet thickness $t = 0.355$ mm. An example of a manufactured square-honeycomb (without the steel face-sheets) made from the woven material with $\bar{\rho} = 0.05$, comprising 6×6 cells and a cell aspect ratio $H/L = 3$ is shown in Figure 3.

---

[2]Intertronics, 17 Station Field Industrial Estate, Banbury Road, Kidlington, Oxfordshire, OX5 1JD, UK.
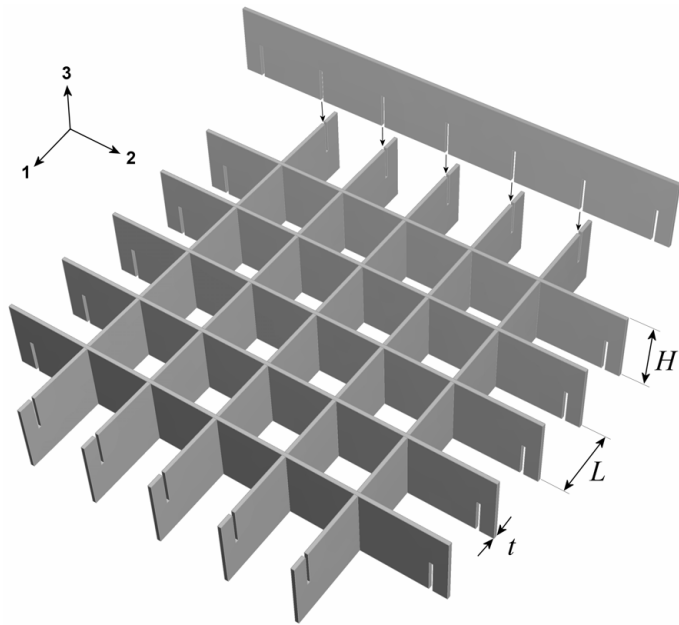[3]Hexcel Composites, Duxford UK.

Figure 2. Sketch of the square-honeycomb manufacturing technique. The coordinate system associated with the honeycomb and the notation used to indicate the dimensions of the honeycomb are also shown.
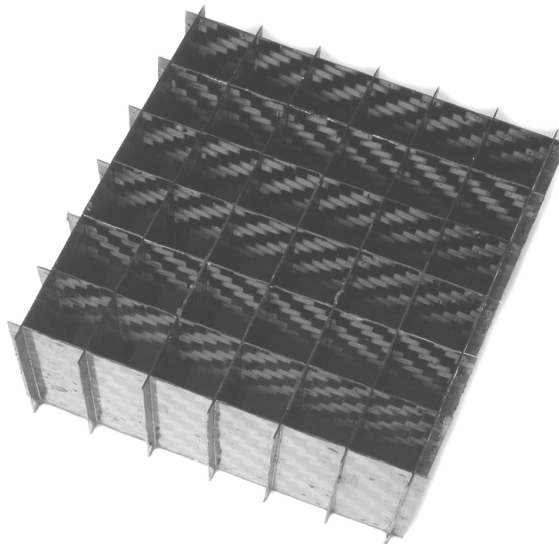

Figure 3. Photograph of the $\bar{\rho} = 0.05$ square-honeycomb made from the 0–90° woven material and comprising 6×6 cells with a cell aspect ratio $H/L = 3$.
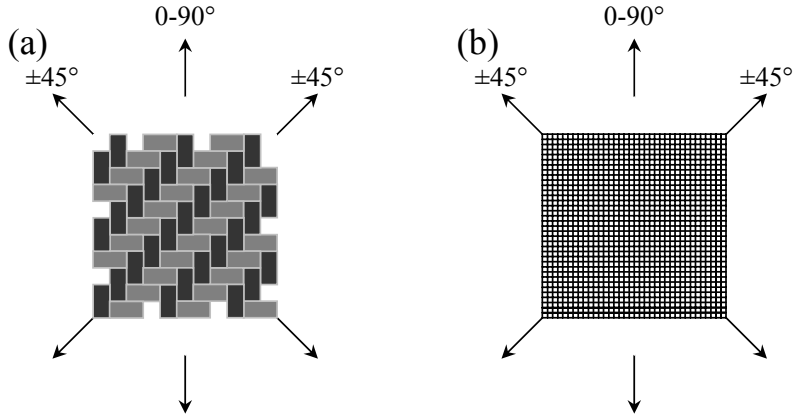
Figure 4. Sketch illustrating the 0–90° and ±45° orientations in which compression and tensile tests were conducted on the parent (a) woven and (b) laminate materials.

3. Mechanical measurements

3.1. *The parent materials.* Tensile and compression tests were conducted on the woven and laminate materials in two directions, labelled 0–90° and ±45° in Figure 4. The angles denote the directions along which the fibres lie with respect to the tensile or compression axes.

Rectangular tensile specimens of dimension 20 mm × 140 mm were cut from the composite sheets and aluminium tabs of dimension 20 mm × 40 mm were bonded to the ends of the specimens to facilitate gripping. Tensile tests were conducted in a screw driven test machine at an applied nominal strain rate 10^{-3} s^{-1} with the applied load measured via the load cell of the test machine and the strain inferred from displacements measured using a laser interferometer. The measured tensile responses in the 0–90° and ±45° directions are plotted in Figure 5. In the 0–90° direction the composites exhibit an approximately

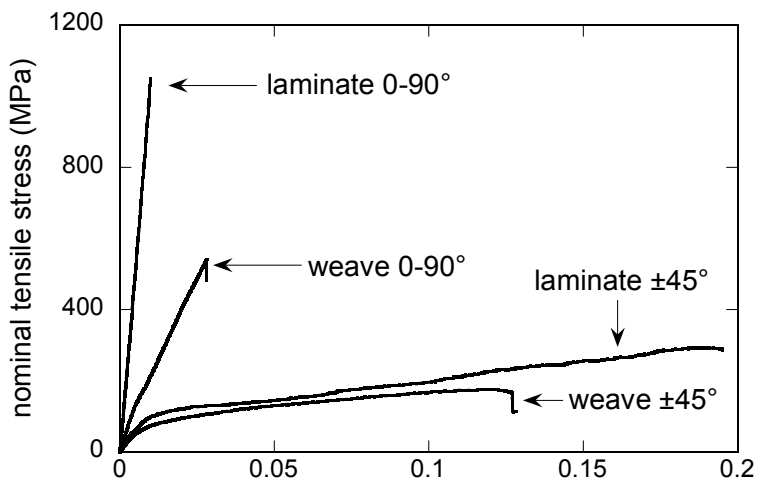**Figure 5.** The measured uniaxial tensile responses of the woven and laminate composite materials in the 0–90° and ±45° orientations.

linear response prior to failure. The peak strengths of the woven and laminate materials were 558 MPa and 1.05 GPa, respectively and their corresponding tensile ductilities 2.98% and 0.97%. Both materials exhibited significantly greater ductility when loaded in the ±45° direction with failure strains of 12% and 19% for the woven and laminate materials, respectively. However, this was accompanied by significantly reduced peak strengths of 161 MPa (woven) and 294 MPa (laminate). These differences arise from the fibre orientation: in the ±45° direction, matrix deformation dominates the response, while in the 0–90° direction the is load primarily sustained by the fibres.

The small sheet thickness of the composites employed in this study meant that it was difficult to conduct standard Celanese type compression tests on these materials while avoiding macrobuckling of the specimens. Thus, the specimens were tested using a sandwich column configuration as sketched in Figure 6a. The sandwich specimens were constructed by epoxy bonding the composite sheets to an aluminium hexagonal honeycomb core of relative density 6%, cell size 6.35 mm and wall thickness 0.381 mm. These specimens were then cut into a dog-bone configuration with dimensions as sketched in Figure 6a. This configuration had a high bending stiffness to obviate the possibility of macrobuckling. Moreover, the in-plane compression of the hexagonal honeycomb core had a negligible contribution to the measured loads. Strain gauge rosettes were bonded to both face-sheets of the sandwich column to measure the compressive strains in the face-sheets (and their Poisson expansion) and the stress in each of the composite sheets was deduced from the load cell of the test machine. The compression tests were conducted at an applied nominal strain rate $10^{-3}\,\mathrm{s}^{-1}$. The strains in both face-sheets were observed to be within 10% of each other. This confirmed that the sandwich columns underwent negligible bending and thus the measurements are representative of the compressive responses of the composite sheets. The compressive stress versus strain responses of the woven and laminate sheet materials in the 0–90° and
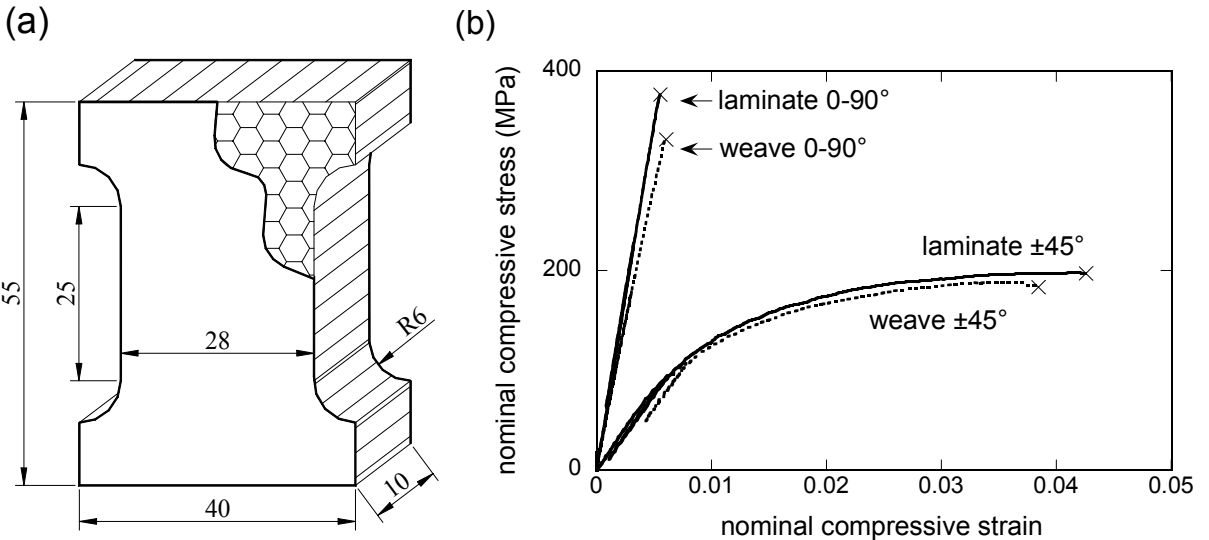

Figure 6. (a) Sketch of the sandwich column configuration used to conduct compression tests on the composite sheet materials. All dimensions are in mm. (b) The measured uniaxial compressive responses of the woven and laminate composite materials in the 0–90° and ±45° orientations.

$\pm 45°$ directions are plotted in Figure 6b. Similar to the tensile responses, the composite sheets have a high strength but low failure strain in the 0–90° direction and vice-versa in the $\pm 45°$ direction. Interestingly, both the woven and laminate materials have approximately the same compressive strength in the 0–90° direction suggesting that fibre waviness even in the laminates significantly reduces its peak compressive strength. We note that in the 0–90° direction, the composite sheets have a lower compressive strength compared to the tensile strength due to the fact that the tensile strength is governed by the failure strength of the fibres while the compressive strength of the materials is governed by fibre waviness which causes microbuckling failure of the composite materials.

3.2. *Compressive response of the honeycombs.* Compressive tests were conducted on the composite square honeycombs to investigate the effects of (i) relative density $\bar{\rho}$, (ii) parent material type and orientation, (iii) cell geometry as characterized by the aspect ratio H/L and (iv) number of cells in the compressive test specimen. The compression tests were conducted in a screw driven test machine at a nominal applied strain rate $10^{-3} \, \text{s}^{-1}$. The compressive stress was inferred from the load cell output of the test machine while the average compressive strain was deduced from laser inferometer measurements of the relative approach of the two steel face sheets of the test specimens. A few loading-unloading cycles were conducted during each test in order to infer the compressive Young's modulus of the honeycombs. At least one repeat test was conducted on each of the specimens in order to confirm the repeatability of the results presented subsequently.

3.2.1. *Effect of specimen geometry.* The majority of the tests were conducted on square-honeycomb specimens manufactured from the woven composite material oriented such that one set of fibres was aligned with the compression direction; such square-honeycombs are referred to as the 0–90° woven honeycombs and the effect of specimen geometry is investigated using these types of honeycombs. The

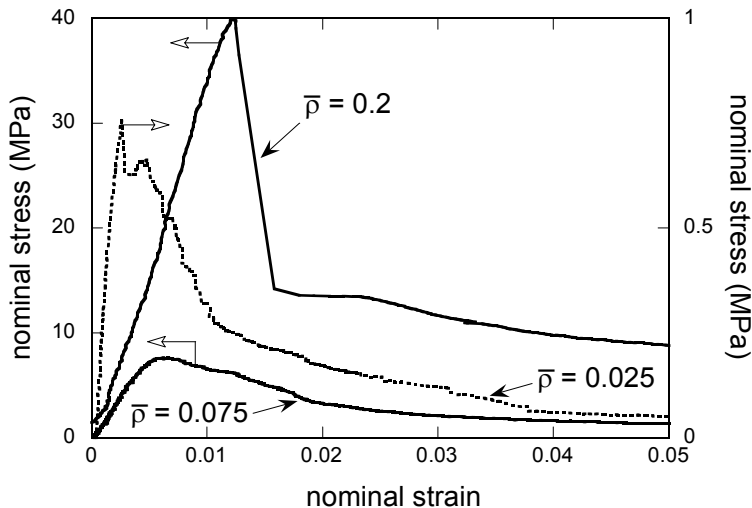**Figure 7.** Measured compressive stress versus strain response of the honeycombs made from the 0–90° woven composite material for selected values of the specimen relative densities $\bar{\rho}$. All measurements are reported on specimens with 6×6 cells and $H/L = 3$.

$\bar{\rho}$	aspect ratio (H/L)		
	1	**3**	**5**
0.025	6×6	$4 \times 4, 6 \times 6$	–
0.05	6×6	$4 \times 4, 6 \times 6, 12 \times 12$	–
0.075	6×6	$4 \times 4, 6 \times 6, 12 \times 12$	–
0.1	6×6	$4 \times 4, 6 \times 6, 12 \times 12$	6×6
0.15	–	$4 \times 4, 6 \times 6, 12 \times 12$	6×6
0.2	–	$4 \times 4, 6 \times 6, 12 \times 12$	6×6

Table 1. List of the types of square-honeycomb specimens made from the woven composite material (0–90° orientation) that were manufactured and tested in compression in this study. The number of cells in each of the specimen types is indicated in the table.

range of 0–90° woven honeycomb specimens investigated here are summarized in Table 1 (the table lists the number of cells in the specimen for each value of H/L and $\bar{\rho}$ investigated). The range of samples tested was limited by the use of sheets with a thickness $t = 0.355$ mm to make all specimens. This implies that (i) low density specimens with a high value of H/L are extremely large and thus impractical to test in a laboratory setting (e.g. $\bar{\rho} = 0.025$ and $H/L = 5$) and (ii) high density specimens with a low value of H/L are too small to manufacture with any degree of accuracy (e.g. $\bar{\rho} = 0.2$ and $H/L = 1$). Even so, a sufficiently wide range of specimen geometries were tested to make the necessary inferences about the effects of specimen geometry. The reference test geometry comprised 6×6 cells with an aspect ratio $H/L = 3$. Unless otherwise specified, this reference geometry was employed in all tests.

The measured compressive stress versus strain response of the 0–90° woven honeycombs is plotted in Figure 7 for selected values of the relative density $\bar{\rho}$. The response is reasonably linear up to the peak stress. The subsequent softening beyond the peak stress is rather dramatic for the $\bar{\rho} = 0.2$ case suggesting a microbuckling failure of the composite sheets. By contrast, the stress falls more gradually for the lower density honeycombs suggesting a failure by elastic buckling of the honeycomb webs.

Evidence for buckling is seen in the montage of photographs of the $\bar{\rho} = 0.05$ specimen at selected levels of applied compressive strain (Figure 8a). The associated compressive stress versus strain curve is plotted in Figure 8b. The deformation of the cell walls is essentially uniform for strains less than about 0.3%. Distinct wrinkling of the cell walls is observed at larger strains due to the onset of buckling. Now consider the $\bar{\rho} = 0.2$ honeycomb. As discussed above we anticipate that the high density honeycombs ($\bar{\rho} = 0.2$) undergo microbuckling failure. However, this mode of failure is not evident in the image shown in Figure 9a, as the cell walls towards the edge of the specimen are unconstrained and thus undergo a macrobuckling collapse mode. However, we expect the constrained cell walls in the interior of the
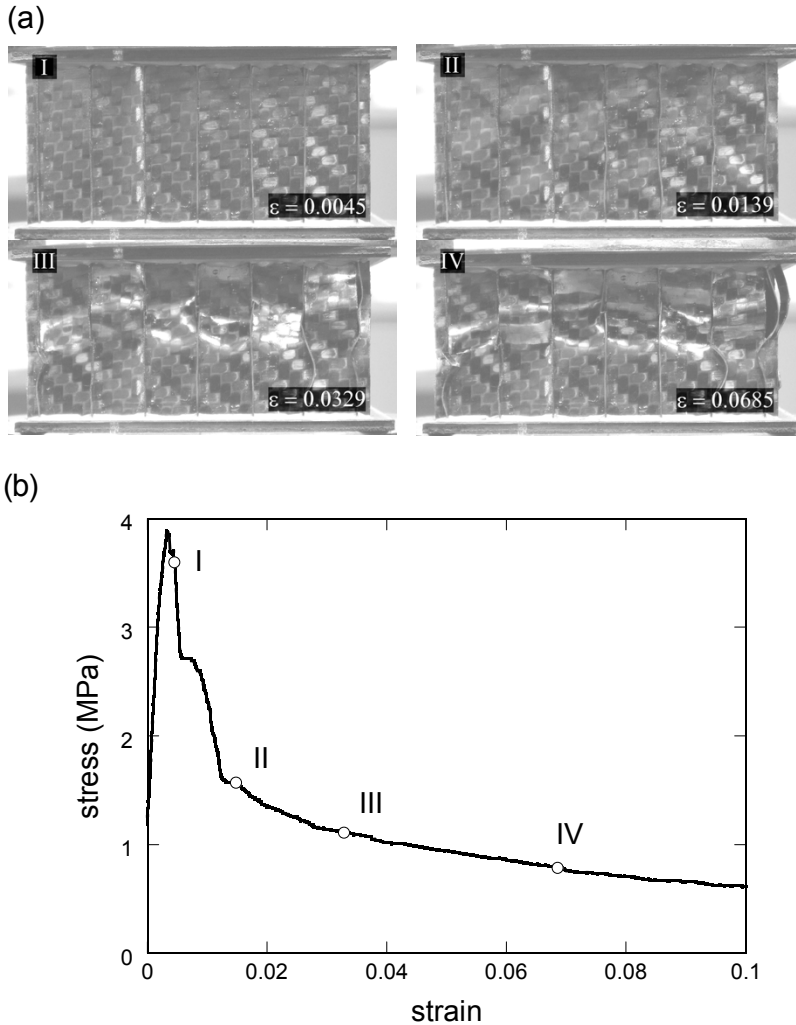
Figure 8. (a) Photographs at selected values of the compressive strain ε showing the compressive deformation mode of the $\bar{\rho} = 0.05$ honeycomb made from the 0–90° woven composite material. (b) Associated measured compressive stress versus strain response.

specimen to fail by microbuckling. In order to test this hypothesis we used X-ray tomography to observe the failure mechanism in the $\bar{\rho} = 0.2$ ($H/L = 3$) specimen comprising 4×4 cells. The specimen was compressed using the fixture sketched in Figure 10. The specimen was first compressed to the required strain in the screw-driven test machine and the bolts on the fixture tightened so that the specimen did not unload upon removal from the test machine. The specimen was then scanned using a X-ray tomography system. This procedure was repeated for four values of applied strain as marked on the measured stress versus strain response included in Figure 9b. The X-ray images along the two sections marked in Figure 9a are shown in Figure 11 at the four levels of applied strain indicated in Figure 9b. The contrast between the middle and edge of the specimen is evident in Figure 11: (i) the cell walls bend near the edge of the specimen, prior to the peak stress, while they remain straight in the middle of the specimen; (ii) just
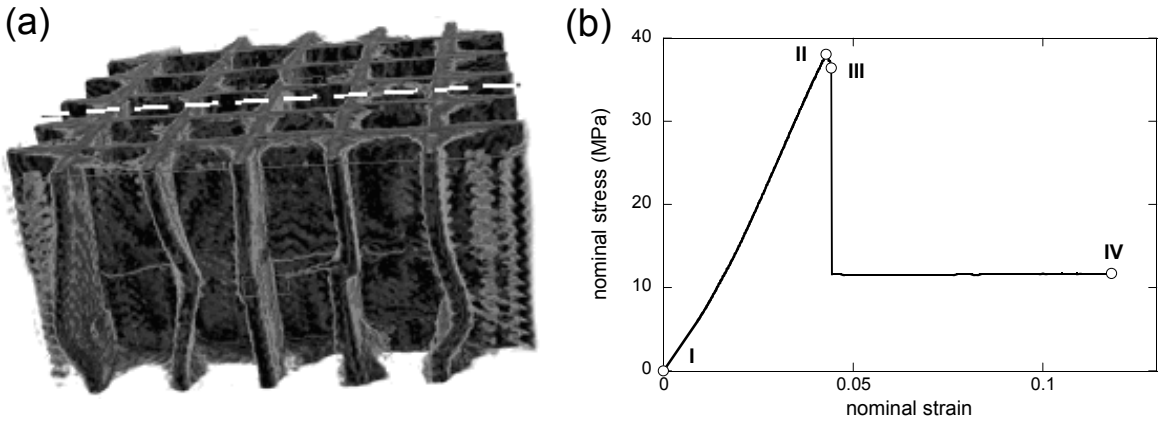
Figure 9. Compressive deformation modes of the $\bar{\rho} = 0.2$ honeycomb made from the 0–90° woven composite material. The specimen comprised 4×4 cells. (a) Photograph of the specimen deformed to a strain $\varepsilon = 0.12$. The sections along which the X-ray images are taken are also marked. (b) The measured compressive stress versus strain response with the strains at which X-ray images were taken labelled on the plot.
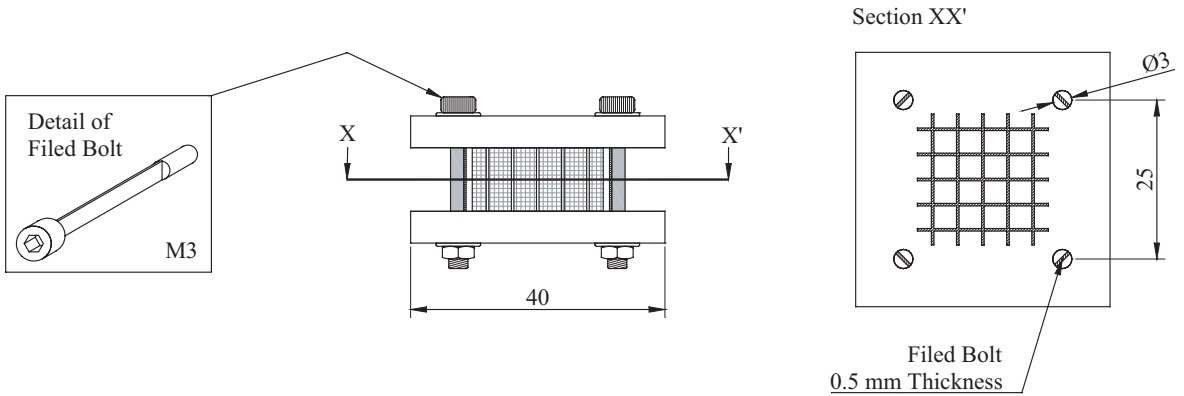

Figure 10. Sketch of the fixture used to compress the specimen used and then scan in X-ray tomography system. The fixture prevents unloading of the specimen when it is removed from the test machine.

beyond the peak stress a small kink is seen to develop in the cell walls in the middle of the specimen that is reminiscent of a microbuckle failure.

The measured unloading modulus E and peak stresses σ_p of the honeycomb specimens with 6×6 cells are plotted in Figure 12 as a function of the relative density $\bar{\rho}$, for three values of H/L. Note that for $H/L = 1$ and $H/L = 5$ data does not exist for some values of $\bar{\rho}$, as detailed in Table 1. Nevertheless the trends are clear: both E and σ_p increase approximately linearly with increasing $\bar{\rho}$ while the cell aspect ratio H/L has a negligible effect for the range of aspect ratios considered here.
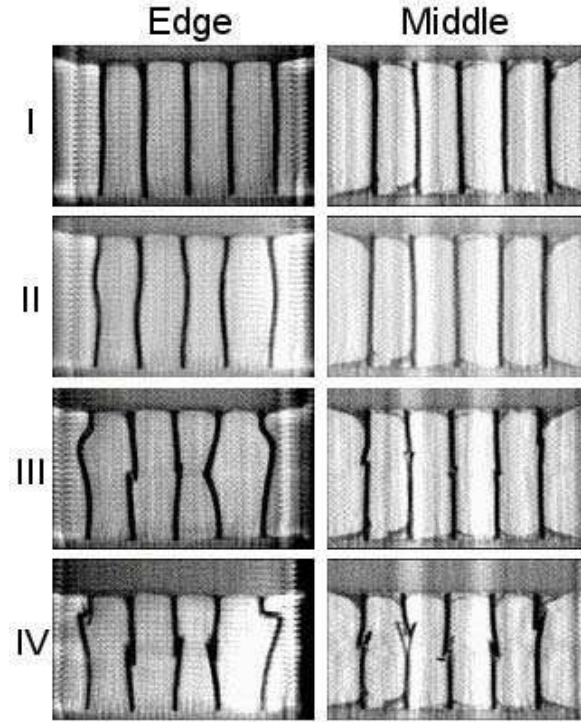
Figure 11. X-ray images of the honeycomb specimen along the two sections marked in Figure 9a and strain values indicated in Figure 9b.
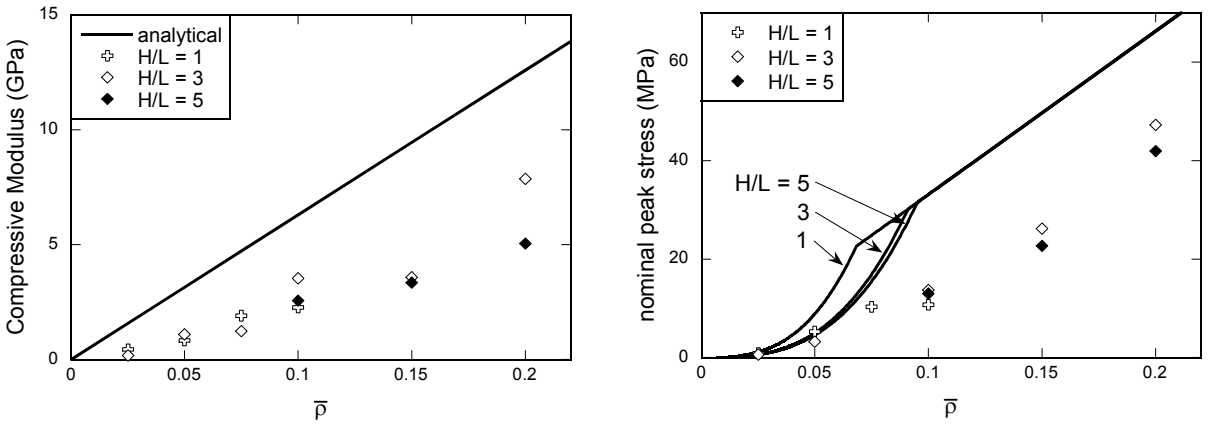
Figure 12. The measured Young's modulus E (left) and peak strength σ_p (right) of the honeycombs made from the 0–90° woven composite material as a function of the relative density $\bar{\rho}$. Measurements are shown for specimens comprising 6×6 cells and selected values of the aspect ratio H/L. The predictions of the analytical models are also included as solid lines.

Figure 13. Measured peak strength σ_p of the honeycombs made from the 0–90° woven composite material as a function of the relative density $\bar{\rho}$. Measurements are shown for specimens with a cell aspect ratio $H/L = 3$ and for specimens with 4×4, 6×6 and 12×12 cells. Predictions of the analytical model are also included.

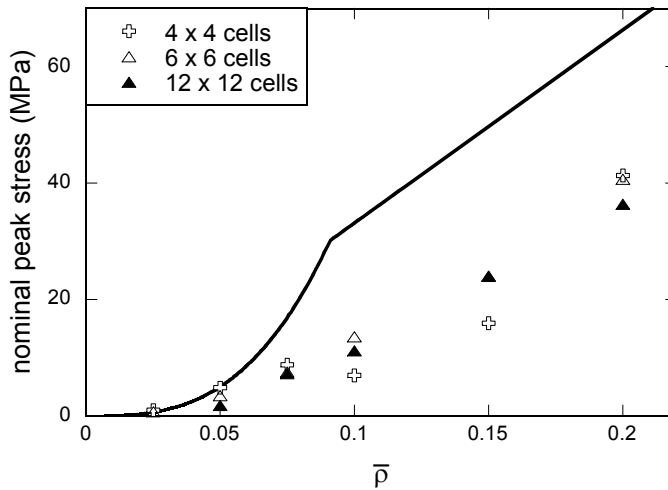The X-ray tomographs in Figure 11 show that the deformation modes of the cell walls in the middle of the specimen and towards the specimen edge differ substantially. This suggests that the measured compressive response of the honeycombs might be sensitive to the number of cells in the specimens. In addition to the reference value of 6×6 cells, tests were conducted on honeycomb specimens comprising 4×4 and 12×12 cells, all with an aspect ratio $H/L = 3$. The measured peak stresses σ_p from these tests are plotted in Figure 13 as a function of $\bar{\rho}$. The measurements from specimens with 6×6 and 12×12 cells are almost identical confirming that the reference specimen employed in this study provides data that is reasonably independent of the number of cells in the specimens. However, the measured peak strengths from the specimens with 4×4 cells were slightly lower than those of the 6×6 and 12×12 cell specimens suggesting that edge effects play a more dominant role in the deformation of the 4×4 (and smaller) cell specimens.

3.2.2. *Effect of material type and orientation.* The measured compressive stress σ versus strain ε response of the composite square honeycombs made from the laminate material with fibres at 0–90° with respect to the compression axis and the woven composite material oriented in the $\pm 45°$ direction (such that the fibres were at $\pm 45°$ with respect to the compression direction) are plotted in Figure 14 for selected values of $\bar{\rho}$. These measurements were conducted on the reference specimen geometry comprising 6×6 cells with $H/L = 3$. Consistent with the measured compressive responses of the materials (Figure 7), the honeycombs made from $\pm 45°$ weave have a lower strength compared to the 0–90° laminate honeycombs. On the other hand, the $\pm 45°$ woven honeycombs display a more gradual softening beyond the peak stress compared to the 0–90° laminate honeycombs. This is because the compressive response of the 0–90° laminate is dominated by the compression of the fibres, while that of the $\pm 45°$ weave is dominated by matrix deformation.
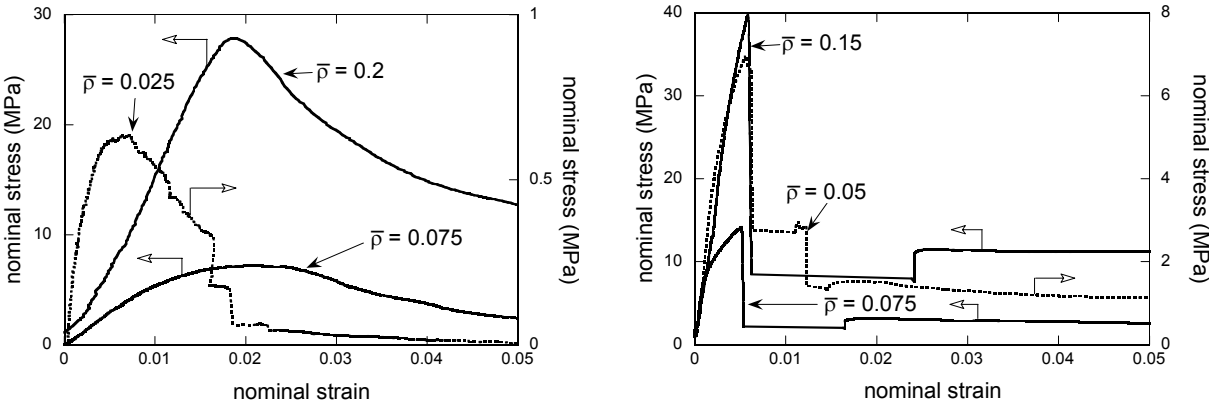
Figure 14. The measured compressive stress versus compressive strain responses of the honeycombs made from the $\pm 45°$ woven material (left) and the 0–90° laminate material (right). Results are shown for selected values of $\bar{\rho}$ for specimens comprising 6×6 cells and a cell aspect ratio $H/L = 3$.
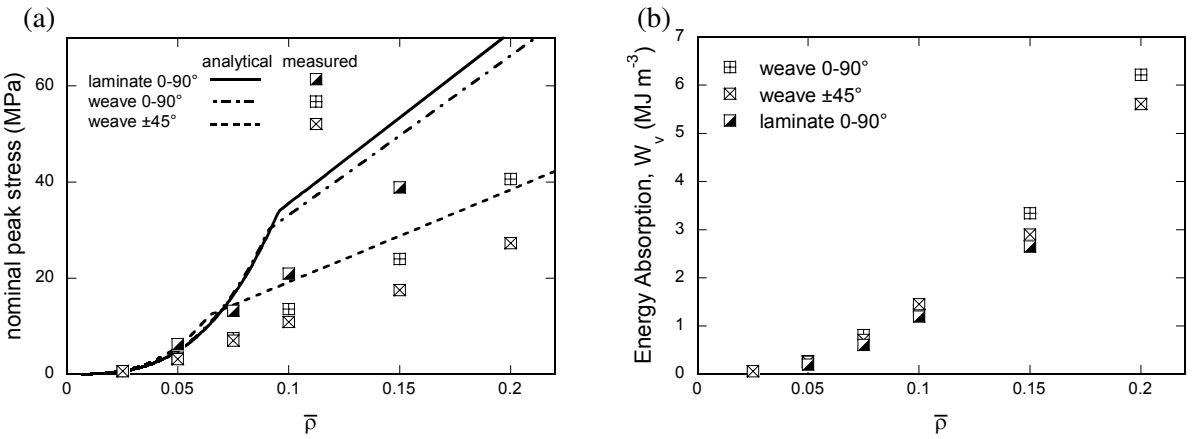
Figure 15. A comparison of the measured (a) peak compressive strengths σ_p and (b) energy absorption capacities per unit volume W_v of the honeycombs made from the $\pm 45°$ woven, 0–90° woven and 0–90° laminate materials as a function of $\bar{\rho}$. The measurements are for specimens comprising 6×6 cells and a cell aspect ratio $H/L = 3$, compressed to a strain of 40%.

The measured peak compressive strengths of honeycombs (reference geometry) made from the 0–90° weave, 0–90° laminate and $\pm 45°$ weave are compared in Figure 15a for relative densities in the range $0.025 \leq \bar{\rho} \leq 0.2$. Consistent with our expectations from the measured compressive responses of these materials (Figure 7) we observe that for a given value of $\bar{\rho}$ the 0–90° laminate has the highest value of σ_p followed by the 0–90° weave with the honeycomb made from the $\pm 45°$ having the lowest value of peak strength. However, recall that honeycombs made from materials with the 0–90° fibre orientation

typically undergo a catastrophic collapse beyond the peak stress and loose all energy absorption capacity, while the honeycombs made from the $\pm 45°$ woven materials have a more benign response beyond the peak stress. These differences are expected to alter the rankings of the materials in terms of their energy absorption capacity per unit volume W_v defined as

$$W_v = \int_0^{\bar{\varepsilon}} \sigma \, d\varepsilon. \tag{2}$$

W_v is plotted in Figure 15b with the choice of strain $\bar{\varepsilon} = 0.4$ as a function of $\bar{\rho}$ for the three configurations considered in Figure 15a. The results indicate that honeycombs made from the 0–90° weave, 0–90° laminate and $\pm 45°$ weave all have approximately the same energy absorption capacity per unit volume over the range of $\bar{\rho}$ investigated here. This is rationalised by noting that the lower peak strength of the $\pm 45°$ woven honeycomb is compensated by its higher energy absorption beyond its peak stress compared to the honeycombs with a 0–90° fibre orientation.

3.3. *Shear response of the honeycombs.*

A more limited study was conducted to investigate the out-of-plane shear stress τ_{31} versus shear strain γ_{31} response of the composite honeycombs made from the woven material with a cell aspect ratio $H/L = 1$. The shear tests were conducted using a single-lap shear set-up (Figure 16) in accordance with the ASTM standard C273-00 [ASTM 2000] for shear tests on sandwich cores. The standard demands a specimen aspect ratio $\ell/H \geq 12$, where ℓ is the length of the specimen as shown in Figure 16. The shear specimens investigated here comprised 14 and 4 cells along the length and width, respectively. Thus, in line with the requirements of the ASTM standard, the shear specimens employed here have an aspect ratio $\ell/H = 14$. The shear tests were performed on a screw driven test machine at an applied macroscopic nominal shear strain-rate of $10^{-3} \, \mathrm{s}^{-1}$. The load was measured by the load cell of the test machine and was used to define the nominal shear stress, while a clip gauge mounted on the single-lap shear test fixture was employed to measure the relative displacement between the two faces of the square honeycomb specimens and thereby give the applied shear strain. Load/unload cycles were also conducted during these tests in order to extract the unloading shear moduli of the specimens.

The measured shear responses of the honeycombs made from the 0–90° and $\pm 45°$ woven materials are plotted in Figure 17. Again, in the 0–90° orientation one set of fibres are aligned with the plane of shear while in the $\pm 45°$ orientation the fibres are at $\pm 45°$ with respect to this plane. Three relative densities $\bar{\rho} = 0.025, 0.05$ and 0.1, were investigated. The 0–90° specimens display a ductile response

Figure 16. Sketch of the single-lap shear set-up with the critical dimensions labelled.
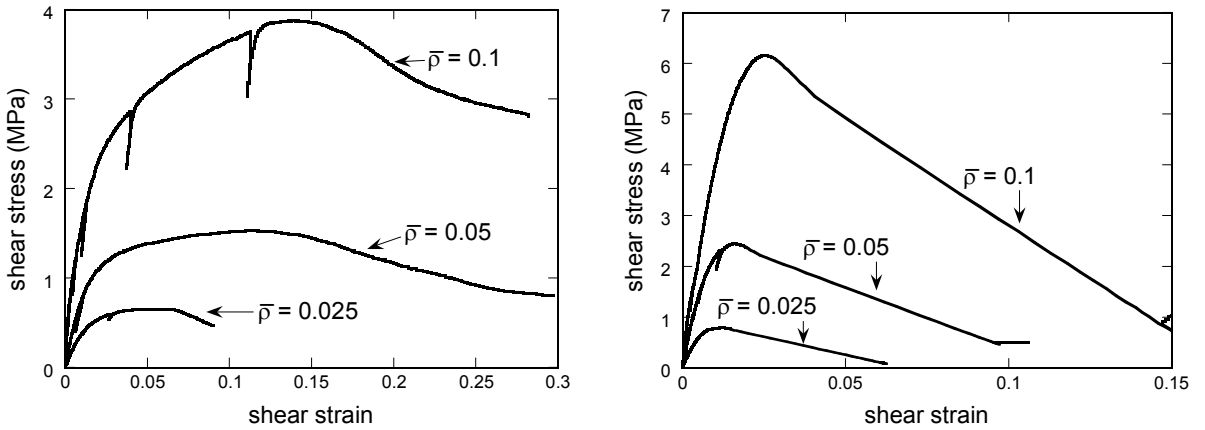
Figure 17. The measured shear stress versus shear strain response of the honeycombs made from the 0–90° (left) and ±45° (right) woven materials at selected values of $\bar{\rho}$. All the shear specimens comprised 14×4 cells with a cell aspect ratio $H/L = 1$.

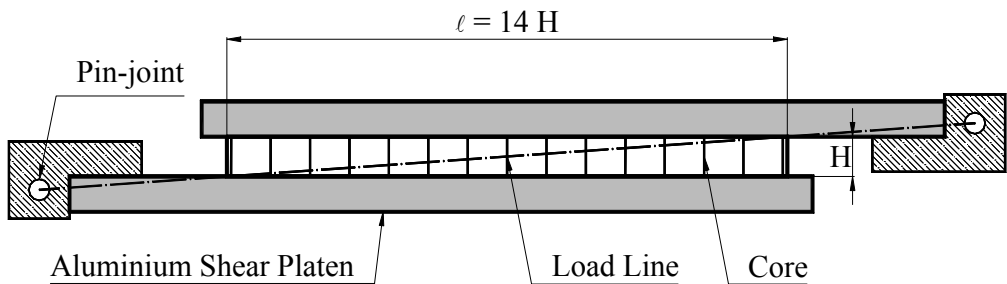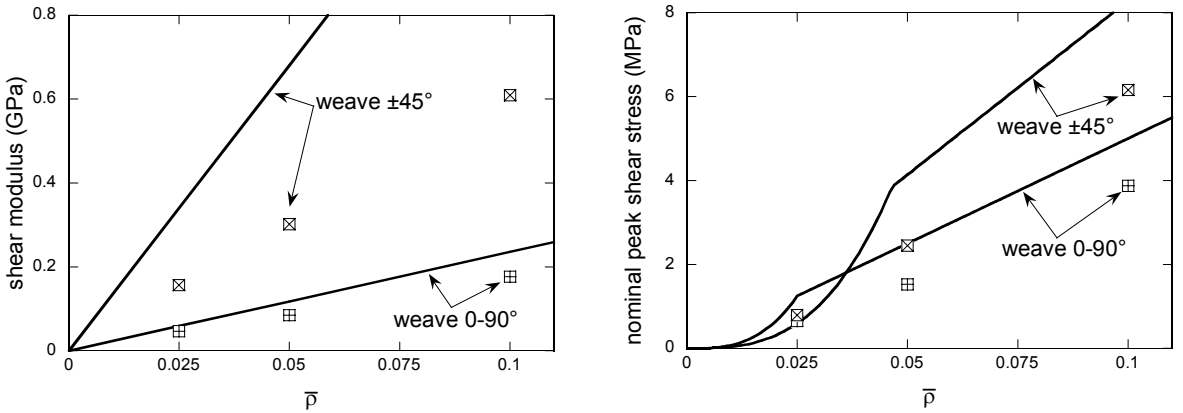**Figure 18.** The measured shear modulus (left) and peak shear strength τ_p (right) of the honeycombs made from the 0–90° and ±45° woven materials. The predictions of the analytical model are also included as solid lines.

reminiscent of the tensile and compressive response of the ±45° woven material (Figures 5 and 6b). By contrast, the ±45° specimens display a stiff linear response up to their peak strength similar to the tensile and compressive responses of the woven material in the 0–90° orientation; post-peak a strongly softening response is observed. Moreover, the ±45° specimens have a significantly higher peak shear strengths compared to equal density 0–90° honeycomb specimens. These results clearly indicate that the shear response of the 0–90° specimens is dominated by the deformation of the matrix of the woven composites while the fibres govern the shearing of ±45° specimens. The measured shear moduli and peak shear strengths are plotted in Figure 18 as a function of $\bar{\rho}$. The modulus and strength of both the 0–90° and ±45° specimens increases with increasing $\bar{\rho}$ with the ±45° honeycombs being stiffer and stronger than the 0–90° honeycombs.

4. Analytical models for the compressive and shear response

Approximate expressions can be derived for the elastic properties and collapse strengths of the composite honeycombs subject to the compressive and shear loadings described above. The properties for the composite sheet are denoted by a subscripted s.

4.1. *Compression response.* Under compressive loading, all cell walls of the honeycomb are equally loaded. Thus, when the honeycomb is subjected to an out-of-plane compressive stress, σ, each cell wall is subjected to a line load P per unit length

$$P = \sigma \frac{L}{2},\tag{3}$$

where L is the cell width (Figure 2). The Young's modulus E of the square honeycombs then follows as

$$\frac{E}{E_{3s}} = \bar{\rho},\tag{4}$$

where E_{3s} is the Young's modulus of the composite sheet material in the x_3-direction.

The peak compressive strength of the honeycombs is governed by a competition between (i) elastic buckling and (ii) plastic microbuckling of the cell walls. We consider each of these modes in turn.

A recent experimental study [Côté et al. 2004] on the compressive collapse of square honeycombs made from type 304 stainless steel suggests that the elastic buckling mode resembles torsional-axial buckling of a square tube, as shown in Figure 19 representing a view of a section through the plane normal to x_3. We expect this mode to exist for the composite honeycombs investigated here. This buckling mode is modelled by the buckling of a single plate with fully clamped top and bottom edges and simply supported sides. [Ericksen and March 1958] have analysed this reduced problem for a plate
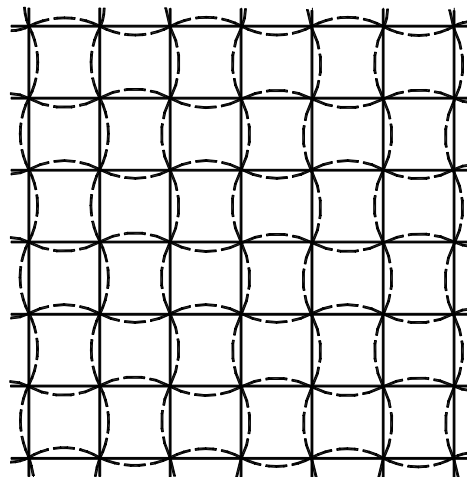

Figure 19. Sketch of the torsional buckling mode of the square honeycombs used in deriving the analytical models for the elastic buckling of the honeycombs. The undeformed honeycomb is shown by the solid lines and the buckle shape sketched with dashed lines.

made from orthotropic faces, and use their analytical results directly. The bifurcation line load reads

$$P_{\text{buck}} = \frac{K\pi^2 D}{L^2}, \tag{5}$$

where K is a buckling coefficient as prescribed by [Ericksen and March 1958] and D is the bending stiffness of the composite cell wall. In our problem, we assume the composite to be an orthotropic material and the appropriate bending stiffness D is given as

$$D = \frac{\sqrt{E_{1s} E_{3s}}}{1 - \nu_{13s}\nu_{31s}} \frac{t^3}{12}, $$

where E_{is} and ν_{ijs} are the Young's modulus and Poisson's ratios of the orthotropic faces along the $x_i = (x_1, x_3)$ directions as defined in Figure 2. For both the 0–90° and ±45° materials the Young's moduli are equal along directions x_1 and x_3.

The formula for the buckling coefficient K is explicit and for the assumed buckling mode sketched in Figure 19 is given by

$$K = \left(\frac{3H^2}{4L^2} \sqrt{\frac{E_{1s}}{E_{3s}}} + 2\beta + \frac{41L^2}{5H^2} \sqrt{\frac{E_{3s}}{E_{1s}}} \right), \tag{6}$$

where β is given in terms of the shear modulus G_{13s} as

$$\beta = \frac{1 - \nu_{13s}\nu_{31s}}{\sqrt{E_{1s} E_{3s}}} \left(\frac{E_{1s}\nu_{31s}}{1 - \nu_{13s}\nu_{31s}} + 2G_{13s} \right). \tag{7}$$

The elastic buckling stress of the honeycomb then follows from Equation (3) as

$$\sigma_{\text{buck}} = \frac{2P_{\text{buck}}}{L} = \frac{P_{\text{buck}}\bar{\rho}}{t}. \tag{8}$$

The cell walls of the square honeycombs can also fail by plastic microbuckling. With the plastic microbuckling stress of the cell wall material in the x_3-direction given by σ_c, collapse stress of the honeycomb is given by

$$\sigma_{mb} = \bar{\rho}\sigma_c. \tag{9}$$

The operative collapse mode of the honeycombs is the one associated with the lowest load, and thus the peak stress σ_p of the honeycombs is

$$\sigma_p = \min(\sigma_{mb}, \sigma_{\text{buck}}). \tag{10}$$

4.2. Shear response. Under a shear stress τ_{31}, the cell walls of the square honeycomb in the plane normal to x_2 undergo shear straining while the walls in the plane normal to x_1 deform by bending and carry a negligible fraction of the load. Thus neglecting the contribution of the cell walls in the plane normal to x_1, the overall shear modulus of the square honeycombs is given as

$$\frac{G}{G_{31s}} = \frac{\bar{\rho}}{2}, \tag{11}$$

in terms of the shear modulus G_{31s} of the composite sheet material. The peak shear strength of the honeycombs is again governed either by the elastic buckling of the cell walls or by the shear strength τ_{31s} of the composite sheet material when subjected to a shear stress τ_{31}. We consider each of these mechanisms in turn.

Consider the elastic buckling of the cell walls that lie along the x_1-direction direction. The principal bending rigidities of this cell wall are given as

$$D_1 = \frac{E_{1s}t^3}{12(1 - \nu_{13s}\nu_{31s})}, \quad D_3 = \frac{E_{3s}t^3}{12(1 - \nu_{31s}\nu_{13s})}, \quad D_{31} = \frac{G_{31s}t^3}{12}. \tag{12}$$

The elastic shear buckling stress of a plate clamped along the edges $x_3 = 0$ and $x_3 = H$ and simply supported along the other two edges is given in terms of the above rigidities as [Seydel 1930]

$$\tau_{\mathrm{b}} = K_s \frac{\pi^2}{tL^2} \sqrt[4]{D_1 D_3^3}. \tag{13}$$

In this case the factor K_s is only a function of the nondimensional group

$$\eta \equiv \frac{D_{31}}{\sqrt{D_1 D_3}}, \tag{14}$$

and lies in the range $7 \le K_s \le 14$ for η in the range 0 to 2.0 as specified in [Krivetsky 1959]. The elastic buckling strength of the honeycomb then follows as

$$\tau_{\mathrm{buck}} = \tau_b \frac{\bar{\rho}}{2}. \tag{15}$$

When the peak stress of the honeycomb is governed by the shear failure of the composite material, the strength τ_s of the honeycombs is given in terms of the strength τ_{13s} of the cell wall material as

$$\tau_s = \tau_{31s} \frac{\bar{\rho}}{2}. \tag{16}$$

Combining, Equations (15) and (16), the peak shear strength of the honeycombs is

$$\tau_p = \min(\tau_s, \tau_{\mathrm{buck}}). \tag{17}$$

Note that this analysis remains unchanged for shear loading τ_{32}.

4.3. *Extraction of material properties.* The compressive tests on the sandwich specimen described in Section 3.1 were used to extract the material properties required to use in the models discussed above. The moduli $E_{1s} = E_{3s}$, and peak compressive strength σ_c for the woven and laminate materials follow directly from the measurements plotted in Figure 7 for the materials in the 0–90° and ±45° orientations. The Poisson's ratios $\nu_{13s} = \nu_{31s}$ were also measured in these tests using strain gauge rosettes (see Section 3.1). These measured material properties for the woven and laminate materials are listed in Table 2.

The required shear elastic properties of the composite sheets were estimated from compression tests conducted by rotating the composite sheet material through 45° as described subsequently. In order to determine the shear modulus G_{31s} of the woven material in the 0–90° orientation, consider the compression test on the ±45° woven material plotted in Figure 7. Write the applied compressive stress as σ_x, and the corresponding axial strain and transverse strains as ε_x and ε_y, respectively. Then, the required shear stress τ versus shear strain γ relation is obtained via the connections $\tau = \sigma_x/2$ and $\gamma = \varepsilon_x - \varepsilon_y$. The shear modulus G_{31s} follows immediately as the initial slope of the τ versus γ response and we take the shear strength of the material to be given as $\tau_{31s} = \sigma_c/2$, where σ_c is the peak measured values of

Property	Woven 0–90° orient.	Woven ±45° orient.	Laminate 0–90° orient.
$E_{1s} = E_{3s}$	63 GPa	16 GPa	65 GPa
G_{31s}	4.7 GPa	27 GPa	4.7 GPa
ν_{13s}	0.16	0.70	0.10
σ_c	331 MPa	80 MPa	356 MPa
τ_{31s}	40 MPa	166 MPa	45 MPa
ρ	1370 kgm^{-3}		1590 kgm^{-3}

Table 2. Measured material properties of the woven and laminate composite materials.

σ_x. Similar procedures are followed to determine the shear properties of the woven material in the ±45° orientation and the laminate in the 0–90° orientation. These shear properties are also listed in Table 2.

4.4. *Comparison of measurements and predictions.* Predicted values of the moduli and peak strengths of the square honeycombs are included as continuous lines in Figures 12–15 for compressive loading and in Figure 18 for shear loading. Reasonable agreement is observed between measurements and predictions of the moduli and strength in the ±45° orientation for compression and 0–90° orientation for shear. By contrast, the analytical models over-predict the moduli and strengths of the honeycombs in the 0–90° and ±45° orientations for compression and shear, respectively. These results indicate that when the deformation of the honeycombs is primarily governed by the deformation of the matrix in the composite materials the models give reasonable predictions, while when fibre deformation is the primary deformation mode the analytical models significantly over-predict the measurements. We rationalise this by recalling that the compression of fibre composites along the fibre direction is very imperfection sensitive. An imperfection such as wavy cell walls results in a reduction in strength and stiffness of the honeycomb for two reasons: a geometric effect that induces bending moments in the cell walls, and an additional misalignment of the fibres with respect to the loading direction. The geometric effect is investigated by a limited finite element (FE) investigation reported in the Appendix but the effect of fibre misalignment is not included in the continuum cell wall models analysed here but can be summarised as follows. The microbuckling strength σ_c of composite is given as [Rosen 1965; Argon 1972; Budiansky 1983]

$$\sigma_c = \frac{k}{\bar{\phi}} \tag{18}$$

in terms of the matrix shear strength k and misalignment angle $\bar{\phi}$ between the fibres and loading direction. The misalignment angle $\bar{\phi}$ in case of the honeycombs has two contributions; the initial misalignment of the fibres in the laminate and the additional misalignment caused by the wavy cell walls of the honeycomb.

5. Comparison with competing metallic cellular sandwich cores

The performance of the composite square-honeycombs is compared with that of metallic sandwich cores in Figure 20, which includes data for stainless steel pyramidal cores [Côté et al. 2007], diamond cores and
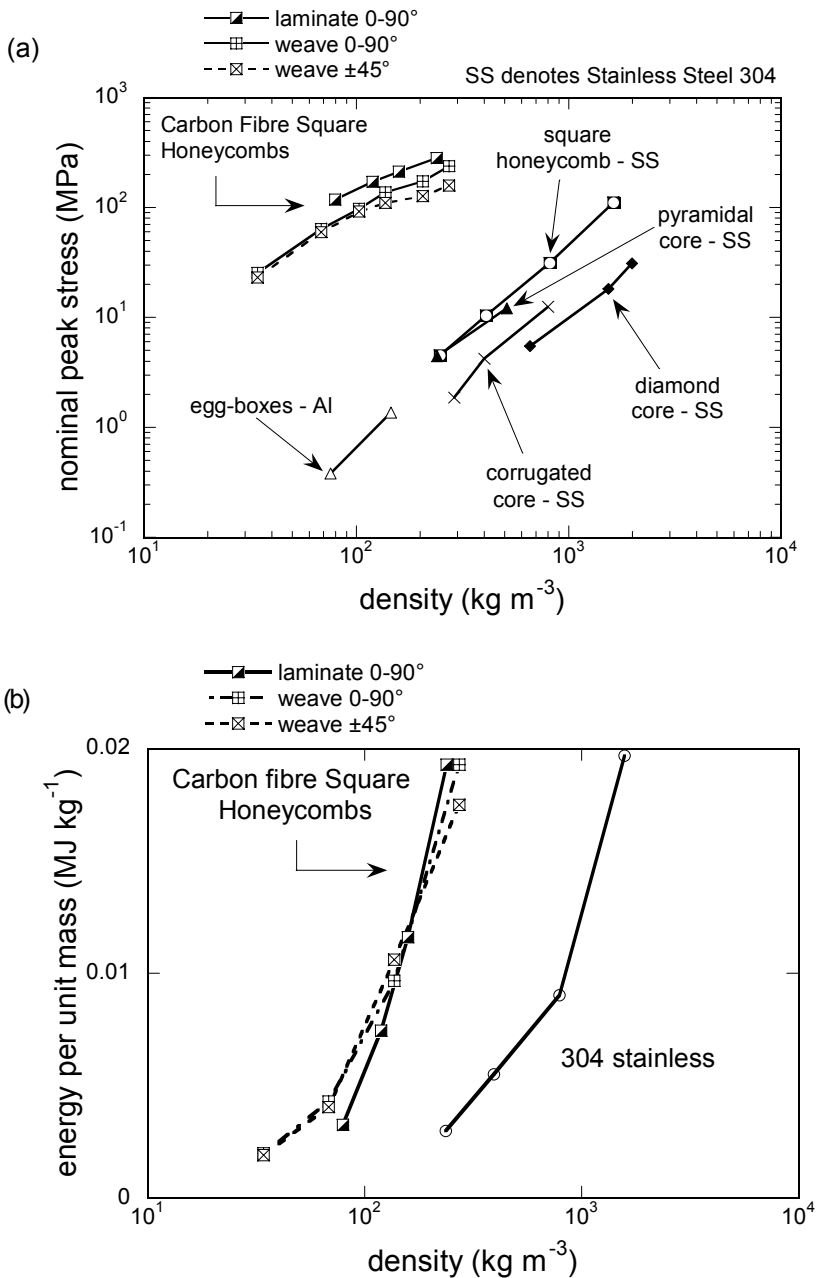

Figure 20. A comparison between the measured (a) peak compressive strengths σ_p and (b) energy absorption capacities per unit mass (up to a compressive strain $\bar{\varepsilon} = 0.4$) of competing metallic and composite sandwich cores as a function of the density $\rho \equiv \bar{\rho}\rho_s$.

corrugated cores [Côté et al. 2006] as well as aluminium egg-boxes [Zupan et al. 2003]. This comparison is presented for the compressive peak strength in Figure 20a and the compressive energy absorption per unit mass W_v/ρ up to a strain $\bar{\varepsilon} = 0.4$ in Figure 20b. For a given core density $\rho \equiv \bar{\rho}\rho_s$, where ρ_s is the density of the solid cell wall material, the composite square honeycombs outperform metallic cores both in terms of their peak strength and energy absorption capacity. More significantly, the composite materials appear to lie in an area of material space where metallic materials do not seem to exist at all.

To further explore the potential of composite cellular materials, consider the Ashby material property chart [Ashby and Bréchet 2003] shown in Figure 1. Aluminium foams and lattices occupy the low density region of material strength – density space. It also reveals a gap between the strength of existing lattice materials and the unattainable materials limit. The compressive strengths of composite honeycombs measured in the current study are included in Figure 1 and clearly show that cellular composite materials explored here reside in the gap in the material strength versus density space. Also included in Figure 1 is the theoretical prediction of the compressive strength of the 0–90° laminate (solid line). It is clear that topologically structuring composite materials in configurations such as the square honeycomb show promise for filling gaps in the strength versus density map of all known materials; the challenge is found in manufacturing these materials with minimum imperfections so as to attain their ideal strengths.

6. Concluding remarks

A preliminary investigation of the mechanical properties of square-honeycomb sandwich structures manufactured from carbon fibre reinforced polymers has been conducted. Honeycomb cores with relative densities $\bar{\rho}$ in the range 2.5% to 20% were manufactured by slotting, assembling and adhesively bonding composite sheets. Their out-of-plan compressive and shear response are measured as a function of relative density, ratio of the specimen height to cell width, and number of cells in the specimen. The effect of the composite material type (laminate and woven) and material orientation on the compressive and shear responses of the honeycombs is also reported. The measurements indicate that the response is relatively insensitive to the ratio of the specimen height to cell width and number of cells in the specimen, but strongly dependent on the material type and orientation. In particular, the compressive strength of the honeycombs made from laminates with fibres aligned with the compression direction (i.e., 0-90° honeycombs) was greater than that of the honeycombs made from the woven material with fibres at ±45° with respect to the compression direction. However, the energy absorption capacities of these two types of honeycombs were almost equal. The role of material orientation reversed for shear loading with the shear strength of the ±45° honeycombs exceeding that of the 0–90° honeycombs.

In compression the honeycombs failed by either elastic buckling or plastic microbuckling while in shear the two main failure modes were elastic buckling or shear failure of the composite sheet material. Analytical models are derived for both collapse modes. The predicted strengths are substantially higher than the measurements especially when fibre deformation dominates the deformation of the composite sheets. These discrepancies result from imperfections arising in the manufacturing of the honeycombs and not accounted for in the analytical models. A limited finite element investigation quantified the significant effects of geometric imperfections on the compressive strength of the composite honeycombs.

The measurements and predictions reported here indicate that composite cellular materials with a square honeycomb topology reside in a gap in the strength versus density material property space, providing new opportunities for lightweight, high strength structural design.

Appendix A. Finite element calculations of the compressive response of the square honeycombs

The measured values of the peak strengths of the composite honeycombs are substantially below the analytical predictions. We have attributed this discrepancy to the presence of imperfections in the manufactured honeycombs that are not accounted for in the analytical model. In this Appendix we report a limited set of finite element (FE) calculations in order to gauge the effect of geometrical imperfections on the compressive response of the honeycombs.

A1. *Details of the FE calculations.* Finite deformation FE calculations were performed using the standard version of the commercial FE package ABAQUS (version 6.5). Calculations were performed on the honeycomb specimens comprising 6×6 cells with a cell aspect ratio $H/L = 3$ and made from the 0–90° woven material. In the honeycombs used in the experiments, cell wall thickness t was kept constant whilst varying the cell size L. However, in the FE model the cell size of the honeycombs was fixed at $L = 10$ mm and the relative density varied by changing the cell wall thickness t. The honeycomb were discretised using 8-noded shell elements with reduced integration (S8R in the ABAQUS notation) with 5 integration points across the shell thickness. In all the calculations presented here square elements of length $L/10 = 1$ mm were employed; further mesh refinements gave no appreciable change to the results reported. The FE model assumed perfect bonding along the cell edges and so did not account for the slotting and gluing procedure employed to manufacture the honeycombs. In all the calculations presented here geometrical imperfections were introduced into the FE model in the form of the eigen-mode shown in Figure 21a. This eigen-mode is in close agreement with the observed elastic collapse mode (Figure 8) and that of the analytical model. The magnitude of the imperfections is characterized by the maximum amplitude of the displacements of the cell walls from their original configuration: for each
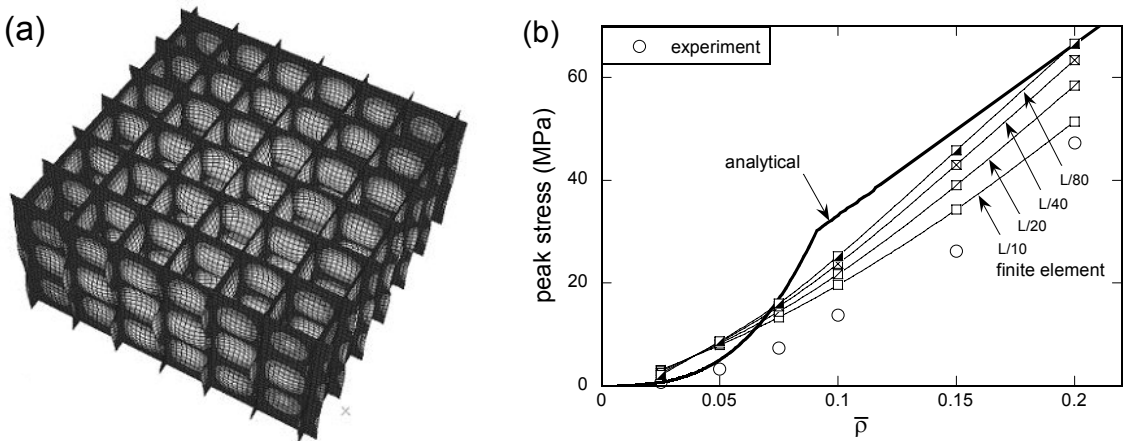
Figure 21. (a) The eigen-mode used to introduce geometrical imperfections in the FE models. (b) Comparison of the FE predictions and measured values of the peak compressive strengths of the honeycombs. FE predictions for 4 selected values of the imperfection magnitude are included along with the analytical predictions. All results are for the honeycombs made from the $0 - 90°$ woven material with 6×6 cells and a cell aspect ratio $H/L = 3$.

value of the relative density $\bar{\rho}$, we shall report calculations with imperfection amplitudes $L/10$, $L/20$, $L/40$ and $L/80$.

The top and bottom surfaces of the honeycomb were tied to two rigid surfaces with all degrees of freedom of the bottom surface constrained. A displacement rate $\dot{\delta} = 0.002\,\text{ms}^{-1}$ in the x_3 direction was applied to the top surface with displacements of that surface in the x_1 and x_2 directions prevented. The applied stress on the honeycomb was inferred from the work conjugate force to the applied displacement in the x_3 direction.

Unless otherwise specified, the cell wall material was modelled as an elastic-plastic solid. While the elastic response was assumed to be orthotropic (elastic properties listed in Table 2) for the 0–90° woven composite, the failure of the composite material under compression was assumed to be approximately captured by a nonhardening J2 flow theory plastic response with a yield strength given by the compressive strength σ_c listed in Table 2.

A2. *Summary of findings.* The FE predictions of the compressive peak strength of the honeycombs are plotted in Figure 21b as a function of $\bar{\rho}$ for selected values of the imperfection magnitude. The measured values of the peak strengths and the corresponding analytical predictions are also included in Figure 21b. We observe that the imperfections not only significantly reduce the peak strengths of the honeycombs but also affect the form of the variation of the peak strength σ_p with relative density $\bar{\rho}$ when compared with the analytical predictions. Reasonable agreement between the measurements and FE predictions, especially at high values of $\bar{\rho}$, is observed for the largest imperfection magnitude of $L/10$.

Recall that under compression, the composite displays a strongly softening response; while in the FE results presented in Figure 21b, the material was assumed to be ideally plastic. In order to explore the validity of the material model, we conducted some additional FE calculations with the material described by a softening post-yield material response as sketched in Figure 22a. In particular the material was assumed to be orthotropic elastic up to the yield strength σ_c. Subsequently the material was again assumed as a J2 flow theory material but with a linearly softening post-yield response. The softening rate in terms of the uniaxial stress versus strain response was assumed $-d\sigma/d\varepsilon = 0.5E_{3s}$. FE predictions of the peak strengths with this new material model are plotted in Figure 22b (for an imperfection magnitude $L/10$) along with the corresponding FE calculations assuming nonhardening plasticity from Figure 21b and the experimental measurements. Including the softening post-yield response of the composite material appears to have a negligible effect on the peak strength of the honeycombs and thus suggesting that a nonhardening plasticity model is an adequate representation of the composite material in terms of modelling the peak strength of the honeycombs.

In addition to the FE calculations presented here, we also performed the following FE calculations in order to further explore the origins of the rather low measured strengths of the honeycombs:

(i) In order to investigate the effect of loading asymmetry in the experiments, a loading rate $\dot{\delta} + \omega x_2$ was imposed on the top rigid surface with the rotation rate $\omega = 0.03\,\text{rad s}^{-1}$. This had a negligible effect on the predicted peak strengths.

(ii) Recall that the honeycombs were manufactured by slotting together sheets and gluing the assembly. The effect of this manufacturing process was modelled in the FE calculations by detaching the cells walls along half the height of the honeycomb (using the "seams" option in ABAQUS). FE predictions using this model gave results very similar to those presented in Figure 22b.
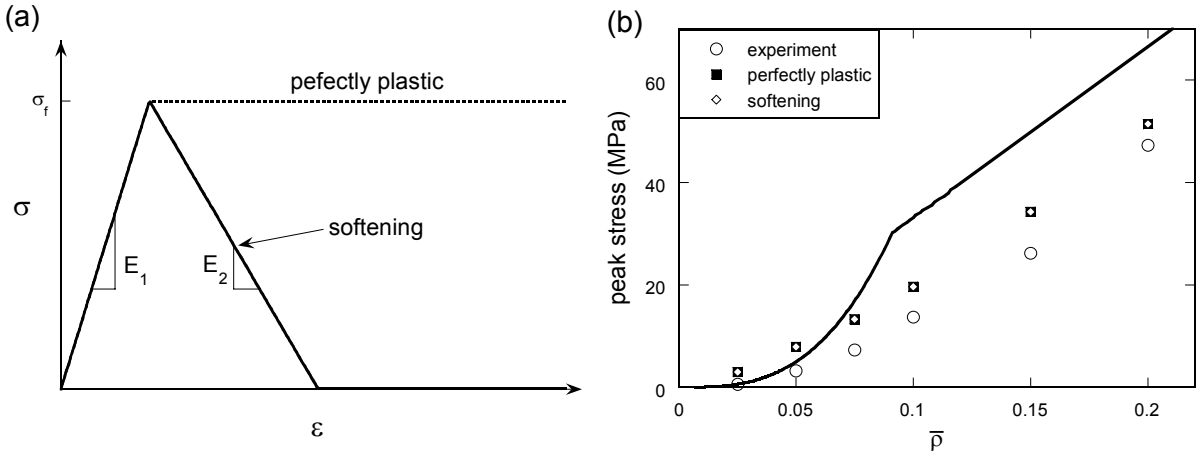
Figure 22. (a) Sketch of the nonhardening and softening uniaxial stress versus strain responses employed to model the solid composite material in the FE calculations. (b) Comparison of the FE predictions of the peak compressive strengths of the honeycombs with measurements. FE predictions for the nonhardening and softening material models with an imperfection magnitude $L/10$ are included along with the analytical predictions. All results are for the honeycombs made from the 0–90° woven material with 6×6 cells and a cell aspect ratio $H/L = 3$.

We conclude that imperfections in terms of wavy cell walls seem to be the main source of the discrepancy between the measured values and analytical predictions of the peak strength of the composite honeycombs, of which both geometrical effects and fibre misalignment effects contribute to the reduction in peak stress.

Acknowledgements

References

[Argon 1972] A. S. Argon, "Fracture of composites", *Treatise Mater. Sci. Technol.* **1** (1972), 79–114.

[Ashby and Bréchet 2003] M. F. Ashby and Y. J. M. Bréchet, "Designing hybrid materials", *Acta Mater.* **51**:19 (2003), 5801–5821.

[Ashby et al. 2000] M. F. Ashby, A. G. Evans, N. A. Fleck, L. J. Gibson, J. W. Hutchinson, and H. N. G. Wadley, *Metal foams: a design guide*, Butterworth-Heinemann, Boston MA, 2000.

[ASTM 2000] ASTM, "Test method for shear properties of Sandwich core materials", 2000. Volume 15.03.

[Budiansky 1983] B. Budiansky, "Micromechanics", *Comput. Struct.* **16** (1983), 3–12.

[Côté et al. 2004] F. Côté, V. S. Deshpande, N. A. Fleck, and A. G. Evans, "The out-of-plane compressive behavior of metallic honeycombs", *Mater. Sci. Eng. A* **380**:1–2 (2004), 272–280.

[Côté et al. 2006] F. Côté, V. S. Deshpande, N. A. Fleck, and A. G. Evans, "The compressive and shear responses of corrugated and diamond lattice materials", *Int. J. Solids Struct.* **43**:20 (2006), 6220–6242.

[Côté et al. 2007] F. Côté, N. A. Fleck, and V. S. Deshpande, "Fatigue performance of sandwich beams with a pyramidal core", *Int. J. Fatigue* **29**:8 (2007), 1402–1412.

[Deshpande et al. 2001a] V. S. Deshpande, M. F. Ashby, and N. A. Fleck, "Foam topology: bending versus stretching dominated architectures", *Acta Mater.* **49**:6 (2001), 1035–1040.

[Deshpande et al. 2001b] V. S. Deshpande, N. A. Fleck, and M. F. Ashby, "Effective properties of the octet-truss lattice material", *J. Mech. Phys. Solids* **49**:8 (2001), 1747–1769.

[Ericksen and March 1958] W. S. Ericksen and H. W. March, "Compressive buckling of sandwich panels having dissimilar facings of unequal thickness", Report 1583-B, Forest Products Laboratory, Madison, WI, 1958.

[Evans et al. 1998] A. G. Evans, J. W. Hutchinson, and M. F. Ashby, "Multifunctionality of cellular metal systems", *Prog. Mater. Sci.* **43**:3 (1998), 171–221.

[Finnegan et al. 2007] K. Finnegan, G. Kooistra, H. N. G. Wadley, and V. S. Deshpande, "The compressive response of carbon fiber composite pyramidal truss sandwich cores", *Int. J. Mater.* (2007), 1264–1272.

[Fleck and Deshpande 2004] N. A. Fleck and V. S. Deshpande, "The resistance of clamped sandwich beams to shock loading", *ASME J. Appl. Mech.* **71** (2004), 386–401.

[Gibson and Ashby 1997] L. J. Gibson and M. F. Ashby, *Cellular solids, structure and properties*, 2nd ed., Cambridge University Press, Cambridge, 1997.

[Krivetsky 1959] A. Krivetsky, "Buckling of orthotropic plates (corrugated plate applications)", Report 7-60-941001, Bell Aerospace Company, 1959.

[Marasco et al. 2006] A. I. Marasco, D. D. R. Cartié, I. K. Partridge, and A. Rezai, "Mechanical properties balance in novel Z-pinned sandwich panels: Out-of-plane properties", *Compos. A: Appl. Sci. Manuf.* **37**:2 (2006), 295–302.

[Rosen 1965] B. W. Rosen, "Mechanics of composite strengthening", Chapter 3, pp. 37–75 in *Fiber composite materials*, American Society for Metals, Metals Park, OH, 1965.

[Seydel 1930] E. Seydel, "Jahrbuch 1930 der Deutschen Versuchsanstalt fur Luftfahrt", NACA Technical Memorandum 602, 1930.

[Wadley 2002] H. N. G. Wadley, "Cellular materials manufacturing", *Advanced Eng. Mat.* **4**:10 (2002), 726–733.

[Wadley 2006] H. N. G. Wadley, "Multifunctional periodic cellular metals", *Phil. Trans. R. Soc. A* **364** (2006), 31–68.

[Xue and Hutchinson 2004] Z. Xue and J. W. Hutchinson, "A comparative study of impulse-resistant metal sandwich plates", *Int. J. Impact Eng.* **30**:10 (2004), 1283–1305.

[Zupan et al. 2003] M. Zupan, C. Chen, and N. A. Fleck, "The plastic collapse and energy absorption capacity of egg-box panels", *Int. J. Mech. Sci.* **45**:5 (2003), 851–871.

BENJAMIN P. RUSSELL: bpr23@cam.ac.uk
Engineering Department, Trumpington Street, University of Cambridge, Cambridge CB2 1PZ, United Kingdom

VIKRAM S. DESHPANDE: vsd@engineering.ucsb.edu
Engineering Department, Trumpington Street, University of Cambridge, Cambridge CB2 1PZ, United Kingdom

HAYDN N. G. WADLEY: haydn@virginia.edu
Department of Materials Science and Engineering, University of Virginia, 395 McCormick Road, Charlottesville VA 22904, USA

SHAPE OPTIMIZATION IN AN ELASTIC PLATE UNDER REMOTE SHEAR: FROM SINGLE TO INTERACTING HOLES

SHMUEL VIGDERGAUZ

An elastic plate with two closely spaced identical holes of fixed area is taken as a two-dimensional sample geometry to find the interface shape which minimizes the energy increment in a homogeneous shear stress field given at infinity. This is a transient model between a single energy-minimizing hole and a regularly perforated plate, both numerically solved by a genetic optimization algorithm together with a fast and accurate fitness evaluation scheme using the complex-valued elastic potentials which are specifically arranged to incorporate a traction-free hole boundary. Here the scheme is further enhanced by a novel shape-encoding procedure through a conformal mapping of a *single* hole rather than *both holes simultaneously* as is done in standard practice. The optimized shapes appear to be slightly rounded elongated quadrangles aligned with the principal load axes. Compared to the single (square-like) optimal hole, they induce up to 12% less energy depending on the hole spacing. Qualitatively, it is also shown that the local stresses, computed along the optimal shapes as a less accurate by-product of the optimization, exhibit a tendency to be *piecewise constant* with no local concentration.

1. Introduction

Multiple closely spaced holes are widely employed in engineering design. Fulfilling technological functions, they weaken the structure and hence may substantially reduce its mechanical performance. This happens due to high local stresses and energy concentration induced by the holes in an applied external field. The resulting stress state of the structure depends on the holes' shapes, areas and mutual arrangement. Amongst these geometrical factors, the shapes are of less technological importance and can be used by designers to achieve a more favorable stress state of the construction.

Quantitatively, the state is assessed by any of three interrelated criteria:

(A) the maximum of the von Mises stresses along the hole shapes;

(B) the maximum of the squared tangential stress variations. In the ideal case of zero variations (a constant or piecewise constant stress distribution) no stress concentrations occur along the boundary;

(C) the energy increment brought by the holes into a given outer stress field.

Minimization of A, B or C gives some optimal properties to the perforated plate. Here, we deal with the energy criterion C. The following considerations weigh in favor of our choice. First, for a finite number of holes, this increment is the zeroth-order approximation of the measurable effective moduli of an elastic perforated structure and hence has a clear physical meaning. The lesser the energy, the stiffer the plate. Second, the tangential stress constancy (criterion B) is the necessary condition of the energy

minimum (criterion C) as shown by Banichuk [1977] through variation of the energy integral. In other words, the energy-minimizing holes simultaneously smooth the stress distribution. At the same time, the integral criterion C is computationally much easier than A and B, both of local nature.

Finally, there is the strong practical correlation between the criteria A and C. For a single hole under remote shear, it was semianalytically found in [Vigdergauz 2006] that the energy-minimizing hole provides almost the global minimum of the stresses (criterion A). Moreover, in the opposite case of uniform loads of the same sign, we proved analytically in [Vigdergauz 1976] that all three criteria are minimized for the same holes, called *equistress holes* (in accordance with criterion B). They are found by applying the equistress principle [Cherepanov 1974], which says that the tangential stresses along the optimal traction-free boundary are uniform. At a given number of holes this allows us to obtain the parametric equations of the equistress shapes depending on the ratio between the far loads and on a number of geometrical parameters which govern the mutual hole arrangement. We note in passing that Waldman et al. [2003] questioned this finding. Their assertion that "it turns out that Cherepanov's solution is for (two) holes that do not interact to any appreciable degree" is simply caused by confusing the parameters. Namely, the modulus of the elliptic integrals in Cherepanov's solution is specifically taken as 1/2, while actually it varies between zero and one, thus covering any holes separation distance. In particular, with the modulus tending to one, the optimal holes come closer and closer together. Further, Waldman et al. [2003] misinterpreted our paper [Vigdergauz 1982] as dealing with two equistress holes in a plane. Actually, a distinctly different case of the equistress hole in a *half*-plane is considered there in an attempt to study the interaction between the hole and the traction-free edge. Nevertheless, the cited paper contains an informative variety of numerical results related to criterion B optimization, which we use later for reference.

Returning to criterion C we note that the increment divided by the total area of the holes depends only on the geometry. The corresponding shape optimization problem reads: *Given a uniform far-field loading, an area of two traction-free identical holes in a thin infinite elastic plate and their spacing, find, among all admissible continuous curves, the hole shape which minimizes the induced energy increment.*

For concreteness, we restrict discussion to only two interacting holes, though most derivations are easily generalized.

From the above it follows that this shape optimization problem is yet unsolved only for remote loads of opposite signs when the equistress principle is no longer valid, as explained in Section 3. In this case, numerical optimization required.

Any optimization process includes an iteration scheme and a repetitively used direct problem solver, both of great importance for converging to true optimum. Generally, the iteration process employs gradient or nongradient methods which perform directional and nondirectional searching, respectively. As in our previous papers [Vigdergauz 2001a; 2001b; 2006] we use here a nondirectional genetic optimization algorithm (GA). The feasibility of GA-based shape optimization in continuum mechanics has firstly been witnessed by Schoenauer et al. [1996]. The major advantage of this approach is that it explores the solution space by testing parameter combinations simultaneously to avoid local minima and requires no derivative information [Osyczka 2001].

We couple GA with the direct problem solver based on the one-potential formulation given in [Vigdergauz 2001a] of the complex-valued Kolosov–Muskhelishvili (KM) functions [Muskhelishvili 1963]. The forward problem is then reduced to solving a system of linear algebraic equations where only the first unknown is needed for the energy evaluation of a given hole shape. The main difficulty here is evaluating

the shape integrals which enter into the system coefficients. Within the GA optimization, it induces the question of how to effectively encode an arbitrary hole shape. The serious disadvantage of the commonly used nodal points discretization is that the nodes simultaneously serve as design variables and as integration points. As a consequence, the number of nodes should be large enough (typically several tens or hundreds) for both adequate shape description and accurate integration. This impairs the convergence of the optimization process because it needlessly enlarges the problem size and hence raises the computation time.

Here we suggest an alternative approach which *separates* the design variables and the integration points. To this end, the fact is employed that the exterior of a unit circle can be conformally mapped holomorphically onto the exterior of any closed shape [Alfors 1979]. We use the first several coefficients of its Laurent expansion as the design variables while the integration is performed over a circle at fixed points independent of the optimization. This novelty drastically reduces the computational efforts and permits us to obtain detailed results at reasonable accuracy.

In contrast to common practice, neither the elastic domain nor the stress-strain equations are really transformed. The mapping is used for the pure geometrical purpose of encoding the searched shapes.

Our contribution is thus twofold: (i) a new, effective, and easily adaptive shape-decoding scheme for gradientless searching algorithms is proposed, and (ii) the energy-minimizing interacting holes in an elastic plane are numerically found on this basis.

Of course, the proposed scheme is not the only possible one. Good results have recently been obtained by Waldman et al. [2003]. They use the finite element analysis within a specific gradientless shape optimization method to identify the stress-constant holes (criterion B). In our opinion, both methods complement each other. Numerical examples show that the finite element method (FEM) gives the stresses with better accuracy, especially under a pure shear loading. The reason for this is explained in Section 7. On the other hand, the KM functions can easily tackle an infinite domain and hence are more suitable for the current purpose of minimizing the energy increment. It would thus be interesting to combine the direct FEM solver with the proposed shape encoding scheme within a gradientless searching to solve the stress minimization problem. However, this is beyond the scope of our paper.

Following is the outline of the rest of the paper. In Section 2 the two-dimensional boundary value elastostatic problem for a multiconnected infinite region is formulated in complex-variable terms for further references and the inverse shape identification problem is stated in detail. In Section 3 some closed-form identities are derived for assessing the future numerical results. The forward problem solver is described in Section 4 which is also concerned with the numerical validation of the proposed solver by comparison with alternatively obtained results available in literature. A key Section 5 presents the novel shape encoding scheme based on conformal mapping. Section 6 displays the GA framework specifically designed for our current purposes. In Section 7 numerical results are presented in detail and the capabilities of the scheme are tested, depending on the quantitative parameters involved. The paper ends with some concluding remarks in Section 8.

2. Basic relations in two-dimensional elastostatics

Consider the setup in Figure 1. Let a thin infinite plate be weakened by two identical holes, each of area F, symmetrically located on the X-axis of the complex plane $E : z = x + iy$. The hole boundary
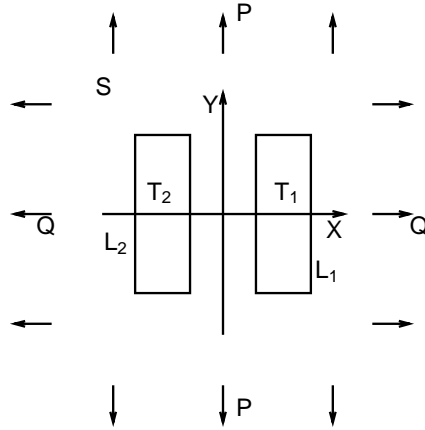
Figure 1. Schematic of the problem: an infinite plate with two identical holes under uniform stresses, the cases $P = Q$ and $P = -Q$ correspond to remote bulk and shear, respectively. The piecewise smooth hole shape is symmetric about the x-axis and may have a finite number of angular points.

$L = L_2 + L_1$ divides E into the isolated regions $\{T_1, T_2 : T_1 + T_2 = T\}$ inside the holes and the outer connected region $S = E - T$ occupied by a linearly elastic material with bulk and shear moduli K and μ, respectively. The half-spacing d_0 between the holes is measured as the minimal distance of the right hole to the y-axis:

$$d_0 = \min x : x + iy \equiv t \in L_1; \qquad d_0 \geq 0. \tag{2.1}$$

Furthermore, let the plate be remotely loaded by uniform nontangential stresses:

$$\sigma_{xx}^\infty = P_0, \quad \sigma_{yy}^\infty = Q_0, \quad \sigma_{xy}^\infty = 0. \tag{2.2}$$

The cases $P_0 = Q_0$ and $P_0 = -Q_0$ correspond to remote bulk and shear, respectively. Both settings preserve twofold geometrical symmetry, by which the regions S and T go into themselves when rotating around the origin through the angle π.

The resulting stresses in S are governed by the biharmonic Airy function which, though useful as a theoretical tool, is numerically ineffective. Far more advantageous is the complex variable approach of replacing the Airy function with a pair of holomorphic functions $\varphi_0(z)$, $\psi_0(z)$, $z \in S + L$ (the KM potentials [England 1971; Muskhelishvili 1963, Sections 47–51]) with the remote field asymptotics governed by (2.2):

$$\varphi_0(z) = B_0 z + \varphi(z), \quad \psi_0(z) = \Gamma_0 z + \psi(z) \qquad \text{for } z \in S + L, \tag{2.3a}$$

$$\varphi(z) = \frac{2a_1}{z} + O\left(|z|^{-2}\right), \ \psi(z) = \frac{2b_1}{z} + O\left(|z|^{-2}\right) \qquad \text{as } z \to \infty, \tag{2.3b}$$

$$4B_0 = \text{Tr}\{\sigma^\infty\} = Q_0 + P_0, \quad 2\Gamma_0 = \text{Dev}\{\sigma^\infty\} = Q_0 - P_0, \quad \text{Im } B_0, \quad \text{Im } \Gamma_0 = 0. \tag{2.3c}$$

The leading asymptotic terms $2a_1$, $2b_1$ with the multiplier 2 are written thus for later convenience.

Due to the setup symmetry, the potentials $\varphi(z)$, $\psi(z)$ are uneven:

$$\varphi(-z) = -\varphi(z), \quad \psi(-z) = -\psi(z) \qquad \text{for } z \in S + L, \tag{2.4}$$

and take conjugate values at complex conjugate points [Muskhelishvili 1963]:

$$\varphi(\bar{z}) = \overline{\varphi(z)}, \quad \psi(\bar{z}) = \overline{\psi(z)} \qquad \text{for } z \in S + L. \tag{2.5}$$

With this in view, the following Laurent expansions are valid in $S + L$ [Alfors 1979]:

$$\varphi(z) = \sum_{k=1}^{\infty} a_k \Big(\frac{1}{(z-c)^k} - \frac{(-1)^k}{(z+c)^k} \Big), \qquad \psi(z) = \sum_{k=1}^{\infty} b_k \Big(\frac{1}{(z-c)^k} - \frac{(-1)^k}{(z+c)^k} \Big),$$

$$\operatorname{Im} a_k = \operatorname{Im} b_k = 0 \quad \text{for } k = 1, 2, \ldots, \tag{2.6}$$

where c is a fixed point on the X-axis inside the hole T_1 ($\operatorname{Im} c = 0$, $c > d_0$). In conformity with (2.3b), we have

$$\lim_{z \to \infty} z\varphi(z) = 2a_1, \quad \lim_{z \to \infty} z\psi(z) = 2b_1. \tag{2.7}$$

By residue theory [Alfors 1979], the first coefficients a_1, b_1 in (2.6) are equally expressed as

$$2a_1 = -\frac{1}{2\pi i} \int_L \varphi(t)\, dt, \qquad 2b_1 = -\frac{1}{2\pi i} \int_L \psi(t)\, dt. \tag{2.8}$$

Dimensionally, they are proportional to the hole area F [Muskhelishvili 1963]

$$a_1 = \alpha_1 F, \qquad b_1 = \beta_1 F, \tag{2.9}$$

where, in turn, F is given by the contour integral [Alfors 1979]

$$2F = \frac{1}{2i} \int_L \bar{t}\, dt = \frac{1}{i} \int_{L_j} \bar{t}\, dt \qquad \text{for } j = 1, 2, \tag{2.10}$$

while

$$\frac{1}{2\pi i} \int_{L_j} t^n dt = 0, \quad \frac{1}{2\pi i} \int_{L_j} \frac{dt}{(t-z)^n} = \delta_{n,1} \qquad \text{for } n = 0, 1, \ldots, \ z \in L_j, \ j = 1, 2. \tag{2.11}$$

Here δ is the Kronecker delta. All the integrals above are traversed counterclockwise.

For simplicity in further manipulations, suppose that the hole boundary L is traction-free:

$$\sigma_{\rho\rho}(t) = \sigma_{\rho\tau}(t) = 0 \quad \text{for all } t \in L, \tag{2.12}$$

where $\sigma(t) = \{\sigma_{\rho\rho}, \sigma_{\tau\tau}, \sigma_{\rho\tau}\}$ represents the stress tensor in a local system of curvilinear orthogonal coordinates (ρ, τ) at a point $t \in L$. With the KM potentials, (2.12) possesses the form

$$\overline{\varphi(t)} + \bar{t}\varphi'(t) + \psi(t) = -2B_0\bar{t} - \Gamma_0 t + C_j \qquad \text{for } t \in L_j, \ j = 1, 2. \tag{2.13}$$

Here the C_j are free complex-valued constants not affecting the stress field. Identity (2.13) forms a boundary value problem in the holomorphic functions $\varphi(z)$, $\psi(z)$ with first-order vanishing conditions (2.3) at infinity. For a proper choice of the constants C_j, this problem is uniquely solvable [Muskhelishvili 1963] in a broad class $\{L\}$ of continuous hole shapes. The solved functions $\varphi(z)$, $\psi(z)$ completely describe

the hole-induced distortion of the homogeneous field (2.2). Remarkably, the Cartesian displacements $u_x(t)$, $u_y(t)$ of the boundary points $t \in L$ are expressed only through $\varphi(z)$ [Vigdergauz 2001a]:

$$u_x(t) + i u_y(t) = \left(\frac{1}{K} + \frac{1}{\mu} \right) (B_0 t + \varphi(t)) \qquad \text{for } t \in L, \tag{2.14}$$

as is the nonzero stress component $\sigma_{\tau\tau}(t)$ [Muskhelishvili 1963]:

$$\sigma_{\tau\tau}(t) = 4 B_0 + 4 \, \mathrm{Re} \, \varphi'(t) \qquad \text{for } t \in L. \tag{2.15}$$

Combining (2.14) and (2.15), we arrive at an interesting identity which holds only at a traction-free hole boundary

$$\sigma_{\tau\tau}(t) = 4 \left(\frac{1}{K} + \frac{1}{\mu} \right)^{-1} \mathrm{Re}(u'_x(t) + i u'_y(t)). \tag{2.16}$$

Application of the maximum principle to the harmonic function $\mathrm{Re} \, \varphi_0(z)$ provides (after some algebra) the interesting lower bound [Vigdergauz 1976]

$$\max |\mathrm{Re} \, \varphi_0(t)| \ge |\varphi_0(\infty)| \implies \mathcal{M} \equiv \max |\sigma_{\tau\tau}(t)| \ge 4 |B_0| \qquad \text{for } t \in L, \tag{2.17}$$

which turns out to be attainable (see the next section). At a free boundary $|\sigma_{\tau\tau}(t)|$ coincides with the von Mises stresses.

The stresses at any point inside S are also expressed in $\varphi(z)$, $\psi(z)$. We omit the corresponding formulae to save room.

At a given loading, the potentials $\varphi(z)$, $\psi(z)$ and hence the stress distortion depend only on the hole shapes and their mutual location defined by the dimensionless parameter $\lambda = d_0 \sqrt{\pi/F}$ (the multiplier π serves for convenient comparison with the literature data where a unit circle with $F = \pi$ is usually considered). This one-parameter dependence brings up the optimization problem:

To find the hole shapes that minimize the stress distortion as measured through the induced strain energy increment ΔW divided by the total hole area $2F$.

$$\Delta W(B_0, \Gamma_0, \lambda, L) \xrightarrow[\{L\}]{} \min(B_0, \Gamma_0, \lambda), \tag{2.18}$$

The lesser the increment, the stiffer the plate weakened by the holes. Mathematically, ΔW takes the form of the first-order approximation to the effective moduli of a regularly perforated plate when the volume fraction of the hole is vanishingly small. Due to its averaging nature, the energy increment involves only the first terms (2.9) of the expansion (2.6) [Jasiuk 1995; Vigdergauz 2001a]

$$\Delta W = 8 \pi (2 \Gamma_0 \alpha_1 + B_0 \beta_1) \left(\frac{1}{K} + \frac{1}{\mu} \right). \tag{2.19}$$

Nevertheless, ΔW can be extracted and optimized only from the full-size solution of the problem (2.13). The optimization strategy depends on whether the ratio $\left| \mathrm{Dev}\{\sigma^\infty\} / \mathrm{Tr}\{\sigma^\infty\} \right|$ in (2.3c) is less than 1. Physically, this ratio measures the far-field anisotropy.

3. Bulk load: analytical relations for the equistress shapes

When the deviatoric part of σ^∞ is no larger than its trace

$$|\delta_0| \leq 1; \quad \delta_0 \equiv \frac{\text{Dev}\{\sigma^\infty\}}{\text{Tr}\{\sigma^\infty\}} = \frac{Q_0 - P_0}{Q_0 + P_0} = \frac{\Gamma_0}{2B_0}, \tag{3.1}$$

or, equivalently, the far loads are of the same sign, the inverse problem (2.18) admits a remarkable solution dating back to the pioneering work by Cherepanov [1974]. Namely, if $\varphi(z)$ is identical to zero,

$$\varphi(z) \equiv 0, \qquad z \in S + L, \tag{3.2}$$

then the traction-free condition (2.13) goes into the resolving equation for $\psi(z)$:

$$\psi(t) = -2B_0\bar{t} - \Gamma_0 t + C_j \qquad \text{for } t \in L_j, \ j = 1, 2. \tag{3.3}$$

Actually, identity (3.3) presents the *inverse* problem of finding the shapes which bear the given values of a holomorphic function vanishing at infinity. With (3.1) and, possibly, nonzero constants C_j, this problem is proven to be uniquely solvable under the necessary condition

$$\|\Gamma_0\| \leq 2\|B_0\|. \tag{3.4}$$

Indeed, differentiating (3.3) with respect to t and taking the real parts of both sides we arrive at

$$\text{Re}\,\psi'(t) = -\Gamma_0 - 2B_0\,\text{Re}\,\frac{\partial\bar{t}}{\partial t} \qquad \text{for } t \in L_j, \ j = 1, 2, \tag{3.5}$$

where the harmonic function $u(x, y) \equiv \text{Re}\,\psi'(t)$ vanishes at infinity. The Mean Value theorem [Alfors 1979] implies that $u(x, y)$ has at least one zero on L, so that

$$\Gamma_0 = -2B_0\,\text{Re}\,\frac{\partial\bar{t_0}}{\partial t_0} \qquad \text{for } t_0 \in L. \tag{3.6}$$

The well-known inequality $\|\partial\bar{t}/\partial t\| \leq 1$ [Alfors 1979] makes (3.6) equivalent to (3.4). The corresponding function $\psi(z)$ is further referred to as the domain characteristic function $\Omega_0(z) \equiv \psi(z)$ [Vigdergauz 1988]. The resultant holes exist for any mutual arrangement, up to their touching. They simultaneously possess some analytically derived optimal properties:

• First, substitution of (3.2) into (2.15) shows that the stress distribution along the hole shapes (3.3) is *uniform*:

$$\sigma_{\tau\tau}(t) = \text{Const} = 4B_0 \qquad \text{for } t \in L, \tag{3.7}$$

with no local concentration potentially harmful for the plate strength. Because of (3.7) these are called equistress or equistrength holes [Cherepanov 1974].

• Second, the equistress condition (3.2) saturates inequality (2.17), thus giving the global minimum to the maximum von Mises stresses over all possible hole shapes:

$$\min_{\{L\}} \max_{t \in L} |\sigma_{\tau\tau}(t)| = \min_{\{L\}} \max_{t \in L} \mathcal{M} = 4B_0 \qquad \text{for } \delta_0 \leq 1. \tag{3.8}$$

• Finally, substituting (3.3) into (2.19) and making use of (2.10), (2.11) we arrive at the energy increment value

$$\Delta W = 4B^2 \Big(\frac{1}{K} + \frac{1}{\mu} \Big), \tag{3.9}$$

which again turns out to be the global minimum [Gibiansky and Cherkaev 1984].

All three criteria (3.7)–(3.9) are independent of the far stresses deviator Γ_0 and the relative distance between the holes, while the equistress shapes do depend on both, as dictated by (3.3). Particularly, the equistress *isolated* hole is simply an ellipse [Cherepanov 1974] with eccentricity δ_0 elongated along the far field eigendirection of the maximum $|P_0|$, $|Q_0|$. Some specific arrangements of the optimal *interacting* holes are found in [Cherepanov 1974; Vigdergauz 1976; Grabovsky and Kohn 1995; Vigdergauz 1996]. Commonly, the equistress shapes are smooth with no angular points.

Pairs of equistress holes are numerically reproduced in [Waldman et al. 2003]. As compared to the analytical shape equation derived in [Cherepanov 1974] (and generalized as explained in the Introduction), these findings bring no novelty to the equistress solutions but they help to verify the proposed FEM-based stress optimization scheme.

With the properties we have shown, we are now in a position to derive a guiding inequality for ΔW *outside* the interval (3.1). Indeed, let a plate with equistress holes be subject to an arbitrary far load: P, Q with $4B = P + Q$, $2\Gamma = Q - P$. Integration of the traction-free condition (2.13) over L separately with respect to dt and $\overline{dt}$ gives:

$$\int_L \overline{\varphi(t)} dt + \int_L \bar{t} \varphi'(t) dt + \int_L \psi(t) dt = -2B \int_L \bar{t} dt - \Gamma \int_L t dt + C_1 \int_{L_1} dt + C_2 \int_{L_2} dt, \tag{3.10a}$$

$$\int_L \overline{\varphi(t)} d\bar{t} + \int_L \bar{t} \varphi'(t) d\bar{t} + \int_L \psi(t) d\bar{t} = -2B \int_L \bar{t} d\bar{t} - \Gamma \int_L t d\bar{t} + C_1 \int_{L_1} d\bar{t} + C_2 \int_{L_2} d\bar{t}. \tag{3.10b}$$

Consider the first identity (3.10a). With (2.10) and (2.11), all integrals, excepting the first two, are taken in the form independent of the holes shapes. For the equistress boundaries, the remaining integrals can also be written explicitly. To this end, separately differentiating the characteristic Equation (3.3) with respect to t and $\bar{t}$,

$$dt = (-2B_0)^{-1} \big(\overline{\Omega_0'(t)} + \Gamma_0 \big) d\bar{t}; \qquad B_0 \neq 0, \tag{3.11a}$$

$$d\bar{t} = (-2B_0)^{-1} \big(\Omega_0'(t) + \Gamma_0 \big) dt, \tag{3.11b}$$

we have

$$\int_L \overline{\varphi(t)} \, dt = (-2B_0)^{-1} \int_L \overline{\varphi(t)} (\overline{\Omega_0'(t)} + \Gamma_0) \, d\bar{t}. \tag{3.12}$$

The first integral on the right-hand side of (3.12) is the conjugate value of the residue at infinity of the holomorphic function $\varphi(z)\Omega_0'(z)$. It vanishes because, in view of (2.3b), we have $\varphi(z)\Omega_0(z)' = O(|z|^{-3})$ as $z \to \infty$. Finally, from (2.8) we get

$$\int_L \overline{\varphi(t)} \, dt = (-2B_0)^{-1} \Gamma_0 \int_L \overline{\varphi(t)} d\bar{t} = 2\pi i \frac{\Gamma_0}{B_0} a_1 = 4\pi i \delta_0 a_1. \tag{3.13}$$

Similarly, in view of (3.11b), the remaining integral in (3.10a) takes the form

$$\int_L \bar{t}\varphi'(t)\,dt = -\int_L \varphi(t)d\bar{t} = 2\pi i \frac{\Gamma_0}{B_0}a_1 = 4\pi i \delta_0 a_1. \tag{3.14}$$

The second identity (3.10b) is treated in same manner so that (3.10) goes into a (2×2) system of linear algebraic equations in the unknown residues a_1, b_1 of the potentials $\varphi(z)$, $\psi(z)$:

$$2\delta_0 a_1 + b_1 = \frac{2B}{\pi}F, \quad (1+\delta_0^2)a_1 + \delta_0 b_1 = \frac{\Gamma}{\pi}F, \tag{3.15}$$

with the solution

$$a_1 = \frac{\Gamma - 2B\delta_0}{\pi(1-\delta_0^2)}F, \quad b_1 = \frac{B(1+\delta_0^2)-\Gamma\delta_0}{\pi(1-\delta_0^2)}2F, \tag{3.16}$$

substitution of which into (2.19) yields

$$\Delta W = \frac{4\left(B^2(1+\delta_0^2)+\Gamma^2-3\delta_0 B\Gamma\right)}{1-\delta_0^2}\left(\frac{1}{K}+\frac{1}{\mu}\right). \tag{3.17}$$

Of course, (3.17) returns to (3.9) for the initial load parameters: $B = B_0$, $\Gamma = \Gamma_0$.

Again, this equistress relation involves neither the number of holes nor their arrangement and hence may serve as a geometry-independent upper assessment of min ΔW under predominating shear when the equistress necessary condition (3.1) is not valid or, equivalently, the far loads are of opposite signs. In particular, taken at the bulk-type initial load $(\Gamma_0, \delta_0 = 0)$, the equistress holes induce the following increment under pure shear $(B = 0, \Gamma = 1)$:

$$\Delta W(0, 1, \lambda, L) = 4\left(\frac{1}{K}+\frac{1}{\mu}\right), \tag{3.18}$$

which is larger than the global minimum:

$$\Delta W(0, 1, \lambda, L) \approx 3.71449\left(\frac{1}{K}+\frac{1}{\mu}\right), \tag{3.19}$$

known in the limiting case $\lambda \to \infty$ of a single hole and attained at the square-like shape [Vigdergauz and Cherkayev 1986]. Though not sharp, the upper bound (3.18) is useful in assessing numerical results (Section 7).

4. Pure shear: fast direct solver

In contrast, a shear-dominated remote loading (outside interval (3.1)) admits no closed-form optimal solution and hence must be treated numerically. Any numerical optimization involves, in one way or another, repeated solving of the direct problem (2.13), (2.3). The more accurate and faster the direct solver is, the better the optimization scheme works as a whole. Besides, the solver should match stringent requirements of the computer memory, speed and computational stability.

Particularly relevant here is the approach first proposed and implemented by the author for a single hole [Vigdergauz 2001a;2006] and for a regularly perforated plate [Vigdergauz 2001b]. The key idea is to solve the KM potentials in *tandem rather than in parallel*. Since the basic features of the approach are

covered in the above-referenced papers, here we specifically focus on its application to a multiconnected region.

Identity (2.13) resolved for $\psi(t)$ and differentiated with respect to t

$$-\psi'(t) = 2\frac{\partial \bar{t}}{\partial t}\operatorname{Re}\varphi'(t) + \bar{t}\varphi''(t) + 2B_0\frac{\partial \bar{t}}{\partial t} + \Gamma_0, \qquad t \in L, \tag{4.1}$$

implies that the right hand-side of (4.1) is the boundary value of a function holomorphic in S and vanishing at infinity. Then the Cauchy-type integral

$$\int_{L_1+L_2} \frac{2\frac{\partial \bar{t}}{\partial t}\operatorname{Re}\varphi'(t) + \bar{t}\varphi''(t) + 2B_0\frac{\partial \bar{t}}{\partial t} + \Gamma_0}{t - z}\,dt \tag{4.2}$$

is identically zero at any point $z \in T$ [Muskhelishvili 1963]. The symmetry relations (2.4) reduce the integration path in (4.2) to only L_1. With (2.11), some algebra yields

$$2\int_{L_1} \operatorname{Re}\varphi'(t)\rho_0(t, z)\,d\bar{t} + \int_{L_1} \bar{t}\varphi''(t)\rho_0(t, z)\,dt = -4B_0\int_{L_1}\rho_0(t, z)d\bar{t} - 2\Gamma_0,$$

$$\rho_0(t, z) \equiv \frac{1}{t - z} + \frac{1}{t + z} \qquad \text{for } z \in T. \tag{4.3}$$

Cauchy-type integrals in (4.3) are holomorphic functions of z in the hole's region T. Consequently, this identity holds everywhere in T if and only if it holds for all derivatives with respect to z at a given point $z = c \in T_1$ [Muskhelishvili 1963]:

$$2\int_{L_1} \operatorname{Re}\varphi'(t)\rho_k(t, c)d\bar{t} + \int_{L_1} \bar{t}\varphi''(t)\rho_k(t, c)dt = -4B_0\int_{L_1}\rho_k(t, c)d\bar{t} - 2\Gamma_0\delta_{k,0},$$

$$\rho_k(t, c) \equiv \frac{1}{k!}\frac{\partial^k \rho_0(t, z)}{\partial z^k}\Big|_{z=c} = \frac{1}{(t-c)^{k+1}} + \frac{(-1)^k}{(t+c)^{k+1}} \qquad \text{for } k = 0, 1, 2\ldots \tag{4.4}$$

As one would expect, the Laurent expansion (2.6) for $\varphi(z)$ and its derivatives similarly involve the kernels $\rho_k(z, c)$. Substitution of them into the left-hand side of (4.4) gives an infinite system of linear algebraic equations in the desired unknowns $\{a_1, a_2, \ldots\}$ from (2.6) with the matrix $A = \{A_{kl}\}$:

$$A_{kl} = 2l\int_{L_1} \operatorname{Re}(\rho_{l+1}(t, c))\rho_k(t, c)\,d\bar{t} + l(l+1)\int_{L_1} \bar{t}\rho_{l+2}(t, c)\rho_k(t, c)\,dt. \tag{4.5}$$

Due to the adopted symmetry, the system is purely real. For computation purposes it is necessarily truncated to a finite order N. This is all the more relevant since the first coefficient a_1 alone appears in the energy increment for pure shear. As mentioned in Section 2, the displacements (2.14) and the tangential stresses (2.15) along a free boundary are also expressed only through $\varphi(z)$. In other words, the second potential $\psi(z)$ is not involved in the current solution process, thus halving the computational efforts as compared to more traditional approaches. This feature is particularly appealing for repetitive use within evolutionary optimization algorithms.

For a circular hole $L_1 : |t - c| = 1$

$$\bar{t} = c + \frac{1}{t - c}, \qquad \frac{\partial \bar{t}}{\partial t} = -\frac{1}{(t - c)^2} \qquad \text{for } t \in L_1, \tag{4.6}$$

the integrals in (4.5) are expressed analytically. Indeed, with (4.6), the conjugates $\overline{\rho_k(t, c)}$ can be expanded around the point $t = c$ as

$$\overline{\rho_k(t, c)} = \frac{1}{(\bar{t} - c)^{k+1}} + \frac{(-1)^k}{(\bar{t} + c)^{k+1}} = (t - c)^{k+1} + \frac{(-1)^k}{2c} \sum_{j=0}^{\infty} \binom{-m}{j} \left(\frac{t - c}{2c}\right)^j, \quad (4.7)$$

where

$$\binom{-m}{j} = (-1)^j \frac{(m + j)!}{m!\, j!}.$$

The series (4.7) converges absolutely since $2c > 1$. Substituting (4.6) and (4.7) into (4.5) and computing the integrand's residue at the isolated pole $z = a$ we obtain the similar series for A_{kl} and, when necessary, for the bulk-related right-hand side (4.4) of the system. The resultant expressions are not displayed here to save room.

It is interesting to verify the derived formulae by comparing the results against alternatively obtained solutions of the boundary value problem (2.13). The literature suggest various approaches to find the stress distribution along two interacting circular holes under remote loading. In parallel with rapid expansion in computer capabilities, the numerical schemes progressed from a closed-form solution with infinite sums in the bipolar coordinates [Ling 1948] and the alternative iterations [Ting et al. 1999] to the advanced FE analysis [Waldman et al. 2003] and to the highly accurate solution of the Sherman-type integral equation [Helsing and Jonsson 2000]. Tables 1 and 2 compare literature data against our results

		[Ting et al. 1999]	[Helsing and Jonsson 2000]	Present
x-axial tension	Max	2.611		2.61038805
$(P = 1, \quad Q = 0)$	Min	-0.918		-0.91768252
y-axial tension	Max	6.107	6.106040764542	6.10604077
$(P = 0, \quad Q = 1)$	Min	-0.962		-0.96154890

Table 1. Maximum and minimum tangential stresses (2.15) for two equal circular holes aligned with the x-axis at $\lambda = 0.2$.

λ	[Ling 1948]	[Waldman et al. 2003]	Present	λ	[Ling 1948]	[Waldman et al. 2003]	Present
0.0200	—	—	12.475899	0.5000	2.887	2.906	2.8874965
0.2101	—	3.955	3.9153632	1.0000	2.411	2.426	2.4108275
0.2500	—	3.682	3.6561422	2.0000	2.155	2.172	2.1545912
0.3500	—	3.259	3.2374789	4.0000	2.049	—	2.0488101
0.4568	—	2.990	2.9684777	7.0000	2.018	—	2.0177007

Table 2. Maximum tangential stresses (2.15) for two equal circular holes aligned with the x-axis under biaxial loading $B_0 = 1$, $\Gamma_0 = 0$ as a function of λ. The relative error of approximation. 1% in [Waldman et al. 2003] can be attributed to taking a finite region instead of an infinite plate.

obtained at $N = 30$ for different load modes and separation distance between holes. The values show close agreement, which should be even better for the less sensitive energy increment.

5. The design variables: an efficient shape parameterization

In contrast to circles, general hole shapes must be treated numerically. Usually, they are presented by equally spaced nodal points whose role is twofold. First, they form a discretization set to compute the integrals (4.5). Second, they serve as optimized design variables. However, this results in a contradiction in the goals, inasmuch as the number of nodes should be sufficiently large to perform an accurate integration but rather small to carry out an efficient optimization over the pool of shapes. In [Vigdergauz 2006] we proposed a much more economic alternative which separates the design variables and the integration points by using for the first purpose the finite-term conformal mapping of a centrally located unit circle γ onto the hole shape L_1. At a given normalized distance λ we have

$$t \in L_1 : t = c + \omega(\xi), \quad \omega(\xi) \equiv \xi + \sum_{m=1}^{M} d_m \xi^{-m}, \tag{5.1a}$$

$$F = \pi \left(1 - \sum_{k=1}^{K} k d_k^2 \right), \quad (\xi = e^{i\vartheta} \in \gamma : |\xi| = 1), \tag{5.1b}$$

$$dt = i\omega'(\xi)\xi d\vartheta, \quad d\bar{t} = i\overline{\omega'(\xi)}\xi^{-1} d\vartheta, \tag{5.1c}$$

where the contour displacement c is defined in conformity with (2.1) as

$$c = -\lambda\sqrt{F/\pi} \min_t \operatorname{Re}(\omega(t)). \tag{5.2}$$

Because of the setup symmetry, $\{d_m\}$ are real. As design variables, the mapping coefficients offer substantial numerical advantages enumerated in [Vigdergauz 2006]. For clarity, we display them here:

(A) They are "naturally" ordered, in the sense that the higher the coefficient, the lesser its global impact on the inclusion shape. This means that even a small number of the first coefficients form a practically representative searching pool — in contrast to the nodal points.

(B) Each mapping coefficient falls into the successively narrowed interval

$$-\frac{1}{\sqrt{m}} \le d_m \le \frac{1}{\sqrt{m}}, \qquad m = 1, 2, \ldots, \tag{5.3}$$

as it follows from the nonnegativeness of the area F inside L_1 [Alfors 1979].

(C) With (5.1c), the path L_1 in (4.5) is transformed into the circle γ where the discrete points for numerical evaluation of the integrals can be taken in the irreducible interval $[0, \pi]$ independently of the design variables $\{d_m\}$. For simplifying further computations we use a trapezoidal rule at N_{int} equal subintervals $[n\pi/(N_{int}; (n+1)\pi/N_{int}], n = 0, 1, \ldots, N_{int} - 1$ which remain unchanged during the optimization.

(D) Specifically, for interacting holes, the hole displacement a is explicitly expressed by (5.2).

Items (B) and (D) are hard to realize in a more traditional approach when the exterior of *all* holes is *simultaneously* mapped onto the plane minus the same number of circles.

We are in a position to verify the proposed approach for noncircular holes. The relevant comparison here is with the stress constancy (3.7) of the analytically known equistress shapes. At $\lambda = 0.3$ the solver gives, after term-by-term differentiation, the stress distribution oscillating around the true value with the maximum relative deviation of 0.9% located along the interacting parts of the holes. However, for rectangle-like shapes the stress computations get worse drastically, because this leads to a very unfavorable situation. The first KM potential $\varphi(z)$ is presented through the polar angle ϑ, small increments of which lead to large increments along the straight line portions of the curves. With term-by-term differentiation, this manifests itself in very large stress oscillations which are further amplified by the fact that all the Laurent coefficients a_k but the first one remain outside the energy optimization. For a single hole this was first reported in [Cherkaev et al. 1998]. In other words, the one-potential scheme, especially structured for the energy assessment, is ineffective (in its current form) in computing the stresses along quadrangle-like holes, be it at $M = 5$ or $M = 100$ first mapping terms. Here, another stress solver should be used for optimization. Exclusively for illustration purposes, we will once again consider the local stresses at the end of Section 7.

6. Outline of the genetic algorithm

The optimization problem (2.18) typically has many local minima, and this fact precludes the use of gradient-based descendent methods. An integer-encoded simple GA was chosen as the global shape optimization approach in the previous author's papers and in the present work.

The GA operates by constructing sets of candidate shapes and solving the forward problem for each. The design variables d_m, $m = \overline{(1, M)}$, are encoded using a discrete 16-bit procedure when each coefficient d_m is approximated in view of (5.3) only by $2^{16} - 1$ separate values in the continuous search space $[-1/\sqrt{m}, 1/\sqrt{m}]$. These values are decoded from a randomly generated integer $p \in [-2^{15}, 2^{15}]$ as $d_m = p/2^{15}/\sqrt{m}$. The genes for different coefficients are concatenated into a $16N$ binary chromosome that encodes a shape to be evaluated with the proposed approach. A randomly generated chromosome population of constant size is subject to bitwise crossover and mutations [Osyczka 2001] to produce the next generation. Then the process is repeated. This mimics the natural process where better members of a population tend to outperform others in the long run. In our situation, "better" means a lower fitness value. When the heuristic probability levels of genetic operations are adjusted correctly, they tend to bias towards better individuals in the population so that better genes are passed down to offspring. To enhance this effect, the best chromosome(s) from one generation are passed, unchanged, to the next (the *elitism* option). So the generations evolve, and if the optimization process is successful, the shapes in each generation are better, in a broad sense, than those in the previous one.

The stopping criterion is a problematic issue in GA, as there no practical means to assess the actual error in real applications. Instead, the optimization is stopped after the first N_{iter} iterations — in the belief that the process really converges. However, at specific stochastic combinations, GAs may become "embedded" far from the global optimum. This is prevented by multiple GA runs performed in the current work for each given problem. Practically, N_{iter} is chosen so that the optimization criterion remains unchanged in successive iterations well before reaching this limit.

In contrast to many other applications, here we have an opportunity to calibrate the GA heuristic parameters by numerically reproducing the optimal equistress shapes with the known global minimum

λ	$M = 3$	$M = 5$	$M = 7$	$M = 9$
0.01	1.22×10^{-2}	2.96×10^{-3}	8.18×10^{-4}	2.33×10^{-4}
0.25	5.69×10^{-3}	2.21×10^{-4}	7.76×10^{-5}	4.60×10^{-5}
0.50	1.39×10^{-3}	9.28×10^{-5}	1.94×10^{-5}	1.94×10^{-5}
1.0	7.15×10^{-5}	1.42×10^{-5}	1.42×10^{-5}	1.42×10^{-5}
2.0	3.67×10^{-6}	3.66×10^{-6}	3.66×10^{-6}	3.66×10^{-6}

Table 3. Relative deviations of the energy increment ΔW from the exact value (3.9) for two holes under the bulk type loading $P = Q = 1$ (equistress shapes) versus the number M of the mapping terms and the normalized distance λ.

(3.9). The results are grouped in Table 3 as a function of the distance λ and on the number M of the mapping coefficients.

In practice, each genetic operator has a lot of various modifications advanced in the literature for different applied purposes. However, a relatively small number M of required design variables permits a fairly simple GA configuration as detailed in Table 4. A typical convergence characteristic for the GA scheme is shown in Figure 2.

7. Numerical results

The GA-based simulations aim to numerically solve the optimization problem (2.18) in the representative interval of the normalized parameter λ. The proximity to the true minimum values can be only evaluated through the internal convergence of the results for successively increasing mapping size M of the problem

GA Parameter	Parameter value(s)
Gene	Integer $[-32767; 32767]$
Individual	Interface shape
Population size	800
Number of genes	up to 9
Initial population	800 random individuals
Selection	Tournament
Elitism	Four best individuals
Crossover	1-point
Crossover rate	0.90
Creep mutation	By randomly changing a bit
Creep mutation rate	0.35
Jump mutation	By adding a random integer, typically in the range $[-4; 4]$
Jump mutation rate	0.35
Stopping criterion	After 1200 iterations
Resolving system size	24
Number of integration points	720 (in the interval $[0, \pi]$)

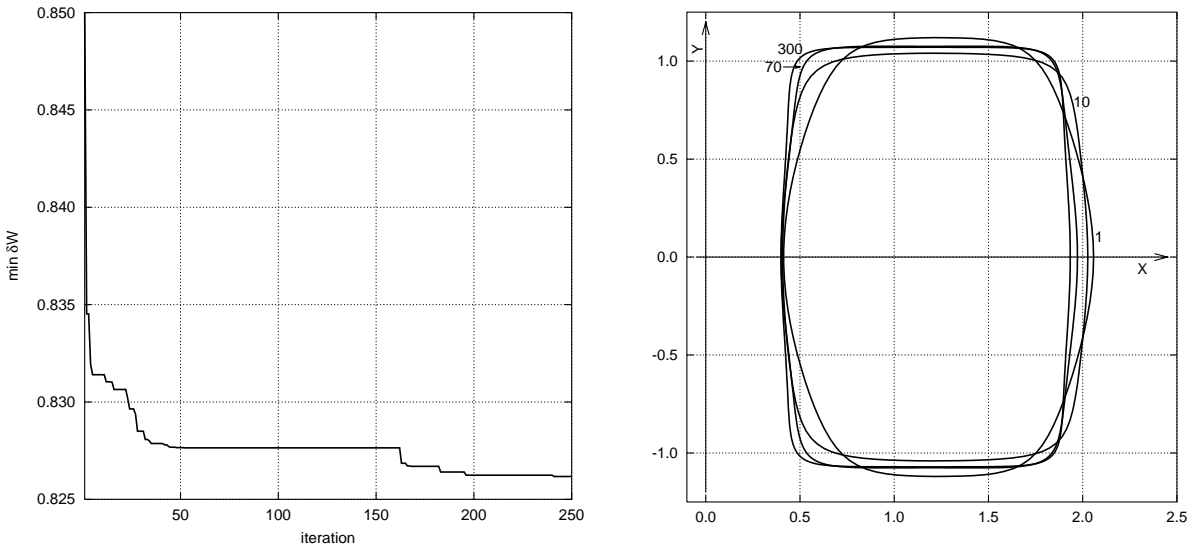**Table 4.** GA operator types, their probability rates and related parameters typically used in further optimizations.

Figure 2. Hole shape identification: progress of a typical genetic optimization run.

as presented in Figure 3 and 4. For convenience, the increment is normalized by its value (3.18) for a circular hole under pure shear. It is seen that the approximants converge remarkably fast for any λ.
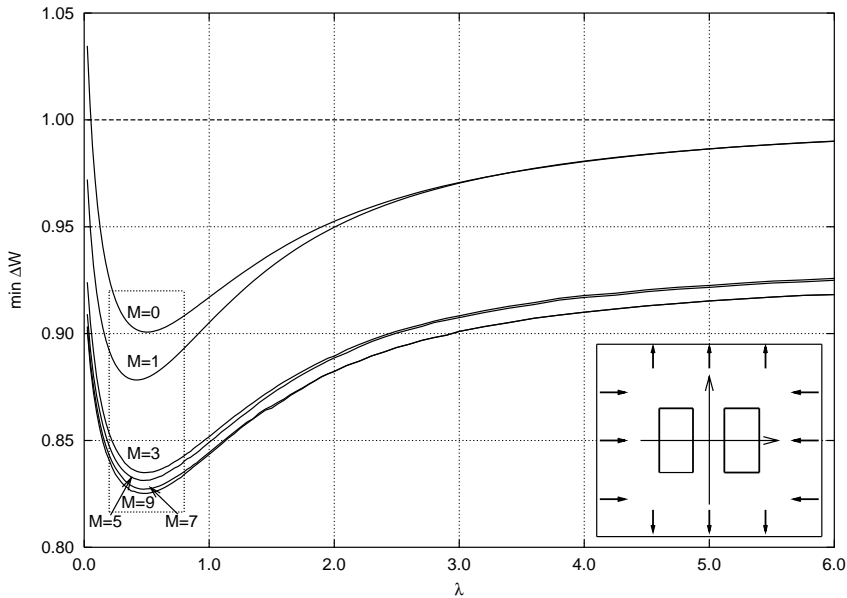

Figure 3. Minimum of ΔW as a function of the distance λ as a function of the problem mapping size M beginning with a circle ($M = 0$). The values are normalized by the equistress-related energy increment (3.18) (the dashed line) added here for comparison. The inset recalls the problem schematic. An enlarged view of the dotted rectangular is given in Figure 4.
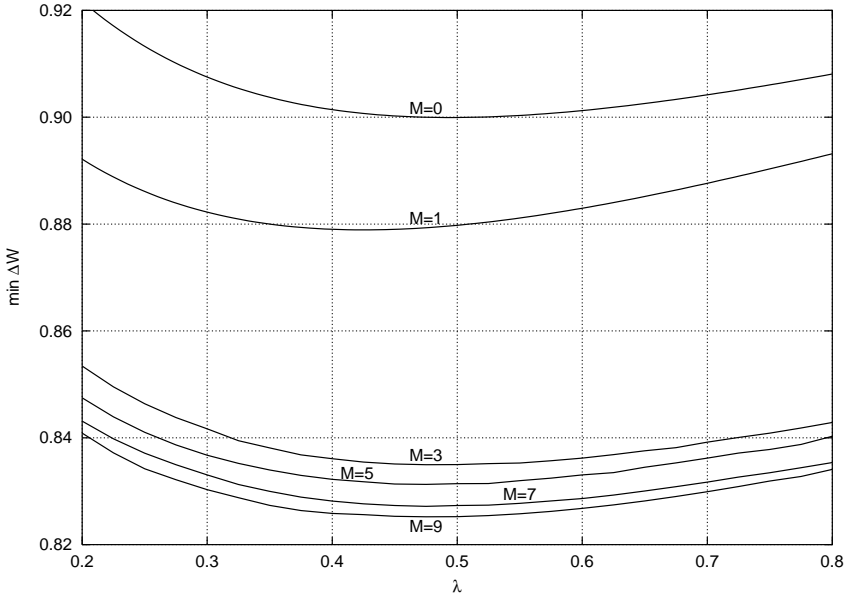
Figure 4. Enlarged fragment of Figure 3 around the global minima of min ΔW at $\lambda \approx 0.45$.

In the limiting case of a single hole ($\lambda \to \infty$) the curves tend asymptotically to either the global minimum (3.19) for $M \geq 3$ or to the bound (3.18) when the given $(M+1)$-fold symmetry ($M \leq 2$) allows for only the equistress circle instead of the truly optimal square-like shape.

The most remarkable finding is that the shear-related optimized energy depends on the separation distance λ between the holes attaining the minimum at $\lambda_{\min} \approx 0.45$. In contrast to equistress holes, whose mutual arrangement has no impact on the induced energy, shear-optimal shapes exhibit a significant collective effect, conjectured and qualitatively explained in [Cherkaev n.d.]. Interaction of the simplest circular holes gives only 3.3% less energy at $\lambda_{\min}$ than the optimal isolated square-like hole. More markedly, the optimized shapes conserve $\approx 12\%$ of the perturbed energy for $M = 9$. This percentage consists of two quite unequal parts: $12\% = 10.7\% + 1.3\%$; the dominating one relates to the first three coefficients while the contribution of the rest is much less. It is pictorially explained by

Figure 5 which shows the optimal shape evolution against the number M of mapping terms beginning with a circle ($M = 0$). One can see that the quadrangle-like optimal shape is formed already at $M = 3$ whereas the higher coefficients only flatten its sides and sharpen the angles. Such local improvements have less effect on the integral-type energy criterion. The analogy with the single optimal hole [Vigdergauz and Cherkayev 1986] suggests that the appearing angular points of the hole shape bring no singularities in the tangential stress distribution.

Figure 6 exemplifies the shape elongation as a function of the distance λ as resulting from the holes interaction. We note in parallel that the square-like single optimal hole also transforms into a rectangle as a function of a nonzero trace component in the remote shear-dominating load $-1 < Q_0/P_0 < 0$. Both elongations present the optimal response in the absence of the setup square symmetry caused by either the holes' location or the applied load. A marked feature of the optimal shapes is that they are vertically symmetric. In other words, the even coefficients d_m, $m = 2, 4, \ldots$ are invariably optimized to zero values.
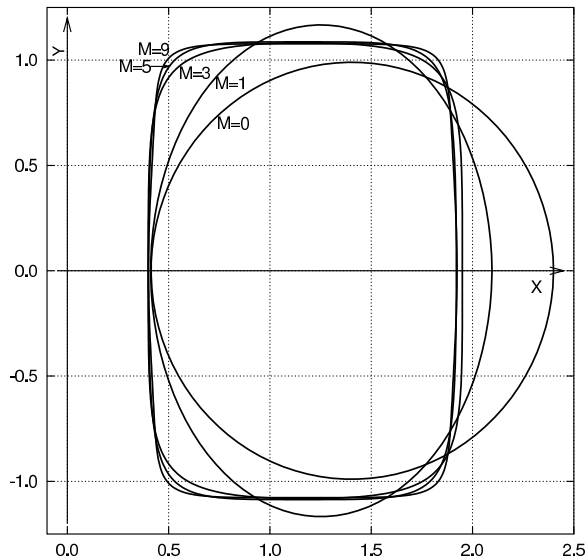
Figure 5. Evolution of the energy-minimizing hole with the number of the mapping terms M at the distance $\lambda = 0.4$.
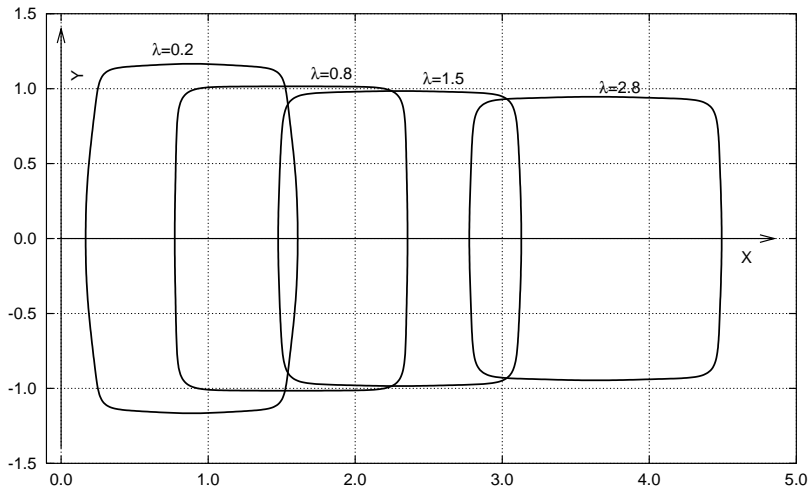

Figure 6. Evolution of the energy-minimizing hole with the distance λ at $M = 9$.

This is in contrast to the horizontal symmetry of the holes as predefined by taking only real values of $d_k, k = 0, 1, 2 \ldots$ before the optimization process.

Table 5 presents the edge separation ratio λ / h introduced in [Waldman et al. 2003] (here h is the half height of the quadrangle) for the optimal shapes at $M = 9$ for different values of λ together with the mapping coefficients. The parametric equation of the shapes then has the form

$$x(\theta) = \frac{\lambda - \operatorname{Re} \omega(\pi) + \operatorname{Re} \omega(\theta)}{F}, \quad y(\theta) = \frac{\operatorname{Im} \omega(\theta)}{F} \qquad \text{for } 0 \le \theta \le 2\pi, \tag{7.1}$$

λ	d_1	d_3	d_5	d_7	d_9	ΔW	λ/h
0.2	-0.2067	-0.1144	0.0240	0.0067	-0.0033	0.8409	0.2195
0.4	-0.1600	-0.1222	0.0187	0.0081	-0.0033	0.8261	0.4425
0.6	-0.1567	-0.1244	0.0167	0.0086	-0.0022	0.8268	0.6643
0.8	-0.1533	-0.1244	0.0160	0.0090	-0.0022	0.8341	0.8850
1.0	-0.1167	-0.1333	0.0080	0.0090	-0.0015	0.8434	1.1108
1.5	-0.1033	-0.1378	0.0047	0.0071	-0.0015	0.8651	1.6717
2.0	-0.0667	-0.1378	0.0033	0.0071	-0.0007	0.8822	2.2350
3.0	-0.0267	-0.1378	0.0013	0.0071	-0.0004	0.9010	3.3529

Table 5. Mapping coefficients, energy increment and the separation ratio λ/h for the optimal shapes at $M = 9$. The even terms d_{2m}, $m = 1, 2, \ldots$ go to zero.

where

$$\omega(\theta) = t + \sum_{m=1,3,\ldots}^{M} d_m t^{-m}, \quad F = 1 - \sum_{m=1,3,\ldots}^{M} m d_m^2, \quad t = \exp i\theta.$$

The displacements (2.14) and the stresses (2.15) along the optimal shape can also be obtained through $\varphi(t)$ and $\varphi'(t)$, respectively, as a by-product of the energy optimization. The remaining figures show them as a function of the contour arc length s:

$$ds = |\omega'(\xi)||d\xi| = |\omega'(\vartheta)|d\vartheta; \qquad \xi = e^{i\vartheta} \in \gamma, \tag{7.2}$$

normalized by the length s_0 of the upper half of the optimal rectangle. Let the contour be traversed in the counterclockwise direction and let $s = 0$ correspond to the right point on the x-axis. Let also $s_{1,2}$ denote the arc length at the upper right and upper left corner points, respectively, so that with a certain approximation we have, setting $t = x + iy \in L$,

$$\begin{aligned} 0 \leq s < s_1 &: ds = dy, \quad dt = i\,dy, \\ s_1 < s < s_2 &: ds = -dx, \quad dt = -dx, \\ s_2 < s \leq s_0 &: ds = -dy, \quad dt = i\,dy. \end{aligned} \tag{7.3}$$

In stating (7.3) the optimal shape is supposed to be a true rectangle. From Figure 7 we may conservatively conclude that the Cartesian displacements of the optimal shape tend to piecewise linear functions in the corresponding coordinates:

$$\begin{aligned} 0 \leq s < s_1 &: u_x(t) = \alpha_1, \\ s_1 < s < s_2 &: u_x(t) = \alpha_2 x + \alpha_3, \\ s_2 < s \leq s_0 &: u_x(t) = \alpha_4, \\ 0 \leq s < s_1 &: u_y(t) = \beta_1 y + \beta_2, \\ s_1 < s < s_2 &: u_y(t) = \beta_3, \\ s_2 < s \leq s_0 &: u_y(t) = \beta_4 y + \beta_5, \end{aligned} \tag{7.4}$$

where the constants α_j, β_j provide the continuity of displacement at the corners s_1, s_2. Now, referring back to the displacement-stress relation (2.16) and making use of (7.3) and (7.4), we conclude that the
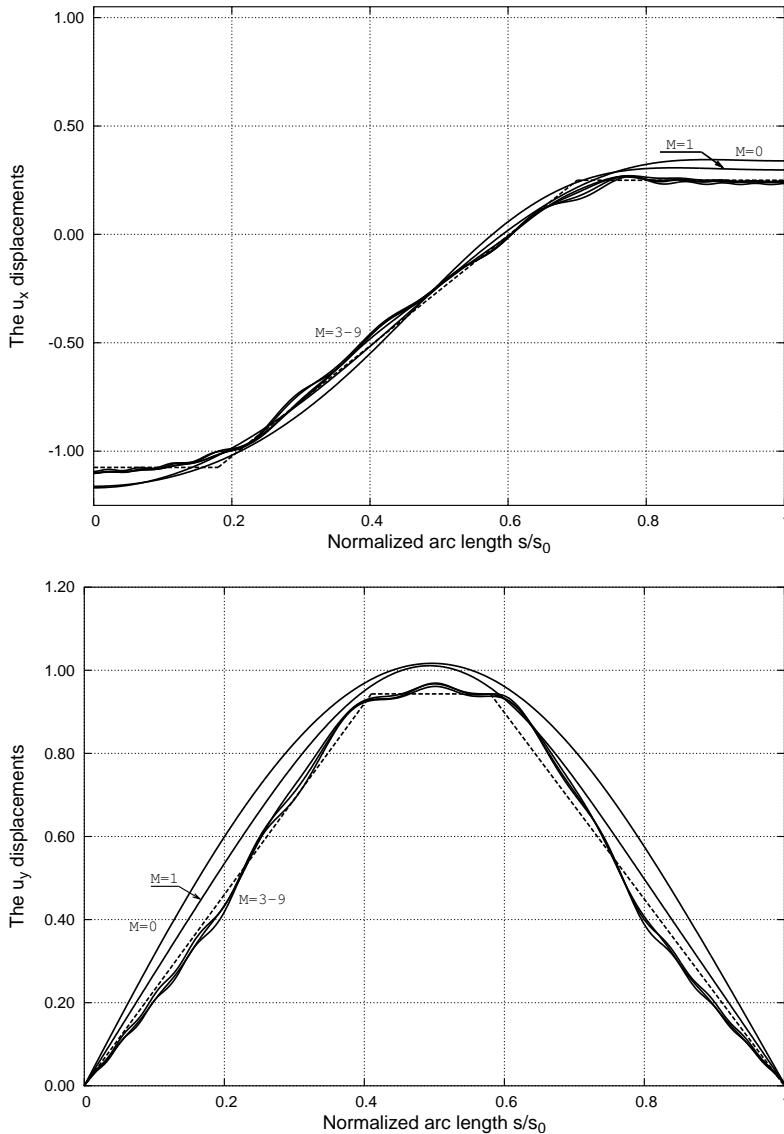
Figure 7. Boundary displacements $u_x(s)$ (top) and $u_y(s)$ (bottom) along the energy-minimizing hole shape as a function of the mapping size M, for $\lambda = 0.4$. The dashed piecewise linear trend line is also added for comparison.

tangential stresses should be then piecewise constant:

$$\begin{aligned}
0 \leq s < s_1 &: \sigma_{\tau\tau}(s) = 4q\,\beta_1, \\
s_1 < s < s_2 &: \sigma_{\tau\tau}(s) = -4q\,\alpha_2, \\
s_2 < s \leq s_0 &: \sigma_{\tau\tau}(s) = 4q\,\beta_4,
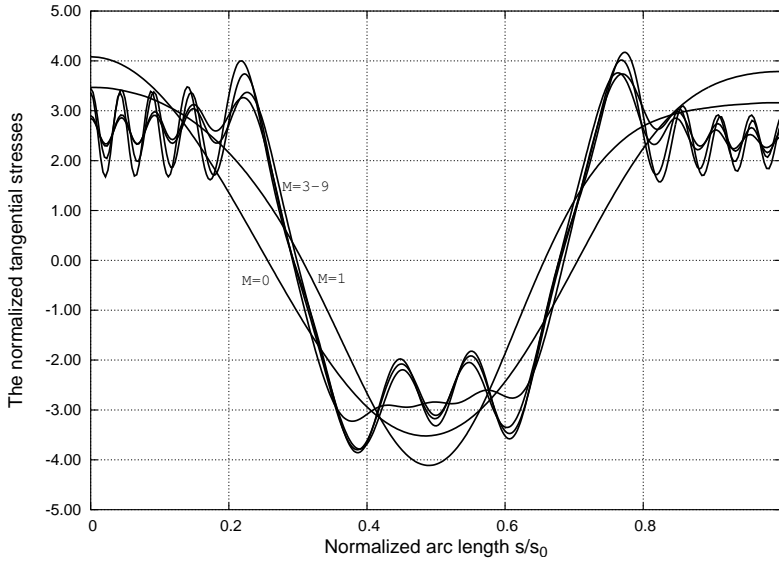\end{aligned} \tag{7.5}$$

Figure 8. Tangential stresses $\sigma_{\tau\tau}(s)$ along the energy-minimizing hole shape as a function of the mapping size M at $\lambda = 0.4$.

where we introduced the symbol

$$q = \left(\frac{1}{K} + \frac{1}{\mu}\right)^{-1}.$$

However, the stress distributions obtained through (2.15) independently of the linearity assumption (7.4) on the displacements exhibit, for $M \geq 2$, unacceptable oscillations (Figure 8) that mask the piecewise constancy trend. They result from numerical term-by-term differentiation, as explained at the end of Section 4.

To improve the situation, we smooth the stresses so computed by numerical expansion in Fourier series followed by convolution with the Feier kernel. Though crude, this analysis shows that the filtered stresses (Figure 9) tend to a piecewise distribution. These numerical conjectures are in keeping with the already known analytical facts that the Cartesian displacements of equistress boundaries are proportional to the corresponding coordinate [Vigdergauz 1988] and that the stress distribution along the optimal shape of a single hole under pure shear is piecewise constant [Vigdergauz and Cherkayev 1986]. Further, Figures 8 and 9 show that the energy minimization with increasing M is accompanied by decreasing the stress concentration. This favors our choice of the energy optimization.

In this context, very interesting results have been independently obtained by Waldman et al. [2003] through FEM analysis within an effective gradientless optimization searching. The quadrangle-like interacting holes were numerically shown to keep the stress constancy which was taken as the optimization criterion. Figure 10 shows a quantitative agreement between the stress distribution along the stress-minimizing [Waldman et al. 2003] and the energy-minimizing holes at shear type (but not pure shear) loading $\Gamma_0/2B_0 = 3$ and at approximately the same hole separation. The observed stress concentration error of 8-9% stems not only from the lesser accuracy of the KM energy solver in computing the stresses
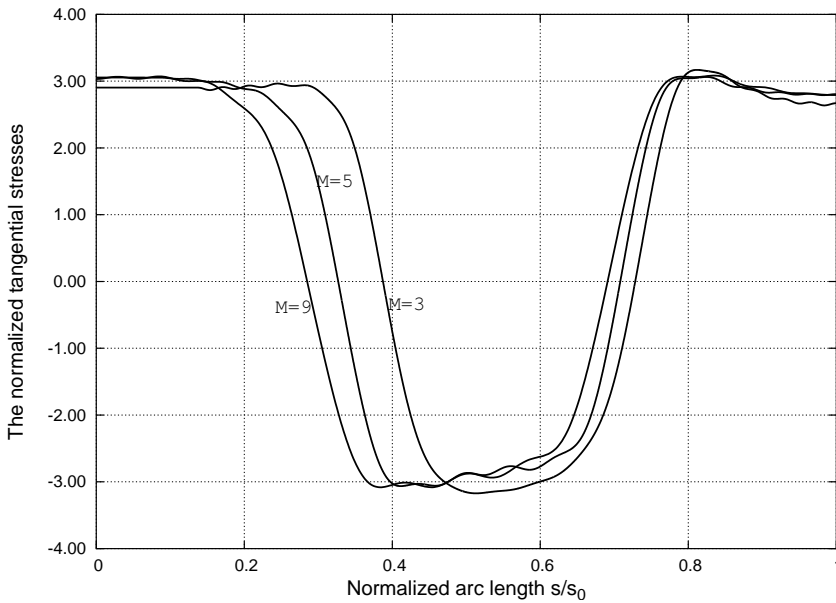
Figure 9. Filtered stress distributions $\sigma_{\tau\tau}(s)$ along the energy-minimizing hole shape as a function of the mapping size M at $\lambda = 0.4$.
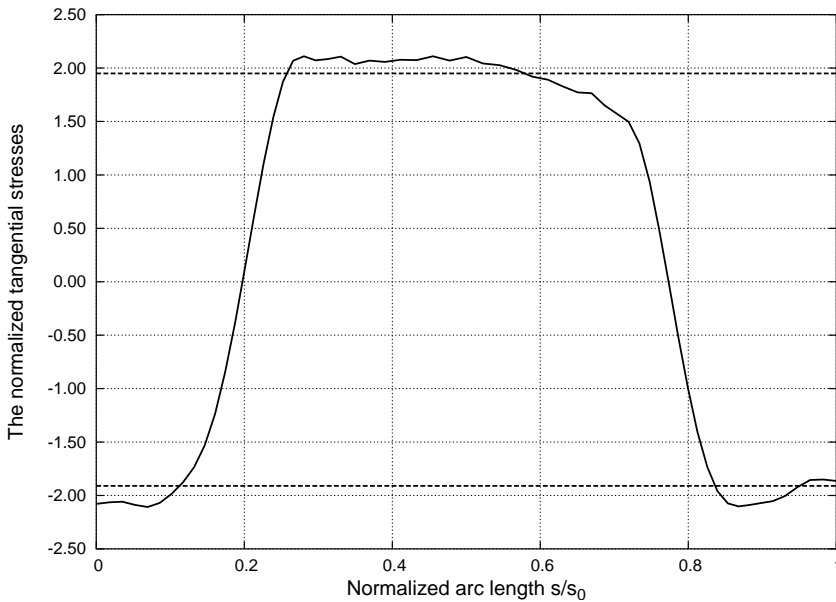

Figure 10. Filtered stress distributions $\sigma_{\tau\tau}(s)$ along the energy-minimizing hole at $\lambda/h \approx 0.322$ and $\Gamma_0/2B_0 = 3$ against the stress constancy optimization levels (the dashed lines) along the quadrangle sides [Waldman et al. 2003].

but also, to some extent, from comparing the *energy*-minimizing hole in an *infinite* plane to the *stress*-constant hole in a *finite* plate. For reference, we also note that the constant-stress value $|\sigma| = 2.84$ reported in [Waldman et al. 2003] for a single hole under pure shear deviates by approximately 2% from the semianalytical value 2.779... [Vigdergauz 2006].

8. Concluding remarks

The essential points in this paper are, first, the novel utilization of the conformal mapping technique to encode the optimized shapes within an evolutionary algorithm and, second, the effective application of this scheme to the rather difficult optimization problem of two-dimensional elastostatics.

In our opinion, the proposed mapping-based shape representation can be a competitive alternative to the nodal points in numerically treating both forward and optimization boundary-value problems of continuum mechanics. This computation-saving technique is easily adapted to evaluate appearing boundary integrals in a variety of direct solvers, from ideally suited integral equations to less open FEMs.

The specific results obtained show that interacting holes under pure shear store less energy and hence are stiffer than a single hole of the same area. Though known as rule-of-thumb, this fact has not yet been investigated numerically. It is of special interest that the stress concentration on the stress-constant holes is numerically shown to be independent of the separation distances [Waldman et al. 2003].

References

[Alfors 1979] L. Alfors, *Complex analysis*, 3rd ed., McGraw-Hill, New York, 1979.

[Banichuk 1977] N. V. Banichuk, "Optimality conditions in the problem of seeking the hole shapes in elastic bodies", *J. Appl. Math. Mech.* **41** (1977), 920–925. MR 80i:73012

[Cherepanov 1974] G. P. Cherepanov, "Inverse problems of the plane theory of elasticity", *Prikl. Mat. Mekh.* **38**:6 (1974), 963–979. In Russian; translated in *J. Appl. Math. Mech.* **38**:5 (1974), 913–931. MR 52 #7254

[Cherkaev et al. 1998] A. V. Cherkaev, Y. Grabovsky, A. B. Movchan, and S. K. Serkov, "The cavity of the optimal shape under the shear stresses", *Internat. J. Solids Structures* **35**:33 (1998), 4391–4410. MR 99e:73040

[Cherkaev n.d.] A. V. Cherkaev, "Optimal shapes of holes in an elastic plane", Web page, n.d., See http://www.math.utah.edu/~cherk/holes/index.html.

[England 1971] A. H. England, *Complex variable methods in elasticity*, Wiley, London, 1971. Reprinted by Dover, New York, 2003. MR 57 #4745

[Gibiansky and Cherkaev 1984] L. V. Gibiansky and A. V. Cherkaev, "Design of composite plates of extremal rigidity", Report 914, Ioffe Physicotechnical Institute, Leningrad, 1984. In Russian; translated as pp. 95–137 in *Topics in the mathematical modelling of composite materials*, edited by A. V. Cherkaev and R. H. Kohn, Progr. Nonlinear Differential Equations Appl. **31**, Birkhäuser, Boston, 1997. MR 1493041

[Grabovsky and Kohn 1995] Y. Grabovsky and R. V. Kohn, "Microstructures minimizing the energy of a two phase elastic composite in two space dimensions, II: The Vigdergauz microstructure", *J. Mech. Phys. Solids* **43**:6 (1995), 949–972. MR 96c:73043

[Helsing and Jonsson 2000] J. Helsing and A. Jonsson, "Complex variable boundary integral equations for perforated infinite planes", *Engineering Analysis with Boundary Elements* **25**:3 (2000), 191–202.

[Jasiuk 1995] I. Jasiuk, "Cavities vis-a-vis rigid inclusions: elastic moduli of materials with polygonal inclusions", *International Journal of Solids and Structures* **32**:3/4 (1995), 407–422.

[Ling 1948] C.-B. Ling, "On the stresses in a plate containing two circular holes", *J. Appl. Phys.* **19** (1948), 77–82. MR 9,395k

[Muskhelishvili 1963] N. I. Muskhelishvili, *Some basic problems of the mathematical theory of elasticity: Fundamental equations, plane theory of elasticity, torsion and bending*, Noordhoff, Leyden, 1963. MR 50 #15516

[Osyczka 2001] A. Osyczka, *Evolutionary algorithms for single and multicriteria design optimization*, Springer, Heidelberg, 2001.

[Schoenauer et al. 1996] M. Schoenauer, L. Kallel, and F. Jouve, "Mechanical inclusions identification by evolutionary computation", *Rev. Européenne Élém. Finis* **5**:5-6 (1996), 619–648. MR 97m:73060

[Ting et al. 1999] K. Ting, K. T. Chen, and W. S. Wang, "Applied alternating method to analyze the stress concentration around interacting multiple circular holes in an infinite domain", *International Journal of Solids and Structures* **36** (1999), 533–556.

[Vigdergauz 1976] S. B. Vigdergauz, "Integral equation of the inverse problem of the plane theory of elasticity", *Prik. Matem. Mekhan.* **40** (1976), 566–569. In Russian; translated in *Journal of Applied Mathematics and Mechanics* **40**:3 (1976), 518–522.

[Vigdergauz 1982] S. B. Vigdergauz, "Equi-strength hole in a half-plane", *Izv. AN SSSR, Mekhanika Tverdogo Tela* **17** (1982), 94–98. In Russian; translated in *Mechanics of Solids* **17**:1 (1982), 87–91.

[Vigdergauz 1988] S. B. Vigdergauz, "Stressed state of an elastic plane with constant-stress holes", *Izv. AN SSSR, Mekhanika Tverdogo Tela* **23** (1988), 101–104. In Russian; translated in *Mechanics of Solids* **23**:3 (1988), 96–99.

[Vigdergauz 1996] S. Vigdergauz, "Rhombic lattice of equi-stress inclusions in an elastic plate", *Quart. J. Mech. Appl. Math.* **49**:4 (1996), 565–580. MR 97g:73074

[Vigdergauz 2001a] S. B. Vigdergauz, "Genetic algorithm perspective to identify energy-optimizing inclusions in an elastic plate", *International Journal of Solids and Structures* **38** (2001), 6851–6867.

[Vigdergauz 2001b] S. B. Vigdergauz, "The effective properties of a perforated elastic plate: Numerical optimization by genetic algorithm", *International Journal of Solids and Structures* **38** (2001), 8593–8616.

[Vigdergauz 2006] S. B. Vigdergauz, "Stress-minimizing hole in an elastic plate under remote shear", *Journal of Mechanics of Materials and Structures* **1** (2006), 387–406.

[Vigdergauz and Cherkayev 1986] S. B. Vigdergauz and A. V. Cherkayev, "A hole in a plate optimal for its biaxial extension-compression", *Prikl. Mat. Mekh.* **50**:3 (1986), 524–528. In Russian; translated in *J. Appl. Math. Mech.* **50**:3 (1986), 401–404. MR 88g:73073

[Waldman et al. 2003] W. Waldman, M. Heller, and L. R. F. Rose, "Shape optimisation of two closely spaced holes for fatigue life extension", Report dsto-rr-0253, Defence Science and Technology Organization, Department of Defence, Australian Government, 2003, See http://www.dsto.defence.gov.au/publications/2558/.

SHMUEL VIGDERGAUZ: smuel@iec.co.il
Research and Development Division, The Israel Electric Corporation, Ltd., P. O. Box 10, Haifa 31000, Israel

MULTIFIELD MODEL FOR COSSERAT MEDIA

ALEKSEY A. VASILIEV, ANDREY E. MIROSHNICHENKO AND MASSIMO RUZZENE

We construct a two-field higher-order gradient micropolar model for Cosserat media on the basis of a square lattice of elements with rotational degrees of freedom. This model includes equations of single-field higher-order gradient micropolar theory, and additional ones, which allow modelling of short wavelength phenomena. We demonstrate an example of short wavelength spatially localized static deformations in a structural system, which could not be obtained in the classical single-field framework, but which are captured by the proposed two-field model.

1. Introduction

Field theories are effectively used for modeling structural systems. In particular, they help to define generalized macrocharacteristics of systems, find analytical solutions by using well-developed mathematical methods, and in cases when it is impossible to make computational investigation by using effective numerical methods and packages based on artificial discretization. There are however structural effects, which are not captured through classical continuum models. This may lead to essential errors in application. The study of such effects within the framework of the field theories requires the development of generalized continuum models. One approach to the development of such models consists in the analysis and evaluation of key physical hypotheses of existing models and, further, their rejection or generalization [Lomakin 1970; Rogula 1985]. For example, in Cosserat and micropolar models [Cosserat and Cosserat 1909; Eringen 1999; Askar 1986; Maugin 1999] rotational degrees of freedom of structural elements are taken into consideration in addition to displacements, while higher derivatives of the fields are taken into account in higher-order gradient models [Triantafyllidis and Bardenhagen 1993; Fleck and Hutchinson 1997; 2001; Peerlings et al. 2001; Askes et al. 2002; Bažant and Jirásek 2002; Aifantis 2003].

For bodies with periodic microstructure, homogenized models are constructed on the basis of an elementary cell of periodicity by using a single vector function of the generalized displacements, defining the degrees of freedom of the elementary cell. Methods of obtaining continuum models from lattice models, comparison between discrete lattice and continuum models, their advantages and applications for solving different problems have been discussed in earlier articles [Noor 1988; Triantafyllidis and Bardenhagen 1993; Pasternak and Mühlhaus 2000; Askes et al. 2002; Suiker and de Borst 2005; Pavlov et al. 2006] and monographs [Born and Huang 1954; Askar 1986; Maugin 1999]. The derivation and analysis of generalized models starting from microstructural models is one of the key approaches to develop, explore, and find practical interpretations of corresponding phenomenological theories. By using a macrocell, comprised of several elementary unit cells, and, accordingly, by increasing the number

of vector fields in order to describe the deformations of the system we come to models of multifield theory [Vasiliev and Miroshnichenko 2005; Vasiliev et al. 2005], which is discussed here.

Underlying hypotheses used in the construction of the above-mentioned theories are mutually independent, complementary, and can be used in various combinations. Single-field higher-order gradient micropolar models and their applications were considered in [Mühlhaus and Oka 1996; Suiker and de Borst 2005; Pavlov et al. 2006]. A nonlocal continuum Cosserat model was presented in [Pasternak and Mühlhaus 2000]. The hierarchical system of multifield micropolar models was derived in [Vasiliev and Miroshnichenko 2005]. In the present article, we derive the higher-order gradient generalization of the two-field micropolar model introduced in [Vasiliev and Miroshnichenko 2005] and compare different models in order to define possible applications of multifield theory.

The article is organized as follows. The discrete model of a square lattice of elements with rotational degrees of freedom and its single-field higher-order gradient micropolar model are presented in Sections 2 and 3. In Section 4 we derive a two-field higher-order gradient micropolar model for a Cosserat medium. In Section 5 the comparative analysis of models for a two-dimensional case is carried out by using plane wave solutions. Particular cases of the models presented in Sections 2–4 for the study of one-dimensional deformations are derived in Section 6. The comparative analysis of the models in the description of spatially localized dynamic and static deformations is presented in Sections 7 and 8. In Section 9 we briefly summarize our results, outline possible fields of applications, and describe further investigations.

2. Cosserat lattice

We consider a Cosserat lattice, that is, a lattice whose deformations are described by displacements u_n, v_n, and by rotations φ_n of its elements. The elements are placed at the nodes of a square lattice as shown in Figure 1a. The potential energy associated with the elastic connection of elements m, k has the
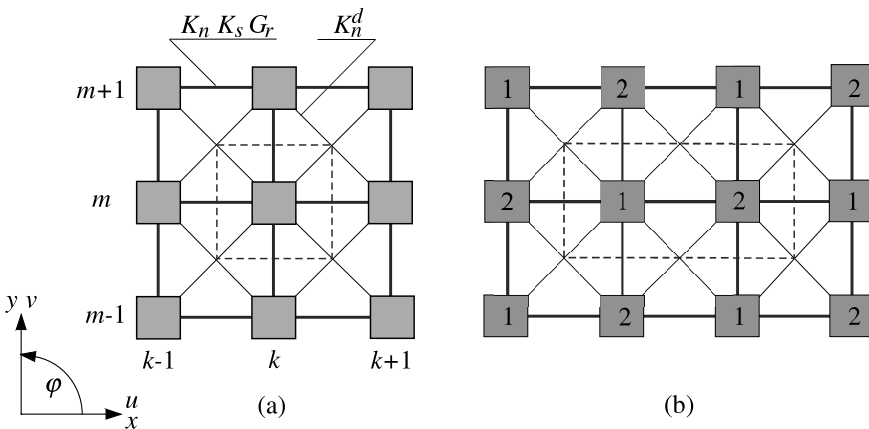

Figure 1. (a) An example of a square lattice consisting of elements with rotational degrees of freedoms. (b) Variant of numeration of identical elements, used for deriving the two-field model. The unit cell and macrocell consisting of two elements are shown by dashed lines.

following form

$$2E_{pot}^{k,m} = K_n^{k,m}(u_m - u_k)^2 + K_s^{k,m}\left[v_m - v_k - r_{k,m}\frac{\varphi_m + \varphi_k}{2}\right]^2 + G_r^{k,m}(\varphi_m - \varphi_k)^2, \tag{1}$$

where $r_{k,m}$ is a length parameter, $K_n^{k,m}$, $K_s^{k,m}$, and $G_r^{k,m}$ characterize the stiffness of the connections in the longitudinal and transverse directions, and the resistance to rotations of elements. This form of potential energy is used in models of granular media [Limat 1988; Pasternak and Mühlhaus 2000; Suiker et al. 2001]. The potential energy of beam finite elements which is often used in lattice models of constructions and materials [Noor 1988], can be considered as a particular case of Equation (1). We use the notations K_n, K_s, and G_r for the elastic constants of the axial connections, while K_n^d is the axial stiffness of the diagonal connections, and we assume that $K_s^d = 0$, $G_r^d = 0$. The last assumptions mean that we assume a string type model for connections of elements in a diagonal direction. Such a model of interactions was assumed in the models of structural media proposed in [Pavlov et al. 2006]. As it was shown in [Suiker et al. 2001] it is required for the long-wave approximation for equation of motion of the square lattice to be equal to the equations of motion of the Cosserat continuum model. Very often, for example in beam lattice constructions, there are no diagonal connections at all, that is, additionally we should assume that $K_n^d = 0$. The parameter $r_{k,m}$ is equal to h and $h\sqrt{2}$ for the axial and diagonal connections, respectively.

The expression for the kinetic energy of elements has the standard form

$$E_{kin}^k = \tfrac{1}{2}M\dot{u}_k^2 + \tfrac{1}{2}M\dot{v}_k^2 + \tfrac{1}{2}I\dot{\varphi}_k^2,$$

where M is the mass and I is the moment of inertia of kth element.

The equations of motion are obtained by using Lagrange's equations and have the form

$$\begin{aligned}
M\ddot{u}_{k,m} &= K_n\Delta_{xx}u_{k,m} + K_s\left(\Delta_{yy}u_{k,m} + \tfrac{1}{2}h\Delta_y\varphi_{k,m}\right) + \tfrac{1}{2}K_n^d(\Delta u_{k,m} + \Delta_{xy}v_{k,m}), \\
M\ddot{v}_{k,m} &= K_n\Delta_{yy}v_{k,m} + K_s\left(\Delta_{xx}v_{k,m} - \tfrac{1}{2}h\Delta_x\varphi_{k,m}\right) + \tfrac{1}{2}K_n^d(\Delta v_{k,m} + \Delta_{xy}u_{k,m}), \\
I\ddot{\varphi}_{k,m} &= \left(G_r - \tfrac{1}{4}K_s h^2\right)(\Delta_{yy}\varphi_{k,m} + \Delta_{xx}\varphi_{k,m}) + \tfrac{1}{2}K_s h(\Delta_x v_{k,m} - \Delta_y u_{k,m} - 4h\varphi_{k,m}),
\end{aligned} \tag{2}$$

where the following notations are used

$$\begin{aligned}
\Delta_x w_{k,m} &= w_{k+1,m} - w_{k-1,m}, \quad \Delta_{xx}w_{k,m} = w_{k+1,m} - 2w_{k,m} + w_{k-1,m}, \\
\Delta_y w_{k,m} &= w_{k,m+1} - w_{k,m-1}, \quad \Delta_{yy}w_{k,m} = w_{k,m+1} - 2w_{k,m} + w_{k,m-1}, \\
\Delta_{xy}w_{k,m} &= w_{k+1,m+1} - w_{k+1,m-1} - w_{k-1,m+1} + w_{k-1,m-1}, \\
\Delta w_{k,m} &= w_{k+1,m+1} + w_{k+1,m-1} + w_{k-1,m+1} + w_{k-1,m-1} - 4w_{k,m}.
\end{aligned}$$

3. Higher-order gradient micropolar model

In the micropolar model it is assumed that deformations of a discrete system can be described by using the single vector function $\{u(x, y, t), v(x, y, t), \varphi(x, y, t)\}$, which has the same components of the vector of generalized displacements $\{u_{k,m}(t), v_{k,m}(t), \varphi_{k,m}(t)\}$ of the unit cell. Accordingly, the following equalities are assumed at the nodes of the lattice

$$\{u(x, y, t), v(x, y, t), \varphi(x, y, t)\}\Big|_{\substack{x=kh \\ y=mh}} = \{u_{k,m}(t), v_{k,m}(t), \varphi_{k,m}(t)\}.$$

The substitution $w_{k\pm1,m\pm1}(t) \to w(x \pm h, y \pm h, t)$ in the finite difference equations (2) leads to the functional difference nonlocal equations in spatial variables. Using Taylor series expansions

$$w(x \pm h, y \pm h, t) = e^{\pm h\partial_x \pm h\partial_y} w(x, y, t) = \sum_{r=0}^{N_x} \sum_{p=0}^{N_y} \frac{(\pm h)^r}{r!} \frac{(\pm h)^p}{p!} \frac{\partial^{r+p} w(x, y, t)}{\partial x^r \partial y^p} \tag{3}$$

gives a set of equations, which are differential with respect to spatial and temporal variables. The expansion (3) is exact and the continuum equations are exact if the Taylor series expansions include all derivatives, that is, $N_x = \infty$ and $N_y = \infty$. Truncation of the series to the Nth order, that is, up to $N_x + N_y \le N$, yields the formulation of approximated continuum models.

Keeping derivatives up to the fourth order leads to the following single-field higher-order gradient micropolar model

$$\begin{aligned}
Mu_{tt} = {} & (K_n + K_n^d)h^2 u_{xx} + (K_s + K_n^d)h^2 u_{yy} + 2K_n^d h^2 v_{xy} + K_s h^2 \varphi_y \\
& + \tfrac{1}{12}(K_n + K_n^d)h^4 u_{xxxx} + \tfrac{1}{12}(K_s + K_n^d)h^4 u_{yyyy} + \tfrac{1}{2} K_n^d h^4 u_{xxyy} \\
& \qquad\qquad\qquad\qquad + \tfrac{1}{3} K_n^d h^4 (v_{xyyy} + v_{xxxy}) + \tfrac{1}{6} K_s h^4 \varphi_{yyy},
\end{aligned}$$

$$\begin{aligned}
Mv_{tt} = {} & (K_s + K_n^d)h^2 v_{xx} + (K_n + K_n^d)h^2 v_{yy} + 2K_n^d h^2 u_{xy} - K_s h^2 \varphi_x \\
& + \tfrac{1}{12}(K_s + K_n^d)h^4 v_{xxxx} + \tfrac{1}{12}(K_n + K_n^d)h^4 v_{yyyy} + \frac{1}{2} K_n^d h^4 v_{xxyy} \\
& \qquad\qquad\qquad\qquad + \tfrac{1}{3} K_n^d h^4 (u_{xyyy} + u_{xxxy}) - \tfrac{1}{6} K_s h^4 \varphi_{xxx},
\end{aligned} \tag{4}$$

$$\begin{aligned}
I\varphi_{tt} = {} & \big(G_r - \tfrac{1}{4}K_s h^2\big)h^2(\varphi_{xx} + \varphi_{yy}) + K_s h^2(v_x - u_y - 2\varphi) \\
& + \tfrac{1}{12}\big(G_r - \tfrac{1}{4}K_s h^2\big)h^4(\varphi_{xxxx} + \varphi_{yyyy}) + \tfrac{1}{6} K_s h^4(v_{xxx} - u_{yyy}).
\end{aligned}$$

The single-field model with derivatives up to the second order and its comparison with a conventional micropolar model are presented in [Suiker et al. 2001].

4. Two-field higher-order gradient micropolar model

The method of deriving a hierarchical system of multifield models was proposed in [Vasiliev and Miroshnichenko 2005]. In the present article, only some basic ideas will be presented, and the two-field higher-order gradient micropolar model will be obtained.

The single-field micropolar model was derived on the basis of the discrete equations of motion for the particles of the unit cell by using the single vector function $\{u(x, y, t), v(x, y, t), \varphi(x, y, t)\}$. The two-field model is derived by considering as a basis a macrocell consisting of two elementary cells. Although, all elements of the system are identical, they are marked with different numbers as shown in Figure 1b. Also, the generalized displacements are denoted as $u_{k,m}^{[n]}$, $v_{k,m}^{[n]}$, $\varphi_{k,m}^{[n]}$ where the superscript $n = 1, 2$ identifies the generalized displacements of the elements included in the macrocell. Two vector functions $\{u^{[n]}(x, y, t), v^{[n]}(x, y, t), \varphi^{[n]}(x, y, t)\}$, $n = 1, 2$, are used in the two-field theory to describe the displacements and rotations of the particles marked by numbers $n = 1, 2$, respectively. The behavior of

the macrocell is governed by six discrete equations of motion. The application of Taylor series expansions leads to six continuum equations of the multifield model.

The following new field functions are introduced:

$$u^{[n]}(x, y, t) = u(x, y, t) + (-1)^n \tilde{u}(x, y, t),$$
$$v^{[n]}(x, y, t) = v(x, y, t) + (-1)^n \tilde{v}(x, y, t),$$
$$\varphi^{[n]}(x, y, t) = \varphi(x, y, t) + (-1)^n \tilde{\varphi}(x, y, t), \quad n = 1, 2,$$

in order to decouple the six equations of the two-field model onto two subsystems.

The equations for the vector function $\{u(x, y, t), v(x, y, t), \varphi(x, y, t)\}$ coincide with Equations (4). The other three equations for $\{\tilde{u}(x, y, t), \tilde{v}(x, y, t), \tilde{\varphi}(x, y, t)\}$ have the following form

$$M\tilde{u}_{tt} = (-K_n + K_n^d)h^2\tilde{u}_{xx} + (-K_s + K_n^d)h^2\tilde{u}_{yy} + 2K_n^d h^2\tilde{v}_{xy} - 4(K_n + K_s)\tilde{u}$$
$$- K_s h^2\tilde{\varphi}_y - \frac{1}{12}(K_n - K_n^d)h^4\tilde{u}_{xxxx} - \frac{1}{12}(K_s - K_n^d)h^4\tilde{u}_{yyyy} + \frac{1}{2}K_n^d h^4\tilde{u}_{xxyy}$$
$$+ \frac{1}{3}K_n^d h^4(\tilde{v}_{xxxy} + \tilde{v}_{xyyy}) - \frac{1}{6}K_s h^4\tilde{\varphi}_{yyy},$$

$$M\tilde{v}_{tt} = 2K_n^d h^2\tilde{u}_{xy} + (-K_s + K_n^d)h^2\tilde{v}_{xx} + (-K_n + K_n^d)h^2\tilde{v}_{yy} - 4(K_n + K_s)\tilde{v}$$
$$+ K_s h^2\tilde{\varphi}_x - \frac{1}{12}(K_s - K_n^d)h^4\tilde{v}_{xxxx} - \frac{1}{12}(K_n - K_n^d)h^4\tilde{v}_{yyyy} + \frac{1}{2}K_n^d h^4\tilde{v}_{xxyy}$$
$$+ \frac{1}{3}K_n^d h^4(\tilde{u}_{xxxy} + \tilde{u}_{xyyy}) + \frac{1}{6}K_s h^4\tilde{\varphi}_{xxx},$$

$$I\tilde{\varphi}_{tt} = -\left(G_r - \frac{1}{4}h^2 K_s\right)h^2(\tilde{\varphi}_{xx} + \tilde{\varphi}_{yy}) + K_s h^2(\tilde{u}_y - \tilde{v}_x) - 8G_r\tilde{\varphi}$$
$$- \frac{1}{12}\left(G_r - \frac{1}{4}K_s h^2\right)h^4(\tilde{\varphi}_{xxxx} + \tilde{\varphi}_{yyyy}) + \frac{1}{6}K_s h^4(\tilde{u}_{yyy} - \tilde{v}_{xxx}). \quad (5)$$

Thus, the two-field model consists of Equation (4) of the single-field theory and Equation (5), the meaning of which will be clarified by the following analysis.

5. Plane wave solutions: the comparative analysis of the models

We are looking for solutions of the discrete equations of motion (2) in the following form

$$u_{k,m} = \tilde{U} \exp\left[i(\omega t - kK_x - mK_y)\right],$$
$$v_{k,m} = \tilde{V} \exp\left[i(\omega t - kK_x - mK_y)\right], \quad (6)$$
$$\varphi_{k,m} = \tilde{\Phi} \exp\left[i(\omega t - kK_x - mK_y)\right],$$

where $K_x = k_x h$, $K_y = k_y h$, k_x and k_y are wave numbers, $\tilde{U}$, $\tilde{V}$, and $\tilde{\Phi}$ are amplitudes, and ω is the angular frequency.

By substituting the expressions in Equation (6) into (2) we obtain a system of three linear equations

$$(a_{11} + M\omega^2)\tilde{U} + a_{12}\tilde{V} + a_{13} i\tilde{\Phi} = 0,$$
$$a_{12}\tilde{U} + (a_{22} + M\omega^2)\tilde{V} + a_{23} i\tilde{\Phi} = 0, \quad (7)$$
$$a_{13}\tilde{U} + a_{23}\tilde{V} + (a_{33} + I\omega^2)i\tilde{\Phi} = 0,$$

with coefficients

$$
\begin{aligned}
a_{11} &= 2(\cos K_x - 1)K_n + 2(\cos K_y - 1)K_s + 2(\cos K_x \cos K_y - 1)K_n^d, \\
a_{12} &= -2K_n^d \sin K_x \sin K_y, \\
a_{13} &= -hK_s \sin K_y, \\
a_{23} &= hK_s \sin K_x, \\
a_{22} &= 2(\cos K_y - 1)K_n + 2(\cos K_x - 1)K_s + 2(\cos K_x \cos K_y - 1)K_n^d, \\
a_{33} &= -(2 + \cos K_x + \cos K_y)h^2 K_s/2 + 2(\cos K_x + \cos K_y - 2)G_r.
\end{aligned}
\tag{8}
$$

In the continuum models, the following plane-wave solution is considered

$$
u(x, y, t) = \tilde{U} \exp\left[i(\omega t - k_x x - k_y y)\right],
\tag{9}
$$

$$
v(x, y, t) = \tilde{V} \exp\left[i(\omega t - k_x x - k_y y)\right],
\tag{10}
$$

$$
\varphi(x, y, t) = \tilde{\Phi} \exp\left[i(\omega t - k_x x - k_y y)\right],
\tag{11}
$$

which is the continuum analog of the discrete solution (6).

Substituting (9)–(11) into Equations (4) leads to (7) with coefficients

$$
\begin{aligned}
c_{11} &= (-K_x^2 + K_x^4/12)K_n + (-K_y^2 + K_y^4/12)K_s \\
&\quad + (-K_x^2 - K_y^2 + K_x^4/12 + K_x^2 K_y^2/2 + K_y^4/12)K_n^d, \\
c_{12} &= (-2K_x K_y + K_x K_y^3/3 + K_x^3 K_y/3)K_n^d, \\
c_{13} &= -(K_y - K_y^3/6)hK_s, \\
c_{23} &= -c_{13}(x \leftrightarrow y), \\
c_{22} &= c_{11}(x \leftrightarrow y), \\
c_{33} &= (-8 + K_x^2 + K_y^2 - K_x^4/12 - K_y^4/12)h^2 K_s/4 + (-K_x^2 - K_y^2 + K_x^4/12 + K_y^4/12)G_r.
\end{aligned}
\tag{12}
$$

These coefficients essentially can be recognized as the Taylor series expansions of the coefficients (8) of the discrete system around the point $(K_x, K_y) = (0, 0)$ up to the fourth order. In the case of classical micropolar model, the coefficients (12) include the terms of the Taylor series expansion of the coefficients in Equation (8) up to the second order. Accordingly, the dispersion curves of the conventional and higher-order gradient single-field models coincide with the dispersion curves of the discrete system at the point $(K_x, K_y) = (0, 0)$ and approximate them around this point. The higher-order gradient model improves the accuracy of the approximation at this point in comparison with the classical micropolar model. However, for short wavelength waves both single-field micropolar models produce results with an essential error.

The two-field model includes the equations of the single-field model, Equations (4), and additional (5). Six dispersion surfaces for the two-field model are defined in the area $|K_x \pm K_y| \leq \pi$. They can be split into two groups.

The surfaces of the first group correspond to those of the single-field model defined in the area $|K_x \pm K_y| \leq \pi$. Thus, two-field models possess the properties of single-field models and provide a good approximation of the dispersion surfaces for the discrete system for long wavelength waves.

The dispersion relations of the second group of surfaces correspond to Equations (5) of the two-field model. The substitution of expressions (9)–(11) into these equations leads to a system of Equations (7) with coefficients

$$
\begin{aligned}
\tilde{c}_{11} &= \left(-4 + K_x^2 - K_x^4/12\right)K_n + \left(-4 + K_y^2 - K_x^4/12\right)K_s \\
&\quad + \left(-K_x^2 - K_y^2 + K_x^4/12 + K_x^2 K_y^2/2 + K_y^4/12\right)K_n^d, \\
\tilde{c}_{12} &= \left(-6K_x K_y + K_x^3 K_y + K_x K_y^3\right)K_n^d/3, \\
\tilde{c}_{13} &= (K_y - K_y^3/6)h K_s, \\
\tilde{c}_{23} &= -\tilde{c}_{13}(x \leftrightarrow y), \\
\tilde{c}_{22} &= \tilde{c}_{11}(x \leftrightarrow y), \\
\tilde{c}_{33} &= \left(-K_x^2 - K_y^2 + K_x^4/12 + K_y^4/12\right)h^2 K_s/4 \\
&\quad + \left(-8 + K_x^2 + K_y^2 - K_x^4/12 - K_y^4/12\right)G_r.
\end{aligned}
\tag{13}
$$

These coefficients can be obtained by replacing $K_x \to -\pi + K_x$ and $K_y \to -\pi + K_y$ in the co-efficients in Equation (8) for the discrete system and their Taylor series expansions around the point $(K_x, K_y) = (0, 0)$ up to fourth order terms. Because of invariance of the dispersion relations under the transformation of variables $(K_x, K_y) \leftrightarrow (-K_x, -K_y)$, the dispersion surfaces of the two-field model plotted for the coefficients (13) in the area $K_x + K_y \leq \pi$, $K_x \geq 0$, $K_y \geq 0$ being reflected about the line $K_x = \pi/2$, $K_y = \pi/2$ coincide with the dispersion surfaces of the discrete system at $(K_x, K_y) = (\pi, \pi)$ and approximate them in the area $K_x + K_y \geq \pi$, $K_x \leq \pi$, $K_y \leq \pi$ around this point. The inclusion of higher-order derivatives into the model improves the accuracy.

Figure 2 illustrates the results of the comparative analysis of the models, the accuracy of the approximation of the dispersion surfaces of the discrete system through the dispersion surfaces of single-field (Figure 2a) and two-field (Figure 2b) models, and the influence on accuracy of the order of derivatives in the models. The dispersion curves for the discrete system in sections $K_y = 0$, $K_x = \pi$, $K_x = K_y$ are represented by solid lines. The same curves obtained for the field models with derivatives up to second and fourth orders are represented by dotted and dashed lines, respectively. We fix the parameters K_n, h, M and consider dimensionless quantities $\bar{K}_s = K_s/K_n = 1/3$, $\bar{K}_n^d = K_n^d/K_n = 0.74$, $\bar{G}_r = G_r/K_n h^2 = 1/3$, $\bar{I} = I/Mh^2 = 1/8$. Frequency is also presented in dimensionless form according to the following expression $\bar{\omega} = \omega\sqrt{M/K_n}$. The curves for the single-field and the two-field models coincide in the area $K_x + K_y \leq \pi$ and give a good approximation of the curves for the discrete system in the area of the long wavelength waves with wave numbers around the Γ-point. The two-field models give additionally good approximation for short waves in area around the M-point, where the single-field models give significant inaccuracy. The models containing the derivatives up to fourth order improve the approximation in comparison with the models with derivatives up to the second order.

6. One-dimensional models

We consider the one-dimensional deformations of a lattice placed between two rigid components (see Figure 3). Assuming that the generalized displacements are constant for elements along the diagonals, that is, for $k + m = \text{const}$, we denote components $U_{k,m}$, $V_{k,m}$, and $\Phi_{k,m}$ by using the abbreviated notations
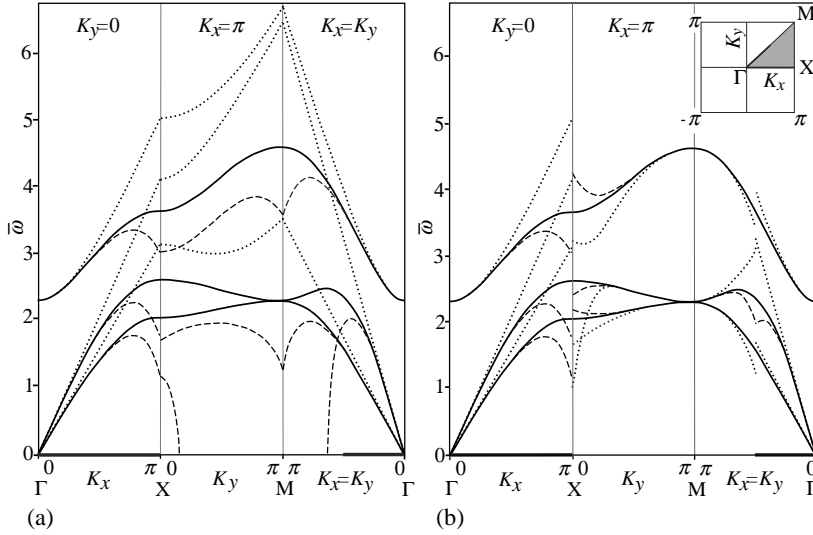
Figure 2. The dispersion curves in the sections $K_y = 0$, $K_x = \pi$, $K_x = K_y$ of the dispersion surfaces for discrete system (solid lines). The same curves obtained by using the single-field (a) and two-field (b) models with derivatives up to second (dotted lines) and fourth orders (dashed lines).

U_m, V_m, and Φ_m. The equations for U_m and V_m, Φ_m are decoupled, and we will concentrate on the solutions for U_m only.

By introducing the new coordinates $O\xi\eta$ and performing a change of variables in Equation (2), one obtains the discrete equation of motion for one-dimensional deformations:

$$M\ddot{U}_m = (K_n + K_s)(U_{m-1} - 2U_m + U_{m+1}) + K_n^d(U_{m-2} - 2U_m + U_{m+2}). \tag{14}$$

By changing the variables $(x, y) \to (\xi, \eta)$ in Equation (4) and considering one-dimensional displacements, we obtain the single-field higher-order gradient variant of Equation (14)

$$MU_{tt} = (K_n + K_s + 4K_n^d)H^2 U_{\xi\xi} + \tfrac{1}{12}(K_n + K_s + 16K_n^d)H^4 U_{\xi\xi\xi\xi}, \tag{15}$$
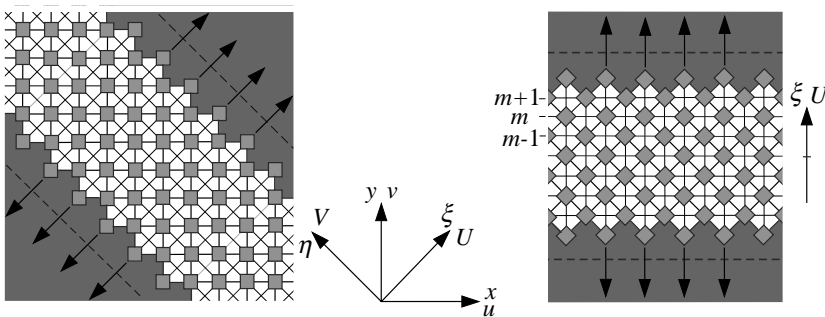

Figure 3. Representation of a thin lattice layer in a problem of tension between two rigid parts in different coordinate systems.

where $H = \sqrt{2}h/2$ is distance between layers. Equation (15) can be obtained independently by using Taylor series expansions in Equation (14).

Similarly, changing the variables $(x, y) \to (\xi, \eta)$ in Equation (5) and considering one-dimensional displacements leads to the second equation of the two-field model

$$M\tilde{U}_{tt} = -4(K_n + K_s)\tilde{U} - (K_n + K_s - 4K_n^d)H^2\tilde{U}_{\xi\xi} - \tfrac{1}{12}(K_n + K_s - 16K_n^d)H^4\tilde{U}_{\xi\xi\xi\xi}. \quad (16)$$

In order to explain the notations and to illustrate the method of derivation of the multifield models, we will obtain Equations (15) and (16) of the two-field model directly from Equation (14).

Although the unit cell in the problem under consideration consists of the single layer, we assume that a cell of periodicity consists of two layers and use the notations $U_{2n}^{[1]}(t)$ and $U_{2n+1}^{[2]}(t)$ with different superscripts [1] and [2] for displacements of the layers with coordinates $\xi = 2nH$ and $\xi = (2n+1)H$, respectively. Equation (14) can thus be rewritten in the form

$$M\ddot{U}_{2n}^{[1]} = (K_n + K_s)\big(U_{2n-1}^{[2]} - 2U_{2n}^{[1]} + U_{2n+1}^{[2]}\big) + K_n^d\big(U_{2n-2}^{[1]} - 2U_{2n}^{[1]} + U_{2n+2}^{[1]}\big), \quad (17)$$

$$M\ddot{U}_{2n+1}^{[2]} = (K_n + K_s)\big(U_{2n}^{[1]} - 2U_{2n+1}^{[2]} + U_{2n+2}^{[1]}\big) + K_n^d\big(U_{2n-1}^{[2]} - 2U_{2n+1}^{[2]} + U_{2n+3}^{[2]}\big). \quad (18)$$

We use two functions $U^{[1]}(x, t)$ and $U^{[2]}(x, t)$ in order to describe displacements of odd and even layers

$$U^{[1]}(\xi, t)|_{\xi=2nH} = U_{2n}^{[1]}(t), \qquad U^{[2]}(\xi, t)|_{\xi=(2n+1)H} = U_{2n+1}^{[2]}(t).$$

The Taylor series expansions of the displacements in Equations (17) and (18) up to fourth order terms around the points for which these equations were obtained, gives the system of coupled equations for the two-field model

$$MU_{tt}^{[1]} = \bar{L}U^{[1]} - \tilde{L}(U^{[1]} - U^{[2]}), \quad (19)$$

$$MU_{tt}^{[2]} = \bar{L}U^{[2]} + \tilde{L}(U^{[1]} - U^{[2]}), \quad (20)$$

where we separate the operator for the single-field model, Equation (15),

$$\bar{L} = (K_n + K_s + 4K_n^d)H^2\frac{\partial^2}{\partial\xi^2} + \tfrac{1}{12}(K_n + K_s + 16K_n^d)H^4\frac{\partial^4}{\partial\xi^4}$$

from the additional operator

$$\tilde{L} = (K_n + K_s)\left(2 + H^2\frac{\partial^2}{\partial\xi^2} + \frac{1}{12}H^4\frac{\partial^4}{\partial\xi^4}\right),$$

which describes the interaction of the fields. This representation of the model can be useful for the interpretation and the generalization of two-field models, in particular in the presence of nonlinearities. In the linear case, it is convenient to split the system of coupled equations (19) and (20) in two independent equations (15) and (16) by introducing the new field functions

$$U = \tfrac{1}{2}\big(U^{[2]} + U^{[1]}\big), \qquad \tilde{U} = \tfrac{1}{2}\big(U^{[2]} - U^{[1]}\big). \quad (21)$$

7. One-dimensional dynamic problem: comparative analysis of models

7.1. *Discrete model.* We consider solutions of the discrete equation of motion (14) of the form

$$U_m(t) = \tilde{U} e^{i\omega t - Km} \tag{22}$$

with complex values $K = K_{\text{Re}} + i K_{\text{Im}}$. Substituting Equation (22) into (14) leads to the relation

$$\bar{\omega}^2 = 2(1 - \cosh K) + 2\gamma(1 - \cosh 2K), \tag{23}$$

where $\bar{\omega} = \omega\sqrt{M/(K_n + K_s)}$ and $\gamma = K_n^d/(K_n + K_s)$.

Substituting $K = i K_{\text{Im}}$ into Equation (23), and letting $\Omega = \bar{\omega}^2$, $Z = 4\sin^2(K_{\text{Im}}/2)$ gives

$$\Omega = (1 + 4\gamma)Z - \gamma Z^2. \tag{24}$$

The analog (24) of the dispersion relation (23) is useful for the analysis of the dispersion curves of the discrete system because there is a remarkable correspondence between the curves $\bar{\omega} = \bar{\omega}(K_{\text{Im}}, K_{\text{Re}})$ in three-dimensional space $\omega \geq 0$, $0 \leq K_{\text{Im}} \leq \pi$, $K_{\text{Re}} \geq 0$ and the curve $\Omega = \Omega(Z)$ in the two-dimensional space $\Omega \geq 0$, $-\infty < Z < \infty$. Namely, the dispersion curves $\omega = \omega(K_{\text{Im}}, K_{\text{Re}})$ in the planes $K_{\text{Im}} = 0$, $K_{\text{Re}} = 0$, and $K_{\text{Im}} = \pi$ correspond to parts of the parabola $\Omega = \Omega(Z)$ in the intervals $Z < 0$, $0 < Z < 4$, and $Z > 4$, respectively. The branch $\omega = \omega(K_{\text{Im}}, K_{\text{Re}})$ defined in the area of complex values ($K_{\text{Im}} \neq 0$, $K_{\text{Re}} \neq 0$) is located at frequencies Ω, at which there are no points of the curve $\Omega = \Omega(Z)$.

The complex dispersion relation (23) determines three dispersion curves of qualitatively different solutions.

The curve in the plane $K_{\text{Re}} = 0$ is defined by the relation

$$\bar{\omega}^2 = 2(1 - \cos K_{\text{Im}}) + 2\gamma(1 - \cos 2K_{\text{Im}}). \tag{25}$$

It corresponds to points of the parabola inside the interval $0 < Z < 4$. This is the branch corresponding to harmonic solutions $\bar{\omega} = \bar{\omega}(K_{\text{Im}}, 0)$.

The curve in the plane $K_{\text{Im}} = \pi$

$$\bar{\omega}^2 = 2(1 + \cosh K_{\text{Re}}) + 2\gamma(1 - \cosh 2K_{\text{Re}}) \tag{26}$$

corresponds to points of parabola for the values $Z > 4$. This is the branch associated with rapidly varying spatially localized solutions, which correspond to evanescent waves.

The branch $\bar{\omega} = \bar{\omega}(K_{\text{Im}}, K_{\text{Re}})$ for the complex values $K_{\text{Re}} \neq 0$, $K_{\text{Im}} \neq 0$ is defined in the parametric form $K_{\text{Re}} = K_{\text{Re}}(\bar{\omega})$, $K_{\text{Im}} = K_{\text{Im}}(\bar{\omega})$ by the equations

$$\cos K_{\text{Im}} \cosh K_{\text{Re}} = -1/4\gamma, \quad \cos^2 K_{\text{Im}} + \cosh^2 K_{\text{Re}} = (\bar{\omega}^2 - 2)/4\gamma. \tag{27}$$

It is located in the area of frequencies Ω above the value $\bar{\Omega}_{\text{max}} = (2\sqrt{\gamma} + 1/2\sqrt{\gamma})^2$. This value corresponds to the maximum of the parabola, located at $Z_{\text{max}} = 2 + 1/2\gamma$, which belong to the interval $2 < Z_{\text{max}} < 4$ for $\gamma > 1/4$ or to the half-line $Z_{\text{max}} > 4$ for $\gamma < 1/4$. Hence, the curve (27) begins at the point of maximum of the curve defined by Equation (25) for $\gamma > 1/4$ or (26) for $\gamma < 1/4$.

Since the parabola is not defined for $Z < 0$, $\Omega > 0$, there are no dispersion curves of the discrete system in the plane $K_{\text{Im}} = 0$, and, accordingly, Equation (14) does not possess slowly varying spatially localized solutions of the form (22).

7.2. *Single-field models*. The analysis of the single- and two-field models is based on the following solution

$$U(\xi, t) = \bar{U} e^{i\omega t - K\xi/H}, \tag{28}$$

which is the analog of the discrete solution (22) in the continuum case.

The substitution of expression (28) into Equation (15) of the single-field model with derivatives up to the second order leads to the dispersion relation for harmonic solutions $\bar{\omega}^2 = (1 + 4\gamma) K_{\mathrm{Im}}^2$. The corresponding curve belongs to the plane $K_{\mathrm{Re}} = 0$ and defines the tangent line to the dispersion curve of the discrete system defined by Equation (25) at the point $\omega = 0$, $K_{\mathrm{Im}} = 0$. For short wavelength waves in the area $K_{\mathrm{Im}} \approx \pi$ the model shows considerable inaccuracy.

In the case $K_{\mathrm{Re}} = 0$, the single-field model with derivatives up to fourth order, Equation (15), gives the following dispersion relation $\bar{\omega}^2 = (1 + 4\gamma) K_{\mathrm{Im}}^2 - (1 + 16\gamma) K_{\mathrm{Im}}^4 / 12$, which corresponds to a Taylor series expansion up to the fourth order of the dispersion relation of the discrete system (25) around $K_{\mathrm{Im}} = 0$. From a physical point of view, this means that the higher-order gradient model describes the dispersive behavior. This model has better accuracy over a larger range of wavelengths with respect to the model with derivatives up to the second order, but still suffers from severe inaccuracies in the short wavelength limit.

The single-field model with derivatives up to the fourth order, Equation (15), characterized by dispersion curve in the complex plane ($K_{\mathrm{Im}} \neq 0$, $K_{\mathrm{Re}} \neq 0$) similar to the dispersion curve of the discrete system defined by Equation (27). However, inaccuracy in the description of this curve is large because it begins at the point of maximum of the curve, defined by Equation (25) or (26). This point belongs to the area of middle and short waves. As previously discussed, the single-field model for these waves is affected by considerable inaccuracy.

It should be noted that both single-field models do not provide dispersion curves in the plane $K_{\mathrm{Im}} = \pi$ which are similar to those of the discrete system defined by Equation (26). Hence, single-field models do not capture the spatially localized short wavelength solutions.

7.3. *Two-field models*. The two-field model, Equations (15) and (16), includes the equation of the single-field model, Equation (15). Therefore, like the single-field model, the two-field model is able to capture the properties of the discrete system in the range $0 \leq K_{\mathrm{Im}} < \pi/2$, where the single-field model has a good accuracy.

Equations (16) of the two-field model in the case when only derivatives up to the second order are taken into account leads to $\bar{\omega}^2 = 4 + (1 - 4\gamma) K^2$. This complex dispersion relation gives two branches

$$\bar{\omega}^2 = 4 - (1 - 4\gamma) K_{\mathrm{Im}}^2, \tag{29}$$

$$\bar{\omega}^2 = 4 + (1 - 4\gamma) K_{\mathrm{Re}}^2 \tag{30}$$

in the area $0 \leq K_{\mathrm{Im}} < \pi/2$, $K_{\mathrm{Re}} \geq 0$.

The relation (29) defines dispersion curve in the plane $K_{\mathrm{Re}} = 0$. It can be obtained by replacing $K_{\mathrm{Im}} \to \pi - K_{\mathrm{Im}}$ in Equation (25) and its Taylor series expansion around the point $K_{\mathrm{Im}} = 0$ up to second order terms. Hence, the dispersion curve defined by Equation (29), reflected about the line $K_{\mathrm{Im}} = \pi/2$, approximates the branch of harmonic wave solutions of the discrete system, Equation (25), in the area of short wavelength around the point $K_{\mathrm{Im}} = \pi$.

The relation (30) defines the dispersion curve in the plane $K_{\text{Im}} = 0$, which, after reflection about the plane $K_{\text{Im}} = \pi/2$, approximates the curve for short wavelength localized solutions of the discrete system, Equation (26), in the plane $K_{\text{Im}} = \pi$ around the point $K_{\text{Re}} = 0$.

By taking into consideration derivatives up to the fourth order in the additional Equation (16) for the two-field model, we can improve approximation for the branches of the harmonic, Equation (25), and spatially localized, Equation (26), short wavelength solutions of the discrete system at $(K_{\text{Im}}, K_{\text{Re}}) = (\pi, 0)$ up to the fourth-order terms. The corresponding approximate relations have the form

$$\bar{\omega}^2 = 4 - (1 - 4\gamma)(K_{\text{Im}} - \pi)^2 + (1 - 16\gamma)(K_{\text{Im}} - \pi)^4/12,$$
$$\bar{\omega}^2 = 4 + (1 - 4\gamma)K_{\text{Re}}^2 + (1 - 16\gamma)K_{\text{Re}}^4/12.$$

Thus, the two-field model has the properties of the single-field model in the area of long waves $(K_{\text{Im}} \approx 0)$ and additionally demonstrates a good accuracy for the short wavelength harmonic wave solutions $(K_{\text{Im}} \approx \pi, K_{\text{Re}} = 0)$ and for short wavelength solutions with weak spatial localization $(K_{\text{Im}} = \pi, K_{\text{Re}} \approx 0)$. Taking into account derivatives up to the fourth order in the equations of the two-field model improves the accuracy around $(K_{\text{Im}}, K_{\text{Re}}) = (0, 0)$ and $(K_{\text{Im}}, K_{\text{Re}}) = (\pi, 0)$. For $\gamma > 1/16$ the two-field model with derivatives up to the fourth order gives also the dispersion curve in the area of complex values, $K_{\text{Im}} \neq 0$, $K_{\text{Re}} \neq 0$, similar to the curve defined by Equation (27) for the discrete system.

Spatially localized short-wavelength, high frequency excitations, which exist and propagate in nonlinear discrete systems, are known as intrinsic localized modes, or discrete breathers [Sievers and Takeno 1988; Flach and Willis 1998]. The development of continuum models capable of providing good descriptions for both long and short wavelength phenomena gives an opportunity to study them separately and to investigate their potential interactions.

Figure 4 illustrates the results of the analysis. The dispersion curves in the planes of the harmonic $(K_{\text{Re}} = 0)$ and spatially localized short wavelength $(K_{\text{Im}} \approx \pi)$ solutions for the discrete system (solid
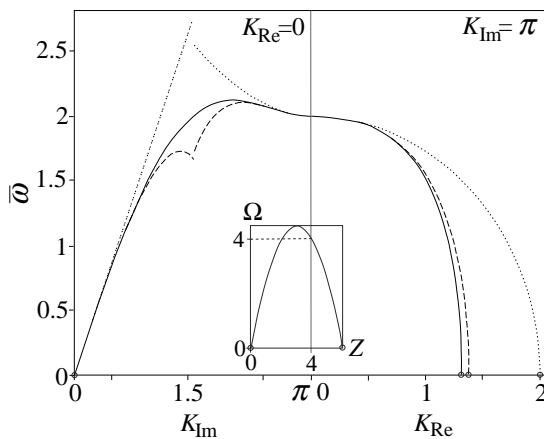

Figure 4. Dispersion curves of discrete system for harmonic, $K_{\text{Re}} = 0$, and localized short-wave solutions, $K_{\text{Im}} = \pi$, are shown by solid lines. The same curves obtained by using two-field models with derivatives up to second and fourth orders are presented by dotted and dashed lines, respectively.

lines), the two-field models $K_{\text{Re}} = 0$, $K_{\text{Im}} = \pi$ with derivatives up to the second (dotted lines) and fourth (dashed lines) orders are presented for $\gamma = 1/2$. In the area of long wavelength solutions ($K_{\text{Im}} < \pi/2$, $K_{\text{Re}} = 0$), the dispersion curves of the two-field model coincide with the dispersion curves of the single-field model and give a good approximation of the dispersion curves of the discrete system in the area of long waves ($K_{\text{Im}} \approx 0$). Moreover, the two-field model produces branches that approximate the dispersion curves of the discrete system corresponding to the short wavelength harmonic and spatially localized solutions around the point $(K_{\text{Im}}, K_{\text{Re}}) = (\pi, 0)$. The points of intersection of the dispersion curses with the axis $\bar{\omega} = 0$ for different models are depicted by small circles. These points correspond to static solutions, which are analyzed in the next section.

8. Static one-dimensional solutions

8.1. *Discrete model.* The parabola defined by Equation (24) intersects the axis $\Omega = 0$ at $Z_1 = 0$ and $Z_2 = 4 + 1/\gamma$. Since $Z_2 > 4$, the point where the dispersion curve intersects the plane $\bar{\omega} = 0$ belongs to the line $K_{\text{Im}} = \pi$ and, hence, the corresponding static solution has rapidly varying exponentially localized form.

The characteristic equation of the discrete Equation (14) in the static problem has roots

$$K_{\text{Im}} = 0, \qquad K_{\text{Re}} = 0 \tag{31}$$

and

$$K_{\text{Im}} = \pi, \qquad K_{\text{Re}} = \pm\lambda, \tag{32}$$

where $\lambda = \ln\left[(1 + 1/2\gamma) + \sqrt{(1 + 1/2\gamma)^2 - 1}\right]$ is the solution of the equation

$$1 + \cosh\lambda + \gamma(1 - \cosh 2\lambda) = 0. \tag{33}$$

The general static solution of Equation (14) has the form

$$U_m = C_0 + mC_1 + (-1)^m e^{\lambda m} C_2 + (-1)^m e^{-\lambda m} C_3. \tag{34}$$

This solution consists of linear and rapidly varying terms that are defined by the roots (31) and (32), respectively. The parameter λ defines the degree of localization of the solution, and the constants C_n are defined by the particular set of assigned boundary conditions.

8.2. *Single-field models.* The results of the comparative analysis between discrete and field models for dynamic solutions (Section 7) will be used here for comparison of the static solutions.

Single-field models with derivatives up to second and fourth orders both approximate the branch of the discrete system defined by Equation (25) for long waves, $K_{\text{Re}} = 0$, $K_{\text{Im}} \approx 0$, at low frequencies, $\bar{\omega} \approx 0$. Therefore, the characteristic polynomial for the static equations of the single-field models has trivial solution $K_{\text{Re}} = 0$, $K_{\text{Im}} = 0$, Equation (31), of the second order. Consequently, both single-field models give the linear slowly varying part of the solution (34).

Due to the fact that the Equation (15) in case when derivatives up to fourth order are taken into account gives a polynomial of the fourth order for static solutions, additional roots are found in the plane $\bar{\omega} = 0$. Because of that, one may expect that the single field model in this case gives the rapidly varying exponentially localized part of the static solution of the discrete system. However, as it was established

during the previous analysis on the dynamic solutions, Section 7.2, the single-field models do not predict the branch of spatially localized solutions (26) with root (32). The additional roots of the model belong to the branch of the harmonic solutions in the plane $K_{\text{Re}} = 0$.

Thus, single-field models allow us to find only the linear slowly varying part of the static solution, but they do not predict the rapidly varying spatially localized solutions.

8.3. *Two-field model.* The continuum approximation for the static solution for the discrete system (34) can be found through Equations (15) and (16) obtained for the two-field model with derivatives up to the second order. Equation (15) gives the following linear static solution $U(\xi) = c_0 + c_1 \xi / H$. By using Equation (16) it is possible to find the localized part of the solution $\tilde{U}(\xi) = e^{\Lambda \xi / H} c_2 + e^{-\Lambda \xi / H} c_3$, where Λ is found from Equation (30) in the case $\bar{\omega} = 0$, that is,

$$4 + (1 - 4\gamma)\Lambda^2 = 0. \tag{35}$$

This equation gives the point K_{Re} of the intersection of the plane $\bar{\omega} = 0$ by the dispersion curve of the two-field model defined by Equation (30) in the plane $K_{\text{Im}} = \pi$.

From Equation (21), $U^{[n]}(\xi) = U(\xi) + (-1)^n \tilde{U}(\xi)$, we obtain a static solution

$$U^{[n]}(\xi) = c_0 + c_1 \xi / H + (-1)^n e^{\Lambda \xi / H} c_2 + (-1)^n e^{-\Lambda \xi / H} c_3, \tag{36}$$

where $n = 1, 2$.

Thus, the continuum solution (36), obtained by using the two-field model is qualitatively similar to the discrete solution (34). It contains the linear part as well as the localized one with rapidly varying envelope. In regards to the quantitative comparison, let us note that the parameters λ in the discrete and Λ in the continuum solutions are equal to the values K_{Re} of intersections of the plane $\omega = 0$ with the dispersion curves defined by Equations (26) and (30), respectively. As established in Section 7.3, the curve defined by Equation (30) of the two-field model approximates the curve defined by Equation (26) of the discrete model at the point $(K_{\text{Im}}, K_{\text{Re}}) = (\pi, 0)$. Furthermore, Equation (35) for the parameter Λ can be obtained from Equation (33) for λ by using its Taylor series expansion up to the second-order terms $2(1 + \cosh \lambda) + 2\gamma(1 - \cosh 2\lambda) = 4 + (1 - 4\gamma)\lambda^2 + O(\lambda^4)$.

Thus, we have demonstrated that the short wavelength spatially localized static deformations, which could not be obtained through the single-field approach (see Section 8.2), can be found by using the two-field model.

The accuracy of the two-field model for the derivation of static solutions is good in the case of weak localization. The solution (36) for the model in the case when only derivatives up to the second order are taken into account exists for $1/\gamma < 4$. While for $1/\gamma > 4$ the solution of the discrete system is highly localized. This explains the lack of accuracy of the two-field model, when the parameter $1/\gamma$ approaches its threshold value $1/\gamma \to 4$, and the reason why the solutions cannot be found when $1/\gamma > 4$.

Figure 5 shows the dependence of the localization parameters λ and Λ on the parameter $1/\gamma = (K_n + K_s)/K_n^d$ of the discrete system, calculated from the discrete model (solid line) and from the two-field models with derivatives up to second (dotted line) and fourth (dashed line) orders. The inclusion of fourth-order derivatives increases both the accuracy of the derivation of the localization parameter λ, and the region of parameters γ where spatially localized static solution can be found. Let us note that there exist systems with small parameter λ. In such systems short wavelength solutions are weakly localized.
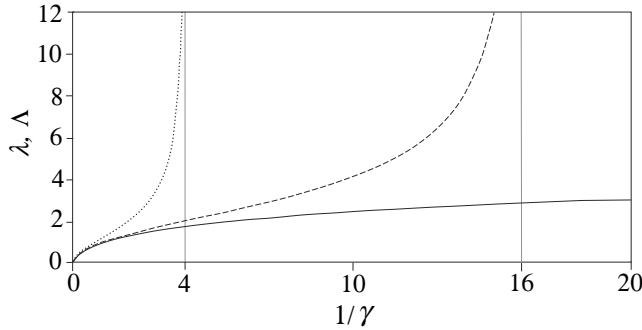
Figure 5. The dependencies of the localization parameters, λ and Λ, on the parameter $1/\lambda = (K_n + K_s)/K_n^d$ of the discrete system calculated by using the discrete model (solid line) and two-field models with derivatives up to second (dotted line) and fourth (dashed line) orders.

The two-field model with derivatives up to the second order produces rather exact results and there is no need to use higher-order gradient two-field model in this case.

The static solution for tension (compression) of a layer between two rigid parts (Figure 3) with boundary conditions

$$U_{-N+1} = -U_*, \qquad U_{-N+2} = -U_*, \qquad U_{N-1} = U_*, \qquad U_N = U_* \qquad (37)$$

is presented in Figure 6a. We choose the dimensionless parameter $\gamma = 1$. The number of layers is equal to ten, that is, $N = 5$. The displacements are given in dimensionless form $\bar{U}_m = U_m/U_*$. The displacements
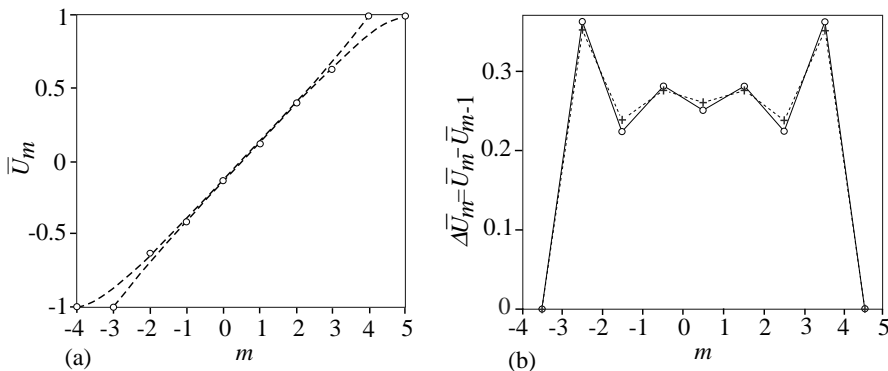
Figure 6. (a) Displacements of layers of the lattice are shown by circles. Their approximations by using two slowly varying functions in the two-field model are presented by dashed lines. (b) The differences of the displacements of neighboring elements calculated by using the discrete and two-field models are presented by circles and crosses, respectively. Continuous and dashed lines are drawn to underline short wavelength behavior of the solutions near the boundaries.

of the discrete system are found by using the static solution (34) of the discrete Equation (14) with bound-
ary conditions (37). They are shown by small circles in Figure 6a. The displacements obtained through
the two-field solution (36) are represented as dashed lines. In order to underline the short-wavelength
behavior of the solutions near the boundaries, the difference of displacements $\Delta \bar{U}_m = \bar{U}_{m+1} - \bar{U}_m$ is shown
in Figure 6b. The values calculated by using discrete and two-field models are represented as circles and
crosses, respectively. Figure 6a demonstrates that both slowly varying displacements in the center and
rapidly varying displacements near the boundaries in the discrete system are effectively described by
two smooth field functions. The approximated models were derived through the Taylor series expansion
(3) of the displacements $U(x \pm mH, t)$ keeping derivatives of the lowest order under assumption that
$U(x, t)$ varies slowly with respect to spatial variable. This may help qualitatively understand why two-
field models provide good approximations for both slowly and rapidly varying displacements. When we
try to describe the short wavelengths deformations by using a single function it should rapidly vary in
the corresponding areas. The single-field models with lower gradient terms do not capture the rapidly
varying static localized solutions and may lead to significant errors in the prediction of displacements in
areas where such solutions may take place (near boundaries, defects, localized forces, and so on). The
two-field model makes it possible to describe these effects within the framework of the field theory.

We have considered the application of the two-field model, Equations (4) and (5), for the solution of
one-dimensional problem (Figure 3) in order to demonstrate its advantages in comparison with single-
field models. Another interesting problem is the determination of the shear deformations of the layer in
the case of transverse displacements of the rigid parts in different directions. In this case there exists a
range of parameters of the discrete system for which smooth exponential localization of deformations
takes place. The deformations in this case can be studied by using the single-field theory. For other
parameters, the localized deformations have short wavelength form and the equations of the single-field
theory are not sufficient to capture them. The two-field model, Equations (4) and (5), enables us to study
deformations in both cases. The analysis of this problem deserves a dedicated study, which is currently
being carried out by the authors, and which will be the subject of a future paper.

9. Conclusions

The classical model for Cosserat media has wide applications in problems where not only displacements,
but also rotations of structural elements should be taken into account. Rotational degrees of freedom
naturally appear, for example, for bodies with elements having finite sizes and bodies with beam-like
microstructure. Some examples are granular media [Limat 1988; Mühlhaus and Oka 1996; Pasternak
and Mühlhaus 2000], beam lattices [Noor 1988], masonry walls [Casolo 2004], auxetics [Lakes 1991;
Vasiliev et al. 2002; Grima et al. 2007], bodies with chiral structure [Spadoni and Ruzzene 2007], liquid
crystals, dielectric crystals [Pouget et al. 1986; Askar 1986; Maugin 1999], thin films [Randow et al.
2006], among others.

The discrete model of square lattice of elements with rotational degrees of freedom is used to obtain
generalized continuum models which describe essential structural effects in Cosserat media with mi-
crostructure. We utilize ideas and methods of the well-developed micropolar and higher-order gradient
theories and of the multifield theory, which is still being investigated and expanded, and consider the
possibilities and advantages of their applications separately and in combination. The derivation of the

continuum models starting from structural model gives us the possibility to test their accuracy, and to study and compare their properties. We have shown that their application allows describing qualitatively different effects in bodies with microstructure. By increasing the number of fields, the multifield approach gives a natural way to describe both long- and short wavelength deformations. The latter ones are often considered as inaccessible for continuum models. However, it should be noted that such deformations in some cases may become very important, in particular in fracture, instability, and plasticity problems. Their description gives a possibility to study similar phenomena in the framework of generalized continuum mechanics.

References

[Aifantis 2003] E. C. Aifantis, "Update on a class of gradient theories", *Mech. Mater.* **35** (2003), 259–280.

[Askar 1986] A. Askar, *Lattice dynamical foundations of continuum theories*, World Scientific, Singapore, 1986.

[Askes et al. 2002] H. Askes, A. S. J. Suiker, and L. J. Sluys, "A classification of higher-order strain-gradient models – linear analysis", *Arch. Appl. Mech.* **72** (2002), 171–188.

[Bažant and Jirásek 2002] Z. P. Bažant and M. Jirásek, "Nonlocal integral formulation of plasticity and damage: survey of progress", *J. Eng. Mech.* **128**:11 (2002), 1119–1149.

[Born and Huang 1954] M. Born and K. Huang, *Dynamical theory of crystal lattices*, Clarendon Press, Oxford, 1954.

[Casolo 2004] S. Casolo, "Modelling in-plane micro-structure of masonry walls by rigid elements", *Int. J. Solids Struct.* **41** (2004), 3626–3641.

[Cosserat and Cosserat 1909] E. Cosserat and F. Cosserat, *Théorie des Corps Déformables*, Hermann A. et Fils, Paris, 1909.

[Eringen 1999] A. C. Eringen, *Microcontinuum Field Theories: Foundations and Solids*, Springer-Verlag, New York, 1999.

[Flach and Willis 1998] S. Flach and C. R. Willis, "Discrete breathers", *Phys. Rep.* **295** (1998), 181–264.

[Fleck and Hutchinson 1997] N. A. Fleck and J. W. Hutchinson, "Strain gradient plasticity", *Adv. Appl. Mech.* **33** (1997), 295–361.

[Fleck and Hutchinson 2001] N. A. Fleck and J. W. Hutchinson, "A reformulation of strain gradient plasticity", *J. Mech. Phys. Solids* **49** (2001), 2245–2271.

[Grima et al. 2007] J. N. Grima, V. Zammit, R. Gatt, A. Alderson, and K. E. Evans, "Auxetic behaviour from rotating semi-rigid units", *Phys. Status Solidi (b)* **244**:3 (2007), 866–882.

[Lakes 1991] R. Lakes, "Deformation mechanisms in negative Poisson's ratio materials: structural aspects", *J. Mater. Sci.* **26** (1991), 2287–2292.

[Limat 1988] L. Limat, "Percolation and Cosserat elasticity: Exact results on deterministic fractal", *Phys. Rev. B* **37** (1988), 672–675.

[Lomakin 1970] V. A. Lomakin, *Statistical problems of the mechanics of deformable solids*, Nauka, Moscow, 1970. (in Russian).

[Maugin 1999] G. A. Maugin, *Nonlinear waves in elastic crystals*, Oxford Mathematical Monographs, OUP, 1999.

[Mühlhaus and Oka 1996] H.-B. Mühlhaus and F. Oka, "Dispersion and wave propagation in discrete and continuous models for granular materials", *Int. J. Solids Struct.* **33** (1996), 2841–2858.

[Noor 1988] A. K. Noor, "Continuum modelling for repetitive lattice structures", *Appl. Mech. Rev.* **41**:7 (1988), 285–296.

[Pasternak and Mühlhaus 2000] E. Pasternak and H.-B. Mühlhaus, "Cosserat and non-local continuum models for problems of wave propagation in fractured materials", pp. 741–746 in *Structural failure and plasticity - IMPLAST2000*, edited by X. L. Zhao and R. H. Grzebieta, Pergamon, Amsterdam, 2000.

[Pavlov et al. 2006] I. S. Pavlov, A. I. Potapov, and G. A. Maugin, "A 2D granular medium with rotating particles", *Int. J. Solids Struct.* **43** (2006), 6194–6207.

[Peerlings et al. 2001] R. H. J. Peerlings, M. G. D. Geers, R. de Borst, and W. A. M. Brekelmans, "A critical comparison of nonlocal and gradient enhanced softening continua", *Int. J. Solids Struct.* **38** (2001), 7723–7746.

[Pouget et al. 1986] J. Pouget, A. Askar, and G. A. Maugin, "Lattice model for elastic ferroelectric crystals: continuum approximation", *Phys. Rev. B* **33** (1986), 6320–6325.

[Randow et al. 2006] C. L. Randow, G. L. Gray, and F. Costanzo, "A direct continuum model of micro- and nano-scale thin films", *Int. J. Solids Struct.* **43** (2006), 1253–1275.

[Rogula 1985] D. Rogula, "Non-classical material continua", pp. 339–353 in *Theoretical and applied mechanics, IUTAM*, edited by F. I. Niordson and N. Olhoff, Elsevier Science Publishers B.V., North Holland, 1985.

[Sievers and Takeno 1988] A. J. Sievers and S. Takeno, "Intrinsic localized modes in anharmonic crystals", *Phys. Rev. Lett.* **61** (1988), 970–973.

[Spadoni and Ruzzene 2007] A. Spadoni and M. Ruzzene, "Numerical and experimental analysis of static compliance of chiral truss-core airfoils", *J. Mech. Mater. Struct.* **2**:5 (2007), 965–981.

[Suiker and de Borst 2005] A. S. J. Suiker and R. de Borst, "Enhanced continua and discrete lattices for modelling granular assemblies", *Philos. Trans. Royal Soc. A* **363** (2005), 2543–2580.

[Suiker et al. 2001] A. S. J. Suiker, A. V. Metrikine, and R. de Borst, "Comparison of wave propagation characteristics of the Cosserat continuum model and corresponding discrete lattice models", *Int. J. Solids Struct.* **38** (2001), 1563–1583.

[Triantafyllidis and Bardenhagen 1993] N. Triantafyllidis and S. Bardenhagen, "On higher order gradient continuum theories in 1-D nonlinear elasticity. Derivation from and comparison to the corresponding discrete models", *J. Elasticity* **33**:3 (1993), 259–293.

[Vasiliev and Miroshnichenko 2005] A. A. Vasiliev and A. E. Miroshnichenko, "Multi-field modelling of Cosserat solids", *J. Mech. Behav. Mater.* **16**:6 (2005), 379–392.

[Vasiliev et al. 2002] A. A. Vasiliev, S. V. Dmitriev, Y. Ishibashi, and T. Shigenari, "Elastic properties of a two-dimensional model of crystals containing particles with rotational degrees of freedom", *Phys. Rev. B* **65** (2002), 094101.

[Vasiliev et al. 2005] A. A. Vasiliev, S. V. Dmitriev, and A. E. Miroshnichenko, "Multi-field continuum theory for medium with microscopic rotations", *Int. J. Solids Struct.* **42**:24-25 (2005), 6245–6260.

ALEKSEY A. VASILIEV: aleksey.vasiliev@tversu.ru
Department of Mathematical Modelling, Tver State University, Sadoviy per. 35, 170002 Tver, Russia
http://homepages.tversu.ru/~p000149/

ANDREY E. MIROSHNICHENKO: aem124@rsphysse.anu.edu.au
Nonlinear Physics Centre, Research School of Physical Sciences and Engineering, The Australian National University, Canberra ACT 0200, Australia
http://www.rsphysse.anu.edu.au/nonlinear

MASSIMO RUZZENE: Massimo.ruzzene@ae.gatech.edu
School of Aerospace Engineering, Georgia Institute of Technology, 270 Ferst Drive, Atlanta GA 30332, United States
http://www.ae.gatech.edu/people/mruzzene/

ANALYSIS OF THE RUN-IN EFFECT IN FIBER-REINFORCED ISOLATORS UNDER VERTICAL LOAD

JAMES M. KELLY

Previous work on experimental and theoretical studies on fiber-reinforced bearings has shown the feasibility of using them as lightweight low-cost elastomeric isolators for application to housing, schools and other public buildings in highly seismic areas of the developing world. The theoretical analysis covered the mechanical characteristics of these bearings where the reinforcing elements, normally steel plates, are replaced by fiber reinforcement. The fiber in the fiber-reinforced isolator, in contrast to the steel in the conventional isolator (which is assumed to be rigid both in extension and flexure), is assumed to be flexible in extension, but completely without flexural rigidity. This leads to an extension of the theoretical analysis on which the design of steel-reinforced isolators is based that accommodates the stretching of the fiber-reinforcement. Several examples of isolators in the form of long strips were tested at the Earthquake Engineering Research Center Laboratory.

The theoretical analysis suggests, and the test results confirmed, that it is possible to produce a fiber-reinforced strip isolator that matches the behavior of a steel-reinforced isolator. The fiber-reinforced isolator is significantly lighter and can be made by a much less labor-intensive manufacturing process. The advantage of the strip isolator is that it can be easily used in buildings with masonry walls.

The main difference between the behavior of a fiber-reinforced and a steel-reinforced bearing is the degree of run-in under vertical loading. In this context we mean by run-in that a certain amount of vertical load must be applied to the bearing before its vertical stiffness can be developed.

The most likely source of the run-in is that the fibers are initially not straight and as they have no bending stiffness, the vertical stiffness cannot be developed until they have been straightened by the action of the applied vertical load. Straightening the fibers requires them to push against the surrounding rubber. This causes an increasing force in the fiber, and as it is straightening, there will be a transition to the stretching of the fiber and to the consequent stiffness of the composite system. These bearings can be used in a wide range of applications in addition to seismic protection of buildings including bridge bearings and vibration isolation bearings, so there is a need to be able to predict how much vertical load or vertical displacement is needed before the full vertical stiffness can be achieved. In this paper a theoretical analysis of the effect has been developed in an attempt to formulate a prediction for the transition from the initially bent to the finally straight fiber.

The method takes the already formulated analysis for the straight fiber and modifies it by treating the fiber as a curved string on an elastic foundation, adds to this an estimate of the subgrade reaction of this foundation, and, using the basic equations of the fiber-rubber composite, calculates the effective compression modulus as a function of the vertical compression strain or pressure.

1. Introduction

The motivation for proposing the use of fiber-reinforced seismic isolators is the fact that the major loss of life in earthquakes happens when the event occurs in developing countries. Even in relatively moderate

earthquakes in areas with poor housing many people are killed by the collapse of brittle heavy unreinforced masonry or poorly constructed concrete buildings. Modern structural control technologies such as active control or energy dissipation devices can do little to alleviate this but it is possible that seismic isolation could be adopted to improve the seismic resistance of poor housing and other buildings such as schools and hospitals in developing countries. The possibility of using fiber-reinforced elastomeric isolators was reviewed by the author, Kelly [2002].

The problem with using isolation in developing countries is that conventional isolators are large, expensive and heavy. An individual isolator can weigh one ton or more and cost many thousands of dollars. To extend this earthquake-resistant strategy to housing and commercial buildings, the cost and weight of the isolators must be reduced.

The primary weight in an isolator is that of the steel reinforcing plates used to provide the vertical stiffness of the rubber-steel composite element. A typical rubber isolator has two large end-plates around 25 mm (1 inch) thick and 20 thin reinforcing plates around 3 mm (1/8 inch) thick. The high cost of producing the isolators reflects the labor involved in preparing the steel plates and laying-up of the rubber sheets and steel plates for vulcanization bonding in a mold. The steel plates are cut, sand blasted, acid cleaned and then coated with bonding compound. Next, the compounded rubber sheets with the interleaved steel plates are put into a mold and heated under pressure for several hours to complete the manufacturing process. Both the weight and the cost of isolators could be reduced if the steel reinforcing plates were eliminated and replaced by fiber reinforcement. As fiber materials are available with an elastic stiffness that is of the same order as that of steel, the reinforcement needed to provide the vertical stiffness may be obtained by using a similar volume of very much lighter material. There is also the fact that more steel is used than is needed to ensure the required vertical stiffness of the isolator because it is difficult to sand blast very thin plates. With carbon fiber, bonding can be done without this cleaning so that only the required minimum of reinforcement is needed. The cost savings may be possible if the use of fiber allows a simpler, less labor-intensive manufacturing process such as building the isolators in long rectangular strips, with individual isolators cut to the required size. All steel-reinforced isolators are currently manufactured as either circular or square. Rectangular isolators in the form of long strips would have distinct advantages over square or circular isolators when applied to buildings where the lateral-resisting system is walls. When isolation is applied to buildings with structural walls, additional wall beams are needed to carry the wall from isolator to isolator. A strip isolator would have a distinct advantage for retrofitting masonry structures and for isolating residential housing constructed from concrete or masonry blocks.

The vertical stiffness of a steel-reinforced bearing is approximated by assuming that each individual pad in the bearing deforms in such a way that horizontal planes remain horizontal and points on a vertical line lie on a parabola after loading. The plates are assumed to constrain the displacement at the top and bottom of the pad. Linear elastic behavior with incompressibility is assumed, with the additional assumption that the normal stress components are approximated by the pressure. This leads to the well-known pressure solution which is generally accepted as an adequate approximate approach for calculating the vertical stiffness. The extensional flexibility of the fiber reinforcement can be incorporated into this approach, and the resulting vertical stiffness calculated.

A number of carbon fiber-reinforced rubber strip isolators were tested on a small isolator test machine. The tests show that the concept is viable. The vertical and horizontal stiffnesses of the strip isolator are

less than those for the equivalent steel-reinforced isolator but still adequate and they proved to be easy to cut with a standard saw, in contrast to steel-reinforced isolators which are difficult to cut and need special saws. They are light and can be put in place without the use of lifting equipment.

While no fiber-reinforced isolators have been used to date in any building project the idea appears to have gained some attention in other countries. For example in Korea a group of researchers associated with Pusan University has studied the manufacturing of the bearings and their use for a shock absorbing system [Moon et al. 2003]. In Italy a group of researchers has tested rectangular carbon fiber-reinforced bearings as isolators for liquid storage tanks at refineries and petrochemical facilities [Summers et al. 2004]. Recent experimental work at McMaster University in Canada has confirmed that these bearings are a viable option for the base isolation of ordinary low-rise buildings [Toopchi-Nezhad et al. 2007]. All of this testing work indicates that these isolators are practical and it should lead to their widespread use.

2. Vertical stiffness of fiber-reinforced bearings

The essential characteristic of the elastomeric isolator is the very large ratio of the vertical stiffness to the horizontal stiffness. This is produced by the reinforcing plates, which in current industry standard are thin steel plates. These plates prevent lateral bulging of the rubber, but allow the rubber to shear freely. The vertical stiffness can be several hundred times the horizontal stiffness. The steel reinforcement has a similar effect on the resistance of the isolator to bending moments, referred to as the bending stiffness. This important design quantity makes the isolator stable against large vertical loads.

2.1. *Compression of pad with rigid reinforcement.* A linear elastic theory is the most common method used to predict the compression and the bending stiffness of a thin elastomeric pad. The first analysis of the compression stiffness was done using an energy approach by Rocard [1937]; further developments were made by Gent and Lindley [1959] and Gent and Meinecke [1970]. A very detailed description of the theory is given by Kelly [1996] and need not be repeated here. The analysis is an approximate one based on the kinematic assumptions that:

  (i) points on a vertical line before deformation lie on a parabola after loading;

 (ii) horizontal planes remain horizontal.

We consider an arbitrarily-shaped pad of thickness t and locate a rectangular Cartesian coordinate system, (x, y, z), in the middle surface of the pad, as shown in Figure 1(a). Figure 1(b) shows the
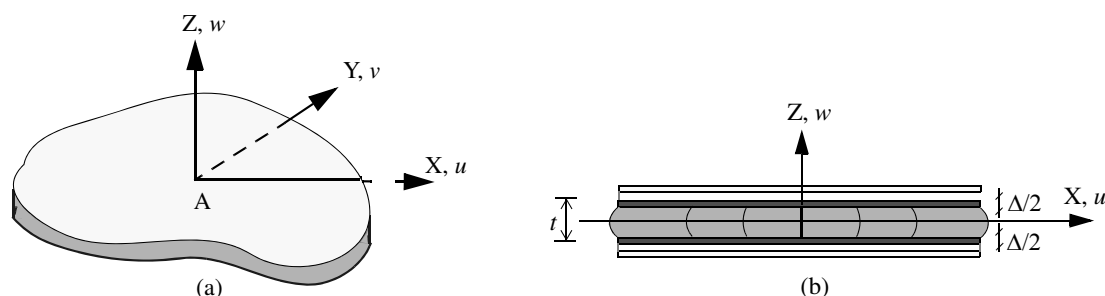

Figure 1. Constrained rubber pad and coordinate system.

displacements, (u, v, w), in the coordinate directions under assumptions (i) and (ii):

$$u(x, y, z) = u_0(x, y)(1 - 4z^2/t^2),$$
$$v(x, y, z) = v_0(x, y)(1 - 4z^2/t^2), \tag{1}$$
$$w(x, y, z) = w(z).$$

This displacement field satisfies the constraint that the top and bottom surfaces of the pad are bonded to rigid substrates. The assumption of incompressibility produces a further constraint on the three components of strain, ϵ_{xx}, ϵ_{yy}, ϵ_{zz}, in the form

$$\epsilon_{xx} + \epsilon_{yy} + \epsilon_{zz} = 0, \tag{2}$$

and this leads to

$$(u_{0,x} + v_{0,y})(1 - 4z^2/t^2) + w_{,z} = 0,$$

where the commas imply partial differentiation with respect to the indicated coordinate. When integrated through the thickness, this gives

$$u_{0,x} + v_{0,y} = \frac{3\Delta}{2t} = \frac{3}{2}\epsilon_c, \tag{3}$$

where the change of thickness of the pad is Δ ($\Delta > 0$ in compression), and $\epsilon_c = \Delta/t$ is the compression strain.

The other assumptions of the theory are that the material is incompressible and that the stress state is dominated by the pressure, p, in the sense that the normal stress components can be taken as $-p$. The vertical shear stress components are included but the in-plane shear stress is assumed to be negligible.

These assumptions and the equations of stress equilibrium lead to the pressure solution

$$p_{,xx} + p_{,yy} = \nabla^2 p = -\frac{12G\Delta}{t^3} = -\frac{12G}{t^2}\epsilon_c. \tag{4}$$

The boundary condition, $p = 0$, on the perimeter of the pad completes the system for the pressure distribution, $p(x, y)$, across the pad. The effective compression modulus E_c of the pad is obtained by computing $p(x, y)$ in terms of the compression strain ϵ_c, and integrating it over the area of the pad to determine the resultant load P. The effective compression modulus is then given by

$$E_c = \frac{P}{A\epsilon_c}. \tag{5}$$

The value of E_c for a single rubber layer is controlled by the shape factor S defined as

$$S = \frac{\text{loaded area}}{\text{free area}},$$

which is a dimensionless measure of the aspect ratio of the single layer of the elastomer. For example, in an infinite strip of width $2b$, and with a single layer thickness of t, $S = b/t$, and for a circular pad of diameter Φ and thickness t, $S = \Phi/(4t)$, and for a square pad of side a and thickness t, $S = a/(4t)$.

In this paper we are only interested in the theory for a long strip when the effects of the ends can be neglected and the strip is taken to be infinite. For an infinite strip of width $2b$ (see Figure 2), Equation
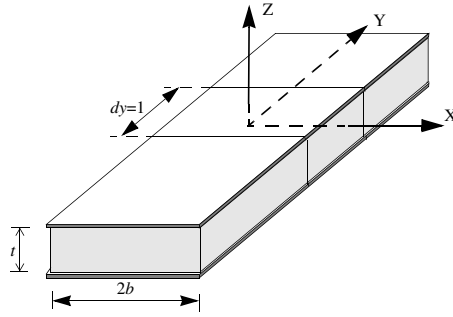
Figure 2. Infinitely long rectangular pad showing dimensions.

(4) reduces to

$$\nabla^2 p = \frac{d^2 p}{dx^2} = -\frac{12G}{t^2}\epsilon_c,$$

which, with $p = 0$ at $x = \pm b$, gives

$$p = \frac{6G}{t^2}(b^2 - x^2)\epsilon_c.$$

In this case the load per unit length of the strip, P, is given by

$$P = \int_{-b}^{b} p\,dx = \frac{8Gb^3}{t^2}\epsilon_c. \tag{6}$$

Since the shape factor S is given by $S = b/t$, and the area per unit length is $A = 2b$,

$$E_c = \frac{P}{A\epsilon_c} = 4GS^2. \tag{7}$$

2.2. Compression stiffness with flexible reinforcement. Before looking at the analysis for the bearing reinforced by fibers that are initially not straight it is necessary to review that for the initially straight fiber.

In developing the solution for the compression of a pad with flexible reinforcement, the rubber, as before, is assumed incompressible and the pressure is assumed to be the dominant stress component. The kinematic assumption of quadratically variable displacement is supplemented by an additional displacement that is constant through the thickness and is intended to accommodate the stretching of the reinforcement. Thus in this case the displacement pattern given in Equation (1) is replaced by

$$u(x, z) = u_0(x)(1 - 4z^2/t^2) + u_1(x),$$
$$w(x, z) = w(z), \tag{8}$$

The constraint of incompressibility of Equation (2) remains, and, modified for the additional stretch of the reinforcement, becomes

$$u_{0,x} + \frac{3}{2}u_{1,x} = \frac{3\Delta}{2t}. \tag{9}$$

The only equation of stress equilibrium in this case is $\sigma_{xx,x} + \tau_{xz,z} = 0$, and the assumption of elastic behavior means that
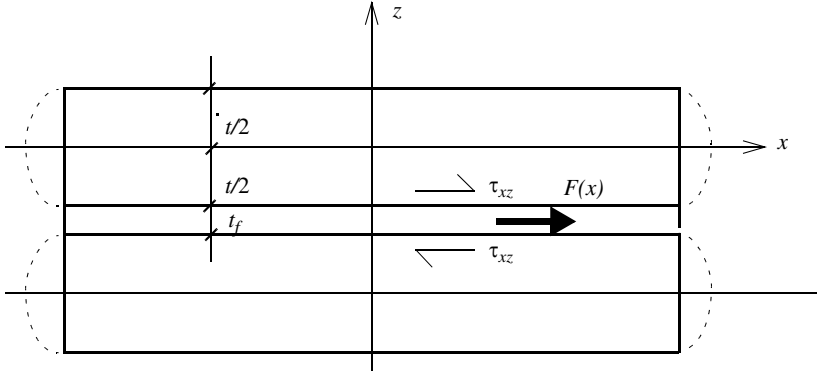
$$\tau_{xz} = G\gamma_{xz}, \tag{10}$$

Figure 3. Force in equivalent sheet of reinforcement.

and calculating γ_{xz} from Equation (8) gives

$$\gamma_{xz} = -\frac{8z}{t^2}u_0. \tag{11}$$

The assumption that $\sigma_{xx} = \sigma_{zz} = -p$, when applied to the sole equation of equilibrium, provides

$$p_{,x} = -\frac{8Gu_0}{t^2}. \tag{12}$$

The individual fibers are replaced by an equivalent sheet of reinforcement of thickness t_f. The internal force, $F(x)$, per unit width of the equivalent reinforcing sheet is related to the shear stresses on the top and bottom of the pad by

$$\frac{dF}{dx} - \tau_{xz}\big|_{z=t/2} + \tau_{xz}\big|_{z=-t/2} = 0,$$

as shown in Figure 3. The shear stresses on the top and bottom of the pad are given by

$$\tau_{xz}\big|_{z=t/2} = -\frac{4Gu_0}{t}, \qquad \tau_{xz}\big|_{z=-t/2} = \frac{4Gu_0}{t},$$

leading to

$$\frac{dF}{dx} = -\frac{8Gu_0}{t}. \tag{13}$$

When the fiber is assumed to be initially straight the extensional strain ϵ_f in the reinforcement is related to the stretching force through the elastic modulus of the reinforcement E_f and the thickness t_f such that

$$\epsilon_f = u_{1,x} = \frac{F}{E_f t_f}, \tag{14}$$

which, when combined with Equation (13), gives

$$u_{1,xx} = -\frac{8G}{E_f t_f t}u_0. \tag{15}$$

The complete system to be solved consists of Equations (9), (12) and (15) above.

The boundary conditions used are the vanishing of the pressure p and the reinforcement force F at the edges of the strip, $x = \pm b$ leading to $p(\pm b) = 0$, $u_{1,x}(\pm b) = 0$; and the assumption of a symmetric

displacement pattern gives $u_1(0) = 0$, $u_0(0) = 0$. The results for p and F from [Kelly 1999] are

$$p = \frac{E_f t_f}{t}\left(1 - \frac{\cosh \alpha x/b}{\cosh \alpha}\right)\epsilon_c, \qquad F(x) = E_f t_f\left(1 - \frac{\cosh \alpha x/b}{\cosh \alpha}\right)\epsilon_c, \tag{16}$$

where

$$\alpha^2 = \frac{12Gb^2}{E_f t_f t}. \tag{17}$$

The load per unit length of the strip, P, is given by

$$P = \frac{E_f t_f}{t}2\int_0^b \left(1 - \frac{\cosh \alpha x/b}{\cosh \alpha}\right)dx\,\epsilon_c = \frac{2E_f t_f}{\alpha t}b(\alpha - \tanh \alpha)\epsilon_c. \tag{18}$$

This result can be interpreted as an effective compression modulus, E_c, given by

$$E_c = \frac{E_f t_f}{t}\left(1 - \frac{\tanh \alpha}{\alpha}\right). \tag{19}$$

We note that when $\alpha \to 0$, i.e., $E_f \to \infty$, we have $E_c = 4GS^2$ as before. The formula also shows that $E_c < 4GS^2$ for all finite values of E_f.

The effect of the elasticity of the reinforcement on E_c can be illustrated by normalizing the compression modulus E_c, by dividing by $4GS^2$, giving from Equation (19)

$$\frac{E_c}{4GS^2} = \frac{3}{\alpha^2}\left(1 - \frac{\tanh \alpha}{\alpha}\right), \tag{20}$$

which is shown in Figure 4 for $0 \le \alpha \le 5$. Note how the stiffness decreases with decreasing E_f.

It is worthwhile to note that α also depends on the shape factor S, through

$$\alpha^2 = 12\frac{G}{E_f}S^2\frac{t}{t_f}.$$

In the case of carbon fiber reinforcement the ratio G/E_f will be extremely small although S^2 and t/t_f are certain to be large.
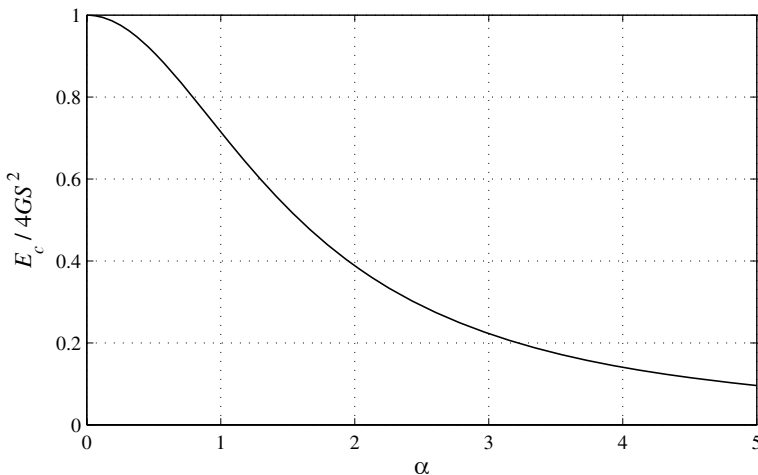

Figure 4. Normalized effective compression modulus as a function of $\alpha = (12Gb^2/E_f t_f t)^{1/2}$.

Figure 5. Fiber-reinforced bearing under vertical load.

2.3. *Analysis for initially imperfect fiber reinforcement.* There is one essential difference between the behavior of a fiber-reinforced bearing and a steel-reinforced bearing, and that is the degree of run-in before the full vertical stiffness is developed. In a steel-reinforced bearing the run-in is relatively small as shown in the examples in Figures 5, 6 and 7. In Figure 5 we see a fiber-reinforced bearing in the test machine under vertical load in this case generating a pressure of 6.9 MPa. The resultant force deflection curve is shown in Figure 6. The corresponding curve for a steel-reinforced bearing is shown in Figure 7. There is of course some run-in in this case but it is much less than that for the fiber bearing. It should be noted for comparison purposes that the steel bearing has much larger thickness of rubber. The steel plates are more or less rigid so their in-plane flexibility plays no role in the stiffness. The reason there is any run-in is probably that in the manufacturing process the plates are initially not quite parallel with the end plates and a slight amount of adjustment takes place as the vertical load is applied. In a fiber-reinforced bearing it is always much larger and one could speculate that the reason for this is that linear behavior is only developed when significant tension is produced in the fiber. This cannot be the explanation since if the fiber is straight it is its elastic extensibility that affects the vertical stiffness not the force in the fiber.

The most likely source of the run-in is that the fibers are initially not straight and as they have no bending stiffness, the vertical stiffness cannot be developed until they have been straightened by the action of the applied vertical load. Straightening the fibers requires the fiber to push against the surrounding rubber. This causes an increasing force in the fiber but as the fiber is straightening there will be a
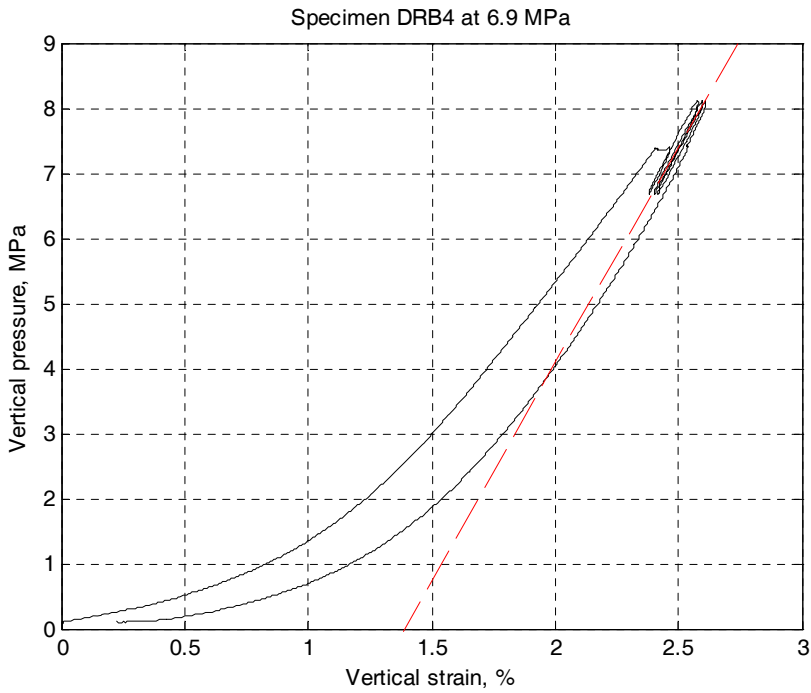
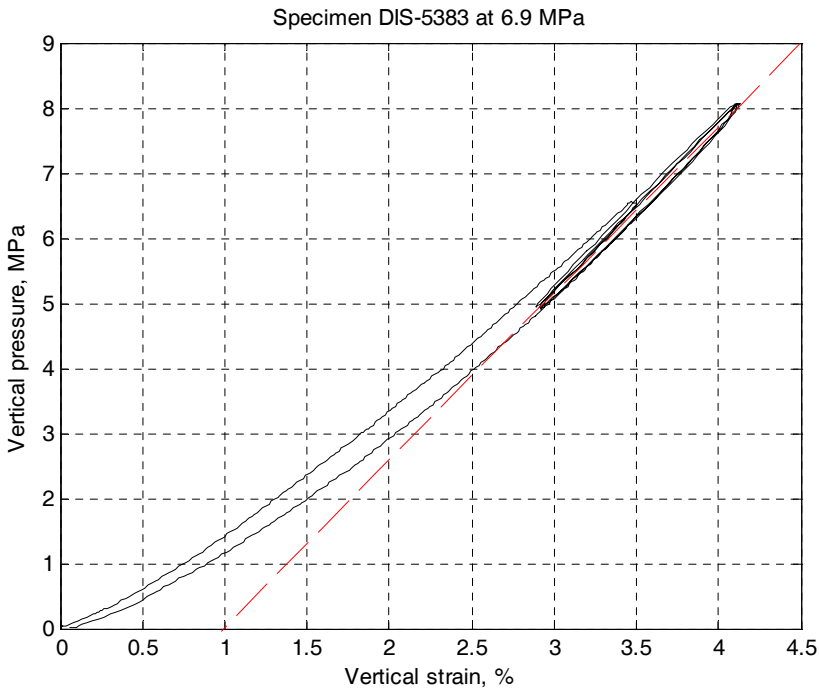**Figure 6.** Pressure deflection curve for fiber bearing.

Figure 7. Pressure deflection curve for steel bearing.

transition to the tensile extensionality of the fiber and the consequent stiffness of the composite system. These bearings can be used in a wide range of applications including seismic protection of buildings, bridge bearings and vibration isolation bearings, so there is a need to develop a method for predicting how much vertical load or vertical displacement is needed before the full vertical stiffness can be achieved. The analysis here is an attempt to formulate a prediction for the transition from the initially bent to the finally straight fiber.

The method takes the already formulated analysis for the straight fiber and modifies it by treating the fiber as a string on an elastic foundation, adds to this an estimate of the subgrade reaction of this founda- tion, and, using the basic equations of the fiber-rubber composite, calculates the effective compression modulus as a function of the vertical compression strain.

If it is no longer assumed that the force in the fiber is related solely to the extensional strain as in Equation (14) the basic equations are Equations (4), (7) and (8) and a further constitutive equation for F is required, which will be derived in the next two sections.

2.4. *String on an elastic foundation.* The equation for the deflection $v(x)$ of a tightly stretched string under the action of a lateral load $p(x)$ is

$$T_0 \frac{d^2 v}{dx^2} + p = 0,$$

where T_0 is the constant x-component of the tension force in the string. The lateral load in this case is given by

$$p = k(v_0 - v),$$

where v_0 is the initial shape of the string, giving as the equation for the deflection of the string

$$T_0 \frac{d^2 v}{dx^2} - kv = kv_0.$$

If we assume that $v_0(x) = v_0 \sin(\pi x / l)$ and $v(x) = v \sin(\pi x / l)$ where now v_0 and v are taken as constants we have

$$T_0 = k \frac{l^2 (v_0 - v)}{\pi^2 v} \quad \text{or} \quad v = \frac{v_0}{1 + T_0 \pi^2 / (kl^2)},$$

showing that $T_0 \to \infty$ as $v \to 0$ and vice versa. The initial projected length of a half wavelength of the string is l and the curved length L is given by

$$L = l + \frac{1}{2} \int_0^l \left(\frac{d}{dx} v_0(x) \right)^2 dx.$$

We assume that the curved length remains constant so that as the string tension increases the deformed projected length increases to become $l + \delta$, such that

$$L = l + \delta + \frac{1}{2} \int_0^l \left(\frac{d}{dx} v(x) \right)^2 dx,$$

from which the change in length δ becomes

$$\delta = \pi^2 \frac{(v_0^2 - v^2)}{4l},$$

and with v in terms of T_0 and v_0 from the above equation we have

$$\frac{\delta}{l} = \pi^2 \frac{v_0^2(2 + \pi^2 T_0/(kl^2))}{4l^2(1 + \pi^2 T_0/(kl^2))^2} \pi^2 \frac{T_0}{kl^2}.$$

To this result we add the stretch of the string due to its own elasticity, giving

$$\frac{\delta}{l} = \frac{T_0}{EA} + \pi^2 \frac{v_0^2(2 + \pi^2 T_0/(kl^2))}{4l^2(1 + \pi^2 T_0/(kl^2))^2} \pi^2 \frac{T_0}{kl^2}, \tag{21}$$

where E is the modulus of elasticity of the string and A is the cross sectional area.

At this point it is necessary to change from the variables of the string equations to the quantities of the fiber bearings. Thus $T_0 \to F$, $EA \to E_f t_f$ and $\delta/l \to du_1/dx$. We note that F now has the dimension of force/unit width and t_f is area/unit width.

2.5. *Estimation of subgrade stiffness between fiber and rubber.* We assume that the half-wavelength of the initial lack of straightness is much smaller than the thickness of the rubber layer and assume that the deformation takes place in a semiinfinite space and that the state of strain is plane strain. The material is assumed to incompressible.

Under these assumptions the stress strain relations

$$\epsilon_{xx} = \frac{1}{E}[(1 - v^2)\sigma_{xx} - v(1 + v)\sigma_{yy}], \qquad \epsilon_{yy} = \frac{1}{E}[(1 - v^2)\sigma_{yy} - v(1 + v)\sigma_{xx}], \qquad \gamma_{xy} = \frac{1}{G}\tau_{xy},$$

become

$$\epsilon_{xx} = \frac{1}{4G}[\sigma_{xx} - \sigma_{yy}], \tag{22}$$

$$\epsilon_{yy} = \frac{1}{4G}[\sigma_{yy} - \sigma_{xx}], \tag{23}$$

$$\gamma_{xy} = \frac{1}{G}\tau_{xy}. \tag{24}$$

The stress function Φ given by

$$\frac{\partial^4}{\partial x^4}\Phi + 2\frac{\partial^2}{\partial x^2}\frac{\partial^2}{\partial y^2}\Phi + \frac{\partial^4}{\partial y^4}\Phi = 0,$$

takes the form

$$\Phi = f(y)\sin\frac{\pi x}{l},$$

with

$$f = Ae^{\pi y/l} + Be^{-\pi y/l} + C\frac{\pi y}{l}e^{\pi y/l} + D\frac{\pi y}{l}e^{-\pi y/l},$$

where A, B, C and D are constants of integration. For a half space the constants A and C must vanish and Φ reduces to

$$\Phi = \sin\frac{\pi x}{l}\left(Be^{-\pi y/l} + D\frac{\pi y}{l}e^{-\pi y/l}\right),$$

from which the stresses become

$$\sigma_{xx} = \frac{\partial^2 \Phi}{\partial y^2} = \frac{\pi^2}{l^2} \sin \frac{\pi x}{l} \left(B - 2D + D\frac{\pi y}{l}\right) e^{-\pi y/l},$$

$$\sigma_{yy} = \frac{\partial^2 \Phi}{\partial x^2} = -\frac{\pi^2}{l^2} \sin \frac{\pi x}{l} \left(B + D\frac{\pi y}{l}\right) e^{-\pi y/l},$$

$$\tau_{xy} = \frac{\partial^2 \Phi}{\partial x \partial y} = \frac{\pi^2}{l^2} \cos \frac{\pi x}{l} \left(B - D + D\frac{\pi y}{l}\right) e^{-\pi y/l}.$$

At the top surface, $y = 0$, we have $\sigma_{yy} = p \sin (\pi x / l) = (-\pi^2/l^2) \sin (\pi x / l) B$ and $\tau_{xy} = 0$.

Thus $B = D = (l^2/\pi^2) p$ and the stresses become

$$\sigma_{xx} = -p \sin \frac{\pi x}{l} \left(1 - \frac{\pi y}{l}\right) e^{-\pi y/l},$$

$$\sigma_{yy} = -p \sin \frac{\pi x}{l} \left(1 + \frac{\pi y}{l}\right) e^{-\pi y/l},$$

$$\tau_{xy} = p \cos \frac{\pi x}{l} \left(\frac{\pi y}{l}\right) e^{-\pi y/l}.$$

To calculate the displacement field for these stresses we first calculate the strains which for the stress-strain relations from Equations (23), (24) and (25) are

$$\epsilon_{xx} = \frac{p}{2G} \sin \frac{\pi x}{l} \left(\frac{\pi y}{l}\right) e^{-\pi y/l},$$

$$\epsilon_{yy} = -\frac{p}{2G} \sin \frac{\pi x}{l} \left(\frac{\pi y}{l}\right) e^{-\pi y/l},$$

$$\gamma_{xy} = \frac{p}{4G} \cos \frac{\pi x}{l} \left(\frac{\pi y}{l}\right) e^{-\pi y/l}.$$

The resulting displacements obtained by integrating the strain-displacement equations for the first two are

$$u = -\frac{p}{2G} \cos \frac{\pi x}{l} y e^{-\pi y/l} + f_1(y),$$

$$v = \frac{p}{2G} \sin \frac{\pi x}{l} \left(1 + \frac{\pi y}{l}\right) e^{-\pi y/l} + f_2(x),$$

where at this point $f_1(y)$ and $f_2(x)$ are arbitrary functions of their respective variables. Substitution of these two displacement equations into the equation for the shear strain,

$$\gamma_{xy} = \frac{1}{G}\tau_{xy} = \frac{\partial u}{\partial y} + \frac{\partial v}{\partial x},$$

gives

$$\frac{p}{G} \cos \frac{\pi x}{l} y e^{-\pi y/l} + \frac{df_1}{dy} + \frac{df_2}{dx} = \frac{p}{G} \cos \frac{\pi x}{l} y e^{-\pi y/l},$$

from which we conclude that

$$\frac{df_1}{dy} + \frac{df_2}{dx} = 0,$$

and that the functions are equal and opposite constants, and the displacement field takes the form

$$u = -\frac{p}{2G} \cos \frac{\pi x}{l} y e^{-\pi y/l} + c,$$

$$v = \frac{p}{2G} \frac{l}{\pi} \sin \frac{\pi x}{l} \left(1 + \frac{\pi y}{l}\right) e^{-\pi y/l} - c,$$

It is reasonable to choose the upward displacement at the origin to be zero from which

$$v(0, \, 0) = 0 \quad \text{and} \quad c = 0$$

and the displacement of the surface by the applied load is

$$v(x, \, 0) = \frac{p}{2G} \frac{l}{\pi} \sin \frac{\pi x}{l}.$$

In the context of the subgrade reaction we have $p = k\delta$, which, with

$$\delta = v\left(\frac{1}{2}, \, 0\right) = \frac{pl}{2G\pi},$$

leads finally to the result

$$k = 2G \frac{\pi}{l}. \tag{25}$$

In the bearing there is rubber on both sides of the fiber sheet so that the subgrade reaction will be twice this.

2.6. *Calculation of compression modulus.* The main purpose of this paper is to calculate the compression modulus E_c as a function of the compression strain ϵ_c as the fiber is straightened from its initial imperfect condition. The procedure will be to calculate the tension force F in the fiber as a function of the compression strain and from that the pressure distribution $p(x)$, which, when integrated over the area of the bearing, gives the total compression load P. Knowing the load and the strain the modulus is calculated from

$$E_c = \frac{P}{A\epsilon_c}. \tag{26}$$

The basic equations for the fiber-reinforced strip bearing are repeated here to clarify the method. They are the constraint equation of incompressibility

$$\frac{du_0}{dx} + \frac{3}{2} \frac{du_1}{dx} = \frac{3}{2} \epsilon_c,$$

the equilibrium equation relating pressure and shear stress in the rubber

$$\frac{dp}{dx} = -\frac{8Gu_0}{t^2},$$

and the equilibrium equation for the tension force in the fiber

$$\frac{dF}{dx} = -\frac{8Gu_0}{t}.$$

Using the first equation to eliminate u_0, the third equation becomes

$$\frac{d^2F}{dx^2} = \frac{12G}{t}\frac{du_1}{dx} - \frac{12G}{t}\epsilon_c.$$

For a straight fiber, du_1/dx is the tensile strain in the fiber and is related to F through the elasticity of the fiber, but here we use the expression for δ/l from Equation (21), giving

$$\frac{d^2F}{dx^2} - \frac{12G}{t}\left(\frac{F}{E_f t_f} + \frac{\pi^2 v_0^2}{4l^2}\frac{2+F\pi^2/(kl^2)}{\left(1+F\pi^2/(kl^2)\right)^2}\right) = -\frac{12G}{t}\epsilon_c.$$

This can be written in terms of dimensionless groups of variables in the form

$$\frac{d^2}{dx^2}\left(\frac{F\pi^2}{kl^2}\right) - \frac{12G}{E_f t_f t}\left(1 + E_f t_f \frac{\pi^2 v_0^2}{4l^2}\frac{\pi^2}{kl^2}\frac{2+F\pi^2/(kl^2)}{\left(1+F\pi^2/(kl^2)\right)^2}\right)\frac{F\pi^2}{kl^2} = -\frac{12G}{t}\frac{\pi^2}{kl^2}\epsilon_c.$$

We note here that the subgrade reaction calculated in the previous section is now $4\pi G/l$ since the fiber has rubber on both sides. It is now convenient to define the following set of dimensionless variables:

$$\bar{x} = \frac{x}{b}, \quad y = \frac{\pi F}{4Gl}, \quad \alpha^2 = \frac{12Gb^2}{E_f t_f t}, \quad \beta = \frac{\pi^3 v_0^2}{16Gl^3}E_f t_f, \quad s = 3\pi\frac{b^2}{tl}\epsilon_c. \tag{27}$$

In terms of these variables the complete system of equations reduces to

$$\frac{d^2y}{d\bar{x}^2} - \alpha^2\left(1 + \beta\frac{2+y}{(1+y)^2}\right)y = -s, \tag{28}$$

on $-1 \le \bar{x} \le 1$ with $y(-1) = y(1) = 0$. It is worth noting at this point that when $s \to 0$ and $y \to 0$, this equation takes the form

$$\frac{d^2y}{d\bar{x}^2} - \alpha^2(1+2\beta)y = -s,$$

and if s is very large, y also becomes large and the term $\beta(2+y)/(1+y)^2$ tends to zero, and the equation becomes

$$\frac{d^2y}{d\bar{x}^2} - \alpha^2 y = -s.$$

When the fiber is initially straight, i.e., $\beta = 0$, the latter equation prevails, demonstrating that the effect of the initial imperfection is subsumed in the β term.

2.7. Solution Technique. Equation (28), for $y = y(x)$, is essentially unsolvable except by numerical methods, but a good approximation can be obtained by replacing $y(x)$ in the bracketed term by $\bar{y}$ where,

$$\bar{y} = \frac{1}{2}\int_{-1}^{1} y(\bar{x})\,d\bar{x}.$$

We then solve

$$\frac{d^2y}{d\bar{x}^2} - \bar{\alpha}^2 y = -s,$$

where

$$\bar{\alpha}^2 = \alpha^2 \left(1 + \beta \frac{2 + \bar{y}}{(1 + \bar{y})^2}\right).$$

The solution using, symmetry and the boundary conditions at the edges, $y(\pm 1) = 0$, is

$$y = \frac{s}{\bar{\alpha}^2}\left(1 - \frac{\cosh \bar{\alpha}\bar{x}}{\cosh \bar{\alpha}}\right),$$

and the corresponding result for $\bar{y}$ is

$$\bar{y} = \frac{s}{\bar{\alpha}^2}\left(1 - \frac{\tanh \bar{\alpha}}{\bar{\alpha}}\right),$$

finally giving as the equation for $\bar{\alpha}$

$$\bar{\alpha}^2 = \alpha^2 \left(1 + \beta \frac{2 + (s/\bar{\alpha}^2)(1 - (\tanh \bar{\alpha})/\bar{\alpha})}{\left(1 + (s/\bar{\alpha}^2)(1 - (\tanh \bar{\alpha})/\bar{\alpha})\right)^2}\right). \tag{29}$$

The solution technique is to now specify the bearing parameters α^2 and β, vary s, solve the equation for $\bar{\alpha}^2$, and, knowing this calculate first $\bar{y}$ and then $F(\bar{x})$ from

$$F(\bar{x}) = \frac{12Gb^2}{t} \frac{1}{\bar{\alpha}^2}\left(1 - \frac{\cosh \bar{\alpha}\bar{x}}{\cosh \bar{\alpha}}\right)\epsilon_c.$$

From the basic equations for the fiber bearing we have

$$\frac{dp}{dx} = \frac{1}{t}\frac{dF}{dx},$$

giving

$$p(x) = \frac{1}{t}F(x) + A,$$

where A is a constant of integration. The boundary condition on p is $p(b) = p(-b) = 0$, but that for F is also $F(b) = F(-b) = 0$, so that $A = 0$ and

$$p(\bar{x}) = \frac{12Gb^2}{t^2} \frac{1}{\bar{\alpha}^2}\left(1 - \frac{\cosh \bar{\alpha}\bar{x}}{\cosh \bar{\alpha}}\right)\epsilon_c,$$

from which we have

$$P = \frac{12Gb^2}{t^2} \frac{2b}{\bar{\alpha}^2}\left(1 - \frac{\tanh \bar{\alpha}}{\bar{\alpha}}\right)\epsilon_c = E_c(2b)\epsilon_c, \quad E_c = \frac{12Gb^2}{t^2} \frac{1}{\bar{\alpha}^2}\left(1 - \frac{\tanh \bar{\alpha}}{\bar{\alpha}}\right).$$

Since $S = b/t$, this can be written in the form

$$E_c = 4GS^2 \frac{3}{\bar{\alpha}^2}\left(1 - \frac{\tanh \bar{\alpha}}{\bar{\alpha}}\right), \tag{30}$$

where $4GS^2$ is, we recall, the modulus of the steel-reinforced bearing.

2.8. *Orders of magnitude and numerical examples.* The important quantities for any particular solution are α and β. We have

$$\alpha^2 = \frac{4GS^2}{E_f}\frac{t}{t_f}, \qquad \beta = \frac{\pi^3 E_f}{16G}\frac{v_0^2 t_f}{l^3}.$$

Typical properties for a fiber-reinforced bearing are $S = 10$, $G = 100$ psi, $E_f = 20 \times 10^6$ psi and $t/t_f = 10$, from which we get $\alpha \approx 0.25$. To estimate the value of β we assume that the initial lack of straightness v_0 is of order t_f and that there are 10 half-wavelengths across the width of an individual layer which gives a value of 400. The initial modulus is given by

$$E_c^0 = 4GS^2\frac{3}{\alpha^2(1+2\beta)}\left(1 - \frac{\tanh\alpha(1+2\beta)^{1/2}}{\alpha(1+2\beta)^{1/2}}\right),$$

and the fully developed modulus by

$$E_c^\infty = 4GS^2\frac{3}{\alpha^2}\left(1 - \frac{\tanh\alpha}{\alpha}\right).$$

For this selection of parameters the quantity $\alpha(1+2\beta)^{1/2}$ takes the value 7.1 and the initial modulus is

$$E_c^0 = 4GS^2(0.0510),$$

and the asymptotic modulus is

$$E_c^\infty = 4GS^2(0.9756),$$

a ratio of about 19, showing how a small deviation from initial straightness can cause a very large reduction in the stiffness and presumably lead to the observed initial run-in before the full stiffness of the bearing is developed.

The question still to be resolved is the level of vertical compression needed to produce a straight fiber. To determine this it is necessary to calculate the evolution of E_c as a function of s from its initial value at $s = 0$. It should be recalled that s depends on ϵ_c through Equation (27). For the parameters already used, we have $s = 1000\epsilon_c$. The process is now to insert values of s into Equation (29) calculate $\bar{\alpha}$, and then calculate E_c from Equation (30). To evaluate the average pressure on the surface of the bearing that is needed to achieve a certain value of the modulus it is only necessary to multiply the current value of $E_c(\epsilon_c)$ by ϵ_c to provide this information. A number of examples have been computed from the analysis, with the only difference between them being the degree of initial imperfection of the fiber. Thus we fix α and vary s and calculate E_c in terms of ϵ_c and then the average pressure $p = E_c\epsilon_c$ for certain values of b. These examples are shown in Figure 8. It is clear that the initial lack of straightness can have a very large effect on the initial stiffness of the bearing but it is also clear that it is not necessary to have the fiber totally straight for the stiffness to achieve the effective final value.

It is worth noting that at this value of α the effect of the flexibility of the fiber reinforcement is, if the fiber were straight, quite small; the reduction in the compression modulus is only 2.5% and one could speculate that the large effect of the initial lack of straightness could be due to this. To check if this in fact the case the results were computed for the example corresponding to a reduction of the fiber modulus by a factor of sixteen giving $\alpha = 1.00$. These results are shown in Figure 9. It is clear that even with a very flexible fiber the initial lack of stiffness still plays a major role in the evolution of the modulus and the load deflection curve.
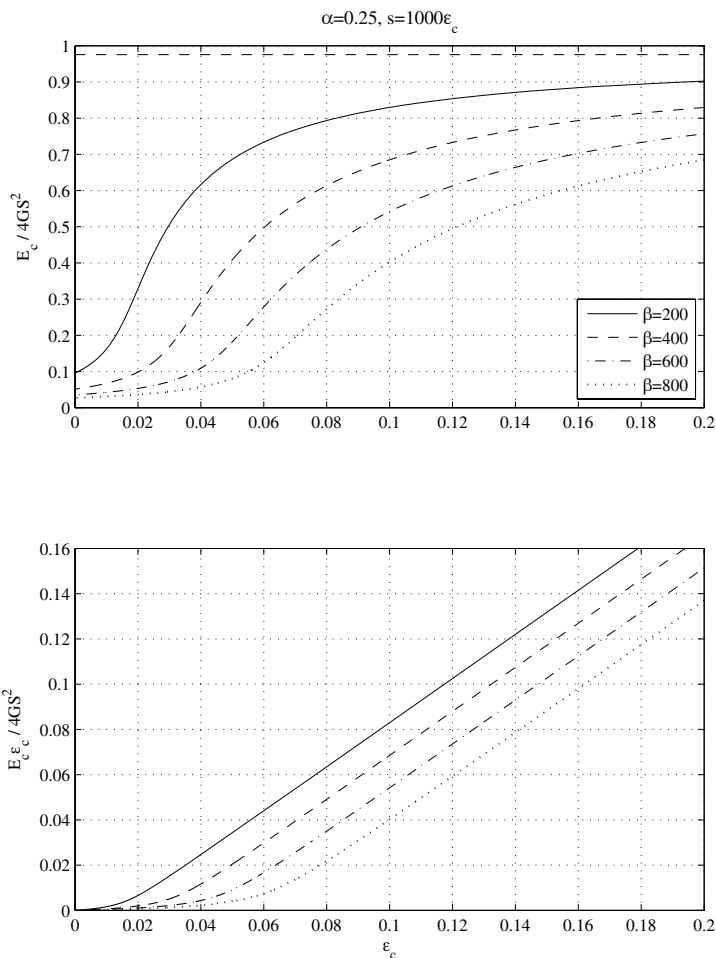
Figure 8. Run-in for high-stiffness fiber case: modulus and pressure vs. strain.

3. Conclusions

The main difference between the behavior of a fiber-reinforced and a steel-reinforced bearing is the degree of run-in under vertical loading. In this paper it has been shown that this can be attributed to an initial lack of straightness in the fiber and since in certain cases it may be necessary to predict this, a theoretical analysis of the effect has been developed. The theory has been based on well-known principles of solid mechanics. The analysis has shown that a quite small initial lack of straightness in the fiber can have a surprisingly large effect on the initial stiffness of the bearing. However the asymptotic value of the stiffness, the stiffness when the fiber is assumed to be completely straight, is actually achieved well before the fiber has completely straightened out. This is an encouraging result since the point of using fiber-reinforced bearings as isolators is to develop a lower-cost manufacturing approach than that for steel-reinforced bearings. An effort to hold the fiber tight during the vulcanization process would lead to higher costs and defeat the purpose of the endeavour.
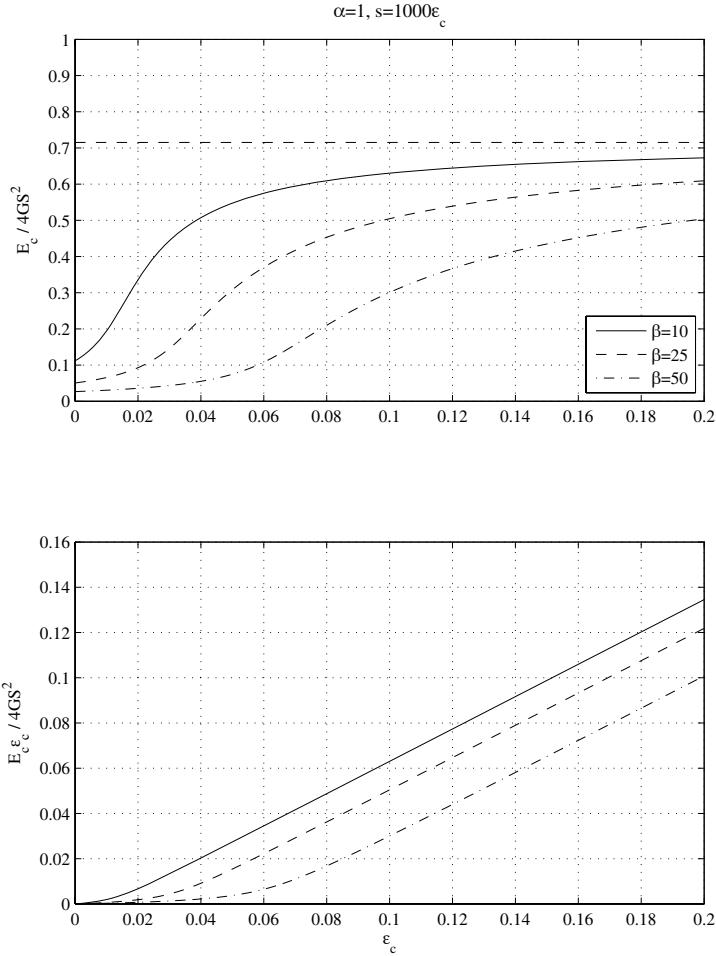
Figure 9. Run-in for low-stiffness fiber case: modulus and pressure vs. strain.

References

[Gent and Lindley 1959] A. N. Gent and P. B. Lindley, "The compression of bonded rubber blocks", *Proceedings Institution of Mechanical Engineers* **173**:3 (1959), 111–117.

[Gent and Meinecke 1970] A. N. Gent and E. A. Meinecke, "Compression, bending and shear of bonded rubberblocks", *Polymer Engineering and Science* **10**:2 (1970), 48–53.

[Kelly 1996] J. M. Kelly, *Earthquake-resistant design with rubber*, 2nd Edition ed., Springer-Verlag, London, 1996.

[Kelly 1999] J. M. Kelly, "analysis of fiber-reinforced elastomeric isolators", *Journal of Seismic Engineering* **2**:1 (1999), 19–34.

[Kelly 2002] J. M. Kelly, "Seismic isolation systems for developing countries", *Earthquake Spectra* **18**:3 (2002), 385–406. EERI Distinguished Lecture 2001.

[Moon et al. 2003] B. Y. Moon, B. S. Khang, and H. S. Kim, "Mechanical property analysis and design of shock absorber system using fiber bearing by experimental method", *JSME International Journal* **46**:1 (2003), 289–296.

[Rocard 1937] Y. Rocard, "Note sur le calcul des propriétés élastiques des supports en caoutchouc adherent", *J. de Physique et le Radium* **8** (1937), 197.

[Summers et al. 2004] P. Summers, P. Jacob, P. Marti, G. Bergamo, L. Dorfmann, G. Castelliano, A. Poggianti, D. Karabalis, H. Silbe, and S. Triantafillou, "Development of new base isolation devices for application at refineries and petrochemical facilities", in *13th World Conference on Earthquake Engineering*, Vancouver, 2004. Paper No. 1036.

[Toopchi-Nezhad et al. 2007] H. Toopchi-Nezhad, M. J. Tait, and R. G. Drysdale, "Testing and modeling of square carbon fiber-reinforced elastomeric seismic isolators", *Structural Control and Health Monitoring* (2007).

JAMES M. KELLY: jmkelly@berkeley.edu
1301 South 46th St., Bldg. 451, Richmond, CA 94804, United States

SUBMISSION GUIDELINES

ORIGINALITY

Authors may submit manuscripts in PDF format on-line. Submission of a manuscript acknowledges that the manuscript is *original and has neither previously, nor simultaneously, in whole or in part, been submitted elsewhere.* Information regarding the preparation of manuscripts is provided below. Correspondence by email is requested for convenience and speed. For further information, write to:

Marie-Louise Steele
Division of Mechanics and Computation
Durand Building, Room 262
Stanford University
Stanford CA 94305

LANGUAGE

Manuscripts must be in English. A brief abstract of about 150 words or less must be included. The abstract should be self-contained and not make any reference to the bibliography. Also required are keywords and subject classification for the article, and, for each author, postal address, affiliation (if appropriate), and email address if available. A home-page URL is optional.

FORMAT

Authors are encouraged to use LaTeX and the standard article class, but submissions in other varieties of TeX, and, exceptionally in other formats, are acceptable. Electronic submissions are strongly encouraged in PDF format only; after the refereeing process we will ask you to submit all source material.

REFERENCES

Bibliographical references should be listed alphabetically at the end of the paper and include the title of the article. All references in the bibliography should be cited in the text. The use of BIBTeX is preferred but not required. Tags will be converted to the house format (see a current issue for examples), however, in the manuscript, the citation should be by first author's last name and year of publication, e.g. "as shown by Kramer, et al. (1994)". Links will be provided to all literature with known web locations and authors are encoraged to provide their own links on top of the ones provided by the editorial process.

FIGURES

Figures prepared electronically should be submitted in Encapsulated PostScript (EPS) or in a form that can be converted to EPS, such as GnuPlot, Maple, or Mathematica. Many drawing tools such as Adobe Illustrator and Aldus FreeHand can produce EPS output. Figures containing bitmaps should be generated at the highest possible resolution. If there is doubt whether a particular figure is in an acceptable format, the authors should check with production by sending an email to:

production@mathscipub.org

Each figure should be captioned and numbered so that it can float. Small figures occupying no more than three lines of vertical space can be kept in the text ("the curve looks like this:"). It is acceptable to submit a manuscript with all figures at the end, if their placement is specified in the text by means of comments such as "Place Figure 1 here". The same considerations apply to tables.

WHITE SPACE

Forced line breaks or page breaks should not be inserted in the document. There is no point in your trying to optimize line and page breaks in the original manuscript. The manuscript will be reformatted to use the journal's preferred fonts and layout.

PROOFS

Page proofs will be made available to authors (or to the designated corresponding author) at a web site in PDF format. Failure to acknowledge the receipt of proofs or to return corrections within the requested deadline may cause publication to be postponed.

Journal of Mechanics of Materials and Structures

Volume 3, № 7   September 2008